FINITE ELEMENT APPLICATION FOR STRENGTH ANALYSIS OF SCARF-PATCH-REPAIRED COMPOSITE LAMINATES

A Thesis by

Chou Shih-Pin

B.S., Chemical Engineering, Chung Yuan Christian University, Taiwan, 1998

Submitted to the Department of Aerospace Engineering
and the faculty of the Graduate School of
Wichita State University
in partial fulfillment of
the requirements for the degree of
Master of Science

December 2006

FINITE ELEMENT APPLICATION FOR STRENGTH ANALYSIS OF SCARF-PATCH-REPAIRED COMPOSITE LAMINATES

I have examined the final copy of this thesis for form and content and recommend that it be accepted in partial fulfillment of the requirements for the degree of Master of Science, with a major in Aerospace Engineering.

_____

Charles Yang, Committee Chairman

We have read this thesis
and recommend its acceptance:

_____

K. Suresh Raju, Committee Member

_____

Hamid M. Lankarani, Committee Member

ACKNOWLEDGEMENTS

Thanks to Dr. Charles Yang, Dr. Bert Smith and Dr. Raju, who inspired me to step into solid mechanism spectrum studying of structural stress and composite science. Together with seniors, Wenjun, Kota, and Santhosh, I was able to perform finite element method-ABAQUS. Thanks to the generosity of Lamia Salah, I was able to implement a comparison of test data with finite element results. This thesis is dedicated to my parents and all of the abovementioned.

ABSTRACT

The composite scarf joint configuration was utilized to simulate scarf-patch-repaired composite panels. An adhesive bonded scarf (tapered) joint was selected due to less peeling and shear stress over the bondline than with a single-lap or butt joint. The rubber-toughened epoxy film adhesive used had been characterized using ASTM D5656 Standard test (single-lap) incorporated with 2-D plane strain finite element analysis to verify its elastic and plastic properties. In addition to physical test, the ultimate shear strength of the adhesive was predicted using the von Mises and Drucker-Prager plasticity models in conjunction with dynamic shear failure criterion in the commercial finite element software ABAQUS. The numerical analysis provided satisfactory results when compared with experimental data under the relative displacement versus ultimate load level. The revised 4-pinned method more accurately predicted relative displacement than did the 3-pinned method in ASTM D5656 Standard. For composite scarf joint analysis, the 3-D stress analysis with transversely isotropic material properties of composites gave better results than the 2-D plane strain analysis. Regarding the tensile strength of repaired laminates, the finite element dynamic analysis based on the adhesive failure incorporated with the 90-degree ply failure provided the best results, which matched the experimental ultimate loads and the surface strain distributions within the overlap. As expected, the edge effects and longitudinal strain variations across the width of the repaired specimens were only observed in 3-D models and were verified by experimental data. Moreover, the 3-D static and dynamic simulations revealed the relations between laminate strength and the edge effects caused by different stacking sequences. Based on the similar geometry, it was also demostrated in this study that the balanced and symmetric stacking sequence about mid-plane of the repaired composite panel exhibits higher tensile strength.

TABLE OF CONTENTS

Chapter			Page
1.	INTRODUCTION AND REVIEW OF LITERATURE		1
	1.1	Background and Motivation	2
	1.2	Review of Literature	6
		1.2.1 Bonded Joint Repair	7
		1.2.2 Scarf (Tapered) Joint	9
		1.2.3 Three-Dimensional Stress/Strain Analysis of Bonded Composite Joints	11
		1.2.4 Progressive Failure Analysis of Bonded Composite Joints	14
	1.3	Overview of the Problem and Research Focus	18
2.	CHARACTERIZATIONS OF AN EPOXY ADHESIVE		22
	2.1	ASTM Designation: D5656 Standard	24
	2.2	Analysis of ASTM D5656 Test Results	25
	2.3	Evaluation of Linear Elastic Properties for the Adhesive	28
		2.3.1 Linear Shear Modulus and Initial Shear Yield Strength	28
		2.3.2 Linear Young's Modulus (E) and Poisson's Ratio (ν)	32
	2.4	Evaluation of Plastic Properties for the Adhesive	33
		2.4.1 Elastic Constitutive Equations	35
		2.4.2 Prandtl-Reuss Theory	37
		2.4.3 Von Mises Yield Criterion	38
		2.4.4 Linear Drucker-Prager Yield Criterion	39
		2.4.5 General Exponent Drucker-Prager Yield Criterion	44
		2.4.6 Definition of the Yield Surface	46
	2.5	Adhesive Property Calculations under ASTM D5656	46
	2.6	Determination of Analysis Model in ABAQUS	50
		2.6.1 Plasticity Model in ABAQUS	51
		2.6.2 Analytical Model in ABAQUS	52
		2.6.3 Failure Mechanism	53
		2.6.4 Shear Dynamic Failure in ABQUS/Explicit	56
		2.6.5 Shear Failure Criterion	57
		2.6.6 Element Removal	58
3.	FINITE ELEMENT ANALYSIS ON ASTM D5656		59
	3.1	Pre-processing of ASTM D5656	60
		3.1.1 Physical Features and Properties of ASTM D5656	60
		3.1.2 Artificial Density and Damping Factor	61
	3.2	Finite Element Modeling of ASTM D5656	63
	3.3	Finite Element Analysis within the Linear Elastic Region	68

Chapter Page

3.3.1 Confirmation of Adhesive Young's Modulus 68
3.3.2 Results and Observation of the Linear Region Finite Element Analysis 73
3.4 Finite Element Analysis within the Non-Linear Plastic Region 76
3.5 Comparison and Discussion of Finite Element Analysis Results 84
3.5.1 Dynamic Analysis 84
3.5.2 Classical Metal Plasticity Model 88
3.5.3 Stability and Accuracy 90
3.5.4 Drucker Prager Plasticity Model 94
3.5.5 Comparison of 3-D and 2-D Analysis 98
3.5.6 Element Type 101
3.5.7 Displacement Correction 102
3.6 Conclusions of Finite Element Analysis on ASTM D5656 106

4. SCARF-PATCH-REPAIRED COMPOSITE LAMINATES 109

4.1 Fundamentals of Scarf-Patch-Repaired Composite Laminates 111
4.1.1 Pre-Processing of OPT53 Composite Scarf Joint 111
4.1.2 Material Properties of Lamina and Adhesive 114
4.1.3 Stacking Sequences and Characteristics of Composite Laminates 116
4.2 Elastic Material Property Model in ABAQUS 121
4.2.1 Isotropic Elasticity 122
4.2.2 Orthotropic Elasticity in Terms of Engineering Constants 123
4.2.3 Orthotropic Elasticity in Terms of Elastic Stiffness Matrix 124
4.2.4 Orthotropic Elasticity in Plane Stress 124
4.2.5 Transversely Isotropic Elasticity 125
4.2.6 Anisotropic Elasticity 125
4.3 Material Property Calculations of OPT53 Composite Laminates 126
4.3.1 Material Property Assumption 127
4.3.2 Anisotropic Material Model 127
4.3.3 Orthotropic Material Model 138
4.3.4 Equivalent Isotropic Material Model 141

5. FINITE ELEMENT ANALYSIS ON SCARF-PATCH-REPAIRED COMPOSITE LAMINATES 143

5.1 Finite Element Analysis Results of OPT53 Composite Scarf Joints 149
5.1.1 Standard/Static Analysis 149
5.1.2 Comparison and Observation of Standard/Static Finite Element Analysis Results 170
5.2 Explicit/Dynamic Analysis 174
5.2.1 90-Degree Ply Failure 176
5.2.2 Adhesive Combined with 90-Degree Ply Failure 179

Chapter Page

5.2.3 Comparison and Observation of Explicit/Dynamic Finite Element Analysis Results 189
5.3 Interlaminar Stress and Edge Effect 194
5.4 Conclusions and Remarks Regarding Finite Element Analyses on Scarf-Patch-Repaired Composite Laminates 201

LIST OF REFERENCES 207

APPENDIX 214

LIST OF TABLES

Table		Page
2.1	ASTM D5656 Test Data of Metlbond FM 1515-3	26
2.2	G and S_{xy} Obtained from the 0.2% Offset Method	31
2.3	Shear Yield Strength Obtained by Different Methods	33
2.4	Calculation of Plastic Properties from Tensorial Shear Strain under the Same Shear Modulus for each Specimen	49
2.5	Calculation of Plastic Properties from Tensorial Nominal Shear Strain under Individual Shear Modulus of each Specimen	49
2.6	Calculation of Plastic Properties from Tensorial True Shear Strain under Individual Shear Modulus of each Specimen	50
3.1	Consistent Unit Definition in ABAQUS	60
3.2	Physical Properties of Metlbond FM 1515-3	61
3.3	Physical Properties in Terms of US Units for each Component	61
3.4	The Number of Element in ASTM D5656 Finite Element Analysis Models	65
3.5	ABAQUS Results for E = 175,630 psi and E = 168,167 psi with v = 0.3 from Standard/Static Analysis	69
3.6	ABAQUS Results for E = 193,023 psi and E = 198,796 psi with v = 0.35 from Standard/Static Analysis	70
3.7	ABAQUS Results for E = 213,484 psi and E = 200,172 psi with v = 0.35 from Standard/Static Analysis	71
3.8	ABAQUS Results for E = 190,400 psi and v=0.4 from Standard/Static Analysis	72
3.9	Non-Linear Properties of the Adhesive with Different Stress-Strain Definitions under Classical Metal Plasticity Dynamic Model	79
3.10	Non-Linear Plastic Properties of the Adhesive under Drucker-Prager Linear Model	80

LIST OF TABLES (continued)

Table		Page
3.11	Non-Linear Plastic Properties of the Adhesive under General Exponent Drucker-Prager Static Model	82
3.12	Young's Modulus Obtained from Various Poisson's Ratios Based on Nominal Stress-Strain and True Stress-Strain	84
3.13	ASTM D5656 2-D Finite Element Analysis Results versus 10-Average Test Data	89
3.14	ASTM D5656 Finite Element Analysis Results from Adhesive Density of Composite Scarf Joint Models	90
3.15	ASTM D5656 Finite Element Analysis Results from Artificial Density Models	91
3.16	Elastic and Drucker-Prager Plastic Properties of the Adhesive	97
3.17	Strength and Extension Comparisons from ABAQUS Results between ASTM D5656 2-D and 3-D Simulations	99
4.1	Dimensions of OPT53 Composite Scarf Joint Specimens	114
4.2	Densities for Adhesive and Adherend in OPT53 Composite Scarf Joints	115
4.3	The Volume Ratio of the Full-Scale to Reduced Specimen for each OPT53 Specimen	116
4.4	Torayca 800S/3900-2B Prepreg Properties	116
4.5	Percentage of Each Orientation Ply-Group within OPT53 Models	118
4.6	Engineering Constants for Different Orientations	140
4.7	Inspection of Stability Restrictions for each Orientation Lamina	141
4.8	Equivalent Elastic Properties (psi) Converted from Plane Stress State	142
4.9	Equivalent Elastic Properties (psi) Converted from Plane Strain State	142
4.10	Equivalent Elastic Properties (psi) Converted from 3-D Complete Constitutive Equations	142
5.1	Dimensions of Reduced Models of OPT53 Composite Scarf Joints	146

LIST OF TABLES (continued)

Table		Page
5.2	Information on Mesh in 2-D Reduced OPT53 Finite Element Analysis Models	148
5.3	Information of Mesh in 3-D Reduced (Quarter Size) OPT53 DynamicScarf Joint Models	149
5.4	Ultimate Load Comparison between Test Data and 2-D Anisotropic Dynamic Finite Element Analysis Data	175
5.5	Thickness of the Matrix Layer within a 90-Degree Ply	181
5.6	Ultimate Load Comparison between Test Data and 2-D Anisotropic Dynamic Finite Element Analysis Data	182
5.7	Ultimate Load Comparison between Test Data and 3-D Anisotropic Dynamic Finite Element Analysis Data	185
5.8	Torayca Composite Properties (1)	202
5.9	Torayca Composite Properties (2)	203

LIST OF FIGURES

Figure		Page
1.1	Schematic configuration of a flush scarf patch repair	4
1.2	Conceptual flow charts of finite element analyses from ASTM D5656 to scarf patch repair project	6
1.3	Common types of bonded joint configurations	8
1.4	Configuration of a composite taper-taper joint (a simplified scarf joint)	19
2.1	Geometrical representations of a single-lap joint under tension	23
2.2(a)	Dimensions of ASTM D5656 specimen	25
2.2(b)	KGR-1 Device and its terminology of ASTM D5656 (3-pinned)	26
2.3	ASTM D5656 adherend relative displacement versus load curves (port side)	27
2.4	ASTM D5656 adherend relative displacement versus load curves (star side)	27
2.5	G and S_{xy} obtained from the 0.2% offset method for specimen P-1	29
2.6	G and S_{xy} obtained from the 2-tangent-line method for specimen P-1	30
2.7	S_{xy} from the 2-tangent-line method with G=64,683.3 psi for specimen RP-3	31
2.8	S_{xy} from the 2-tangent-line method with G=52,500 psi for specimen RP-3	32
2.9	Average shear stress-strain curve of ASTM D5656 P-1	34
2.10	Coordinate definition in finite element analysis for ASTM D5656 and scarf joint bonded composite models	35
2.11	Von Mises yield surface on the deviatoric plane	39
2.12	Linear Drucker-Prager yield surface	41
2.13	Variations of yield surface and K of the linear model on the π-plane	42

LIST OF FIGURES (continued)

Figure		Page
2.14	General exponent Drucker-Prager yield surface and hardening in the *p*-*q* plane	44
3.1	The purpose of finite element method for ASTM D5656 test	59
3.2	Geometry and dimensions of ASTM D5656 specimen	60
3.3	Definition of plane stress and plane strain modeling in ABAQUS	64
3.4	2-D finite element mesh of entire ASTM D5656 specimen	64
3.5	Dense mesh in the adhesive region of ASTM D5656 2-D finite element model	64
3.6	(a) Locations (node numbers) of the ASTM D5656 2-D FE model where the KGR-1 device is mounted and (b) after it is deformed (deformation scale factor 30)	68
3.7	Reaction force versus relative displacement of E = 175,630 psi and E = 168,167 psi with v = 0.3 compared to star and port sides, respectively	70
3.8	Reaction force versus relative displacement of E = 193,023 psi and E = 198,796 psi with v = 0.35 compared to star and port sides, respectively	71
3.9	Reaction force versus relative displacement of E = 213,484 psi and E = 200,172 psi with v = 0.4 compared to star and port sides, respectively	72
3.10	Reaction force versus relative displacement of E = 190,400 psi and v = 0.4 compared to star and port sides, respectively	73
3.11	Comparison of ASTM D5656 results from ABAQUS and R-P1 and R-P3 star side test data	74
3.12	ASTM D5656 10-average curve versus individual averaged data curve	75
3.13	Comparison of ASTM D5656 ABAQUS results for different combinations of E and v with average test data within the linear region	75
3.14	Comparison of PEEQ converted from engineering shear strain and tensorial shear strain	77

LIST OF FIGURES (continued)

Figure		Page
3.15	Comparison of 10-average test data converted from nominal and true stress-strain	78
3.16	Finite element analysis trial data curves of the adhesive based on different stress-strain definitions under classical metal plasticity dynamic model	79
3.17	Finite element analysis trial data curve of the adhesive based on true stress-strain hardening under Drucker-Prager linear model	81
3.18	Isotropic hardening curves of the adhesive under different Drucker-Prager static model in ABAQUS	83
3.19	Response trends from ASTM D5656 FE Explicit/dynamic models (artificial density [$f\rho=10^3, \alpha_R=10$] with nominal stress-strain case)	85
3.20	System energy balance trend of ASTM D5656 FE Explicit/dynamic models (artificial density [$f\rho=10^3, \alpha_R=10$] with nominal stress-strain case)	85
3.21	Reaction force-relative displacement trends from classical metal plasticity analyses and 10-average test data	86
3.22	Reaction force-relative displacement trends from different plasticity dynamic analyses and 10-average test data	87
3.23	Linear elastic regions of reaction force-relative displacement curves from different plasticity dynamic models in ABAQUS (E=174,645 psi and ν = 0.35)	87
3.24	Response trends from ASTM D5656 FE Explicit/dynamic models (real adhesive density and adherend density with nominal stress-strain case)	92
3.25	Dynamic responses versus various damping factor α_R (real densities used for adherend and adhesive)	93
3.26	Linear Drucker-Prager model results versus 10-average test data (real density and true stress-strain)	95
3.27	Results from different static Drucker-Prager models versus 10-average test data (real density and true stress-strain)	95

LIST OF FIGURES (continued)

Figure		Page
3.28	Different Drucker-Prager model results versus 10-average test data under linear region (real density and true stress-strains)	96
3.29	Comparison of dynamic responses between ASTM D5656 2-D and 3-D ABAQUS simulations (nominal stress-strain case)	99
3.30	Comparison of different approaches for relative displacement (nominal stress-strain case)	103
3.31	Results from various finite element analysis models versus 10-average test data (based on apparent stress-strain scale) under linear region	103
3.32	Results from various finite element analysis models versus 10-average test data (based on true stress-strain scale) under linear region	104
3.33	Straight line with slope 65,000 versus 10-average test data (based on apparent stress-strain scale) under liner elastic region	105
3.34	Comparison of dynamic plastic models versus 10-average test data	106
4.1	Procedure and mutual relations of finite element analysis from ASTMD5656 to OPT53 composite scarf joint	111
4.2(a)	Geometry and terminology of the flush scarf-type bonded repair plate	113
4.2(b)	Geometry and terminology of the scarf-patch-repaired laminate plate	114
4.3	OPT53-1and 2 composite scarf joint model	115
4.4	OPT53-1and 2 composite stepped joint model	115
4.5	Definition of the coordinate system in ABAQUS	125
4.6	Specially orthotropic material (principal material axes of fiber-reinforced lamina aligned with global axes)	129
4.7	Generally orthotropic material (principal material axes of fiber-reinforced lamina not aligned with global axes)	130
4.8	Definition of plane stress and plane strain modeling surface in finite element model	131

LIST OF FIGURES (continued)

Figure		Page
5.1	OPT53 composite scarf joint 3-D finite element model	144
5.2	OPT53 scarf joint 3-D isotropic ply-merged finite element model	144
5.3	Fine mesh of OPT53-SCF 2-D static model (scarf joint) (non-uniform shape mesh in the adhesive)	147
5.4	Medium mesh of OPT53-SCF 2-D dynamic model (scarf joint) (refined and uniform shape mesh in the adhesive)	147
5.5	Coarse mesh of OPT53-STP 2-D dynamic model (stepped joint) (uniform shape mesh both in the adherends and the adhesive)	147
5.6	Longitudinal surface strain comparison of test data and OPT53-1 SCF 3-D static full-scale model	150
5.7	Longitudinal surface strain comparison of test data and OPT53-2 SCF 3-D static full-scale model	150
5.8	Longitudinal surface strain comparison of test data and OPT53-3 SCF 3-D static full-scale model	151
5.9	Longitudinal surface strain comparison of test data and OPT53-4 SCF 3-D static full-scale model	151
5.10	Longitudinal surface strain comparison of test data and OPT53-5 SCF 3-D static full-scale model	152
5.11	Longitudinal surface strain comparison of test data and OPT53-6 SCF 3-D static full-scale model	152
5.12	Half size OPT53 SCF reduced model	153
5.13	Quarter size OPT53 SCF reduced model	154
5.14a	Longitudinal surface strain comparison of test data and half size OPT53-1 3-D static-reduced model (anisotropic and isotropic properties)	155
5.14b	Longitudinal surface strain comparison of test data and half size OPT53-1 3-D static-reduced model (anisotropic and engineering constant properties)	155

LIST OF FIGURES (continued)

Figure		Page
5.15a	Longitudinal surface strain comparison of test data and half size OPT53-2 3-D static-reduced model (anisotropic and isotropic properties)	156
5.15b	Longitudinal surface strain comparison of test data and half size OPT53-2 3-D static-reduced model (anisotropic and engineering constant properties)	156
5.16a	Longitudinal surface strain comparison of test data and quarter size OPT53-3 3-D static-reduced model (anisotropic and isotropic properties)	157
5.16b	Longitudinal surface strain comparison of test data and half size OPT53-3 3-D static-reduced model (anisotropic and engineering constant properties)	157
5.17a	Longitudinal surface strain comparison of test data and quarter size OPT53-4 3-D static-reduced model (anisotropic and isotropic properties)	158
5.17b	Longitudinal surface strain comparison of test data and quarter size OPT53-4 3-D static-reduced model (anisotropic and engineering constant properties)	158
5.18a	Longitudinal surface strain comparison of test data and quarter size OPT53-5 3-D static-reduced model (anisotropic and isotropic properties)	159
5.18b	Longitudinal surface strain comparison of test data and quarter size OPT53-5 3-D static-reduced model (anisotropic and engineering constant properties)	159
5.19a	Longitudinal surface strain comparison of test data and quarter size OPT53-6 3-D static-reduced model (anisotropic and isotropic properties)	160
5.19b	Longitudinal surface strain comparison of test data and quarter size OPT53-6 3-D static-reduced model (anisotropic and engineering constant properties)	160
5.20a	Longitudinal surface strain comparison of test data and OPT53-1 2-D static-reduced model (anisotropic material properties)	161
5.20b	Longitudinal surface strain comparison of test data and OPT53-1 2-D static-reduced model (engineering constant material properties)	162

LIST OF FIGURES (continued)

Figure		Page
5.20c	Longitudinal surface strain comparison of test data and OPT53-1 2-D static-reduced model (isotropic material properties)	162
5.21a	Longitudinal surface strain comparison of test data and OPT53-2 2-D static-reduced model (anisotropic material properties)	163
5.21b	Longitudinal surface strain comparison of test data and OPT53-2 2-D static-reduced model (engineering constant material properties)	163
5.21c	Longitudinal surface strain comparison of test data and OPT53-2 2-D static-reduced model (isotropic material properties)	164
5.22a	Longitudinal surface strain comparisonsof test data and OPT53-3 2-D static reduced model (anisotropic material properties)	164
5.22b	Longitudinal surface strain comparison of test data and OPT53-3 2-D static-reduced model (engineering constant material properties)	165
5.22c	Longitudinal surface strain comparison of test data and OPT53-3 2-D static-reduced model (isotropic material properties)	165
5.23a	Longitudinal surface strain comparison of test data and OPT53-4 2-D static-reduced model (anisotropic material properties)	166
5.23b	Longitudinal surface strain comparison of test data and OPT53-4 2-D static-reduced model (engineering constant material properties)	166
5.23c	Longitudinal surface strain comparison of test data and OPT53-4 2-D static-reduced model (isotropic material properties)	167
5.24a	Longitudinal surface strain comparison of test data and OPT53-5 2-D static-reduced model (anisotropic material properties)	167
5.24b	Longitudinal surface strain comparison of test data and OPT53-5 2-D static-reduced model (engineering constant material properties)	168
5.24c	Longitudinal surface strain comparison of test data and OPT53-5 2-D static-reduced model (isotropic material properties)	168
5.25a	Longitudinal surface strain comparison of test data and OPT53-6 2-D static-reduced model (anisotropic material properties)	169

LIST OF FIGURES (continued)

Figure		Page
5.25b	Longitudinal surface strain comparison of test data and OPT53-6 2-D static-reduced model (engineering constant material properties)	169
5.25c	Longitudinal surface strain comparison of test data and OPT53-6 2-D static-reduced model (isotropic material properties) and	170
5.26	Adhesive failure model of cohesive fracture-shear	174
5.27	Stress concentrations within adhesive (OPT53-2 2-D anisotropic dynamic model)	176
5.28	90 and 0-dgree ply bonded areas within free edge parts of the overlap (OPT53-2 3-D anisotropic static model)	176
5.29	Matrix layer modeling within 90-degree ply	178
5.30	Longitudinal surface strain comparison of test data and OPT53-1 2-D anisotropic dynamic-reduced model	182
5.31	Longitudinal surface strain comparison of test data and OPT53-2 2-D anisotropic dynamic-reduced model	183
5.32	Longitudinal surface strain comparison of test data and OPT53-3 2-D anisotropic dynamic-reduced model	183
5.33	Longitudinal surface strain comparison of test data and OPT53-4 2-D anisotropic dynamic-reduced model	184
5.34	Longitudinal surface strain comparison of test data and OPT53-5 2-D anisotropic dynamic-reduced model	184
5.35	Longitudinal surface strain comparison of test data and OPT53-6 2-D anisotropic dynamic-reduced model	185
5.36	Longitudinal surface strain comparison of test data and OPT53-1 3-D anisotropic dynamic-reduced model	186
5.37	Longitudinal surface strain comparison of test data and OPT53-2 3-D anisotropic dynamic-reduced model	186

LIST OF FIGURES (continued)

Figure		Page
5.38	Longitudinal surface strain comparison of test data and OPT53-3 3-D anisotropic dynamic-reduced model	187
5.39	Longitudinal surface strain comparison of test data and OPT53-4 3-D anisotropic dynamic-reduced model	187
5.40	Longitudinal surface strain comparison of test data and OPT53-5 3-D anisotropic dynamic-reduced model	188
5.41	Longitudinal surface strain comparison of test data and OPT53-6 3-D anisotropic dynamic-reduced model	188
5.42	Dynamic trends of OPT53 non-quasi-isotropic composite scarf joint models	192
5.43	Dynamic trends of OPT53 quasi-isotropic composite scarf joint models	192
5.44	OPT53-1SCF 2-D dynamic model—adhesive failure only	193
5.45	OPT53-1SCF 2-D dynamic model—adhesive and 90-degree ply failure	193
5.46	OPT53-1COM-QUA 3-D dynamic model—adhesive and 90-degree ply failure (edge effects accounted)	194
5.47	Transverse strains measured on upper surface within overlap through the Y-direction of OPT53 3-D composite model	196
5.48	OPT53-1 3-D transverse surface strain ε_{yy} through the Y-direction within overlap (anisotropic static model)	197
5.49	OPT53-2 3-D transverse surface strain ε_{yy} through the Y-direction within overlap (anisotropic static model)	197
5.50	OPT53-3 3-D transverse surface strain ε_{yy} through the Y-direction within overlap (anisotropic static model)	198
5.51	OPT53-4 3-D transverse surface strain ε_{yy} through the Y-direction within overlap (anisotropic static model)	198
5.52	OTT53-5 3-D transverse surface strain ε_{yy} through the Y-direction within overlap (anisotropic static model)	199

LIST OF FIGURES (continued)

Figure		Page
5.53	OPT53-6 3-D transverse surface strain ε_{yy} through the Y-direction within overlap (anisotropic static model)	199
5.54a	OPT53-1 3-D delamination of 90-degree ply with matrix layers within overlap from dynamic model contour (edge effect causes delamination)	200
5.54b	Enlarged OPT53-1 3-D delamination of 90-degree ply with matrix layers within the overlap from dynamic model contour	201

CHAPTER 1

INTRODUCTION AND REVIEW OF LITERATURE

The burgeoning interest in utilizing composite materials for a wide spectrum of applications is due to their particular properties. The term 'composite material' means two or more materials mixed (hybrided) or combined homogeneously on a macroscopic level to form a purposeful third material. If designed appropriately, the advantage of composite materials is that they exhibit both the best qualities of their individual components or constituents and as well as qualities that neither constituent possesses by itself. Typically, the properties that can be improved by forming composite materials are [1]:

- Strength
- Stiffness
- Corrosion resistance
- Wear resistance
- Attractiveness
- Weight
- Fatigue life
- Temperature-dependent behavior
- Thermal insulation or conductivity
- Acoustical insulation

Not all of these properties are necessarily improved simultaneously nor is there usually any requirement to do so because some of the properties may actually conflict with one another. The objective is to design a material that possesses those desirable characteristics needed to perform the assigned task.

Applications of composite materials in the aerospace industry include all-composite wing construction, composite spoilers, composite ailerons and vertical fins, prototype composite rudders, composite vertical stabilizers, floor beams and other components of aircraft. Increasingly, military aircraft, missile and spacecraft designs as well as helicopter applications are being based on the exclusive characteristics of composite materials. In addition to design,

composite materials are also being applied as reinforcement (also known as patch), for structural repairs. Unlike metallic materials, composite materials can be easily tailored to form complex shapes and contours, and can achieve the various stiffness required in different orientations to carry combined normal and shear loads. Generally, composite materials can be utilized to repair both metallic (composite-to-metallic) [2-5] and composite (composite-to-composite) structures. Major programs and lab research concerning both primary and secondary structural repairs are currently on going for both military and commercial purposes. In the future, it can be envisioned that, in addition to the design of new structures, the technology of repair will grow in importance in the aero-industry.

1.1 Background and Motivation

In recent decades, the knowledge and techniques required for repairs of advanced composite (such as boron-epoxy, graphite-epoxy, carbon-epoxy, and other non-wood higher modulus and strength fiber-matrix materials) [6] structures have increased significantly. Damaged composite structures may cause considerable economic loss if no appropriate repair technique is developed. The cost of structural repair takes a considerable portion of the total operational and maintenance (O&M) cost for an aircraft [7]. Normally, an aircraft endures severe aerodynamic and structure loads throughout its service life. Repeated landing and take-off, maneuvering, ground handling, environmental degradation, thermal impact, and corrosion, etc., typically cause these loads [2]. Once the inevitable damage or crack has occurred, a substantial saving can be achieved if, rather than being replaced, the damaged structure can be repaired utilizing a durable and reliable process. The objective of any repair method is to restore the damaged part back to its original material strength and durability as much as is possible.

For advanced composites, the critical value 4,000 μin./in. ,established in 1979, on ultimate load strain levels allows strength degradation (due to repair process) and prevents matrix cracking [8]. Any repair which can reach 4,000 μin./in. would be estimated of adequate strength (ultimate load is supported). As for repairability expressed by strength restoration and low cost, a strength restoration to 80% of the tension ultimate allowable [9] is usually considered sufficient to cover all but the most unusual cases, while the compression ultimate allowable (might be higher than tension) is rarely used as the critical design allowable.

Since 1969, repair processes have been performed in small damaged areas and were limited to non-strength critical composite parts [7]. Composite materials have evolved from the early boron/epoxy structures to the graphite/epoxy and hybrid composite structures in current use. The most common technique used to restore a damaged structure is to repair or reinforce the damaged zone with a splice or a doubler of a material having a strength and stiffness higher than the original (parent) material. The earlier technique used to repair advanced composite materials was based on an external patch repair method. Alternate layers with film adhesive were made as a concentric stepped patch to restore some special cases. However, this repair type withstands high shear and peel stress at the edge of the cut-hole. Furthermore, the increased external protrusion will reduce the joint efficiency as the thickness of the laminate and the repair area become larger. As a result, the flush scarf patch repair (scarf-type joint with a co-cured patch flush with the outer model line (OML)) has been adopted to repair advanced composites (Figure 1.1). In the beginning, the strength restoration of flush scarf patch repair only reached 54% of the laminate allowable strength [9]. As repair methodologies have been developed and improved (from well-refined and structurally efficient flush-patch repairs to mechanically

attached metal-patch repairs), newer methods can restore large damaged areas to 80~100% of parent laminate strength [9].

According to the research by Darwish et al. [10], the use of bonded scarf patch repair for composite panel repairs (under static tensile test) can restore up to 93% of their tensile strength. However, this scarf-patch-repaired achieves its best results when used on critical, highly loaded components in which load concentrations and eccentricities must be avoided [11]. Since the flush scarf patch repair seems promising, guidelines or criteria for optimized designs of this type of adhesively bonded repair must be constructed to estimate the best of both strength and durability.

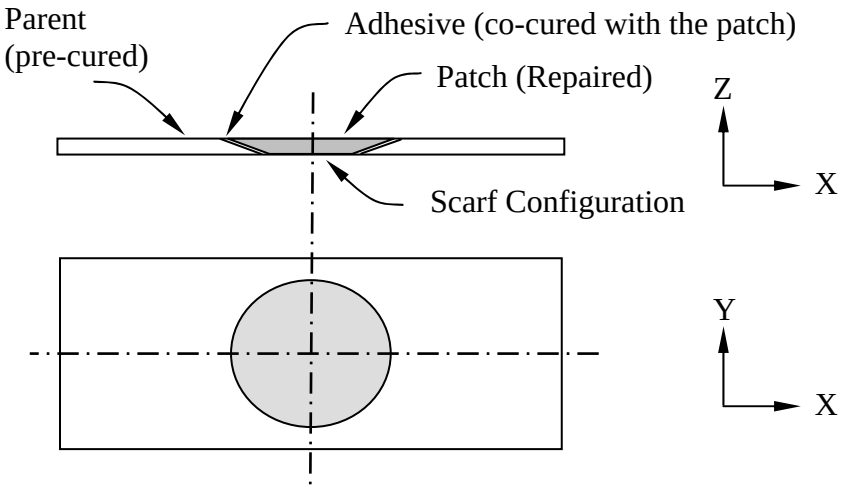

Figure 1.1. Schematic configuration of a flush scarf patch repair.

At present, the repair processes or instructions for commercial aircraft are available from the Boeing commercial aircraft company [12]. For a small damage with less than a maximum of 4 in., the repair can be conducted using the Structural Repair Manual (SRM) issued by the Original Equipment Manufactures (OEM) of the aircraft. For damage too large or too severe to be restored by the airline's shop, the advanced repair method and process should be advised or performed by the OEM. In composite repair, there is an international committee named the

Commercial Aircraft Composite Repair Committee (CACRC), organized to develop standards for composite repair. Nowadays the internet technology is easily accessible. There is an internet-based advisory service (Repair Advisory Service, RAS) [12], which was created to increase the efficiency of the repair process. The RAS system offers integrated design and repair tools for repair techniques, especially in the estimation of scarf and lap repairs based on tensile and shear failure models of repairable composite structures.

Combining computer technique with analytical methods, the computational tools such as computer programs (codes) or more advanced and comprehensive commercial software including post-process (output) have been developed for design and analysis of composite structures. They especially focus on composite joints viz. mechanical joints and adhesive bonded joints, a plethora of computational codes have been created for analysis and design of joints since 1974. An excellent integration of stress analysis codes for joints (including mechanical and adhesive bonded joints) in composite structures and incorporated with its applications and reports published was presented by Rastogi et al. [2,13,14]. Most of the codes were developed by the Air Force in association with other military aircraft companies. The theories, stress-of-state of analysis, limitations, applications (type of joints and linear or non-linear material behaviors) according to each code, and comparisons of stress distributions in adherends and adhesives obtained from some codes were listed and explained in those papers. In particular it was pointed out, MOSAIC and PGLUE codes for bonded joints and SVELT code for bolted joints are applicable to 3-D analysis (PGLUE is quasi 3-D). Commercial software viz. ABAQUS, PATRAN/NASTRAN, ANSYS, CATIA, COMET-AR, FE-77, STAGS and LS-DYNA etc. are commonly available for finite element analysis. These software package offers

particular function, capacity and limitations. Comparisons among these tools can be found in various numerical researches.

Over all existing technology and fundamentals of the scarf patch repair, the motivation is triggered to develop a reliably systematic method using finite element analysis. Confirmed by experimental results, the scenarios start from the basic material property model to systematically analytical model. The final integrated method developed can be applied to correctly calculate stress/strains, predict ultimate strength of scarf-patch-repaired composite laminates, and obtain optimum design parameters. The method should be applicable to nonlinear problems including geometry, material property, and response. The entire conceptual procedures are sketched in the flow charts shown in Figure 1.2.

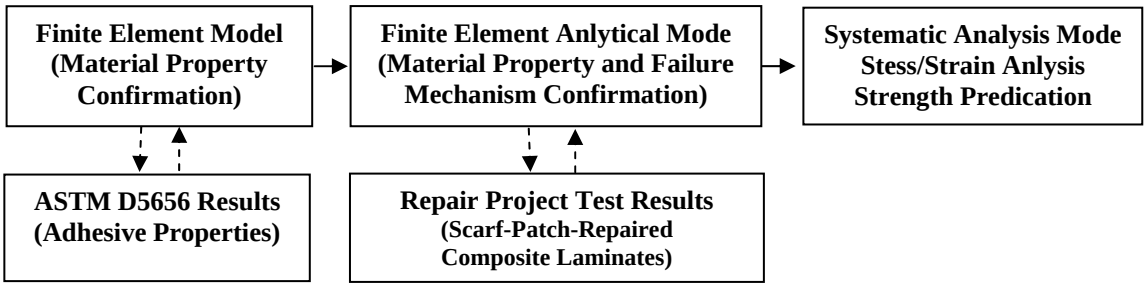

Figure 1.2. Conceptual flow charts of finite element analyses from ASTM D5656 to scarf patch repair project.

1.2 Review of Literature

The repair project is regarding the scarf-patch-repaired (simplified to taper-to-taper joint) composite laminates bonded by an epoxy film adhesive, which intends to take advantage of the highest stress resistance of scarf joint among a variety of joints. The taper or scarf shape of the composite laminate can reduce the severe edge effect and peel stress around the bonding portions, which usually occurs in single lap joints. Before the analysis method and direction decided, the eariler researches should be reviewed. The subjects are basically narrowed down to

bonded joints, three-dimensional stress-strain analysis of bonded composite joints, and progressive failure analysis of bonded composite joints.

1.2.1 Bonded Joint Repair

Advanced composites are employed in a variety of structural assemblies involving the connection of two or more components and between similar or dissimilar material systems. The repair techniques essentially rely on these assembly components usually called bonded joints, which are simplified from repair patches due to symmetry properties. The type of joints designed to combine those individuals are mainly classified as mechanical joints (such as bolted and riveted joint) and non-mechanical joints (namely adhesive bonding, welding, and brazing) [2,13]. As incorporated with advanced composites, an adhesively bonded joint is a preferred and desirable pattern to attain the structural efficiency and improve the structural integrity. In addition, the adhesively composite bonded joints contain higher strength-to-weight ratio as to reduce the weight-penalty that usually happens to conventional non-composite joints. Further in composite assemblies, the use and design of a fastener (including pattern and material), fastener holes, and the damage of the composite layers during machining these holes can be avoided. Therefore, the load is able to transfer more evenly (high stress gradient usually around fastener holes) and over a larger area, increasing the fatigue life of the repaired structure [2]. During the test, mechanical joints (bolts or fasteners) sometimes create alignment problem or specimen damage around the holes due to the friction between the fastener and the specimen.

The common types of the bonded joint applied to patch repairs in aerospace structures are shown in Figure 1.3. All of the joints are simplified (a half part about symmetry axis) from patch-repair panels due to the symmetry of geometry and loading.

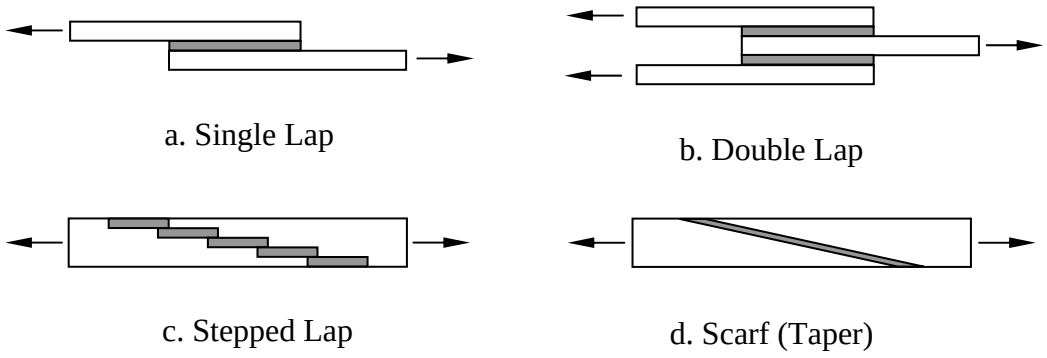

Figure 1.3. Common types of bonded joint configurations [13].

The good design and analysis of the adhesively bonded joints require analytical methodology to obtain accurate and truthful stress/strain distributions through the adherends and the adhesive. These analytical techniques were developed from continuum mechanics, plane strain/stress closed form solutions, 2-D and 3-D finite element methods, and 2-D and 3-D variational approach based on solution. Precise elasticity solutions are, so far, still difficult to obtain.

Back to 1944, Goland and Reissner published the classical work on the analysis of adhesively bonded joints. A single lap joint was analyzed to realize the relationships between the flexibility of the joints and a thin adhesive layer. The assumptions (Goland-Reissner assumptions) that the axial stress in an adhesive layer can be neglected and that normal and transverse shear stresses within an adhesive layer remain constant across the thickness of the adhesive are still followed by current researches or analysis modes [13]. Hart-Smith pointed out many aspects of efficient bonded joint design in composite structures that should be taken into account while designing bonded joints. A series of studies on single lap, double lap, stepped lap and scarf joints was studied using the continuum mechanics approach [15]. The load transfer mechanism in the adhesively bonded joints and practical approaches to minimize the transverse shear and peel stresses in the adhesive layer were included in his works. Vinson and his

colleagues [15] developed analytical and experimental work about adhesively bonded joints along with polymer composite adherends. The effects of transverse shear deformation, transverse normal strain, temperature and moisture variations were included in the analytical tools they developed. An outstanding review of the work done prior to 1969 about adhesively bonded joints was published by Kutscha [16] and Kutscha and Hofer [17]. In 1979, Schliekelmann compiled the leading researches involving analysis and design, failure response, processing and testing of adhesively bonded joints in AGARD lecture series [13]. Regarding closed-form analytical solutions of adhesively bonded joints, Delale et al., Groth, Liu, Pahoja, and Srinivas presented their works. Regarding finite element approach, Adams and Peppiatt, Amijima et al., Roy and Reddy, Sable and Sharifi, Humpherys and Herakovich, Berthelemy et al., and Barker and Hatt carried out excellent works on analysis of bonded joints.

1.2.2 Scarf (Tapered) Joint

Particularly, the scarf (tapered) joint has been shown by Erdogan and Ratwani using equilibrium equations to generate an extremely efficient load transfer between adherends [18]. Myhre and Beck [9] proposed the repair concepts for advanced composite structures using single scarf (taper-taper) joints that were subject to an extensive series of structural tests under different conditions including tension, compression, static, and post-fatigue. Myhre and Labor [8] presented the results of a large composite structure repair program under static tests. A description of the bonded-co-cured scarf joint repair was given with a review of strength and durability test results. Cao and Dancila [19] experimentally compared a modified co-cured fiber-reinforced composite nested overlap joint with a single tapered joint under monotonic tensile test. It was found that the failure load of modified nested overlap joint was 30.8% higher than that of single tapered joint.

Darwish et al. [10] studied the performance of scarf patch repair of full-scale laminated composite panel conducted by the Boeing repair manual. The study includes both nondestructive tests to characterize the quality of repair and destructive tests to evaluate the performance of repaired panels under static and fatigue loading conditions. Metzinger and Guess [4] used tapered steel adherends within tube-joints (double-lap) to reduce adhesive peel stresses. In axial tension and compression tests, the compressive strength of the joint with tapered adherends was greater than the baseline joint (butt joint) for both single-cycle and low-cycle fatigue. Moreover, a minor reduction in tensile strength was observed for joints with tapered adherends when compared with the baseline joint. In another study [5], Metzinger and Guess utilized a numerical analysis incorporated with experimental results to inspect the effects of joint geometries on compressive axial testing. It revealed that the specimens (tube joints) with extra adhesives had a higher monotonic strength and longer low-cycle fatigue lives than did the baseline and adherend-tapered joints. However, the adherend-tapered joint exhibited lower monotonic strength than did the baseline joint, and the reason was not explained clearly in their study.

Soutis and Hu [11,20] used analytical and 3-D numerical models to determine the stresses in scarf-patch-repaired laminates under uniaxial compression. To avoid nonlinear analysis, an average stress failure criterion (ASFC) was used with finite element stress distributions to estimate the ultimate strength of the 3-D repaired configuration. The semi-empirical analysis (2-D analysis) underestimated the strength of the scarf-patch-repaired laminates by more than 40%. It predicted a smaller optimum scarf angle of 4 degrees compared with an angle of almost 7 degrees using the ASFC. The study, presented by Johnson [18], used a 2-D plane stress finite element method to detail stress variations in composite scarf joints (cross-ply laminates) subjected to a unit tensile load. The oscillated stress curves obtained were significantly different

from those smooth curves predicted by closed-form solutions. Because different load-carry capacities of the orientation plies caused irregular distributions, whose characteristics were associated with the location of each ply within a stack.

Research [21] presented using tapered composite structures to prevent delamination and compare with adding soft inner layers (structural adhesive) under uniaxial tensile load. The study utilized a 3-D numerical approach, but the analysis of the laminates, within the model far away from the tapered part, was treated as a 2-D plate problem. The analysis was verified by the solution obtained from the classical laminated plate theory (CLPT). Pervez et al. [22] performed 3-D finite element simulation (ABAQUS) of taper-taper joints (scarf joint) for cross-ply laminates in order to compare the results of stress/strain distributions with the analytical solutions from Helms et al. Various scarf angles, ranging from 30 to 90 degrees, were selected to demonstrate the variation in peel stress with a scarf angle. The numerical results agreed well with the analytical solutions. It was also deduced that, far away from the overlap, the us of CLPT is still valid whereas, in the very vicinity, is inappropriate due to significant transverse shear deformation effects.

1.2.3 Three-Dimensional Stress/Strain Analysis of Bonded Composite Joints

Analyses of laminated composite structures in nature are 3-D problems; especially the variations of stress/strain through the laminate thickness direction (interlaminar stress) are of interest. The variations of stress/strain of sublaminates (interlaminar stress/strain) or through the width of specimens (edge effects) and stress concentrations in the vicinity of geometric changes leading to delamination are considered as factors of failure and fracture mechanisms. Most of the analyses, using a conventional 2-D stress state viz. plane stress or plane strain analysis, cannot cover interlaminar transverse normal, shear stress/strain, and free edge effects on failure

mechanisms. Recently, more researches suggested [2,13,23] or have expanded [17,24-31] the previous 2-D analyses to the 3-D complete stress analysis in order to predict axial strength, fatigue ,and progressive failure mechanism associated with interlaminar stress/strain and edge effects, particularly belonging to laminated composites structures.

Comparisons among the 2-D and the 3-D numerical analysis and experimental results [31] showed that the stress distributions obtained from the SAVE (a 3-D linear elastic structural analysis program developed in FORTRAN language) predicted more accurate qualitative correlation with the experimental observations for various double-lap bonded joint configurations studied. By contrast, BONJO (a closed-form, quasi-2-D analysis program) provided a lower magnitude of the adhesive transverse shear stress (τ_{xz}) for all the cases studied than did that from 3-D SAVE analysis. Research [24] showed that a 3-D model (Mosaic Model) was used to predict the 3-D variational stress/strain and progressive failure analysis of adhesive composite joints and to compare with experimental results. The 3-D analysis provided accurate strain predictions for double-lap composite-to-composite adhesive joints, except for a small region nearby the end of the overlap.

A numerical analysis, presented by Rastogi [32], used variable-order solid elements (rectangular, cylindrical and wedge elements) within a computational tool SAVE to perform the 3-D, linear elastic, hygrothermomechanical analysis of many complex structures, which contain a wide spectrum of material behaviors such as isotropic, orthotropic or monoclinic. In addition, Rastogi et al. [31] compared analytical solutions obtained from a quasi 2-D analysis program BONJO [13] and 3-D SAVE analysis, with experimental results of design parameters in composite double-lap joints. The study spoke that the remarkable difference in stress distributions (including longitudinal, transverse, transverse normal and shear stress along the

longitudinal direction) in the adhesive and adherends within the overlap obtained from these two analytical models.

Bogdanovich and Yushanov [24] presented numerical analyses incorporated with experimental results, in 3-D variational stress/strain and progressive failure analysis of adhesive composite joints. The displacement filed in a composite structure was approximated in terms of triple series with Bernstein basis functions, used for all three coordinate directions. A progressive failure analysis approach, utilizing the strain energy release rate, was adopted to predict various scenarios of cohesive, adhesive or interlaminar crack propagation.

Engelstad et al. [25] published the application of Zig-Zag finite elements (implemented as user element in the ABAQUS commercial finite element software) for composite bonded tee-joint modeling. The family of Zig-Zag elements was developed under the Composite Affordability Initiative (CAI) program. The elements are relatively insensitive to large aspect ratio issues and utilize higher-order thickness direction kinematics for improving ply-level displacements and stresses. The approach successfully reduced the degrees of freedom (problem size) compared with ABAQUS modeling. It still accurately predicted the interlaminar stresses and stress variations across the width of specimens (in agreement with results from StressCheck software).

Vizzini and Lee [26] emphasized that the 2-D modeling of the tapered section of finite-width tapered laminates cannot sufficiently describe effects of the stress-free edges due to discontinuities occurring at the terminated plies and the stress-free edges. As a result, the 3-D modeling was used to perform damage analysis of composite tapered beams. Rybicki expended the procedure to a 3-D analysis of interlaminar stresses, which achieved better agreement with

Pagano solutions [30]. Wang and Choi presented an extensive analysis on the edge singularity and concluded that the state of stress was inherenly 3-D [30].

1.2.4 Progressive Failure Analysis of Bonded Composite Joints

A general methodology for a progressive failure analysis, at each load step, a nonlinear analysis is implemented until the solution is converged without any change of material models. Based on this equilibrium state, the stresses of each lamina are calculated from the nonlinear analysis solution at the current step. These stresses are then compared with material allowables or applied to certain failure criteria. The key features, involving in progressive failure analysis of laminated composite structures are detailed in the work presented by Sleight, Knight, and Wang [33]. Varieties of numerical analyses are mentioned in this study, such as Ocha, Reddy, Pandey, Engblom, and Engelstad, etc. Several criteria are discussed, including the maximum strain criterion, Christensen's criterion, and Hashin's criterion. The progressive failure models can be classified as different the models of failure, such as fiber failure, matrix failure, shear failure, or interaction of failure models.

In study [12], the RAS system also provides a software package for scarf and lap repairs in order to predict the tensile failure and shear failure of repaired structures. Parent laminates and repaired patches, made of fiber-reinforced prepregs, behave linearly elastic. The failure models are on the basis of the maximum strain criterion for tensile failure, while the shear failure model is used for interfacial failure. The shear failure is modified from Hart-Smith models and can be applied to an individual composite layer with anisotropic property. The adhesive between the parent laminate and the repaired patch is treated as an interlayer with elastic-perfectly plastic shear behavior. Typically, the base (parent) laminate and the repaired patch fail in tension, whilst the interlayer adhesive fails in shear.

Another comprehensive discussion of failure analysis of adhesively bonded composite joints was edited by Yarrington et al. [27]. The stress and failure analysis of composite bonded joints have been developed in HyperSizer capacity. HyperSizer can calculate 3-D stresses in order to predict failure loads in bonded composite joints with complex 3-D stress states. Failure prediction requires an accurate stress analysis and an appropriate failure criterion with respect to each specific failure model. For bonded joints, the failure may occur in the adhesive, on the adhesive-adherend interfaces, or in the adherends. The failure models in the adherends might be owing to tension or compression failure of matrix, fiber failure in tension or compression, and delamination, etc. Composite joints fail progressively after a damage is initiated from the adherends or the adhesive. The ultimate failure of joints can be accessed once the progressively accumulated damage exceeds the tolerance. Various failure models associated with linear or nonlinear material properties of the adhesive are discussed combined with comparison of numerical and experimental results in study [27].

A progressive failure analysis approach [24] used the strain energy release rate to predict various scenarios of cohesive, adhesive or interlaminar crack propagation. An initial crack(s) can be located between the adhesive and adherend, inside the adhesive, or between the layers of composite adherends. Generally, the adhesive joint fails by a progressive crack growth so as the appropriate ultimate failure criteria cannot avoid the use of fracture mechanics. Neither gross nor average stress criterion is adequate to describe structure's performance. Accordingly, a structural design must be limited to a fracture criterion. Klug et al. [34] used a stress intensity factor in fracture mechanisms to characterize aluminum cracks and used the distribution of strain energy release rate in composite-metallic repairs. Fatigue crack growth data were evaluated from ultrasonic C-scan and an aluminum crack growth was observed from optical microscope.

Numerical, experimental, and ultrasonic C-scan were incorporated together in the study to characterize and compare the fatigue behaviors of double side and single side bonded composite repairs.

Adhesive Failure

Many earlier researches utilized the strain energy release rate or stress intensity factors including the fracture Mode I, II, and mixed Mode I-II to describe experimental characterizations of fracture toughness. It was believed that crack(s) always propagates inside the adhesive, yet in many cases extremely close to the adherend. Some issues such as the effect of surface preparations, the effect of plastic deformations (especially for toughened adhesive), and micro-crack(s) of the adhesive advancing the main crack front, etc. were addressed. An experimental study of single-lap and double-lap joints with SEM photo inspections presented by Long [35] declared that, in single-lap joints, the crack might start in the adhesive fillet, causing its de-bonding from the edge of the specimen through the prepreg layer close to the adhesive, and then propagate there and cause the final failure. No failure of the adhesive layer was found in their tested single-lap joints. In their double-lap joint tests, the initial adhesive failure was found with the final failure, always occurring within prepreg layers close to the bondline.

Interfacial Failure

In the tests of unidirectional and angle-ply S-glass fiber-reinforced plastics jointed by Hysol EA951 adhesive studied by Renton et al. [36], it was found that a basic pattern of failure was either a cohesive or adhesive failure. In fatigue tests, for most of angle-ply specimens, the resin in the ply adjacent to the adhesive failed first. Composite joints, tested with a toughened epoxy adhesive Ciba-Geigy XD911 studied by Adams [37], were observed that all joints failed by interlaminar fracture of carbon fiber-reinforced prepregs within the adherends. Two possible

mechanisms were proposed. The initial cohesive failure may result in cracks that break through the adhesive to the interface after composite's failure transversely in an interlaminar manner. Another mechanism suggested that the transverse tensile stress at the edge of the joint close to the interface results in the interlaminar failure of the adherend.

From the studies proposed by Donaldson et al. and Roy et al. [38] on double-lap joints under tensile test, an observed crack was generally initiated in the region having a maximum peel stress (at the end of the overlap), and was first detected, when the load level reached 70% of the ultimate failure load. Based on SEM inspections, independent of surface preparation techniques, the failure was clearly observed within the laminate surfaces. The conclusion drawn in these works was to develop 3-D progressive failure criteria for the correlation between the analysis and experiments. Wang and Yau studied interfacial cracks in adhesively bonded scarf joints [15]. Interfacial cracking (de-bonding) is one of the most common encountered failure mechanism the joints. The crack(s) initiates at geometric and material discontinuities such as the edge of adhesive-adherend interfaces. Any assumed failure mechanism without consideration of thin but critical adhesive layers would be inappropriate.

Delamination of Composite

Free-edge delamination problems include the strength of materials and fracture mechanics. The strength of materials approach defines a failure to occur when a critical stress state exceeds material allowables. The fracture mechanics approach suggests that the ignition and growth of a crack depends on the energy state at that local station. Yarrington et al. [27] showed a tapered flange bonded to a skin joint using a 3-D numerical model in HyperSizer to calculate the interlaminar stresses through the thickness of the adherends. The stress analysis results provided a basis for failure analysis. The failure criteria for delamination and matrix

cracking were applied to predict the onset of damage. The failure of test specimens was detected in the skin adherend only. Based on Fenske and Vizzini [30], the delamination can be modeled as the failure of a resin (matrix) rich region between plies. Another premise of fracture mechanics, applied to the delamination of composites, is that the delamination initiates from a crack in the thin, isotropic, homogeneous, and brittle matrix material between plies. In the application of fracture mechanics for composites, presented by O'Brien [39,40], the delamination size and strain energy were required information for delamination. It was concluded that interlaminar flaws at the free edge, originally within the material or caused by a stress singularity, are not sufficient to cause the delamination until a critical strain energy release rate is attained. In Vizzini and Lee's [26] work, a 3-D progressive failure model for tapered $[\pm 45_2/0_4]$s composite beams indicated that the resin pocket failed earlier than the onset of delamination. Damage initiated at the ply drop and not at the root of the taper for the configuration studied.

1.3 Overview of the Problem and Research Focus

The objective of this study is to use numerical analysis (finite element method), utilizing ABAQUS software incorporated, with experimental results to determine the ultimate strength (static/monotonic strength) of single-lap joints (ASTM D5656 models) and scarf joints (scarf-patch-repaired composite laminates) and to explore failure mechanisms. The composite scarf joint analyzed in this investigation is to simulate the 2-D scarf-patch-repaired laminates. A parent, pre-cured composite laminate, is tapered at one end by a design angle. The repair patch is laid up with B-stage prepregs associated with a specified stacking sequence onto the tapered parent laminate. A thin layer of the film adhesive is used to bond the parent laminate and the prepreg to form a taper-taper joint (a simplified scarf or single scarf joint shown in Figure 1.4). The assembly is then co-cured according to the material specs of the prepreg.

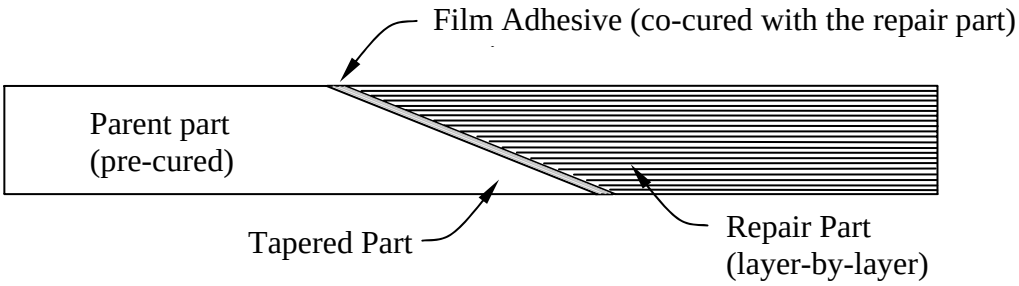

Figure 1.4. Configuration of a composite taper-taper joint (a simplified scarf joint).

The incomparable feature of performing finite element analysis is to compensate for analyses or simulations that the physical test cannot achieve, in the sense that, it makes entire analysis process more rigorous and complete. The ABAQUS was selected to perform the numerical analysis owing to its powerful and comprehensive functions and precision, especially in nonlinear analysis (including nonlinear material property, nonlinear geometry, and nonlinear response). The entire repair project is generally divided into two parts: (1) characterizations of the epoxy adhesive and (2) strength analysis of scarf-patch-repaired composite laminates. Confirmed material data of the adhesive from the first parts will be applied to the second part due to the same material. The types of joint involved in the analyses are single-lap and scarf joints. The research focuses on several issues

- Derivation and confirmation of the material properties for the epoxy film adhesive using yield criteria and various plasticity models
- Strength prediction, based on the failure criteria available in ABAQUS, and discussion of failure mechanisms
- Comparisons of elasticity models for laminated composites
- Exploration of interlaminar stresses and edge effects within scarf-patch-repaired composite laminates

The analysis methods and procedures of this study are briefly described as follows.

The rubber-toughened epoxy film adhesive selected in this project has been tested using ASTM D5656 Standard for displacement/applied force relationship. Comparing the displacement/applied force relationship obtained using the ASTM D5656 tests with the calculated displacement/applied force relationship, using 2-D plane strain finite element analysis, the elastic and plastic material properties of the adhesive can be determined. The von Mises and the Drucker-Prager plasticity models are chosen to simulate and confirm isotropic strain hardening behaviors. The numerical results obtaining from these two plasticity models will be confirmed by comparing with test data and be utilized to perform the subsequent failure analysis.

The scarf-patch-repaired laminates bonded by the adhesive have also been tested for their ultimate loads based on various dimensions, scarf angles, and stacking sequences. The pre-cured parent laminates were fabricated by unidirectional carbon/epoxy prepregs with the same ply thickness. One end of the parent composite is tapered in a desired angle. The repair prepreg is laid up on the tapered parent laminate, bonded and co-cured with the epoxy film adhesive to form a taper-taper joint (Figure 1.4). Both the parent and the repaired laminates have an identical stacking sequence.

Through the whole analysis, the adherends are assumed to be elastic. Several material models, including transversely isotropy, orthotropy (engineering constants), and equivalent isotropy, are used to model the different orientation laminae within the parent and repair laminates. The properties of each different orientation ply are pre-calculated and inputted into the finite element models. After various analysis models (2-D plane strain and 3-D stress analyses) are performed, the results, from various plasticity models for the adhesive and elasticity models for the composite, are compared with test results and evaluated before proceeding the strength and failure analyses.

The failure criterion proposed is based on physical observations and the results from the physical tests, and suitable for both the ASTM D5656 models and the repaired composite laminates (taper-taper joints). Because the shear and peel stresses dominate the failure mechanism of an adhesive within single and taper-taper joints, a 'shear failure criterion' is chosen as a failure criterion for the adhesive in both the single-lap joints (ASTM D5656 test specimens) and the composite taper-taper joint (repair project). The shear failure criterion is expressed in terms of time dependant equivalent/effective plastic strain along with 'element removal' feature within ABAQUS to determine the ultimate load of the adhesive bonded joints. Ultimate loads, force-displacement relationships (for ASTM D5656 tests), and longitudinal surface strain distributions (for repaired composite laminates) from the physical tests are used to verified the numerical analyses with different material models and failure criteria. Various parameters of design for repaired composite laminates viz. scarf angle, stacking sequence, and the size of a panel are evaluated at same time.

Expended from 2-D simulations, 3-D finite element analyses are specially utilized to reveal the interlaminar stress/strain (through thickness-direction) and the free edge effects (across the width) which usually cause the delamination of laminated composites. The failure mechanisms of the repaired composite laminates are constructed by estimating adhesive failure, cohesive failure, matrix failure, weak ply failure, and edge effects, etc.

CHAPTER 2

CHARACTERIZATIONS OF AN EPOXY ADHESIVE

An outstanding design of joints not only withstands higher strength, but also predicts accurate stress distributions in both adhesive and adherend. This essentially relies on the correct methodologies to evaluate reliable mechanical properties, appropriate failure criteria, and reasonable fracture mechanisms for the adhesive materials utilized. Before the scarf-patch-repaired (scarf joint) composite specimens are analyzed and simulated for the prediction of ultimate strength using finite element methods, the required information of the film adhesive should be confirmed in advance.

In general, the stress-strain curve of the adhesive must be known in order to obtain the effective moduli, initial yield strength, ultimate load, and failure load. Furthermore, it also can be extended to acquire failure in shear, tension, and compression [41]. In advanced analysis, the temperature, humidity (moisture content), loading speed (crosshead speed), and test specimens (film or bulk form), and bond configuration should be considered. Generally, the mass density of an adhesive is expressed in terms of the area density rather than the bulk volume density, due to its film shape. The test specimens should be nearly the same surface-area-to-volume ratio as the adhesive bonded in joints. A thin adhesive film is chosen for the adhesive-bonded scarf joint of the repair project, so that mechanical material properties of the film adhesive obtained from bulk form are inappropriate. Without any correction made for Poisson's ratio constraints, the behavior of the adhesive in thin-film form appears to be different from the adhesive in bulk form [42]. As a result, it is suggested that test specimens for determining mechanical properties should be of thin-film configurations.

Since the adhesive layer is designed to carry shear, the adhesive shear properties, such as shear moduli and strength, are intensively focused and must be determined through experimentation. Some difficulties are encountered in obtaining the pure shear or pure tensile stresses required to determine the corresponding properties. As shown in Figure 2.1, due to the bending of the adherends, a high adhesive peel (transverse tensile) stress inevitably occurs at the edges of the overlap. Neither pure nor uniform adhesive shear stress exists in such a lap-joint configuration.

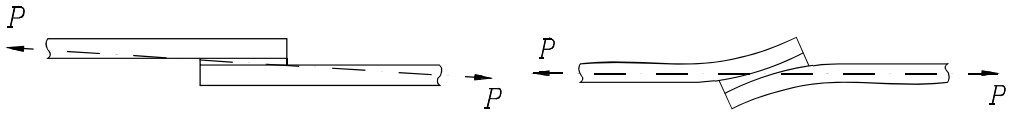

a. before loading b. after loading

Figure 2.1. Geometrical representations of a single-lap joint under tension.

Therefore, certain standardized measures namely, ASTM standards, are needed to obtain accurate mechanical material properties of the film adhesive. Generally, ASTM standards utilize a thin, or film, adhesive and thick adherends in simple single-lap joints under in-plane tensile loading, which is more convenient for analysis. Several common ASTM standard tests related to shear strength of a bonded adhesive are listed as follows:

- ASTM D3983-98'Standard Method of Test for Measuring Strength and Shear Modulus of Nonrigid Adhesives by the Thick-Adherend Tensile-Lap Specimen.'
- ASTM D5656-01 'Standard Test Method for Thick Adherend Metal Lap-Shear Joints for Determination of Stress-Strain Behavior of Adhesives in Shear by Tension Loading.'
- ASTM D3165-00 'Standard Test Method for Strength Properties of Adhesives in Shear by Tension Loading of Single-Lap-Joint Laminated Assemblies.'

The above Standard tests utilize a lap-joint configuration, which is easier to analyze and

has been studied in a wide spectrum. ASTM D3165 is suitable for determining shear strength using thin adherends in large area joints; on the contrary, the adhesive usually responds differently in small area joints. ASTM D3983 is typically used for adhesives having shear moduli ranging up to 700 MPa and is generally used for joints in which the ratio of adherend tensile modulus to adhesive shear modulus is greater than 300 to 1. ASTM 3983 is not appropriate for adhesives that have a high shear modulus in the cured state. Most of the standard tests listed above provide only relative strengths rather than engineering properties directly required for joint design. Those engineering constants are converted from these monotonic stress-strain curves. In order to apply failure criteria or fracture mechanisms to joints, it usually requires stress-strain relations (strain or stress allowable and strain energy release rate) in addition to merely strength data. The standard test, including simpler conversion of lap-shear stress-strain relations, is preferred. As a result, without considerations of temperature and loading speed factors, the standard test for adhesive properties involving thick adherends and a thin adhesive is the ASTM D5656 test.

2.1 ASTM Designation: D5656 Standard [43]

(Standard Test Method for Thick-Adherend Metal Lap-Shear Joints for Determination of the Stress-Strain Behavior of Adhesives in Shear by Tension Loading)

The significance and the use of the ASTM D5656 standard test are:

1. The method is appropriate to test of thick-adherend lap-shear specimens for the evaluation of the shear stress-strain relationship and the proportional-limit of the stress-strain relationship of an adhesive.
2. The method consists of testing thick-adherend lap-shear specimens on which a tension load is applied but the adhesive is under shear.

3. Peel stresses caused by the bending of adherends is minimized due to the significant thickness (0.375 in.) and rigidity of the aluminum (2024-T3) adherend.
4. The revised 4-pinned configuration will be introduced to correct inherent drawbacks of the original ASTM D5656 3-pinned configuration due to scattering test data [42].

The schematic figure of KGR-1 Device (3-pinned) on the ASTM D5656 specimen and terminology are shown in Figure 2.2. The mechanical properties of the adhesive, including elastic and plastic properties, can be converted based on the stress-strain relationships obtained from the ASTM D5656 standard test with certain assumptions and/or calibrations (discussed in section 2.3 and 2.4).

2.2 Analysis of ASTM D5656 Test Results

The adhesive selected is an epoxy film adhesive, Cytec Metlbond FM1515-3. It has been tested following ASTM D5656 Standard under quasi-statically monotonic loading (step loading at 550 lbf/min) and was loaded incrementally until its failure at room temperature. The result data integrated via calibrations and statistics are summarized in Table 2.1. The load-displacement (extension) relations of the adhesive are shown respectively in Figure 2.3 (port side) and Figure 2.4 (star side) and the port and star sides are defined in Figure 2.2(b).

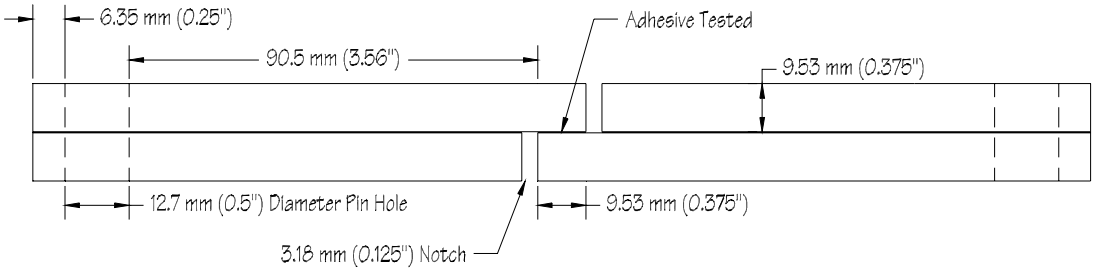

Figure 2.2(a). Dimensions of ASTM D5656 specimen [43].

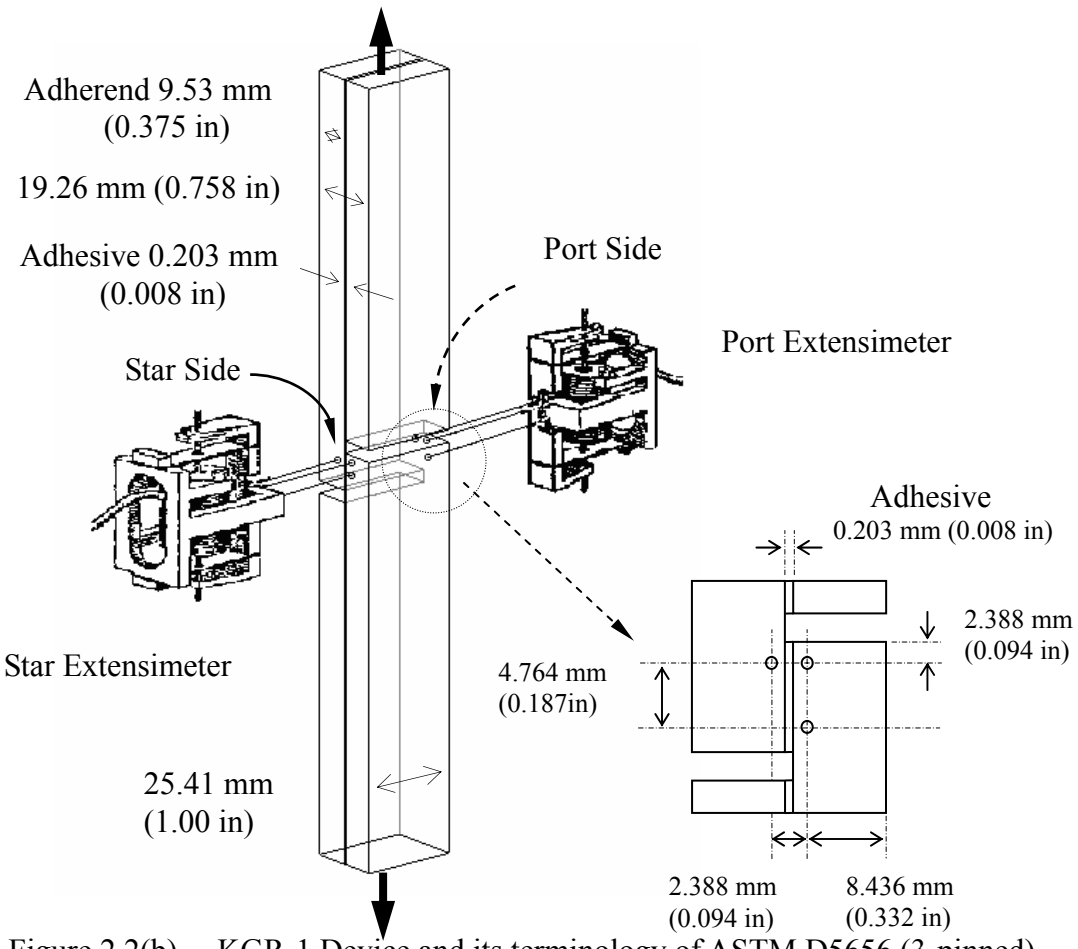

Figure 2.2(b). KGR-1 Device and its terminology of ASTM D5656 (3-pinned).

TABLE 2.1

ASTM D5656 TEST DATA OF METLBOND FM 1515-3

Specimen No.	Bond-line Thickness (in)	Maximum Load (lbf)	Ultimate Shear Strength (ksi)	Elastic Shear Modulus (psi)
P-1	0.00862	2,926.8	7.772	79,068
P-2	0.00796	3,103.3	8.273	59,972
P-3	0.00809	3,111.8	8.190	73,189
P-4	0.00829	3,000.7	7.923	71,490
P-5	0.00793	2,928.7	7.738	73,628
P-6	0.00824	3,013.6	7.999	54,725
P-7	0.00807	2,999.0	7.929	55,084
R-P-1	0.00771	3,183.9	8.421	59,287
R-P-2	0.00821	3,074.6	8.190	-
R-P-3	0.00795	3,110.4	8.279	56,858
R-P-4	0.00800	3,178.7	8.299	48,298
R-P-6	0.00800	3,133.7	8.439	79,917

Average apparent ultimate shear strength = 8.121 ksi. and average ultimate load =3,063.8 lbf.
Average in-plane shear modulus = 64,683 psi. (shear modulus obtained is from apparent stress-strain test data curves).

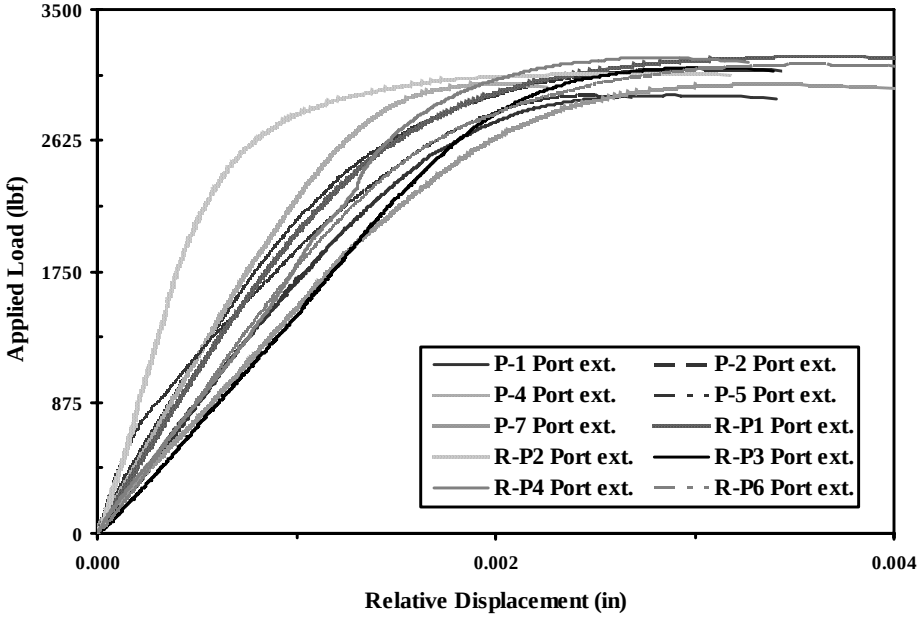

Figure 2.3. ASTM D5656 adherend relative displacement versus load curves (port side).

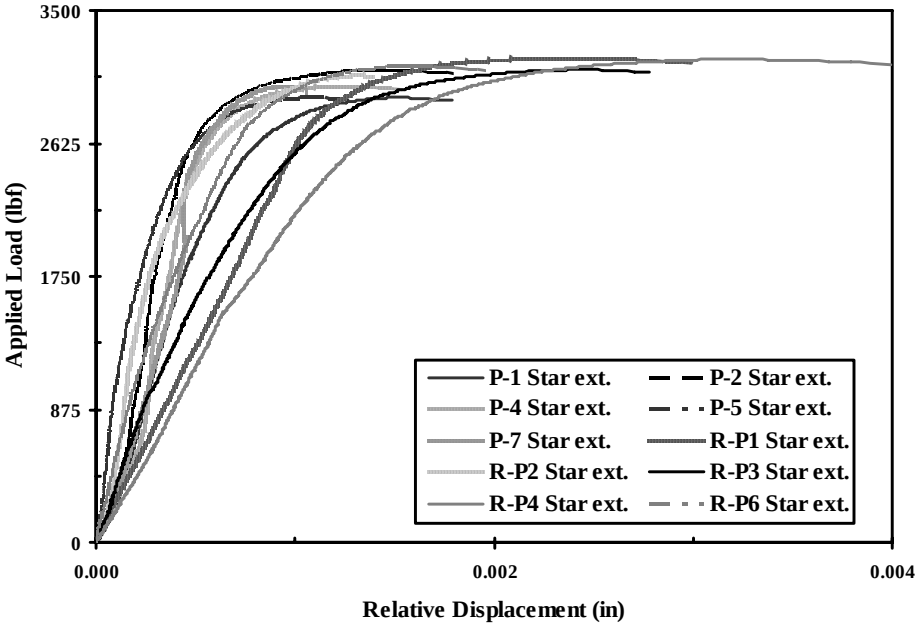

Figure 2.4. ASTM D5656 adherend relative displacement versus load curves (start side).

The material properties of the adhesive are generally treated as an isotropic and homogeneous material. To completely describe its isotropically elastic behavior, the evaluation of, at least, any two of Young's modulus (E), Poisson's ratio (v), and shear modulus (G) is

required. From ASTM D5656 test results, the proportional limit in shear (shear stress at initial yielding or the initial yield strength) and the elastic shear modulus of the adhesive can be determined. Furthermore, the numerical prediction of the ultimate strength of the scarf-patch-repaired composite laminates also requires knowing the plastic properties of the adhesive after yielding as well. Accordingly, based on the ASTM D5656 test data of the adhesive, the elastic constants and equivalent plastic strains and/or effective stresses, after yielding and right at failure, can be converted.

2.3 Evaluation of Linear Elastic Properties for the Adhesive

To begin the analysis of ASTM D5656, the first essential properties required are elastic constants within the linear portion. After confirming the linear section from a monotonic stress-strain curve, the elastic moduli and yield strength can be evaluated. Following the linear elastic determination, the plastic zone can be defined and, in the sense that, the plastic properties can be predicted.

2.3.1 Linear Shear Modulus and Initial Shear Yield Strength

In order to execute the data analysis of ASTM D5656 test, the averaged response data (load-extension raw data recorded from the port and star sides and converted apparent shear strain (γ_{xy})-stress (τ_{xy})) of each specimen are used. Regarding curve approximation methods, two empirical approaches (curve-fit methods) are utilized to approximate the linear shear modulus (G) and initial shear yield stress (S_{xy}). The apparent shear stress and strain mentioned henceforth will be with the nominal shear strain and nominal shear stress relative to true stress (Cauchy stress) and true strain (logarithmic strains). Theoretically, the apparent stress and strain are different from the nominal stress and strain; nevertheless, the apparent stress-strain is assumed to be nominal stress-strain, hypothetically, in this study for convenience.

In respect to these two empirically curve-fit approaches, one approach uses a 0.2% offset (shear strain = 0.2%) straight line parallel to the initial linear segment (with the slope G) of the average stress-strain curve to intersect the entire average shear stress-strain curve. The intersection point accounts for the initial yield strength in shear. The reason for using the 0.2% offset method is that most materials have a well-defined yield point that is a very small percentage of their Young's modulus E (convert to shear modulus G based on the Hooke's law). For example, the yield stress of metals is typically less than 1% of the Young's modulus for the material and its elastic strains will also be less than this percentage. Accordingly, the elastic response of the material can be modeled, quite accurately, as being linear. Hereafter, this method is referred to as 0.2% offset method in this study. An example of the 0.2% offset approach is shown in Figure 2.5, where a 0.2% offset straight line (G = 67,000 psi), parallel to the linear segment of the stress/strain curve, is drawn and intersects the curve at τ_{xy} = 5,540 psi which is determined as the initial shear yield strength S_{xy}.

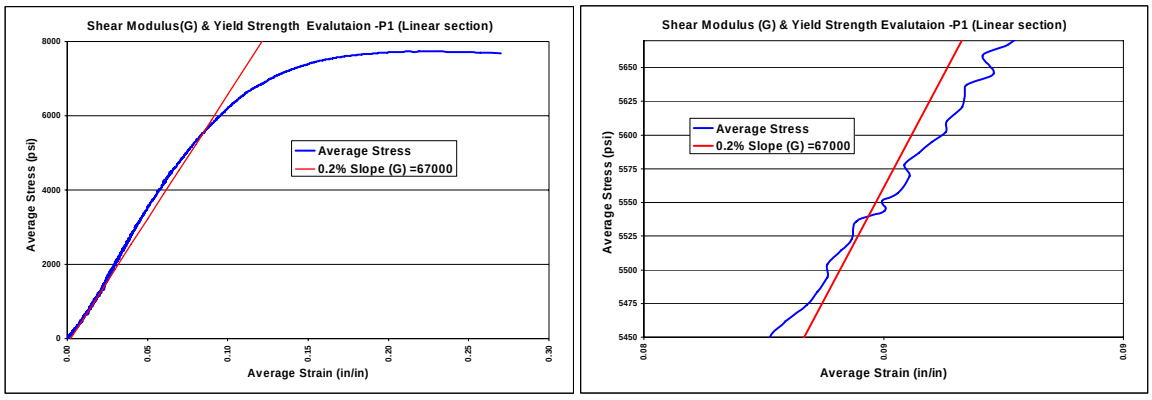

Figure 2.5. G and S_{xy} obtained from the 0.2% offset method for specimen P-1.

Another method used is similar to the ASTM D5656 Standard. One straight line with a proper slope (G) is drawn and is either parallel to or superimposed on the initial linearly rising segment of the average stress-strain curve. The second line is horizontally tangential to the apex within the parabolic plastic segment of the average stress-strain curve. Then the third line

is drawn through the average stress-strain curve bisecting the intersection of the previous two lines. The initial shear yield strength S_{xy} is determined by the intersection of the third line and the average stress-strain curve. This method shown in Figure 2.6 is defined as 2-tangent-line method in this report.

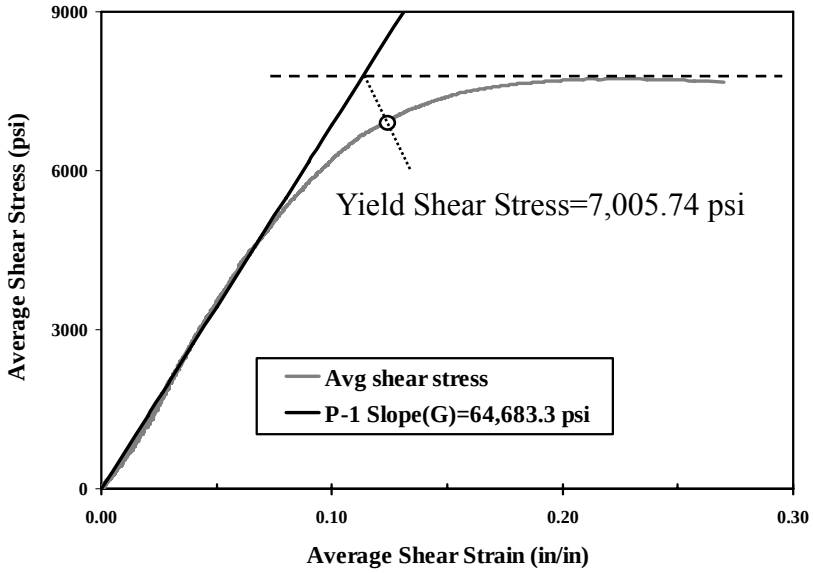

Figure 2.6. G and S_{xy} obtained from the 2-tangent-line method for specimen P-1.

Table 2.2 lists the linear shear modulus and initial shear yield strength of the 10 specimens tested and their average values using the 0.2% offset method. Meanwhile, the shear modulus obtained, based on the linear regression of the selected linear portion within the average apparent (nominal) stress-strain curve of each specimen, is also listed. As seen in Table 2.2, the **Average is obtained by taking the mean value of 7 data points, excluding the extreme values denoted by *. The difference between the average G values from the 0.2% offset method and THE linear regression method is only 0.089%.

In some cases, if only the average value G (64,683.3 psi) is applied to approach the initial yield shear strength, it may not fit the data curve. For instance, in Figure 2.7, the average value G=64,683.3 psi is not applicable to specimen R-P3.

TABLE 2.2

G AND S_{xy} OBTAINED FROM THE 0.2% OFFSET METHOD

	G **(0.2% offset method)**	S_{xy} **(0.2% offset method)**	***G*** **(linear regression from test data)**
P1	67,000	5,543.68	79,068 psi
P2	*90,100	5,685.74	59,972 psi
P3	67,000	-	-
P4	75,000	7,493.24	71,490
P5	*19,0000	-	73,628
P7	56,080	6,709.23	55,084
P-R1	58,800	5,051.04	59,287
P-R2	*190,000	5,754.69	-
P-R3	*52,500	5,099.21	56,858
P-R4	50,000	5,697.79	48,298
P-R6	71,000	5,244.95	79,917
Average	****64,625.71** (psi)	**5,988.78** (psi)	**64,683** (psi)

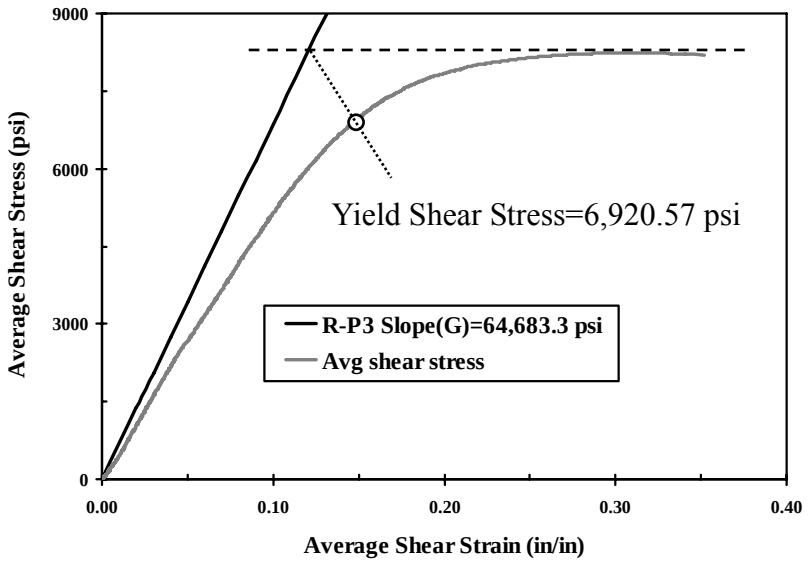

Figure 2.7. S_{xy} from the 2-tangent-line method with *G*=64,683.3 psi for specimen RP-3.

Therefore, the individual *G* value, corresponding to its own specimen, should be used in order to match the test data curves. Then, the amended slope (*G*) is applied to the specimen R-P3 (Figure 2.8) which fits the test data curve satisfactorily.

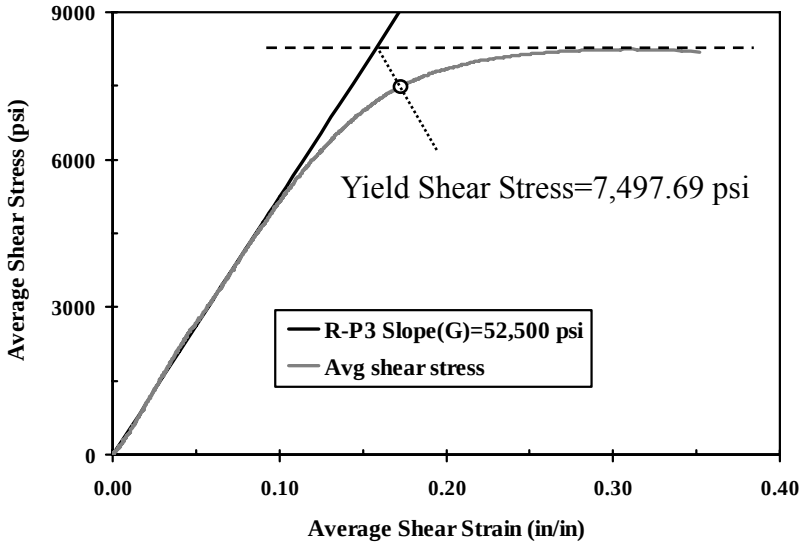

Figure 2.8. S_{xy} from the 2-tangent-Line method with G=52,500 psi for specimen RP-3.

Table 2.3 illustrates the results through the aforementioned two different accesses. In order to compare the S_{xy} values generated by the previous two methods based on stress-strain curves, another data curve expressed by load applied-average extension is also employed to locate the 'knee' value (mentioned in ASTM D5656 Standard 3.2.1, 11.1-11.4).

2.3.2 Linear Young's Modulus (E) and Poisson's Ratio (ν)

Once the linear shear modulus G of the adhesive (considered as isotropic and homogeneous) has been obtained, and then Young's modulus E can be computed by using Hooke's equation (2.1) (based on the assumed Poisson's ratio ν) as

$$E = G\left(2\left(1+\nu\right)\right) \tag{2.1}$$

For most isotropic cases, Poisson's ratio is usually assumed as 0.3~0.35. Various permutation and combination of Young's modulus and Poisson's ratio (via equation 2.1) are inputted to material properties in finite element models to perform simulation. After all, the curve converted from finite element results is superimposed on the test result curve. Using this phenomenological curve-fit method, the desirable and optimum data set could be evaluated.

TABLE 2.3

SHEAR YIELD STRENGTH OBTAINED BY DIFFERENT METHODS

Specimen Code	***Sxy*** ***G*=6,4683.3**(psi)	***Sxy*** ***G*=individual value for each curve** (psi)	***Sxy*** **(Avg. Load & Extension.)**(psi)	**Yield load** (lbf)
P1	7,005.74	7,062.24 (*G*=67,000)	7,062.24	2,674.28
P2	7,607.28	7,219.35 (*G*=90,100)	7,251.78	2,775.52
P4	7,713.77	7,645.37 (*G*=75,000)	7,645.37	2,920.89
P5	7,050.39	5,813.09 (*G*=190,000)	5,752.27	2,202.08
P7	6,905.85	7,406.58 (*G*=56,080)	7,352.05	2,806.64
P-R1	7,237.53	7,544.23 (*G*=58,800)	7,569.91	2,874.69
P-R2	7,937.98	7,101.01 (-)	7,082.36	2,671.27
P-R3	6,920.57	7,497.69 (*G*=52,500)	7,519.71	2,838.28
P-R4	7,546.03	7,618.94 (*G*=50,000)	7,606.17	2,925.1
P-R6	7,440.80	7,645.09 (*G*=71,000)	7,434.76	27,73.68
Average	**7,336.59** (psi)	**7,255.36** (psi)	**7,227.66** (psi)	**2,746.24** (lbf)

2.4 Evaluation of Plastic Properties for the Adhesive

After being loaded beyond their proportional limit (initial yielding point), ductile materials usually behave nonlinearly due to changes in their stiffness associated with the varying deformation. Since the stiffness varies with the displacement/strain, the material's displacement cannot be obtained for any load by multiplying the initial flexibility times the applied load [44]. Because the response of a nonlinear system is not a linear function of the magnitude of the applied load, each load case must be defined and solved as a separate analysis rather than using the superposition method.

Taking ASTM D5656 test data (elasto-plastic curves) as an example (Figure 2.9), once the elastic region and yield strength are evaluated from the previous sections, the plastic portion can be discriminated. After initial yield shear stress (σ_y)-onset of non-linear behavior, the region of non-linear deformation tends to a plateau stage in shear stress. This transition region is called

'strain hardening' in elastic-plastic models. The region prior to failure in which the shear stress slightly ascends, with increasing strain, is denoted as the flow region. Some epoxy-jointed specimen's (bulk or butt joint specimens) response data reveal their highly nonlinear behaviors. Such adhesives made of epoxy, exhibiting large nonlinear stress-strain behaviors, are called rubber-toughened adhesives [45-47]. This ductile material can be stressed to large strains before their failure and allow bonded structures to withstand higher loads remarkably. Accordingly, it is essential to apply certain plasticity models (yield criterion/surface) to in order to analyze such a large post-yielding region of epoxy adhesives. Moreover, the strength analysis or failure mechanism involves many plastic parameters; therefore, an appropriate plasticity model for analysis must be decided.

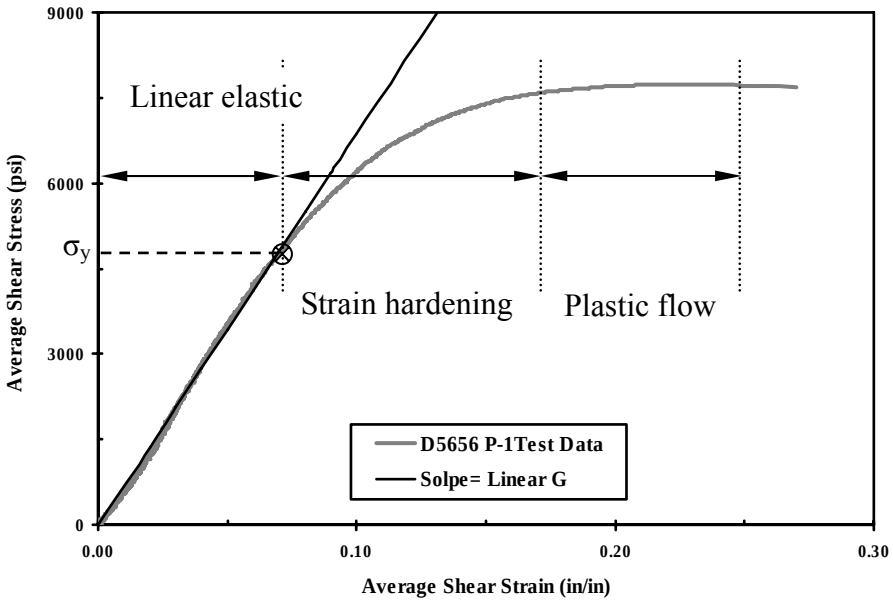

Figure 2.9. Average shear stress-strain curve of ASTM D5656 P-1.

Regarding ductile materials, a useful simpler criterion is either the maximum distortional energy/von Mises yield criterion or the maximum shearing stress/Tresca yield criterion. From most experimental data, the von Mises criterion fits better than the Tresca criterion for ductile

materials. For the application of ABAQUS, the von Mises yield criterion will be the first plastic model selected to compute related plastic material properties, namely plastic strain, equivalent/effective plastic strain, equivalent/effective stress. Furthermore, the more sophisticated and precise model-Drucker-Prager plasticity model, as revised from the von Mises criterion [44-48] to describe the sensitivity of hydrostatic components of stress to the yielding, is introduced to characterize the epoxy adhesive bonded by joints.

2.4.1 Elastic Constitutive Equations

With respect to the ASTM D5656 specimen, the thickness of the adhesive is designed to be 1/125 (0.008 in.) of the width (1 in. wide). It is reasonable to assume that the stress, which the adhesive endures, is pure shear stress only, ignoring any out-of-plane effects. The adhesive is treated as a plane strain model only, without the modeling of width along the *z*-direction (as shown in Figure 2.10). Therefore, the problem is simplified as a 2-D plane strain analysis. The 2-D plane strain model is created on the *x*-*y* plane in finite element analysis instead of the *x*-*z* plane modeling. The plane strain coordinates are symbolized as shown in Figure 2.10.

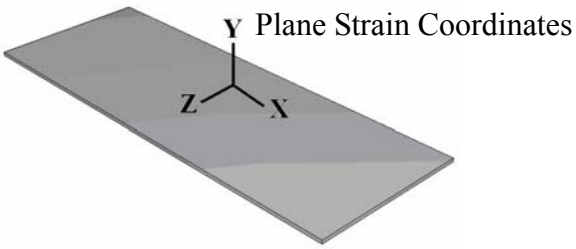

Figure 2.10. Coordinate definition in finite element analysis for ASTM D5656 and scarf joint bonded composite models.

Hooke's Law is applied to isotropically elastic materials when considering their stress-strain relations. The constitutive equation (2.2), in tensorial form, is defined as

$$\varepsilon_i = \frac{1}{E}\left[\sigma_i - \nu\left(\sigma_j + \sigma_k\right)\right] \tag{2.2}$$

The subscripts *i, j* and *k* are from *x, y* and *z* for the Cartesian vector. Furthermore, the thickness of the adhesive, 0.008 in., is relatively small enough when compared with its 1 in. width and its 0.3755 in. length. The specimen is assumed to be under a state of plane strain so that strain components in the *z*-direction are negligible as

$$\varepsilon_z = \gamma_{xz} = \gamma_{yz} = 0 \tag{2.3}$$

Additionally, it has been shown that the peer stress/force (*y*-directional stress) generated during testing is a function of bending in the adherends. The stiffness of the aluminum adherends is far greater than that of the adhesive. The thickness of the aluminum adherends are designed to be so significantly 'thick' adherends that the ASTM D5656 specimens would generate less bending in the adherends as well as negligible peel stress in the adhesive (minimized stress in the *y*-direction). Accordingly, the ASTM D5656 Standard allows the adhesive to experience shear stress only. Since the tension load along the *x*-direction is applied to the adherends rather than to the adhesive directly and the adhesive's analysis is under plane strain state, all the normal stress components of the adhesive become zero. From equations (2.2) and (2.3), all in-plane normal strain components, as well as out-of-plane shear strain components in the adhesive, are equal to zero. Therefore, only the γ_{xy} term is left, which is stated in terms of shear modulus *G* as

$$\gamma_{xy} = \frac{1}{G}\sigma_{xy} \tag{2.4}$$

From equations (2.3-4), it can be shown that out-of-plane shear stress components (τ_{yz} and τ_{xz}) become zero since *G* is not zero. In the following sections, applicable plasticity models will be introduced and a proper plasticity (yield) model will be selected to transform stress and strain components, resulting from non uni-axial loading (multiple loading) or other than tension test to just one meaningful scale equivalent to uni-axial tension test.

2.4.2 Prandtl-Reuss Theory

The generalized equations including both elastic and plastic components of strain were proposed by Prandtl and Reuss and are known as the Prandtl-Reuss equations given by

$$d\varepsilon_{ij}^{p} = S_{ij} d\lambda \tag{2.5}$$

The $d\lambda$ is a factor depending on stress states and is calculated by ensuring equivalence of the plastic strain energy done by all stress states. S_{ij} denotes deviatoric stress tensors, and the superscript 'p' indicates plastic component. The equation (2.5) can also be rewritten in terms of the 3-D (3-dimention) actual stress state as

$$d\varepsilon_{i}^{p} = \frac{2}{3} d\lambda \left[\sigma_i - \frac{1}{2}\left(\sigma_j + \sigma_k\right) \right] \qquad d\varepsilon_{ij}^{p} = d\lambda \sigma_{ij} \tag{2.6}$$

which is similar to Hooke's Law for incompressible material assumption, with v=0.5, in plasticity theory. The equations can be applied to large plastic flows.

Secondly, in order to calculate the parameters defined in elastic-plastic theory, it is necessary to obtain stress values from different tests under the same state of yielding. This requires the definition of an equivalent/effective stress and equivalent/effective plastic strain. The effective stress represents a set of stresses that characterize stress states having the same effective plastic strain. Using the Cartesian tensor, the equivalent/effective stress is defined as

$$\sigma_e = \frac{1}{\sqrt{2}} \sqrt{\left(\sigma_x - \sigma_y\right)^2 + \left(\sigma_y - \sigma_z\right)^2 + \left(\sigma_z - \sigma_x\right)^2 + 6\left(\sigma_{xy}^2 + \sigma_{yz}^2 + \sigma_{xz}^2\right)} \tag{2.7}$$

Similarly, the relations of the equivalent plastic strain increment $d\varepsilon_e$ and plastic strain increment components are described in terms of tensor form as

$$d\varepsilon_e = \frac{\sqrt{2}}{3} \sqrt{\left(d\varepsilon_x^p - d\varepsilon_y^p\right)^2 + \left(d\varepsilon_y^p - d\varepsilon_z^p\right)^2 + \left(d\varepsilon_z^p - d\varepsilon_x^p\right)^2 + 6\left(d\varepsilon_{xy}^p\right)^2 + 6\left(d\varepsilon_{yz}^p\right)^2 + 6\left(d\varepsilon_{xz}^p\right)^2} \tag{2.8}$$

Therefore the constant $d\lambda$ can be expressed as

$$d\lambda = \frac{3}{2}\frac{d\varepsilon_p}{\sigma_e} \tag{2.9}$$

and the stress-strain equations (2.6) becomes as

$$d\varepsilon_i^p = \frac{d\varepsilon_p}{\sigma_e}\left[\sigma_i - \frac{1}{2}\left(\sigma_j + \sigma_k\right)\right] \tag{2.10}$$

or in the compact form as

$$d\varepsilon_{ij}^p = \frac{3}{2}\frac{d\varepsilon_p}{\sigma_e} S_{ij} \tag{2.11}$$

2.4.3 Von Mises Yield Criterion

The von Mises yield criterion is the simplest yield criterion which expresses yielding as a pure shear deformation initiating when the effective shear stress σ_e achieves critical value, σ_o. It also can interpret yielding depending on the deviatoric components of stress and, in turn, yielding occurs when the second invariant of the deviatoric stress tensor ($\sqrt{3J_2}$) reaches the critical value. The von Mises yield criterion can be either interpreted by six stress components as

$$\sigma_o = \frac{1}{\sqrt{2}}\sqrt{\left(\sigma_x - \sigma_y\right)^2 + \left(\sigma_y - \sigma_z\right)^2 + \left(\sigma_z - \sigma_x\right)^2 + 6\left(\sigma_{xy}^2 + \sigma_{yz}^2 + \sigma_{xz}^2\right)} \tag{2.12a}$$

or in terms of three principal stresses (σ_1, σ_2, and σ_3) as

$$\sigma_o = \sqrt{\tfrac{1}{2}\left[(\sigma_1 - \sigma_2)^2 + (\sigma_2 - \sigma_3)^2 + (\sigma_3 - \sigma_1)^2\right]} \tag{2.12b}$$

On the deviatoric plane, the von Mises yield surface [44] is configured as Figure 2.11. The 'p' and 'q' used in ABAQUS are referred to as 'equivalent pressure stress' and 'Mises equivalent stress', respectively. They can be mathematically expressed by

$$q = \sigma_e$$

$$p = -\tfrac{1}{3}(\sigma_1 + \sigma_2 + \sigma_3) = -\tfrac{1}{3} I_1 \tag{2.13}$$

in which I_1 means the first invariant of stress tensor or the trace of stress tensor so that the equation of the yield surface is defined as q=c, where 'c' equal to σ_o.

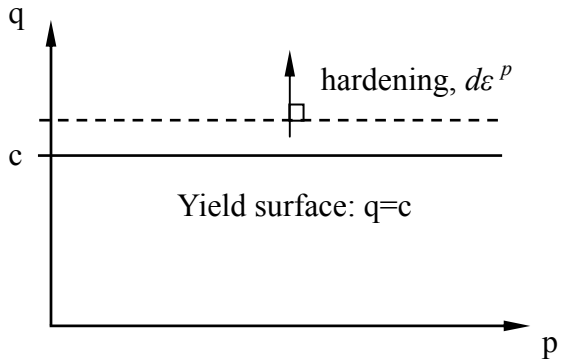

Figure 2.11. Von Mises yield surface on the deviatoric plane.

Therefore, the von Mises yield surface assumes that the yielding of materials is independent of the equivalent pressure stress (p), which has been confirmed experimentally for most ductile materials except for voided materials. Comparing these stress equations (2.7) and (2.12), the equivalent stress becomes the same as the von Mises yield function when σ_o is equal to σ_e. In other words, the original Prandtl-Reuss assumptions imply the von Mises yield criterion.

- **Flow Rule—Associated Plastic Flow**

Since ABAQUS uses associated flow only for the von Mises yield criterion, the inelastic deformation rate (strain rate) is along the direction normal to the yield surface (the plastic strain is volume invariant) (Figure 2.11). This assumption is valid for most ductile metal materials without void, high stress concentration factor, and high localized stress filed or plastic flow.

2.4.4 Linear Drucker-Prager Yield Criterion

Most adhesives under additional stress states, namely shear and compression, show that their yielding has certain sensitivity to the hydrostatic components of stress besides the shear

components, especially for polymeric adhesives/toughened adhesives. Within the regions of strain concentration at the edges of the adhesive layer, those hydrostatic stress components reach a significant magnitude. Merely relying on the von Mises theory (distortional strain energy criterion which cannot predict hydrostatic stress state yielding) cannot truthfully describe realistically the post yielding behavior of the adhesives. The simplest yield criterion, including hydrostatic stress sensitivity, is a modification of the von Mises criterion [45-47]. Combined with the notation defined in ABAQUS, the equation for the yield surface named as linear Drucker-Prager model is given by

$$\begin{aligned} & \sigma_e = \sigma_o - \tan(\beta)[\tfrac{1}{3}(\sigma_1 + \sigma_2 + \sigma_3)] \\ or \quad & \sigma_e = \sigma_o - \tan(\beta)\sigma_m \\ & t = d + \tan(\beta)(p) \end{aligned} \tag{2.14}$$

where σ_o and $\tan(\beta)$ are material parameters stemming from different loadings in test. For σ_o (d, cohesion of the material in ABAQUS), from different hardening sources, the relations associated to the test in uni-axial tension, uni-axial compression, and pure shear (cohesion strength) are

$$d = \sigma_o = \sigma_T = \sigma_C = \sqrt{3}\sigma_S \tag{2.15}$$

which can be derived from equation (2.12a). However, in ABAQUS, the 'd' is modified due to consideration of the factor 'K', which is the ratio of the yield stress in triaxial tension to the yield stress in triaxial compression. Then equation (2.15) is rewritten based on tests in compression, tension, and shear, correspondingly [45-47] as

$$\begin{aligned} d &= (1 - \frac{1}{3}\tan(\beta))\sigma_C \\ d &= (\frac{1}{K} + \frac{1}{3}\tan(\beta))\sigma_T \\ d &= \frac{\sqrt{3}}{2}(1 + \frac{1}{K})\sigma_S \end{aligned} \tag{2.16}$$

As $\tan(\beta)$, which describes the sensitivity of hydrostatic components of stress to adhesive

yielding, can be predicted from tests under two different stress states and is given by

$$\tan(\beta) = 3[(\sqrt{3}\frac{\sigma_S}{\sigma_T}) - 1] = \frac{3(\lambda - 1)}{\lambda + 1} \quad \text{, from shear and tension tests,}$$

$$\tan(\beta) = 3[(1 - \sqrt{3}\frac{\sigma_S}{\sigma_C})] \quad \text{, from shear and compression tests, and} \tag{2.17}$$

$$\tan(\beta) = \frac{3[(\sigma_C / \sigma_T) - 1]}{(\sigma_C / \sigma_T) + 1]} \quad \text{, from compression and tension tests.}$$

The above yield stress in tension, compression, and shear are measured in accordance with the same effective plastic strain. For convenience, it is given by

$$\lambda = \frac{\sqrt{3}\sigma_S / \sigma_T}{2 - \sqrt{3}\sigma_S / \sigma_T} \tag{2.18}$$

On the deviatoric plane, the linear Drucker-Prager yield surface [44] is configured as Figure 2.12.

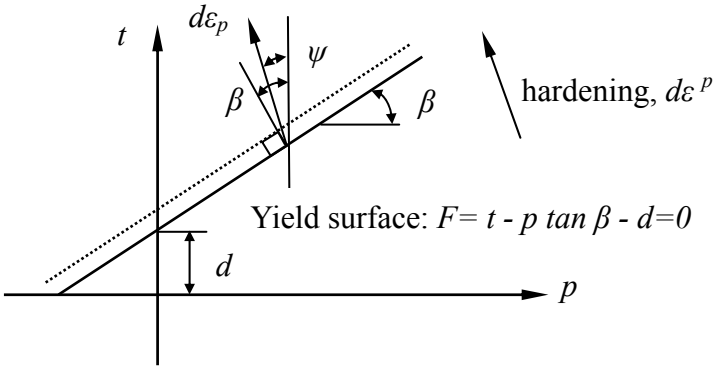

Figure 2.12. Linear Drucker-Prager yield surface [44].

For the possibility of a noncircular yield surface on the deviatoric plane to fit different yield values in triaxial tension and compression (associated plastic flow on the deviatoric plane), ABAQUS separates the dilation (ψ) and the friction (β) angles and defines K (the ratio of the yield stress in triaxial tension to the yield stress in triaxial compression). The other parameter't' in ABAQUS [44] is defined by

$$t = \frac{1}{2} q[1 + \frac{1}{K} - (1 - \frac{1}{K})(\frac{r}{q})^3] \tag{2.19}$$

where '*r*' indicates the third invariant of deviatoric stress. Regarding the function of K, on the π-plane (a deviatoric plane when *p*=0), different values of K will configure different yield surfaces [44] (Figure 2.13), which may not match the circular yield surface (in which K=1.0 stands for von Mises circle and results in $t = q$ from equation (2.18)). Frequently, the value of K may not be equal to 1.0, and should be modified by iteration in ABAQUS. To confirm that the yield surface remains a convex shape [44], the K value should satisfy $0.778 \leq K \leq 1.0$.

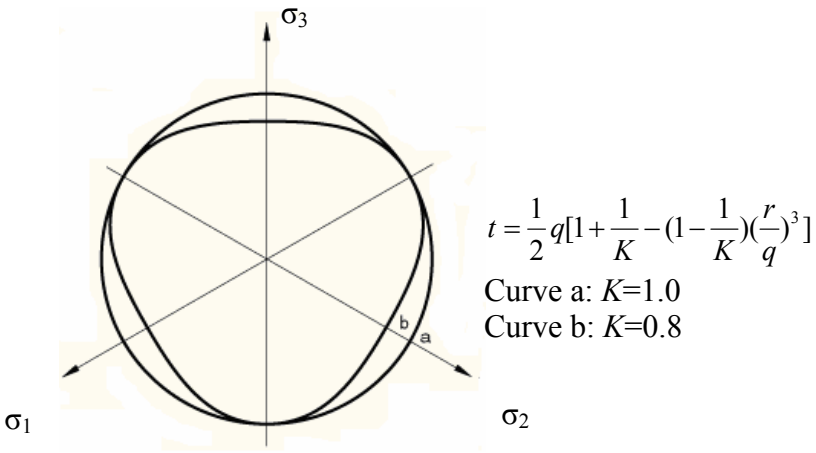

Figure 2.13. Variations of yield surface and K of the linear model on the π-plane [44].

- **Flow Rule—Associated Plastic Flow**

The Prandtl-Reuss equation (2.5) incorporated with a plastic flow potential, *F*, is rewritten as

$$d\varepsilon_{ij}^{p} = d\lambda \frac{\partial F}{\partial \sigma_{ij}} \tag{2.20}$$

When the flow potential, *F*, is related to the yield function, the flow is called associated, in the sense that the linear Drucker-Prager criterion is expressed by

$$F = t - p \tan(\beta) - d = 0 \tag{2.21}$$

The equation is valid when the plastic strain increment ($d\varepsilon^{p}$) is normal to the yield surface during the plastic flow. Therefore, the friction angle (β) is equal to the dilation angle (ψ) (i.e. $\tan(\beta) = \tan(\psi)$), and, accordingly, the stiffness matrix is symmetric.

- **Flow Rule—Non-Associated Plastic Flow**

As a non-associated flow, where a plastic flow potential is not equal to the yield function, the friction angle in equation (2.21) should be replaced by the another parameter, the dilation angle (ψ), i.e.,

$$F = t - p\tan(\psi) - d = 0 \tag{2.22}$$

Accordingly, the friction angle (β) is not equal to the dilation angle (ψ) for non-associated flow as illustrated in Figure 2.12. The $\tan(\psi)$ is also a material parameter and its definition is given experimentally by the measurement of the plastic component of Poisson's ratio in tension or compression [45-47] as

$$\tan(\psi) = \frac{3(1-2\nu_P)}{2(1+\nu_P)} \tag{2.23}$$

The ν_p symbolizes the plastic component of Poisson's ratio measured by uni-axial tension as

$$\nu_p = -\frac{\varepsilon^{p}_{transverse}}{\varepsilon^{p}_{T}} \tag{2.24}$$

The relation between ν_p and $\tan(\psi)$ from other researches [45-47] is constructed by

$$\nu_p = \frac{3-2\tan(\psi)}{2(3+\tan(\psi))} \tag{2.25}$$

Usually the plastic flow of the epoxy adhesive is non-associated (the friction angle (β) being unequal to the dilation angle (ψ) as shown in Figure 2.12), which means the plastic strain increment ($d\varepsilon^{p}$) is not normal to the yield surface (tilted at angle (β-ψ) from the normal of the yield surface). Frequently, but not necessarily, the friction angle (β) is greater than or equal to

the dilation angle (ψ). If the flow is non-associated, it causes the stiffness matrix to be unsymmetrical and produces negative eigenvalues even though there is no softening within the hardening data [44,47]. In finite element analysis under non-associated flow, it will generate difficulty in convergence, especially in the Standard/static or Implicit analysis due to the inverse of the stiffness matrix. If the off-set between tan (ψ) and tan (β) is small, the associated flow can be assumed. The weakness of this hypothesis is the loss of precision and uncertain stress-strain results.

2.4.5 General Exponent Drucker-Prager Yield Criterion

In some materials with a higher component of hydrostatic tension, the linear Drucker-Prager yield criterion may not cover this behavior accurately. Such stress states usually localize in adhesive bonds due to the high constraint enforced by adherends under the force normal to the boning interface. The alternative Drucker-Prager criterion, generally more precise under these circumstances, is introduced and named as 'general exponent yield criterion' in ABAQUS. The yield criterion is written as

$$F = aq^b - p - p_t = 0 \tag{2.26}$$

where 'a' and 'b' are material parameters independent of plastic deformation; and 'p_t' is the hardening parameter representing the hydrostatic tension strength (shown as Figure 2.14).

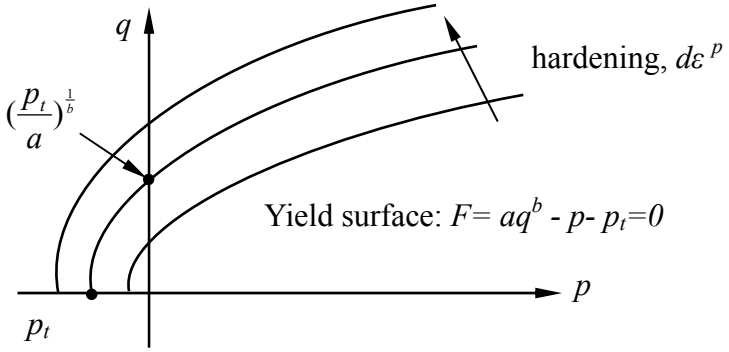

Figure 2.14. General exponent Drucker-Prager yield surface and hardening in the *p*-*q* plane [44].

Based on different test methods, the relations between 'p_t' and test methods (tension, compression, or pure shear) are defined below [44]; and 'p_t' can be replaced by

$$p_t = a\sigma_C^b - \frac{\sigma_C}{3} \quad \text{if hardening is from the uniaxial compression yield stress , } \sigma_C$$

$$p_t = a\sigma_T^b - \frac{\sigma_T}{3} \quad \text{if hardening is from the uniaxial tension yield stress , } \sigma_T \tag{2.27}$$

$$p_t = ad^b \quad \text{if hardening is from the cohesion , } \sigma_S$$

The value of parameter 'b', regarding the shape of the yield surface, is suggested as equal to 2. Under this presumption, the equation (2.26) is rewritten by

$$\sigma_e^2 = \lambda\sigma_T^2 - 3(\lambda - 1)\sigma_T\sigma_m \tag{2.28}$$

in which λ is another hydrostatic stress sensitivity parameter and is associated with tests in tension, compression, and pure shear [45-47]. λ is given by

$$\lambda = \frac{\sigma_C}{\sigma_T} \quad \text{, from compression and tension tests,}$$

$$\lambda = \frac{\sigma_C^2}{3\sigma_S^2} \quad \text{, from shear and compression tests, and} \tag{2.29}$$

$$\lambda = \frac{3\sigma_S^2}{\sigma_T^2} \quad \text{from shear and tension tests.}$$

Comparing equations (2.26) with (2.28), the parameter 'a' is then expressed by

$$a = \frac{1}{3\sigma_T(\lambda - 1)} \quad \text{and} \quad p_t = a\lambda\sigma_T^2 \tag{2.30}$$

since $q=\sigma_e$ and $p=-\sigma_m$ were defined previously.

- **Flow Rule—Non-Associated Plastic Flow**

In ABAQUS, for the general exponent model, the plastic flow is only a non-associated flow ($\psi \neq \beta$) on the *p*-*q* plane (this plane is given when K=1, $t=q$ in equation (2.19)) and the plastic strain increment ($d\varepsilon^{p}$) is not normal to the yield surface. Then the dilation angle (ψ) in equation (2.23) can be determined.

2.4.6 Definition of the Yield Surface

The Von Mises yield surface is generally used to define isotropic yielding for ductile isotropic materials, which means that the yield surface varies its size uniformly in all directions such that the yield stress changes in all stress directions as plastic straining occurs. Since ASTM D5656 test is conducted with monotonic loading but not with cyclic loading, the use of isotropic yielding is more suitable than kinematic yielding. The isotropic hardening in ABAQUS is useful for cases involving gross plastic straining or in cases where the straining at each point is essentially in the same direction in strain space throughout the analysis. The yield surface, including the Drucker-Prager plasticity modes, defined in ABAQUS is given by the value of the uni-axial yield stress as a function of uni-axial equivalent plastic strain, temperature, strain rate, and/or other filed variables. Therefore, all results from multiple loading or non-uniaxial loading cases should be converted to equivalent uni-axial loading stress-strain data form by equation (2.7) and (2.8).

2.5 Adhesive Property Calculations under ASTM D5656

For the adhesive tested under ASTM D5656 Standard, as discussed in section 2.4, all stress components in the adhesive are zero except for shear stress σ_{xy}. The von Mises yield stress (2.12a) is simplified to $\sigma_o = \sigma_e = \sqrt{3}\sigma_{xy}$. The adhesive is under plane strain state in the *z*-direction, i.e.,

$$d\varepsilon_z^p = d\varepsilon_{yz}^p = d\varepsilon_{xz}^p = 0 \tag{2.31}$$

then the equivalent plastic strain equation (2.7) under pure shear becomes as

$$d\varepsilon_e = \frac{\sqrt{2}}{3}\sqrt{6\left(d\varepsilon_{xy}^p\right)^2} = \frac{\sqrt{2}}{3}\sqrt{6\left(\frac{d\gamma_{xy}^p}{2}\right)^2} = \frac{\gamma_{xy}}{\sqrt{3}} \tag{2.32}$$

Notice that in ABAQUS, the definition of equivalent plastic strain is expressed by the tensor form and equation (2.8) should be used, especially for shear strains. Secondarily, the relationship between total strain, elastic strain, and plastic strain is expressed by

$$\varepsilon_{total} = \varepsilon_{elastic} + \varepsilon_{plastic} \quad \rightarrow \quad \varepsilon_t = \varepsilon_E + \varepsilon_P \tag{2.33}$$

For elastic shear strain of the adhesive in the ASTM D5656 test without cyclic loading is expressed in terms of

$$\varepsilon_E = \frac{\sigma_{applied}}{E} = \frac{\sigma_{xy}}{2G} \tag{2.34}$$

then equation (2.27) can be re-written as

$$\varepsilon_P = \varepsilon_t - \varepsilon_E = \varepsilon_t - \frac{\sigma_{xy}}{2G} \tag{2.35}$$

Furthermore, for an infinitesimal increment, the above equation can be expressed as

$$d\varepsilon_P = d\varepsilon_t - d\varepsilon_E = d\varepsilon_t - \frac{d\sigma_{xy}}{2G} \tag{2.36}$$

It should be mentioned that the difference between ε_{ij} and γ_{ij} is that γ_i represents engineering shear strain, and ε_{ij} denotes tensorial shear strain (following the definition in ABAQUS, tensorial shear strains ε_{ij} are used for all calculations and formula in this study). For small deformation (strain), the conversion is given by

$$\varepsilon_{ij} = \frac{\gamma_{ij}}{2} = \frac{\sigma_{ij}}{2G} \quad \text{, when} \quad i \neq j \tag{2.37}$$

Once the initial yield shear stress, applied shear stress σ_{xy}, total shear strain ε_t and G value have been converted for each specimen using ASTM D5656 test results, the above equations can be used to pre-calculate plastic shear strain for each specimen using the test data. In turn, equivalent stresses and strains can be obtained from different stress-strain definitions as follows. Tables 2.4 and 2.5 are based on nominal stress-strain test data while Table 2.6 is integrated from true stress (Cauchy stress) and true strain (logarithmic strain) associated with individual G value. Note that the 'ABS PEEQ' inside tables is particularly required for ABAQUS, and is called the absolute value of equivalent plastic strain, which is a critical factor in shear failure function, and the PEEQ signifies equivalent plastic strain.

From the integrated effective stress-strain curves, the post-yielding portion rises in parabolic form after initial yield shear stress. Based on the entire effective stress-strain curve, the behavior can be regarded as either a perfectly plastic or isotropic hardening plastic model. In fact, the curve develops in some order of exponential form but does not exactly fall into the perfectly plastic model. In ABAQUS, for the Drucker-Prager plasticity model, there are three sub-options which can be chosen, namely the linear Drucker-Prager, the hyperbolic, and the general exponent models. Only the linear Drucker-Prager model can be applied in ABAQUS Explicit/dynamic model and the rest are performed in the Standard/implicit analytic model.

However, from the test results and converted plastic properties, based on the nominal (apparent) stress-strain curves, the behavior of the adhesive shows nearly elastic-perfectly plastic. Within the hardening range, the ultimate load (the maximum load applied before the necking region) is not far away from the failure load (only 0.8% difference). Tactically, it can be simplified as perfectly plasticity using the classical metal plasticity associated with the von Mises criterion for convenience. The drawback of the perfectly plasticity model is that it will

produce the same failure load as the ultimate load and cannot generate the hardening with necking curve similar to the test data after initial yielding and ultimate load, respectively.

TABLE 2.4

CALCULATION OF PLASTIC PROPERTIES FROM TENSORIAL SHEAR STRAIN UNDER THE SAME SHEAR MODULUS FOR EACH SPECIMEN

Conversion From Test Data (***G*= 64,683.3**) in Tensor form based on Mises Criterion (All the stresses and strains converted are on the basis of **nominal stress-strain** test data)							
	Initial Yield Stress(psi)	**Effective Stress(psi)**	**ABS PEEQ**	**(Failure) Relative Displacement(in)**	**Failure Load(lbf)**	**(Ultimate) Relative Displacement(in)**	**Ultimate Load(lbf)**
P-1	7005.74	12,134.298	0.0796	0.00259747	2905.763	0.00219202	2926.760
P-2	7607.28	13,176.195	0.0797	0.00262137	3085.799	0.00219981	3103.295
P-4	7713.77	13,360.634	0.0434	0.00190144	2980.721	0.00165037	3000.730
P-5	7050.39	12,211.634	0.0547	0.00198085	2912.150	0.00179278	2928.730
P-7	6905.85	11,961.283	0.0894	0.00260268	2958.401	0.00217665	2999.008
R-P1	7237.53	12,535.770	0.1586	0.00359002	3154.419	0.00291925	3183.894
R-P2	7937.98	13,748.988	0.0690	0.00228491	3060.903	0.00199405	3074.556
R-P3	6920.57	11,986.779	0.1120	0.00308724	3092.196	0.00275378	3110.402
R-P4	7546.03	13,070.113	0.1493	0.00362841	3142.410	0.00298261	3178.652
R-P6	7440.80	12,887.844	0.1189	0.00310196	3103.718	0.00258270	3133.730
Avg.	**7336.59**	**12,707.35**	**0.0955**	**0.00273963**	**3039.648**	**0.00232440**	**3063.976**

TABLE 2.5

CALCULATION OF PLASTIC PROPERTIES FROM TENSORIAL NOMINAL SHEAR STRAIN UNDER INDIVIDUAL SHEAR MODULUS OF EACH SPECIMEN

Conversion From Test Data (***G*= Individual Value**) in Tensor form based on Mises Criterion (All the stresses and strains converted are on the basis of **nominal stress-strain** test data)			
	Initial Yield Stress(psi)	**Effective Stress(psi)**	**ABS PEEQ**
P-1	7062.24	12,232.158	0.0785
P-2	7219.35	12,504.281	0.0928
P-4	7645.37	13,242.169	0.0470
P-5	5813.09	10,068.567	0.0779
P-7	7406.58	12,828.573	0.0770
R-P1	7544.23	13,066.990	0.1500
R-P2	7101.00	12,299.293	0.1039
R-P3	7497.69	12,986.380	0.0988
R-P4	7618.93	13,196.374	0.1300
R-P6	7645.09	13,241.684	0.1129
Avg.	**7255.36**	**12,566.65**	**0.0969**

TABLE 2.6

CALCULATION OF PLASTIC PROPERTIES FROM TENSORIAL TRUE SHEAR STRAIN UNDER INDIVIDUAL SHEAR MODULUS OF EACH SPECIMEN

Conversion From Test Data (***G*= Individual Value**) in Tensor form based on Mises Criterion (All the stresses and strains converted are on the basis of **true stress-strain** test data)			
	Initial Yield Stress(psi)	**Effective Stress(psi)**	**ABS PEEQ**
P-1	7,924.14	13,725.01	0.0605
P-2	7,213.45	12,494.06	0.0787
P-4	8,722.89	15,108.49	0.0347
P-5	6,260.05	10,842.72	0.0704
P-7	9,040.35	15,658.35	0.0521
R-P1	8,811.16	15,261.38	0.1032
R-P2	6,128.84	10,615.46	0.1061
R-P3	6,748.18	11,688.19	0.0876
R-P4	9,190.38	15,918.21	0.0859
R-P6	7,838.99	13,577.53	0.0951
Avg.	**7,787.84**	**13,488.94**	**0.0775**

By contrast, if the elastic and plastic properties are calculated from true stress and true strain, the adhesive behaves like the linear Drucker-Prager hardening feature and the ultimate load is coincident with the failure load (no necking). Therefore, only the exponent Drucker-Prager and the classical metal plasticity with certain hardening data can produce distinct ultimate and failure load as test result curves. In ABAQUS, either of those sub-options can be imported into the 'Material Module' to perform simulations. The results can be used to decide which plasticity model is a superior approach.

2.6 Determination of Analysis Model in ABAQUS

Before performing the finite element analysis, the assessment and determination of analysis models, supported by ABAQUS, should be made. In this section, the plasticity models, failure criteria, analytic models (ABAQUS/Standard or ABAQUS/Explicit models), and some other features are discussed individually.

2.6.1 Plasticity Model in ABAQUS

Like the general plastic theory, most of the plasticity models, supported by ABAQUS, divide the mechanical strain rate into elastic part and plastic part. The plastic strain part follows 'incremental' theories in which each incremental plastic strain is obtained from associated small load increment/step.

In BAQUS/CAE, it contains a variety of different models of inelastic behavior. Comparing the characteristics between the aforementioned plasticity models, only the classical metal plasticity and the Drucker-Prager plasticity models are appropriate for this study and the comparisons between them are summarized as follows.

Characteristics of Classical metal plasticity:

- It is available in both the ABAQUS/Standard and ABAQUS/Explicit models.
- It uses the von Mises (for isotropic yield) surfaces with associated plastic flow.
- It is appropriate for either the perfect plasticity or isotropic hardening behavior.
- It is good for applications such as crash analyses, metal forming, and general collapse.
- It can be combined with the model of either the 'progressive damage and failure' or the 'dynamic failure' model (shear or tensile failure) in ABAQUS/Explicit (discussed in section 2.6.3) to provide a simple dynamic failure criterion that allows the removal of elements from the mesh.

Characteristics of Extended Drucker-Prager plasticity:

- It can be employed to simulate materials which compressive yield strength is greater than the tensile yield strength, such as composite and polymeric materials.
- It is able to simulate material responses under basically static loading and allows materials to harden and/or soften isotropically.

- It can only be used in conjunction with the models of progressive damage and failure in ABAQUS/Explicit, but not with dynamic failure model such as dynamic shear failure model, to specify different damage initiation criteria and damage evolution laws, which allow for the progressive degradation of the material stiffness and the removal of elements from the mesh.
- It offers three different yield criteria (in the basis of the shape of the yield surface in the meridional or *p*-*q* plane) in the ABAQUS/Standard models (Implicit/dynamic or Standard/static) and can be classified into a linear form, a hyperbolic form, or a general exponent form [44].

Another prerequisite is the use of Explicit/dynamic model in ABAQUS to perform the dynamic failure analysis in order to obtain the ultimate load of specimens. Both the classical metal plasticity and the linear Drucker-Prager plasticity can be implemented in ABAQUS Explicit/dynamic while the Drucker-Prager hyperbolic and general exponent models can only be used in Standard models.

2.6.2 Analytical Model in ABAQUS

Although both ABAQUS/Standard and ABAQUS/Explicit are applicable for various problems, it is important to select the appropriate analysis method based on the characteristics of the problem of interest and the features of these two analysis methods.

The explicit dynamics procedure can efficiently solve a wide variety of nonlinear solid and structural mechanics problems. When non-linear dynamic response is being studied, the direct integration of the system must be used. Explicit direction integration is provided in ABAQUS/Explicit, while implicit direction integration is provided in ABAQUS/Standard. The distinguishing characteristics of the explicit and implicit methods are (from ABAQUS manual):

- Explicit methods require an infinitesimal stable time increment (usually take 10^3 to 10^6 increments) merely based on the highest natural frequencies of the model regardless of the type and duration of loading.
- In implicit methods, there is no inherent limitation on the time increment size. Generally, the increment size is subject to accuracy and convergence considerations. Implicit simulations typically take orders of magnitude in fewer increments than do explicit simulations.
- No global set of stiffness matrix needs to be inversed and solved and no iteration of force equilibrium is required in explicit methods. The cost per increment of an implicit method is far greater than that of an explicit method.
- The main advantage of the explicit analytical model is that the solutions can reach a larger extension than that from standard/implicit method [45,46]. Especially for toughened epoxy adhesive, prior to reaching its failure it can uphold large extension/strain so that the explicit method is suitable.
- To predict a material's failure, the material properties need degrading to represent failure. The degradation of material properties usually causes material stiffness close to zero and leads to convergence difficulties in implicit analysis due to the inversion of the aforementioned global matrices [49,50]. In contrast, the explicit analysis without the inversion of the global matrices can avoid this problem.

2.6.3 Failure Mechanism

Failure indicates a stress or strain state that results in at least one failure criterion being met or exceeded. The failure criterion could be a simple and non-interacting criterion or a more complex and interacting criterion [50]. The failure analysis methodology normally consists of

three steps: (1) evaluating the stress state from the non-linear analysis, (2) substituting these stresses based on the material integration points of each element into a failure criterion selected to obtain the element's integrity, and (3) degrading the material stiffness in the failed elements to represent failure [49]. Failure initiation defines when failure is first detected or initiated in a pristine structure, which contains no initial damage (built in damage) and developed damage (developed from an initially failed region) [50]. The failure mechanism discussed here is limited to 'which part or section of the structure' is going to reach failure criterion first and the failed part is expressed by a failure model (dynamic failure) supported by ABAQUS. The further aspects such as initial and final crack length, crack growth path, growth/propagation rate, and energy release rate, etc. are not interested in this study.

According to physical results, the failure mechanism/model in ASTM D5656 is confined in the adhesive. The bonding interface failure (joint failure) is ignored, i.e., it is assumed the adhesive and the adherend are bonded perfectly. It is also assumed that there is no initial damage (imperfection), crack, void and peer between the adhesive and the adherend. Failure is limited to the adhesive section/part (adhesive failure). This failure given in finite element method (measured in PEEQ) is to simulate the real failure initiated by defects/flaws in real specimen originated from manufacturing. The failure initiates in critical regions, where usually the high stress or strain concentrations are localized, such as the bonded ends, edges, and interfaces, etc. Those regions are expected to have high stress/strain gradients (high PEEQ values) caused by geometric factors and material property mismatch (discontinuity with adjacent materials). In fact, these regions do not experience load directly, i.e., they are traction-free surfaces or regions. Based on the post-processing output contours from ABAQUS, the stress or PEEQ distributions can be displayed and to depict the path/mechanism of failure. Therefore, it

can be estimated whether the failure criterion or model applied is realistic. The failure of certain elements occurs one and only one time throughout the analysis and these failed elements are not able to carry/resist any load. Therefore, in ABAQUS, all stress components of these failed elements are set to be zero (discussed in section 2.6.6) for the next analysis step. However, the failure still progressively propagates to other adjacent elements until the accumulated critical parameter exceeds the failure tolerance, which means the section/structure fails.

Regarding failure models in ABAQUS, a simpler failure criterion can be defined as a critical level of stress or strain, or a combination of these quantities, from which the crack initiates. Via these critical values, ABAQUS/Explicit failure models offer several dynamic failure options to simulate the structural failure and determine the strength of structures.

Progressive Damage and Failure:

ABAQUS/Explicit offers general capability for simulating the progressive damage and failure in the von Mises and the Drucker-Prager plasticity models. The capability supports the specification of one or more damage initiation criteria, including ductile and shear criteria. After damage initiation, the material stiffness is degraded progressively, according to the specified damage evolution response. The progressive damage models allow a smooth degradation of the material stiffness, which makes these models suitable for both quasi-static and dynamic situations over the dynamic failure analysis.

Dynamic Failure:

In ABAQUS/Explicit, it includes two types of dynamic failure models, provided for the von Mises plasticity model. One is the shear failure model, which the failure criterion is decided by the accumulated equivalent plastic strain. Another is the tensile failure model,

which uses the hydrostatic pressure stress as a failure measure to model a dynamic spall or a pressure cutoff.

Comparing these two options of dynamic failure mechanism, the former model (the progressive damage and failure) requires more parameters than the latter. The progressive damage and failure divides the failure mechanism into initiation and evolution steps, which requires PEEQ, shear stress ratio (stress triaxality), strain rate, a material parameter (*Ks*) in the initiation step ,and equivalent plastic displacement or fracture energy per unit area (*Gf*) in the evolution step, correspondingly. In stead, the dynamic failure model requires only PEEQ or hydrostatic pressure stress. As a result, the dynamic failure model is selected due to the ease of execution.

2.6.4 Shear Dynamic Failure in ABQUS/Explicit

Concerning these two dynamic failure (shear and tensile) models, both can be used along with the von Mises plasticity model. Since the classical metal plasticity is based on the von Mises yield surface, it can combine with these two explicit dynamic failure models. Although the specimens are loaded in tension at the adherends of the ASTM D5656 models and of the scarf-patch-repaired composite laminates, the adhesive (the critical and interested part) is primarily under shear. The tension load is basically transferred in shear from one adherend to another; therefore, the shear stress contributes to a large percentage of stress state. In addition, the adhesive is more susceptible to the failure from tensile strain than from either pure shear or compression. Some adhesives are nonlinear behavior dominant and their strain to failure can exceed 100%. The failure model of ductile adhesives usually involves PEEQ (including tension, compression and shear strains); therefore, the dynamic failure model–dynamic shear failure model is preferred. The shear failure model is also mentioned in other researches [12,27],

especially for the adhesive failure [12]. For most lap joints or scarf joints, the failure initiates near the regions withstanding high peel stress. These regions have relatively high components of hydrostatic stress and volumetric strains. However, the hydrostatic stresses are critical but not sufficient enough to determine the failure. Considering the hydrostatic stresses may improve the accuracy of the solution but it cannot dominate the entire failure mechanism. Furthermore, polymer adhesives, which act like ductile materials, usually fail after substantially large plastic deformation and plastic flow have occurred. It is more appropriate to choose a critical strain based failure criterion [47].

2.6.5 Shear Failure Criterion

Research [51] recommended that, for strength investigation of single lap joints, the combination of the linear Drucker-Prager plasticity model along with the maximum shear strain failure criteria is the best approach rather than along with the stress based failure criteria. Therefore, the shear failure criterion is selected and applied to the strength analysis of ASTM D5656 single lap joints and scarf joints within repaired laminate composites.

The shear failure model is based on the value of the equivalent plastic strain (PEEQ) at element integration points (different from nodes) and the failure only occurs once the damage parameter is equal to or exceeds 1. The damage parameter, ω, is defined as [44]

$$\omega = \frac{\bar{\varepsilon}_0^{pl} + \sum \Delta \bar{\varepsilon}^{pl}}{\bar{\varepsilon}_f^{pl}} \tag{2.38}$$

where $\bar{\varepsilon}_0^{pl}$ is any initial value of the equivalent plastic strain, $\Delta \bar{\varepsilon}^{pl}$ is an increment of the equivalent plastic strain, and $\bar{\varepsilon}_f^{pl}$ is the equivalent plastic strain at failure, which is given by the test or iteration of finite element method [52]. The summation of $\Delta \bar{\varepsilon}^{pl}$ is performed over all increments throughout the analysis. This method requires the use of isotropic materials (for

elasticity part) and the von Mises plasticity model (for plasticity part) but not for non-isotropic materials or other plasticity models.

2.6.6 Element Removal

Once any integration point (different from node) inside material elements reaches the shear failure criterion, all stress components will be set to be zero automatically, which means the material point fails. For any material integration point, it can fail only one time throughout the analysis. By default, if all integration points at any section of an element fail, the element is removed from the mesh (or the deviatoric stress components are equal to zero for the integration points and remain zero for the rest of the computation in sequence). In fact, it is not necessary waiting for all integration points within the material element to fail before the element is removed. For 2-D finite element models of the ASTM D5656 lap joints and the scarf-patch-repaired composite laminates, the first-order reduced-integration solid elements are used and the element will be removed once its (only one) integration point fails. From the failure steps described earlier, the element removal can be regarded as a material degradation model. Generally, after the failure initiation has been detected, the elastic mechanical properties of the material are degraded (reduced) by a 'knockdown factor' or a 'material degradation factor' [50]. Based on experience, this factor could be given by certain value or zero. Since the failed element has been removed or the deviatoric stress components of the element are equal to zero in ABAQUS, it implies that the element cannot withstand stress any more and its stiffness degrades into zero, i.e., the degradation factor is set to be zero.

CHAPTER 3

FINITE ELEMENT ANALYSIS ON ASTM D5656

Through the calculation in chapter 2, the admissible elastic and plastic properties of the adhesive have been obtained. The purpose of the performance of finite element model to inspect the ASTM D5656 test is to verify linear Young's modulus (E) and Poisson's ratio (v) of the adhesive from preceding mathematic computations. The confirmation of required parameters for the failure criterion in ABAQUS will be carried out by combining ASTM D5656 test with finite element inspection. The conceptual flowchart of running finite element method is sketched as Figure 3.1.

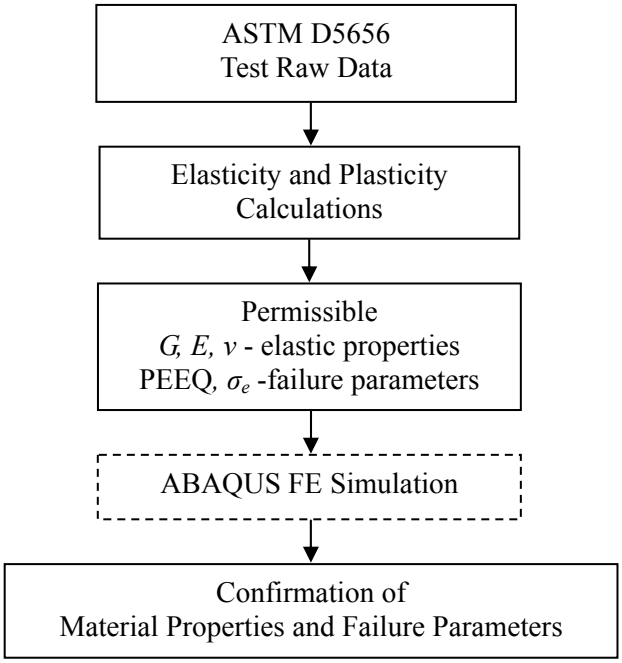

Figure 3.1. The purpose of finite element method for ASTM D5656 test.

3.1 Pre-Processing of ASTM D5656

3.1.1 Physical Features and Properties of ASTM D5656

The geometry and dimensions of ASTM D5656 single-lap joint specimens modeled in ABAQUS are specified in Figure 3.2.

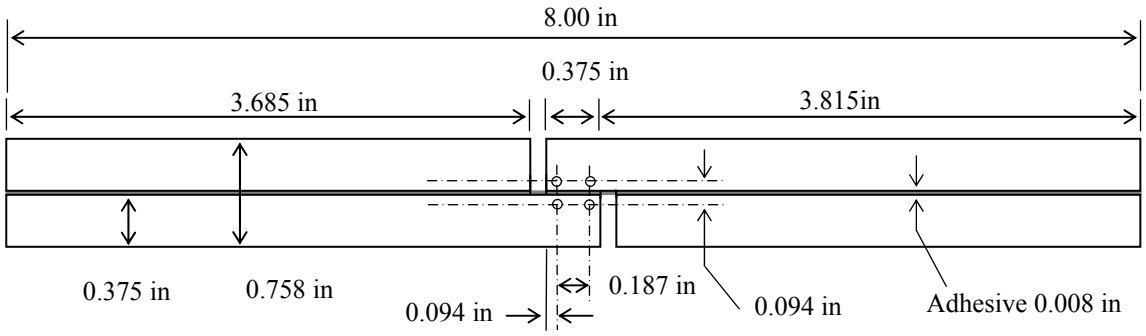

Figure 3.2. Geometry and dimensions of ASTM D5656 specimen.

Concerning the physical properties of ASTM D5656 specimen, the adherend is made of aluminum (2024-T3) and the film adhesive consists of Metlbond FM 1515-3 epoxy polymer. Owing to the consistent unit definition in ABAQUS (Table 3.1), the unit of physical properties should be converted in advance. The density unit will influence the dynamic analysis and end up with different parameter values in the failure criterion (PEEQ and stress limit). In addition, dynamic response, stress and strain, and reaction forces are also involved. The physical property data for Metlbond FM 1515-3 are listed in Table 3.2.

TABLE 3.1

CONSISTENT UNIT DEFINITION IN ABAQUS

	Length	Force	Mass	Time	Stress	Energy	Density
SI Unit	m	N	kg	sec	Pa	J	kg/m^3
US Unit	in	lbf	$lbf\ s^2/in$	sec	psi	in-lbf	$lbf\ s^2/in^4$

The area weight of the film adhesive here is 0.0302 lbf/ ft^2, and the volume density can be converted by area weight 0.0302 lbf/ ft^2 to volume weight 0.0302 lbf/ ft^3 for unit thickness. The thickness of the film adhesive within ASTM D5656 specimens is 0.008 in. and for the same

type of the adhesive within scarf-patch-repaired composite laminates is 0.005 in. The volume density of aluminum is 2.5901×10^{-4} lbf s^2/in^4 (2,768 kg/m^3) and its elastic properties are given by E=10.0 Msi and v = 0.33. The physical properties of each component has been converted and grouped in Table 3.3.

TABLE 3.2

PHYSICAL PROPERTIES OF METLBOND FM1515-3

Metlbond FM 1515-3	
Tg°F(°C)	338(170)
Area density Weight lbf /ft^2 (g/m^2)	0.03~0.10 (146~486)
Cure temp. range, °F(°C)	250~350 (121~177)
Service temp. range, °F(°C)	-65~320 (-54~160)
Color	blue

(Data source from Cytec website)

TABLE 3.3

PHYSICAL PROPERTIES IN TERMS OF US UNITS FOR EACH COMPONENT

	ASTM D5656 Adhesive	Composite Scarf Joint Adhesive	Aluminum
lbf s^2/in^4	1.0890×10^{-4}	1.7427×10^{-4}	2.5901×10^{-4}

3.1.2 Artificial Density and Damping Factor

The processing time required for Explicit/dynamic analysis is extremely longer than the regular Standard/static when running large specimens. For reasons of timesaving in processing, the physical density of each material is multiplied by a factor ($f\rho$) and the damping factor should be taken care of as well. Artificially increasing the physical density is similar to the function 'Mass Scaling Factor' embedded in ABAQUS. The multiplied density (artificial density) can reduce the dilatational wave speed (C_d) which is defined in ABAQUS [44] by

$$C_d \approx \sqrt{\frac{E}{\rho}} \tag{3.1}$$

where ρ is mass density of materials. It should be noticed that the above equation is simplified and suitable for isotropic elastic materials only.

In addition, the increase of stability limit $\Delta\ t_{stable}$ in finite element analysis can significantly reduce computation time, especially for Explicit/dynamic model. In ABABQUS, based on the element-by-element estimate without damping, the stability limit can be simply defined using the element characteristic length, L^e, and the wave speed of materials, C_d:

$$\Delta t_{stable} \approx \frac{L^e}{C_d} \tag{3.2}$$

Actually, the above equation is a simplified form for stability limit in the Explicit/ dynamic analysis. The original stability limit in terms of the highest frequency (ω_{max}) in the system with fraction of critical damping [44] is given by

$$\Delta t_{stable} = \frac{2}{\omega_{\max}}(\sqrt{1+\xi_{\max}{}^2} - \xi_{\max}) \tag{3.3}$$

in which ξ_{max} is the fraction of critical damping in the model with highest frequency. The fraction of critical damping is interpreted as

$$\xi = \frac{\alpha_R}{2\omega} + \frac{\beta_R \omega}{2} \tag{3.4}$$

where ω denotes natural frequency and α_R and β_R mean the mass proportional damping factor and the stiffness proportional damping factor, respectively. The damping system can be expressed by

$$[C]_{damp} = \alpha_R[M] + \beta_R[K] \tag{3.5}$$

where the $[C]_{\text{damp}}$ is a damping matrix and $[M]$ and $[K]$ mean a mass matrix and a stiffness matrix, correspondingly. They are specified in ABAQUS as belonging to Rayleigh damping factors, which can be used in steady-state dynamic analyses to get quantitatively accurate results. The

reason for introducing damping factors into the model is to limit numerical oscillations or to add physical damping to the system. Damping is a convenient manner of including the essential absorption of energy without modeling the effects in detail. The equations (3.3) and (3.4) indicate a tendency for stiffness proportional damping to have a greater effect on the stable time increment than mass proportional damping. Generally, it is recommended [44] to use the mass proportional damping (α_R) rather than the stiffness proportional damping (β_R). Too large a value of α_R will cause significantly rigid body motion and the misuse of β_R causes convergent difficulties.

The critical damping defines the limit between oscillatory and non-oscillatory motion in the context of free-damped vibration. Contrary to engineering intuition, ABAQUS/Explicit introduces a small amount of damping in the form of bulk viscosity to control high-frequency oscillation. The actual high frequency in the system is based on a complex set of interacting factors, and it is not computationally possible to obtain its exact value. It can be shown that the highest element frequency determined on an element-by-element basis is always higher than the highest frequency in the assembled finite element model [44]. The equation (3.1) is an efficient and conservative form.

3.2 Finite Element Modeling of ASTM D5656

In ABAQUS/CAE, the finite element model of the entire ASTM D5656 specimen has been constructed in 2-D space in order to reduce processing time and simplify the stress-strain analyses. The state of stress-strain analysis for adhesives is under the plane strain model due to the modeling facet in ABAQUS (Figure 3.3).

The modeling and mesh of ASTM D5656 2-D specimens and particularly the mesh of analyzed portion within the adhesive layer are shown in Figures 3.4 and 3.5, respectively.

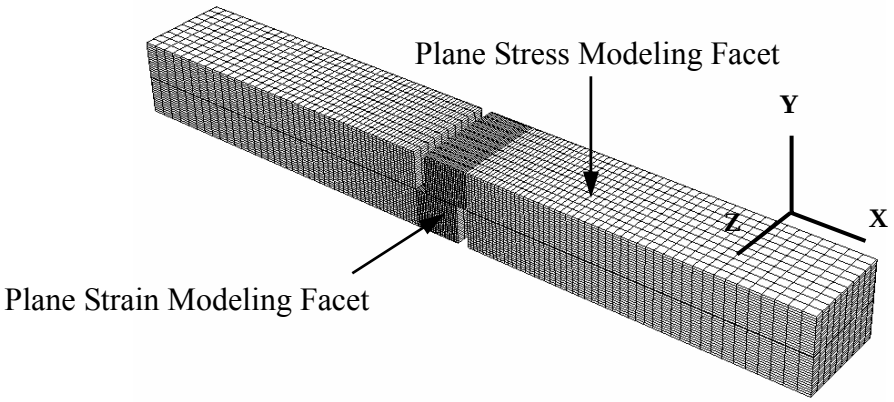

Figure 3.3. Definition of plane stress and plane strain modeling in ABAQUS.

The overlap portion (gauged part) has been meshed tensely so as to produce more precise results (mesh convergence or *h* convergence [53]). The portions away from the overlap are relaxed in mesh using 'biased seed' along the edges of parts. Four-node quadrilateral bilinear elements (CPE4R) are defined for the whole model.

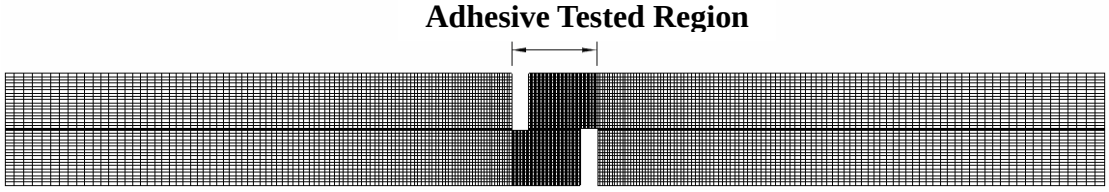

Figure 3.4. 2-D finite element mesh of entire ASTM D5656 specimen.

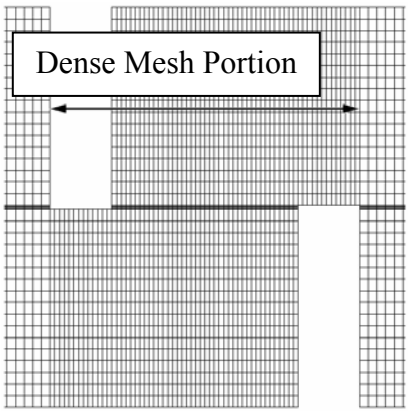

Figure 3.5. Dense mesh in the adhesive region of ASTM D5656 2-D finite element model.

After modeling, Table 3.4 lists the number of elements and the total nodes generated in the adhesive and the adherends corresponding to different plasticity models. For Drucker-Prager plasticity, the analysis is much more difficult to converge, especially under the Standard/static model. The mesh of the overlap within the Drucker-Prager model has been refined rigorously.

TABLE 3.4

THE NUMBER OF ELEMENT IN ASTM D5656 FINITE ELEMENT ANALYSIS MODELS

	Classical Metal Plasticity Model		Drucker-Prager Plasticity Model	
	Overlap	Non-overlap	Overlap	Non-overlap
Adhesive	160	800	240	12,650
Adherend	1,360	7,242	5,200	22,740
Total element	9,562		33,740	
Total node	9,885		34,291	

Regarding each modeling steps in ABAQUS/CAE, they are summarized in brief below (the definition and terminology are defined by ABAQUS exclusively):

Part Module: 2-Dimensional, Deformable, shell model.

Property Module:

1. Elasticity: isotropic for both adherend and adhesive sections.
2. Plasticity 1: the classical metal plasticity (given by tabular isotropic hardening data without strain-rate-dependence) and the dynamic shear failure are given in the adhesive part (only applied with classical metal plasticity model).
3. Plasticity 2: the Drucker-Prager plasticity, linear and general exponent models defined by shear criterion (isotropic, tabular Drucker-Prager hardening data corresponding to true stress-strain test data without strain-rate-dependence) are under Standard/static and Explicit/dynamic (only for linear Drucker-Prager) analyses without the dynamic shear failure.
4. The dynamic shear failure should be manually defined by code are under ‘Property

Module' right after the plastic property in the input file because ABAQUS/CAE does not support it.

Interaction Module: Tie (constrains)

Step Module:

1. Explicit/dynamic and Standard/static analyses are applied alternatively.
2. 'Nlgeom' option is switched on to indicate that geometric non-linearity (due to large displacement or strain >5%, and moderate rotation kinematics [49]) should be accounted for during the analysis step.

Mesh Module:

1. Quadrilateral structural mesh, continuum/solid, 4-node bilinear plane strain quadrilateral, reduced integration, and hourglass control, explicit elements (CPE4R for whole model) are applied under Explicit/dynamic analysis.
2. CPE4R elements are given in adherend sections and 4-node bilinear plane strain quadrilateral, while incompatible elements (CPE4I) are defined in the adhesive section under Standard/static analysis.
3. 2-D 4-node cohesive elements (COH2D4) are given in the adhesive section (used only with ABAQUS 6.5).

Load Module: Displacement control is loaded in the loading direction (*x*-direction).

With respect to element type, in Standard/static of ABAQUS, there are many more options than that in Explicit/dynamic. In Standard/static, the element CPE4I is defined for the adhesive due to the remarkable difference of stiffness from adherends (aluminum). The element CPE4R is specified for adherends. While in Explicit/dynamic, both adherend and adhesive sections are given CPE4R only due to the limitation of ABAQUS.

As described in chapter 2, the purpose of using Explicit/dynamic model is to track the reaction force and displacement at each infinitesimal time increment. The dynamic analysis is based on the premise of a quasi-static dynamic state, which assumes the system is under rate-independent situations (regardless of strain-rate and loading speed). The ASTM D5656 test was performed under a monotonic low speed rate of 0.05 in./min, which ensures the whole system remaining statically in equilibrium for every loading step/increment. When the shear dynamic failure is activated under ABAQUS/Explicit, by default, the stress components of the elements are set to zero once the equivalent plastic strain (PEEQ) reaches the specified failure value at integration points of the elements. Through this procedure, the load can be outputted instantaneously at the exact instant of failure.

The reason for running Standard/static in parallel is to rapidly obtain and confirm the linear elastic properties. Because the behavior of the materials is within the linear behavior region, the relation of stress-strain is completely linear and the time increment of analysis can increase with large span, in turn, reducing computation time. Furthermore, in Standard/static, there are no inertia matrix and acceleration terms. Without inertial force, the consideration of frequency and damping factors can be avoided, which makes the simulation easier to implement.

Concerning loading type, it is suggested taking the advantage of displacement control instead of tension applied directly on the adherend, which make the analysis easier to converge. Compared with force applied, the displacement control can provide a more precise response. In dynamic analysis model, the load/displacement must be given by magnitude along with the 'Amplitude'. Usually by default, VALUE (magnitude) is set equal to RELATIVE (percentage of given load/displacement) for each time increment. All the finite element analyses were performed on a high performance computer system, a SGI Altix 3700 with 32 1.3GHz Intel

Itanium2 (64 bit) processors with 32 GB RAM and 36GB scratch disk and a pair of clusters from Atipa Technologies. Each Atipa cluster has 17 dual 2.666 MHz Xeon (32 bit) processor nodes (2 GB RAM with 77GB scratch disk each) along with 1TB of file storage accessible to all nodes via NFS. All nodes are running Red Hat Linux.

3.3 Finite Element Analysis within the Linear Elastic Region

3.3.1 Confirmation of Adhesive Young's Modulus

From Metlbond FM 1515-3 database on the Cytec website, there is no property data exactly obtained from similar standard as ASTM D5656 to be compared. Different standards sometimes carry out dissimilar results especially for shear tests. As a result, the Standard/static analysis within the linear behavior region, before yielding, is used to determine Young's modulus and Poisson's ratio of the adhesive.

First, ABAQUS records the historical changes of the coordinates of the four nodes specified in Figure 3.6(a), in which the KGR-1 device (4-pinned method [52]) is attached to the specimen during the test. The Figure 3.6(b) shows the deformed ASTM D5656 2-D model and the relative positions of these 4-pinned holes (expressed by node number).

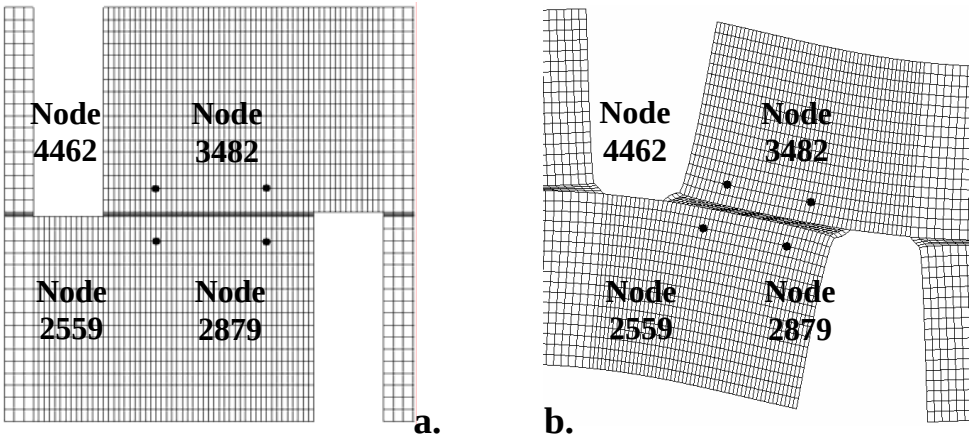

Figure 3.6. (a) Locations (node numbers) of the ASTM D5656 2-D FE model where the KGR-1 device is mounted and (b) after it is deformed (deformation scale factor 30).

Second, based on the recorded historical coordinate data, they can be converted into historical displacement/extension data using the 4-pinned method (Appendix). These converted displacements represent the relative displacement of two adherends along the KGR-1 direction (not along the global *x*-direction). In addition, the converted load-relative displacement data from finite element analysis will be compared with the raw data from the physical tests. In ABAQUS, the reaction force versus relative displacement data (converted by 4-pinned method) are recorded up to the reaction forces reaching approximately 2,400 lbf and are compared with the test data using various combinations of Young's modulus and Poisson's ratio. The reaction force limit 2,400 lbf given here is was determined from test data to ensure the material under linear elastic behavior region. The ABAQUS results are obtained corresponding to several permutation and combination sets of *E* and *v*. The ABAQUS data curves are compared with the star and port side test data, respectively, to seek the data curve with the best fit (Tables 3.5 to 3.8 and Figures 3.7 to 3.10).

TABLE 3.5

ABAQUS RESULTS FOR E = 175,630 psi AND E = 168,167 psi WITH v = 0.3 FROM STANDARD/STATIC ANALYSIS

ABAQUS Data E=175,630 psi v=0.3 Adhesive element-CPE4I Adherend element-CPE4R			ABAQUS Data E=168,176 psi v=0.3 Adhesive element-CPE4I Adherend element-CPE4R		
Time Increment	Reaction Force (lbf)	Relative Displacement (in)	Time Increment	Reaction Force (lbf)	Relative Displacement (in)
1	0.00	0.00000000	1	0.00	0.00000000
2	45.11	0.00002180	2	44.71	0.00002180
3	90.23	0.00003411	3	89.42	0.00003411
4	157.90	0.00006181	4	156.49	0.00006181
5	259.41	0.00009388	5	257.09	0.00009388
6	411.67	0.00015173	6	407.99	0.00015672
7	640.06	0.00022575	7	634.34	0.00024575
8	982.65	0.00035432	8	973.87	0.00036533
9	1496.53	0.00054324	9	1483.16	0.00055927
10	**2267.35**	**0.00081574**	**10**	**2247.10**	**0.00084225**

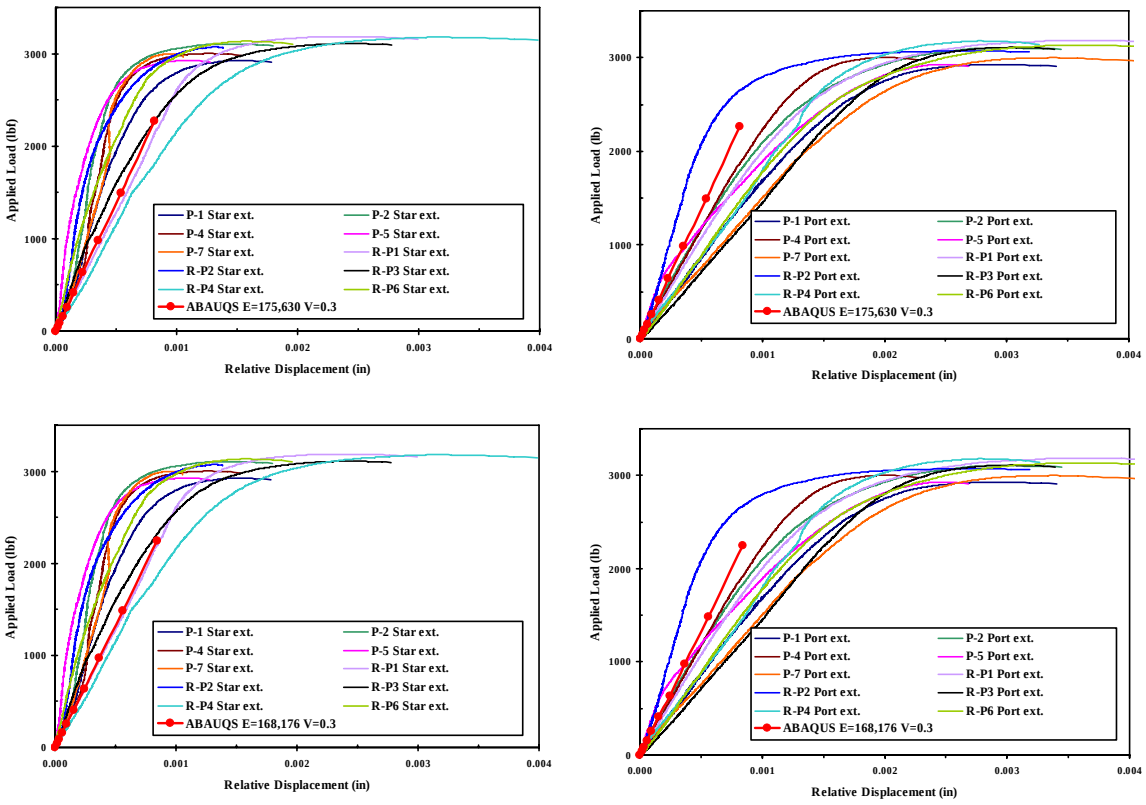

Figure 3.7. Reaction force versus relative displacement of E = 175,630 psi and E = 168,167 psi with v = 0.3 compared to star and port sides, respectively.

TABLE 3.6

ABAQUS RESULTS FOR E = 193,023 psi AND E = 198,796 psi WITH v = 0.35 FROM STANDARD/STATIC ANALYSIS

ABAQUS Data E=19,3023 psi v=0.35 Adhesive element-CPE4I Adherend element-CPE4R			ABAQUS Data E=198,796 psi v=0.35 Adhesive element-CPE4I Adherend element-CPE4R		
Time Increment	Reaction Force (lbf)	Relative Displacement (in)	Time Increment	Reaction Force (lbf)	Relative Displacement (in)
1	0.00	0.00000000	1	0.00	0.00000000
2	45.11	0.00002180	2	46.03	-0.40498154
3	90.23	0.00003411	3	92.05	-0.00003089
4	157.90	0.00006181	4	161.09	0.00005181
5	259.41	0.00009388	5	264.65	0.00008888
6	411.67	0.00015173	6	419.99	0.00014121
7	640.06	0.00022575	7	653.00	0.00022024
8	982.65	0.00035432	8	1002.51	0.00033381
9	1496.53	0.00054324	9	1526.77	0.00051223
10	**2267.35**	**0.00081574**	**10**	**2313.17**	**0.00077473**

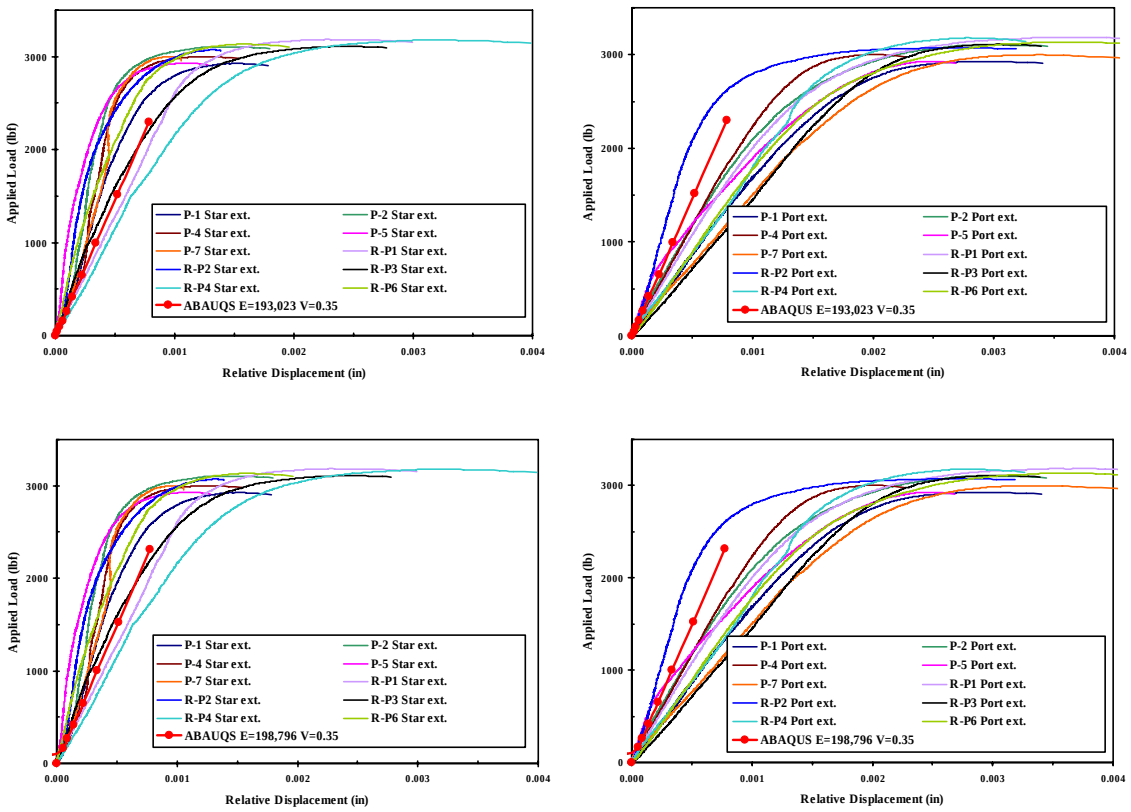

Figure 3.8. Reaction force versus relative displacement of E = 193,023 psi and E = 198,796 psi with v = 0.35 compared to star and port sides, respectively.

TABLE 3.7

ABAQUS RESULTS FOR E = 213,484 psi AND E = 200,172 psi WITH v = 0.35 FROM STANDARD/STATIC ANALYSIS

ABAQUS Data E=213,484 psi v=0.35 Adhesive element-CPE4I Adherend element-CPE4R			ABAQUS Data E=200,172 psi v=0.35 Adhesive element-CPE4I Adherend element-CPE4R		
Time Increment	Reaction Force (lbf)	Relative Displacement (in)	Time Increment	Reaction Force (lbf)	Relative Displacement (in)
1	0.00	0.00000000	1	0.00	0.00000000
2	46.65	0.00001180	2	45.94	0.00001680
3	93.30	0.00002360	3	91.88	0.00003411
4	163.27	0.00005167	4	160.79	0.00006181
5	268.23	0.00008336	5	264.15	0.00009388
6	425.66	0.00013570	6	419.19	0.00014172
7	661.82	0.00020473	7	651.76	0.00022626
8	1016.05	0.00031278	8	1000.61	0.00034085
9	1547.41	0.00048571	9	1523.89	0.00052427
10	**2344.43**	**0.00073719**	**10**	**2308.80**	**0.00078780**

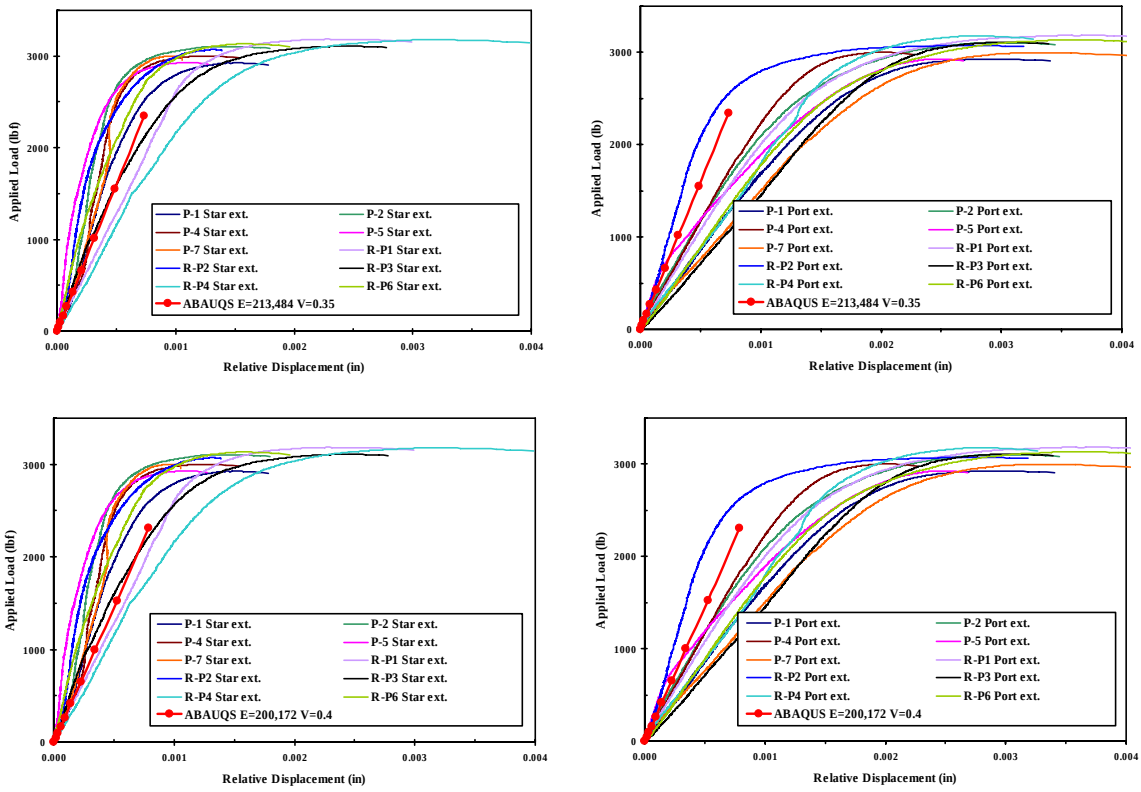

Figure 3.9. Reaction force versus relative displacement of E = 213,484 psi and E = 200,172 psi with v = 0.4 compared to star and port sides, respectively.

TABLE 3.8

ABAQUS RESULTS FOR E = 190,400 psi AND v=0.4
FROM STANDARD/STATIC ANALYSIS

ABAQUS Data E=190,400 psi v=0.4 Adhesive element-CPE4I Adherend element-CPE4I		
Time Increment	Reaction Force (lbf)	Relative Displacement (in)
1	0.00	0.00000000
2	45.55	-0.00000820
3	91.11	0.00003411
4	159.44	0.00006181
5	261.93	0.00009439
6	415.68	0.00015275
7	646.29	0.00022729
8	992.22	0.00035688
9	1511.10	0.00054132
10	**2289.43**	**0.00082087**

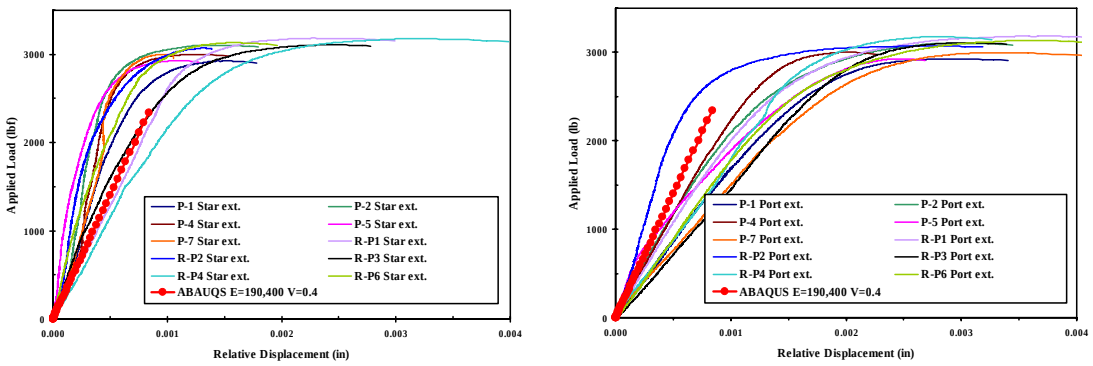

Figure 3.10. Reaction force versus relative displacement of E = 190,400 psi and ν =0.4 compared to star and port sides, respectively.

3.3.2 Results and Observation of the Linear Region Finite Element Analysis

According to finite element results within the linear behavior section, the following observations can be made.

1. From Figures 3.7 to 3.10 and Tables 3.5 to 3.8, the test data from either the star side or the port side cover a wide range so that various combinations of Young's modulus and Poisson's ratio all fall within the ballpark (E from 175,630 to 213,484 psi). The finite element results approach the test data from the star side much more than do those from the port side. In particular, the R-P1 and R-P3 two curves almost bond all data curves from finite element results (Figure 3.11).
2. After yielding, both the port and star side test data curves still scatter widely and diverge with different exponential orders. It is difficult and not efficient to compare those (neither the port nor the star side) test data with finite element results. Furthermore, it is inappropriate merely to choose the linear region of curves to compare the test data with the finite element results. The plastic region curve should be considered as well in finite element analysis to make curve-fit more persuasive and easier to back-check the linear Young's modulus and Poisson's ratio.

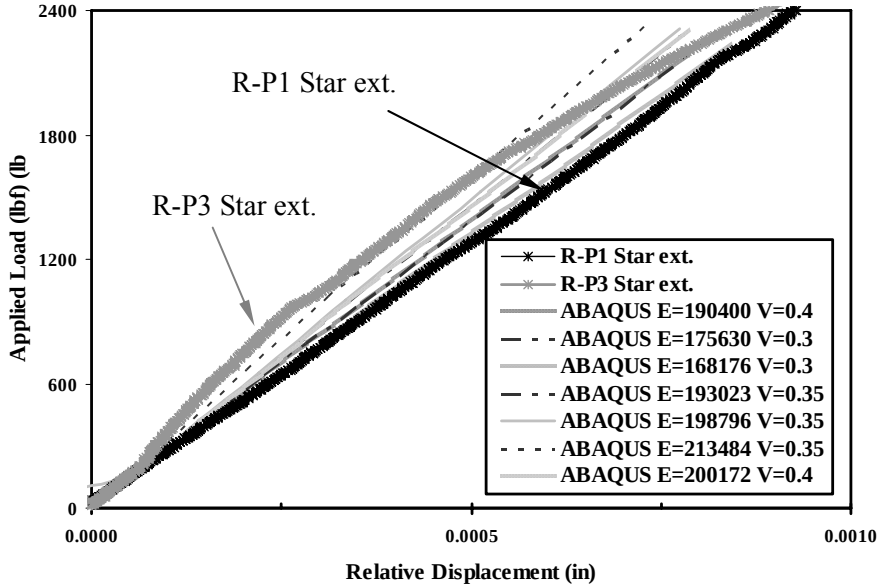

Figure 3.11. Comparison of ASTM D5656 results from ABAQUS and R-P1 and R-P3 star side test data.

3. With similar Young's moduli, the results of Standard/static finite element analysis obtained from several combinations of element type (CPE4R or CPE4I) do not display a significant difference. Either using load control or displacement control under the linear region gives analogous results. The relative displacements calculated using 4-pinned method produce a much more desirable curve closer to the test data, as expected.
4. **Average Data:** To generate a meaningful and normalized test data curve, the total-specimen averaged data must be introduced to represent ASTM D5656 test results to perform curve-fit. The port and star side test data of each specimen are averaged first. Then all specimen's average data are taken on average again, which results in only one total-average curve. Excluding unreasonable test data, only 10 sets were selected to be normalized and will be referred to as the 10-average (10-Avg) in this study (Figure 3.12).
5. **Young's Modulus and Poisson's Ratio of Adhesive:** Once the 10-average data curve has been obtained, the linear region curve-fit can be more easily achieved. Through

linear Standard/static analysis with load-displacement curve-fit (Figure 3.13) without plastic and failure consideration, the elastic properties, E = 174,645 psi and v =0.35, of the epoxy adhesive, Metlbond FM 1515-3 under ASTM D5656 test, are determined.

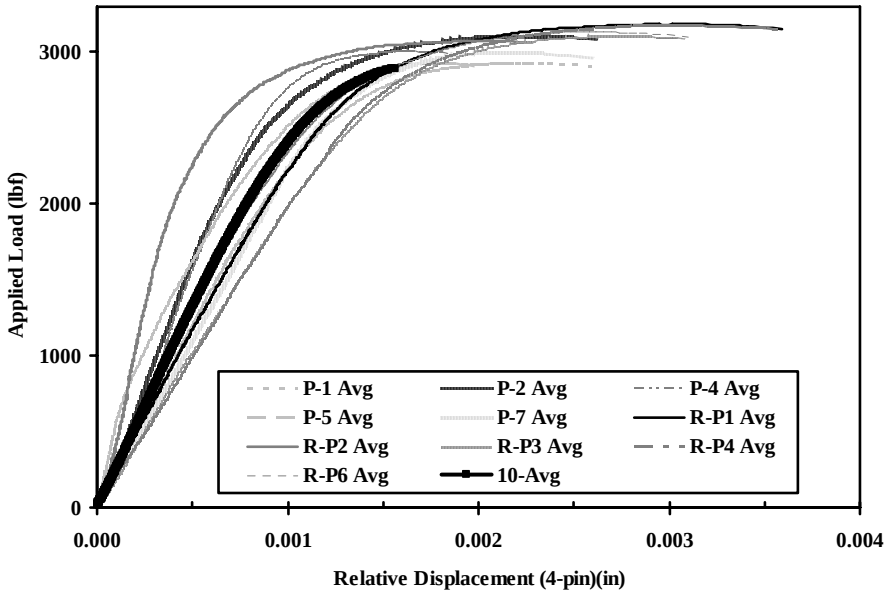

Figure 3.12. ASTM D5656 10-average curve versus individual averaged data curve.

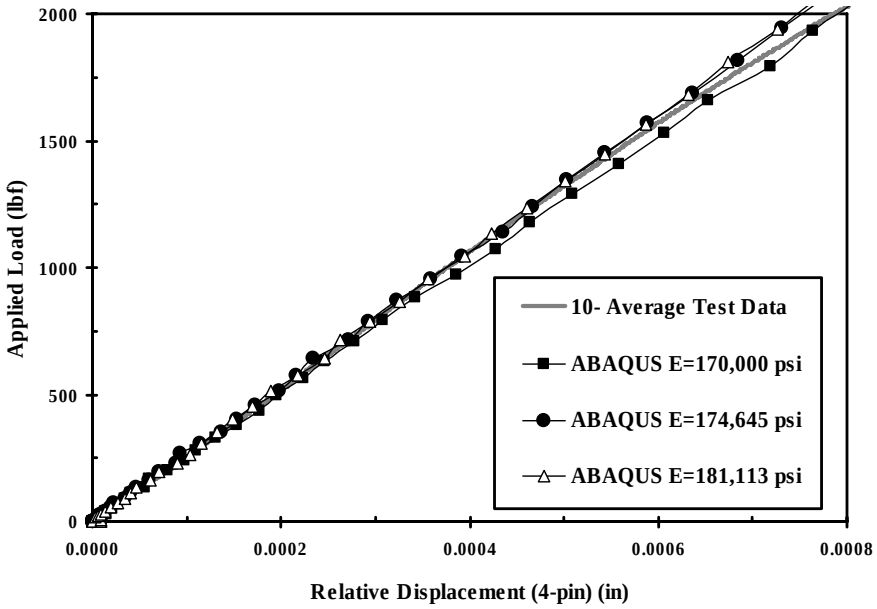

Figure 3.13. Comparison of ASTM D5656 ABAQUS results for different combinations of E and v with average test data within the linear region.

3.4 Finite Element Analysis within the Non-Linear Plastic Region

In non-linear analysis, the Explicit/dynamic analytic model is employed to obtain the ultimate strength and failure load, and to determine the plastic properties of the adhesive at the same time. As described in section 2.6.4 and 2.6.5, the dynamic failure criterion—shear failure is applied only to the adhesive. Once the adhesive within the overlap part fails, the two adherends are torn apart. The nodal reaction force of the left-hand-side adherend (constrained) along the loading direction reduces to zero. In turn, the ultimate and failure load are generated in historical output files. The recorded position coordinate data are output and converted to relative displacements of the four nodes specified which represent 4-pinned holes. The entire elasto-plastic curve can be constructed by plotting the historical reaction force versus the relative displacement curve. Comparing the finite element result curve with the test data curve, the plastic properties are modified until curve-fit accomplished satisfactorily. The degree of curve-fit in the non-linear analysis of the adhesive bonded in ASTM D5656 models will vitally influence the simulation of scarf-patch-repaired composite laminates. Following the procedure in the ASTM D5656 Standard/static model, Young's modulus 17,4645 psi and Poisson's ratio 0.35 are imported to the Explicit/dynamic input file. Only under the 'Property Module', the material property of the adhesive is added by classical metal plasticity model expressed in terms of 'Tabular Data' (defining yield stress/effective plastic stress, σ_e and equivalent plastic strain, PEEQ for each load increment after material's initial yielding). The PEEQ is expressed by tensor form, and the difference between the PEEQ computed from engineering shear strain is shown in Figure 3.14. The absolute PPEQ is defined as the PPEQ after the initial yielding, which increases from zero until the value at material failure. In the 'Step Module', the 'General Static' model is switched to 'Explicit Dynamic' and 'Nlgeom' is automatically activated.

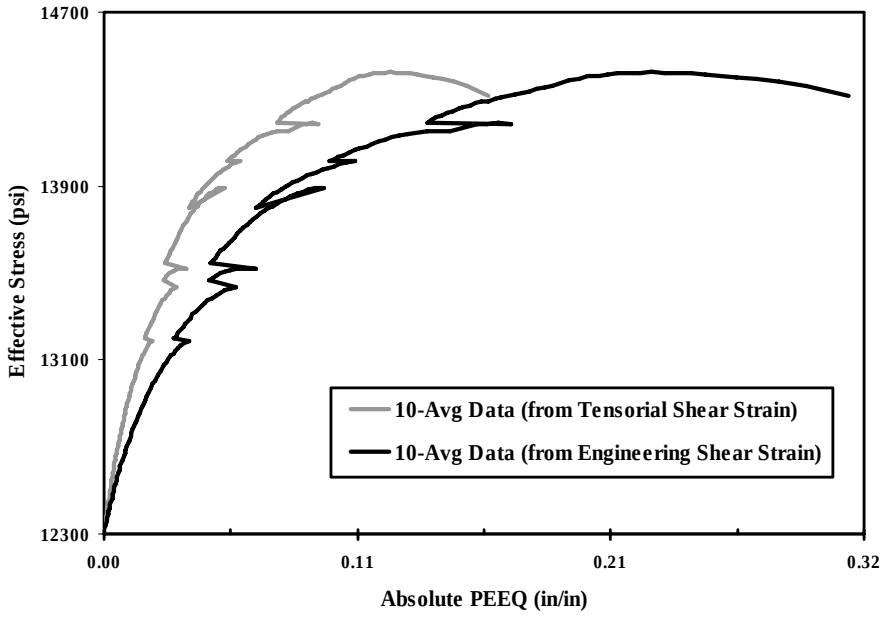

Figure 3.14. Comparison of PEEQ converted from engineering shear strain and tensorial shear strain.

The hardening 'Tabular Data' given in ABAQUS are defined as isotropic hardening (obtained from nominal stress-strain curve) without strain rate-dependence. If the nominal stress-strain relation is converted to true stress-strain, the adhesive's behavior, after yielding, changes to exponent form (Figure 3.15). The significant strain hardening cannot be over-simplified as perfectly plasticity. The adhesive's hardening data should approximate the calculated data in Tables 2.5 and 2.6, and should be modified by the curve fit of the result curves from finite element simulations (load-displacement data converted from the 4-pinned method) to the average load-displacement test data curve.

The shear failure value (denoted by 'S_f' in this study) is determined by the comparison of ultimate load, failure load, and the relative displacement at failure between the 10-average test data and finite element results. From Table 2.4, the percentage of the difference between ultimate and failure loads is merely 0.8 %. The classical metal plasticity with strain hardening data is chosen for the plasticity model and the values of ultimate and failure load may be very

close in the results from dynamic simulations. In addition, the exponent Drucker-Prager model also produces ultimate and failure loads distinctly, whilst the linear Drucker-Prager model cannot discretely simulate ultimate and failure loads.

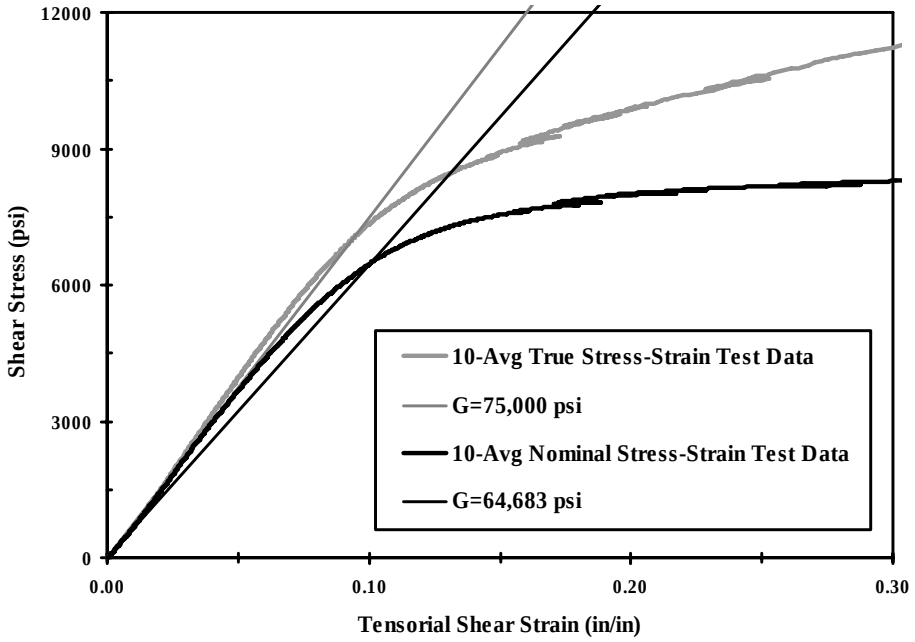

Figure 3.15. Comparison of 10-average test data converted from nominal and true stress-strain.

Through iteration and curve-fit procedures with entire 10-average test data curve under the classical metal plasticity model, it has been found that the absolute PEEQ trial data associated with nominal stress-strain relation lead to acceptable numerical results in ABAQUS when the effective plastic stress rises from 9,700 psi. The classical metal plasticity model following the von Mises yield surface also produces analogous exponent or hyperbolic result curves. Based on the results from ABAQUS and theories discussed in section 2.4, the von Mises yield surface could be regarded as a special case simplified from Drucker-Prager model when the sensitivity to the hydrostatic component stress is not as dominant as the shear component. In each case, the optimum property data sets under the classical metal plasticity

model are tabulated in Table 3.9 and plotted in Figure 3.16. In both nominal and true stress-strain cases, the trial data curve 4 is the optimum, marked as Tn-4 (nominal stress-strain case) and Tt-4 (true stress-strain case), respectively.

TABLE 3.9

NON-LINEAR PROPERTIES OF THE ADHESIVE WITH DIFFERENT STRESS-STRAIN DEFINITIONS UNDER CLASSICAL METAL PLASTICITY DYNAMIC MODEL

Trail Data 4 (Tn-4) **(Nominal stress-strain case)** Explicit/Dynamic Model		Trail Data 4 (Tt-4) **(True stress-strain case)** Explicit/Dynamic Model	
Eff. Stress (psi)	**Abs PEEQ**	**Eff. Stress (psi)**	**Abs PEEQ**
9,700.0	0.00000	9,700.0	0.00000
10,400.0	0.00220	10,400.0	0.00160
11,300.0	0.00630	11,300.0	0.00500
12,100.0	0.01180	12,300.0	0.01150
13,000.0	0.02100	13,050.0	0.02150
13,700.0	0.03500	13,535.0	0.03500
14,070.0	0.05500	13,850.0	0.05500
14,310.0	0.08400	14,050.0	0.08000
14,340.0	0.11000	14,200.0	0.11000
14,310.0	0.14000	14,270.0	0.13000
14,050.0	0.17000	-	-

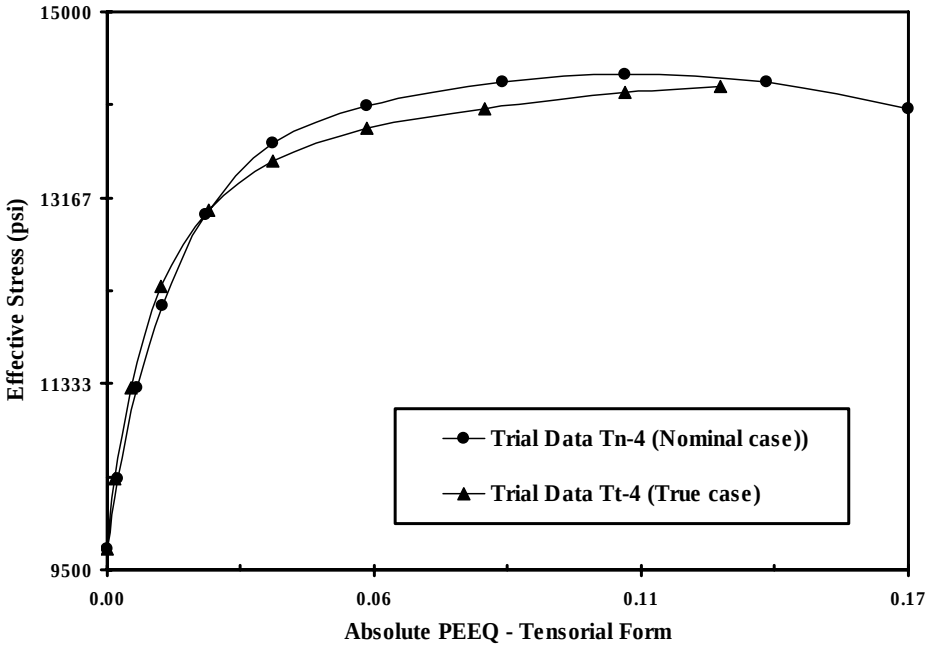

Figure 3.16. Finite element analysis trial data curves of the adhesive based on different stress-strain definitions under classical metal plasticity dynamic Model.

With the Drucker-Prager linear model, owing to the insufficiency of information about the yield stress in tension and in compression, some parameters (β, ψ, a, and b) cannot be predicted. The iteration is again applied to obtain the optimal approximation based on curve-fit. Both the Standard/static (Linear DP-STC) and Explicit/dynamic (Linear DP-DYN) models use displacement control for analysis. The results from the static analytical model are slightly different from the dynamic analytical model because the rate-dependent hardening is simplified as non-rate-dependent. The rate-dependence, including loading speed and strain rate, has significant influence on the final force/extension results [45,46]. The isotropic hardening data are based on the true stress-strain converted data (Tt-4 in Table 3.9) and the most desirable set is given in Table 3.10 and plotted in Figure 3.17.

TABLE 3.10

NON-LINEAR PLASTIC PROPERTIES OF THE ADHESIVE UNDER DRUCKER-PRAGER LINEAR MODEL

Standard/Static Model (True stress-strain case)		**Explicit/Dynamic Model** (True stress-strain case)	
Eff. Stress (psi)	Abs PEEQ	Eff. Stress (psi)	Abs PEEQ
97,00.0	0.00000	9,700.0	0.00000
10,400.0	0.00194	10,400.0	0.00150
11,300.0	0.00440	11,300.0	0.00390
12,300.0	0.00780	12,300.0	0.00740
13,400.0	0.01370	13,400.0	0.01360
14,200.0	0.02300	14,200.0	0.02300
14,600.0	0.03650	14,680.0	0.03650
14,950.0	0.05700	14,980.0	0.05700
15,170.0	0.08000	15,170.0	0.08000
15,250.0	0.11000	15,250.0	0.11000
15,310.0	0.13000	15,310.0	0.13000
Friction Angle (β)	2	Friction Angle (β)	3
Dilation Angle (ψ)	1	Dilation Angle (ψ)	2
K	0.875	K	0.835

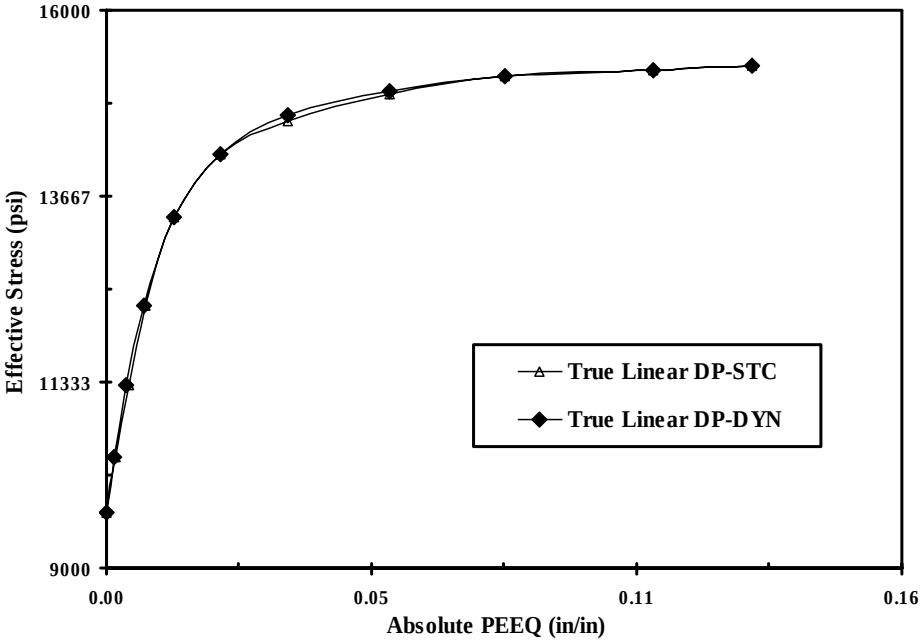

Figure 3.17. Finite element analysis trial data curve of the adhesive based on true stress-strain hardening under Drucker-Prager linear model.

If the linear Drucker-Prager model is extend to the general exponent Drucker-Prager model for comparison, the properties from the linear Drucker-Prager model (as discussed in section 2.4) are implemented to predict a parameter '*a*'. The results of using the tabular data in Table 3.10 overestimate the load-displacement significantly, no matter how much the parameter '*a*' varies. Therefore, the optimum isotropic hardening tabular data based on Table 3.9, modified by the parameters defined in the general exponent model, are grouped in Table 3.11 and Figure 3.18 which shows the difference between linear and exponent tabular data. The iteration data (Figure 3.18) are obtained by using the Standard/static model because the general exponent Drucker-Prager plasticity model cannot be performed in the Explicit/dynamic but only in the Implicit/dynamic.

By observing Figures 3.16 to 3.18, the hardening data arise from the effective stress 9,700 psi which is less than any pre-calculated value in Tables 2.4 to 2.6. The values in Tables

2.4 to 2.6 obtained from either the 0.2% offset method (explained by Figure 2.4) or the 2-tangent-line method (Figure 2.5), mentioned in section 2.3, are not precise. These methods use a straight line extrapolation from the very initial portion of the test data curve, and the slope of this straight line represents the initial linear elastic shear modulus but cannot count for the whole elastic portion. Using these methods to predict the yield stress (strength) is somewhat over the real value, especially using the 2-tangent-line method and the method descried in ASTM D5656 Standard. These similar methods are used to locate the 'knee' point, to be the initial yield stress value, which is far away from the value evaluated from the 0.2% offset method (compared Figures 2.4 and 2.5). In fact, based on the degree of similarity of curve-fit, the acceptable value of the initial yield stress/strength falls in the range 9,000~10,000 psi, which is close to the result (S_{xy}=5,988.78 psi equal to σ_e =10,372.87 psi) predicted by the 0.2% offset method (Table 2.2).

TABLE 3.11

NON-LINEAR PLASTIC PROPERTIES OF THE ADHESIVE UNDER GENERAL EXPONENT DRUCKER-PRAGER STATIC MODEL

Standard/Static Model **(True stress-strain case)**	
Eff. Stress (psi)	Abs PEEQ
9,700.0	0.00000
10,400.0	0.00150
11,300.0	0.00390
12,300.0	0.00740
13,400.0	0.01360
14,200.0	0.02300
14,680.0	0.03650
14,980.0	0.05700
15,170.0	0.08000
15,250.0	0.11000
15,310.0	0.13000
a	0.0025
b	2
Dilation Angle (ψ)	1

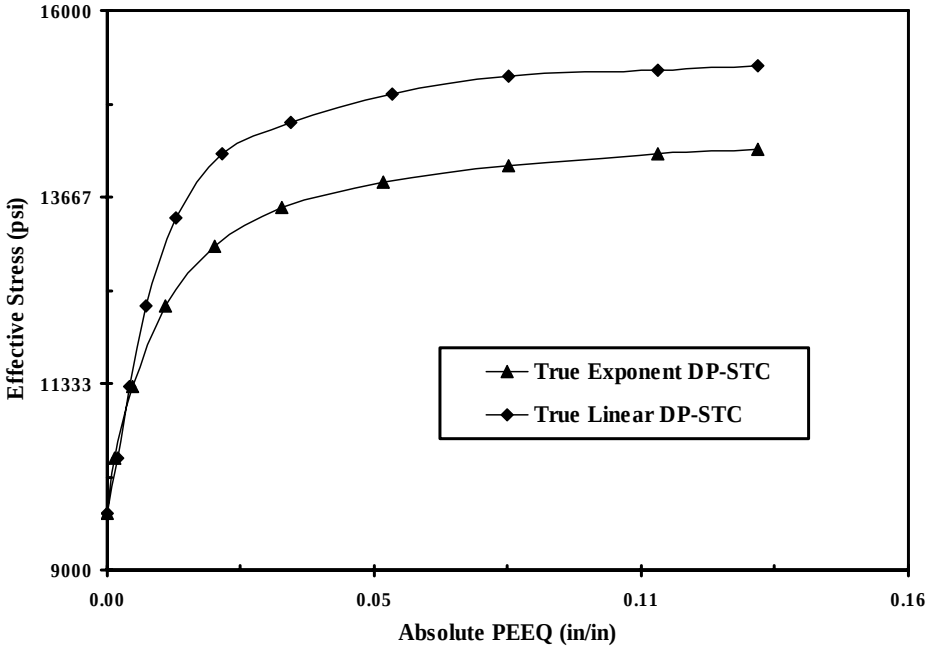

Figure 3.18. Isotropic hardening curves of the adhesive under different Drucker-Prager static model in ABAQUS.

In addition, although the stress-strain hardening data should be defined in true stress-strain form in ABAQUS, the iteration results dictate that the most satisfactory hardening curve is analogous to nominal stress-strain (apparent stress-strain in ASTM D5656 case) rather than in true stress-strain form (Figure 3.15). The linear elastic shear module obtained from true stress-strain data curves will overestimate the test value (64,683.3 psi) significantly and, accordingly, Poisson's ratio and Young's modulus are difficult to confirm. Table 3.12 shows Young's modulus yielded from different Poisson's ratios assumed under the same finite element model but using different stress-strain hardening curves. When using true strain hardening with Poisson's ratio from 0.13 to 0.35, the results in terms of reaction force-relative displacement curve cannot fit the 10-Avg curve as well as when using the nominal strain hardening data. Therefore, in this study, Young's modulus 174,645 psi and Poisson's ratio 0.35 from the nominal stress-strain data will be implemented in the following finite element simulations.

TABLE 3.12

YOUNG'S MODULUS OBTAINED FROM VARIOUS POISSON'S RATIOS BASED ON NOMINAL STRESS-STRAIN AND TRUE STRESS-STRAIN

Poisson's ratio (v)		0.13	0.17	0.20	0.25	0.3	0.33	0.35
Nominal Case	G 64,683.3	146,184.2	151,358.9	155,239.9	161,708.2	168,176.5	172,057.5	174,644.9
True Case	G 75,000.0	169,500.0	175,500.0	180,000.0	187,500.0	195,000.0	199,500.0	202,500.0

(Unit for modulus is psi)

3.5 Comparison and Discussion of Finite Element Analysis Results

3.5.1 Dynamic Analysis

As discussed in chapter 2, while using dynamic failure-shear failure, the elements fail once the accumulated PEEQ reaches the given limit at the integration points within elements. The failed element can no longer carry any load and the other un-failed elements must share the load which the failed element previously withstood. This process is repeated until the whole structure/section fails completely. The disturbance in the dynamic responses can be recorded simultaneously during element's failure one by one throughout the analysis step. Using the example of ASTM D5656, when the adhesive fails (time increment 0.635), the reaction force drops significantly and starts to oscillate drastically (Figure 3.19). Due to the inertial force (mass times acceleration) of the material and given material damping (Rayleigh damping factors discussed in section 3.1.2), the additional energy created by external loading will be damped out or dissipated (Figure 3.19) by the structure's motion. The failed specimen acts like a mass-spring free damped vibratory/oscillation system released from a given initial spring elongation. Due to damping factors, the failed structure keeps oscillating at its natural frequency until the magnitude of the oscillation decreases to zero. The entire system energy goes to zero or remains constant (actually some models cannot reach exactly zero system energy but will satisfy the tolerance or default value embedded in software), as exhibited in Figure 3.20.

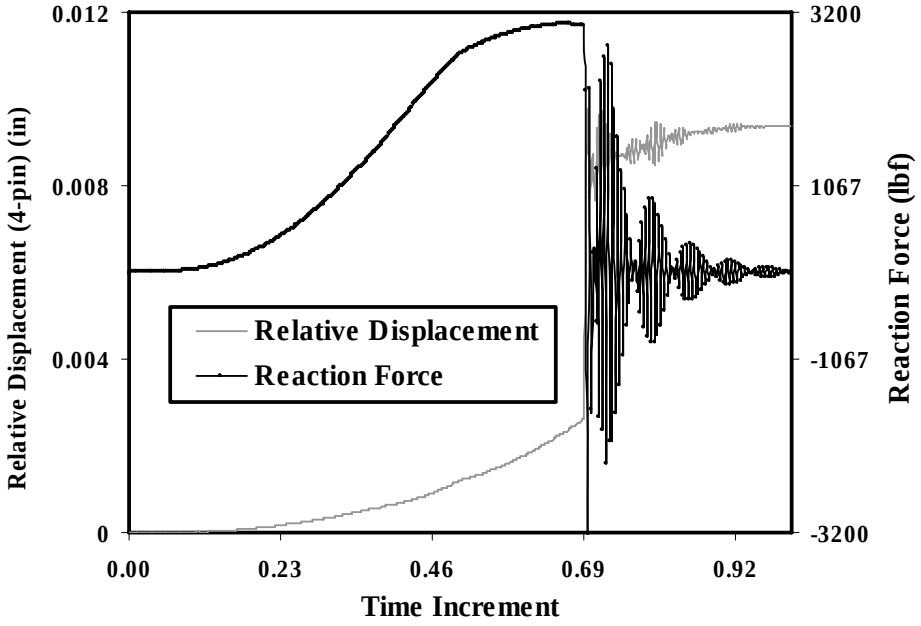

Figure 3.19. Response trends from ASTM D5656 FE Explicit/dynamic models (artificial density [$f\rho=10^3, \alpha_R=10$] with nominal stress-strain case).

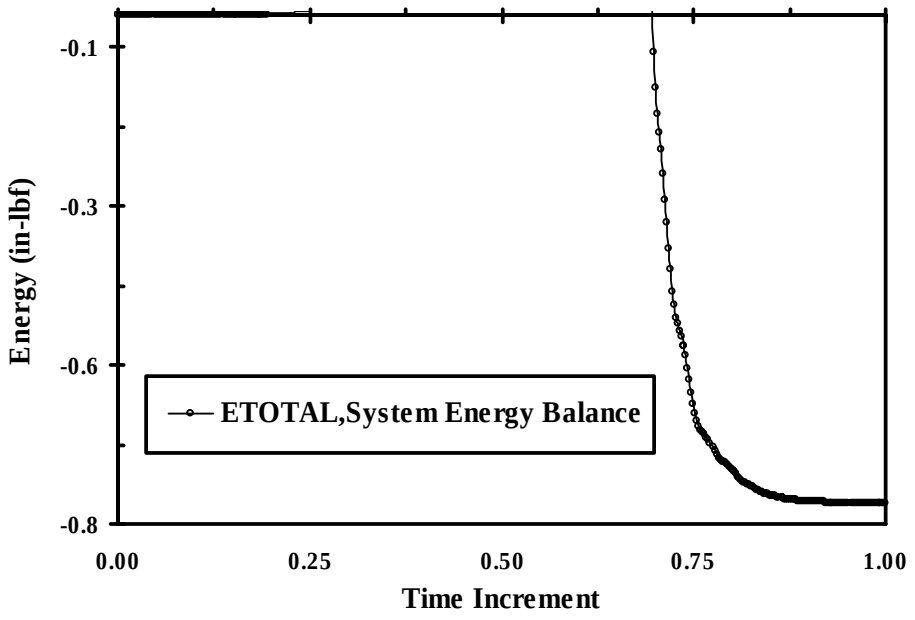

Figure 3.20. System energy balance trend of ASTM D5656 FE Explicit/dynamic models (artificial density [$f\rho=10^3, \alpha_R=10$] with nominal stress-strain case).

Results of Dynamic Analysis

The finite element results are graphically compared with the 10-average test data based on the reaction force and relative displacement relations. The results from the nominal and true strain hardening sources under Explicit/dynamic analysis associated with the classical metal plasticity model are plotted as Figure 3.21. The results from the linear Drucker-Prager model corresponding to Explicit/dynamic analysis are plotted and compared with the classical metal plasticity model in Figure 3.22. Evidently, the dynamic classical metal plasticity model with nominal strain hardening data works better than that with the true strain hardening data based on the reaction force and relative displacement curve. Within the hardening portion, the dynamic linear Drucker-Prager model fits the 10-average test data better than the classical metal plasticity model.

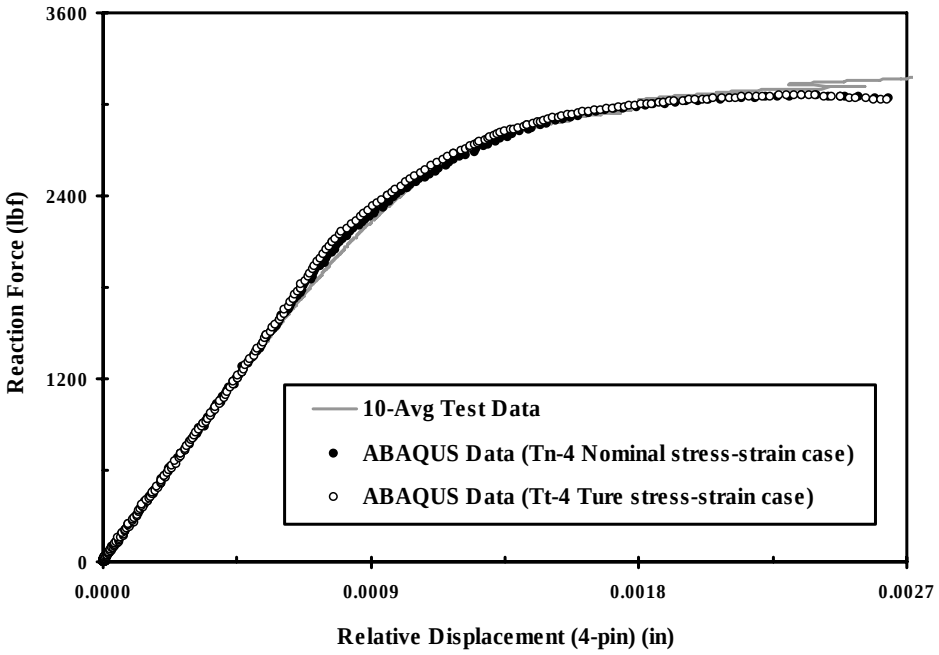

Figure 3.21. Reaction force-relative displacement trends from classical metal plasticity analysis and 10-average test data.

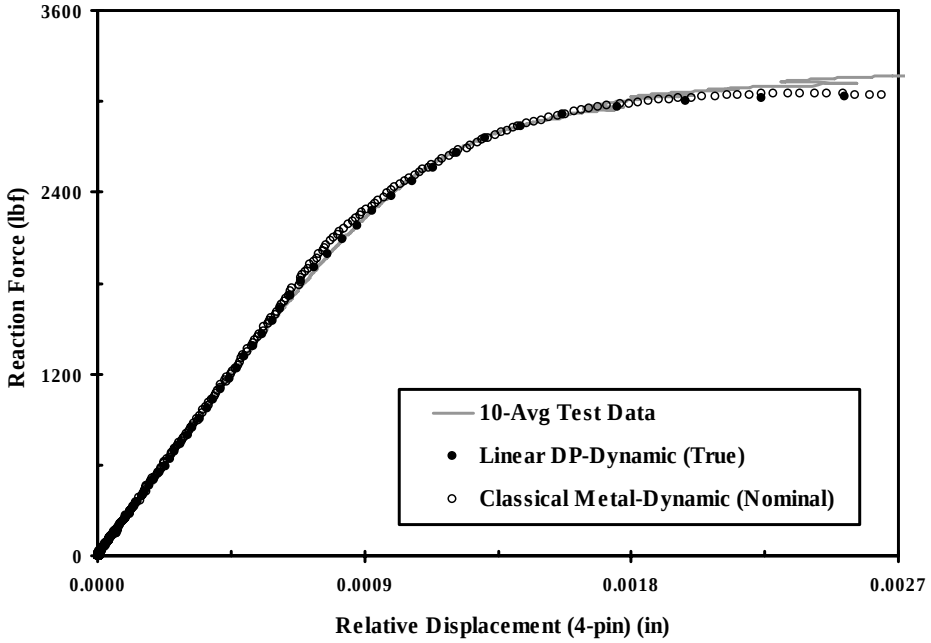

Figure 3.22. Reaction force-relative displacement trends from different plasticity dynamic analyses and 10-average test data.

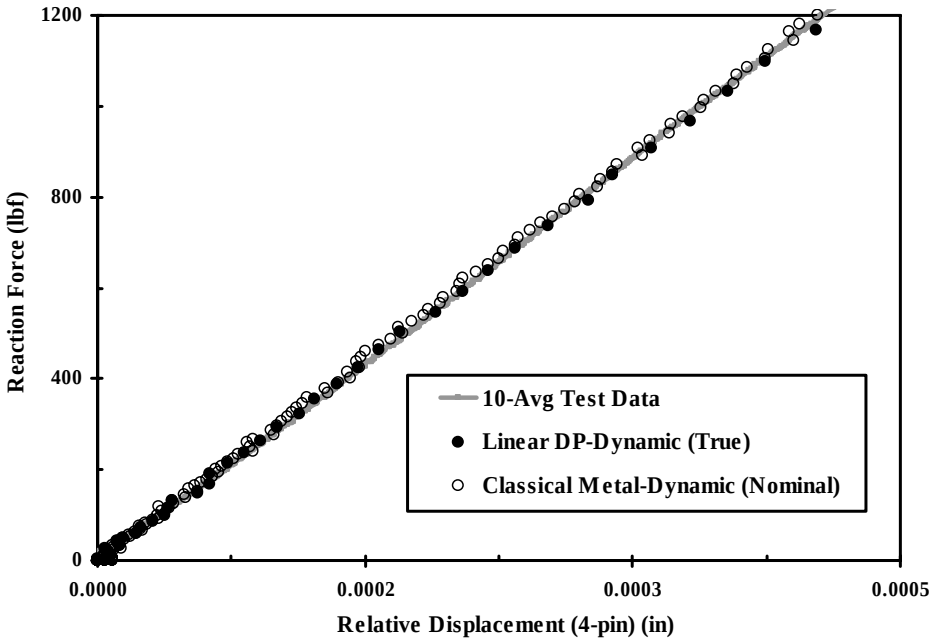

Figure 3.23. Linear elastic regions of reaction force-relative displacement curves from different plasticity dynamic models in ABAQUS (E=174,645 psi and v = 0.35).

The finite element analysis also declares that the entire curve matches the 10-average test data, not only in the post yielding region, but also in the linear region. It is easy to verify which Young's modulus and Poisson's ratio set can overlap the 10-Average test data satisfactory under the linear region. According to the cut-in of all curves within the linear region (shown as Figure 3.23), it is confirmed that the E=174,645 psi and v =0.35 still remains the best curve-fitting set. Compared with previous linear region simulation, the current model, in conjunction with the plastic part, interprets more clear and convincing results.

3.5.2 Classical Metal Plasticity Model

For numerical results under the classical metal plasticity model, the ultimate and failure loads obtained from ABAQUS dynamic simulations are compared with test data and listed in Table 3.13. As shown, the classical metal plasticity model is also able to produce the ultimate and failure loads respectively, since the 'necking' is given within the hardening data. In contrast, based on the true stress-strain hardening curve (Figure 3.15), there is no existence of 'necking'. As a result, the reaction force-relative displacement curve contains neither distinct ultimate and failure loads nor different displacements between at ultimate and at failure. The numerical results (Table 3.13) show that these two data sets yield very similar ultimate loads and relative displacements. In Table 3.10, the rotated angle (φ) at failure depicts that, due to shear, the cross-section of the overlap rotates at a small angle (small bending) about the z-axis (3-axis in ABAQUS) right at the adhesive's failure when the 2-D plate theory—Hencky-Mindlin assumptions (first-order shear deformation theory) are applied. The appendix shows this rotated angle (φ) is derived from the relative displacement of adherends. The deformed contours of the adhesive and the adherends are demonstrated by Figure 3.6b. Compared with

research [52], its rotated angle, obtained from ASTM D5656 model, is smaller due to the weaker properties of the adhesive (Metlbond 408).

TABLE 3.13

ASTM D5656 2-D FINITE ELEMENT ANALYSIS RESULTS VERSUS 10-AVERAGE TEST DATA

Shear Failure Value =0.25 (Nominal Stress-Strain Case) Element-CPE4R			
ρ= real density, α_R=10	FEM Data	Test Data	Error %
Ultimate load (lbf)	3,056.92	3,063.976	-0.23
Failure load (lbf)	3,031.06	3,039.647	-0.28
Relative displacement at Ultimate, in	0.002341	0.0023244	0.71
Relative displacement at Failure, in	0.002637	0.0027396	-3.74
Rotated angle (φ) at Failure, degree	-1.580	-	-
Shear Failure Value =0.249 (True Stress-Strain Case) Element-CPE4R			
ρ= real density, α_R=10	FEM Data	Test Data	Error %
Ultimate/Failure load, lb	3,052.43	3,063.976	-0.37
Relative displacement at Ultimate /Failure, in	0.002956	0.0027396	7.93
Rotated angle (φ) at Failure, degree	-1.760	-	-
Shear Failure Value =0.25 (Nominal Stress-Strain Case) Element-COH2D4			
ρ= real density, α_R=10	FEM Data	Test Data	Error %
Ultimate load, lb	3,115.15	3,063.976	1.67
Failure load, lb	3,046.05	3,039.647	0.21
Relative displacement at Ultimate, in	0.002664	0.0023244	14.6
Relative displacement at Failure, in	0.004356	0.0027396	59.0
Rotated angle (φ) at Failure, degree	-2.600	-	-

Note that the thickness of the adhesive bonded in ASTM D5656 models (0.008 in.) is different from that in composite scarf joint models (0.005 in.) and, in turn, the volume density is different. However, for expedience, the density value of the adhesive within composite scarf joints is substituted for the adhesive within ASTM D5656 finite element models. Regarding the adhesive within composite scarf joints (0.005 in. thick), the dimension of original ASTM D5656 finite element model has been retained (0.008 in. thick). The test data from the adhesive (0.008 in. thick) are still being used for comparison due to the lack of test data using a 0.005 in. thick model. Moreover, results due to the different dimensions are negligible. Within ASTM D5656 specimens, the adhesive of 0.008 in. thickness occupies 1.021 % while the adhesive of

0.005 in. thickness takes 0.641 % out of the whole specimen. As composite scarf joint models, the adhesive contributes 0.274~0.448 % to the entire specimen and 0.95~1.514 % to the trimmed scarf joint specimen (discussed in chapter 5). From the analysis of ASTM D5656 models using the adhesive density of composite scarf joints, the ABAQUS results show the shear failure value, S_f, still remains around 0.25 (Table 3.14). Therefore, the shear failure value 0.25 is reliable

TABLE 3.14

ASTM D5656 FINITE ELEMENT ANALYSIS RESULTS FROM ADHESIVE DENSITY OF COMPOSITE SCARF JOINT MODELS

Shear Failure Value =0.249 (Nominal Stress-Strain Case) Element-CPE4R			
ρ= real density, α_R=10	FEM Data	Test Data	Error %
Ultimate load (lbf)	3,055.42	3,063.976	-0.292
Failure load (lbf)	3,041.99	3,039.647	0.077
Relative displacement at Ultimate, in	0.002399	0.0023244	3.209
Relative displacement at Failure, in	0.002641	0.0027396	-3.599
Rotated angle (φ) at Failure, degree	-1.572	-	-

3.5.3 Stability and Accuracy

Artificial Density

Concerning the artificial density factor (f_ρ) discussed in section 3.1.2, the magnitude of density interferes with the dynamic analysis results crucially, especially the shear failure (S_f) in ASTM D5656 and affects the failure stress limit in composite scarf joint models. The Data of Table 3.13 and 3.14 are collected from the ABAQUS results using the real density. On the other hand, the numerical results from ABAQUS simulations for different artificial densities (the same individual α_R of adhesive and adherend) are grouped in Table 3.15.

Evidently, the ASTM D5656 finite element results are quite comparable for each case, even though the artificial density combinations are different. Therefore, for nominal stress-strain with the CPE4R element case, the value S_f=0.25 is still plausible.

TABLE 3.15

ASTM D5656 FINITE ELEMENT ANALYSIS RESULTS FROM ARTIFICIAL DENSITY MODELS

ASTM D5656 Adhesive's Density (Nominal Stress-Strain Case) Element-CPE4R					
	$\rho_{adhesive}$	$\rho_{adherend}$	(Ultimate/Failure) load (lbf)	Relative displacement Ultimate/Failure (in)	S_f
Density	0.10890	0.25910	3,052.47 / 3,029.56	0.002359 / 0.002618	0.25
	0.01089	0.025910	3,056.84 / 3,029.43	0.002348 / 0.002638	0.25
	0.001089	0.0025910	3,057.07 / 3,030.27	0.002325 / 0.002624	0.25
ASTM D5656 Adhesive's Density (True Stress-Strain Case) Element-CPE4R					
	$\rho_{adhesive}$	$\rho_{adherend}$	(Failure) load (lbf)	Relative displacement at Failure (in)	S_f
Density	0.10890	0.25910	3,048.80	0.002860	0.249
	0.01089	0.025910	3,051.88	0.002879	0.249
	0.001089	0.0025910	3,051.77	0.002858	0.249
ASTM D5656- Adhesive's Density of Composite Scarf Joint (Nominal Stress-Strain Case) Element-CPE4R					
	$\rho_{adhesive}$	$\rho_{adherend}$	(Ultimate/Failure) load (lbf)	Relative displacement Ultimate/Failure (in)	S_f
Density	0.17427	0.25910	3,054.97 / 3,041.42	0.002368 / 0.002655	0.25
	0.017427	0.025910	3,056.98 / 3,030.41	0.002327 / 0.002632	0.25
	0.0017427	0.0025910	3,057.05 / 3,030.25	0.002325 / 0.002629	0.249

With careful control, the only effects of increasing the artificial density with the same damping factor in ASTM D5656 model are processing time and system energy-dissipating trend. The S_f value will reduce when the artificial density (>4.0) is too large, which is not recommended. Figure 3.24 exhibits the real density of both adhesive and adherend and Figure 3.19 illustrates the artificial density (f_ρ=10^3) for both adhesive and adherend. Figure 3.19 implies slightly under-damped and the damping factor should be modified. The increase of ratio of the adhesive density (artificial density) to the density of the adherend (under the same individual damping factor) will yield a smooth oscillating trend.

From researches [45-47], the density of critical elements is artificially multiplied by a factor of 10^2~10^3; however, the resulting data are still admissible. While the f_ρ is larger than 10^4, the responses of result oscillate drastically and it is difficult to estimate curve-fit from stress-strain

result curves [46]. However, the artificial density (f_ρ= 10^4) is still being used throughout the finite element analyses because the damping factor has been magnified (discussed as follows).

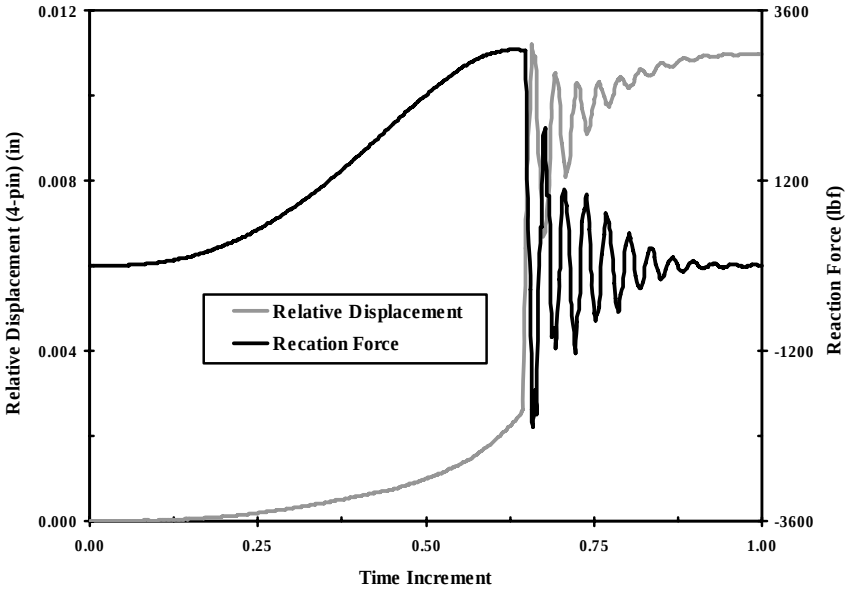

Figure 3.24. Response trends from ASTM D5656 FE Explicit/dynamic models (real adhesive density and adherend density with nominal stress-strain case).

In fact, any other number of the artificial density could achieve admissible results (force-extension curve) in ASTM D5656 finite element analysis, provided the given artificial density does not cause vital/significant inertial force to the system.

Rayleigh Damping

In most dynamic problems, the natural frequency or damping data required of materials are not possible to predict without dynamic test data and specialized research or experience, especially for a large system with massive multi-degrees of freedom [54]. Researches [55-57] how the natural frequency of materials varies with different materials, geometry shapes, boundary conditions/constrains, degrees of freedom, etc, and, in turn, the frequency equation can be expressed in several forms. The equations (3.1) and (3.2) given in ABAQUS hold for

isotropic and elastic materials only. Therefore, the equations for non-linear materials or composites are more intricate. However, the optimum value α_R can be reached when the dynamic response converges quickly and remain in steady state. From the ABAQUS manual and the results from Explicit/dynamic analysis, based on a variety of α_R with the same real density, as demonstrated in Figure 3.25, it is suggested using α_R rather than β_R.

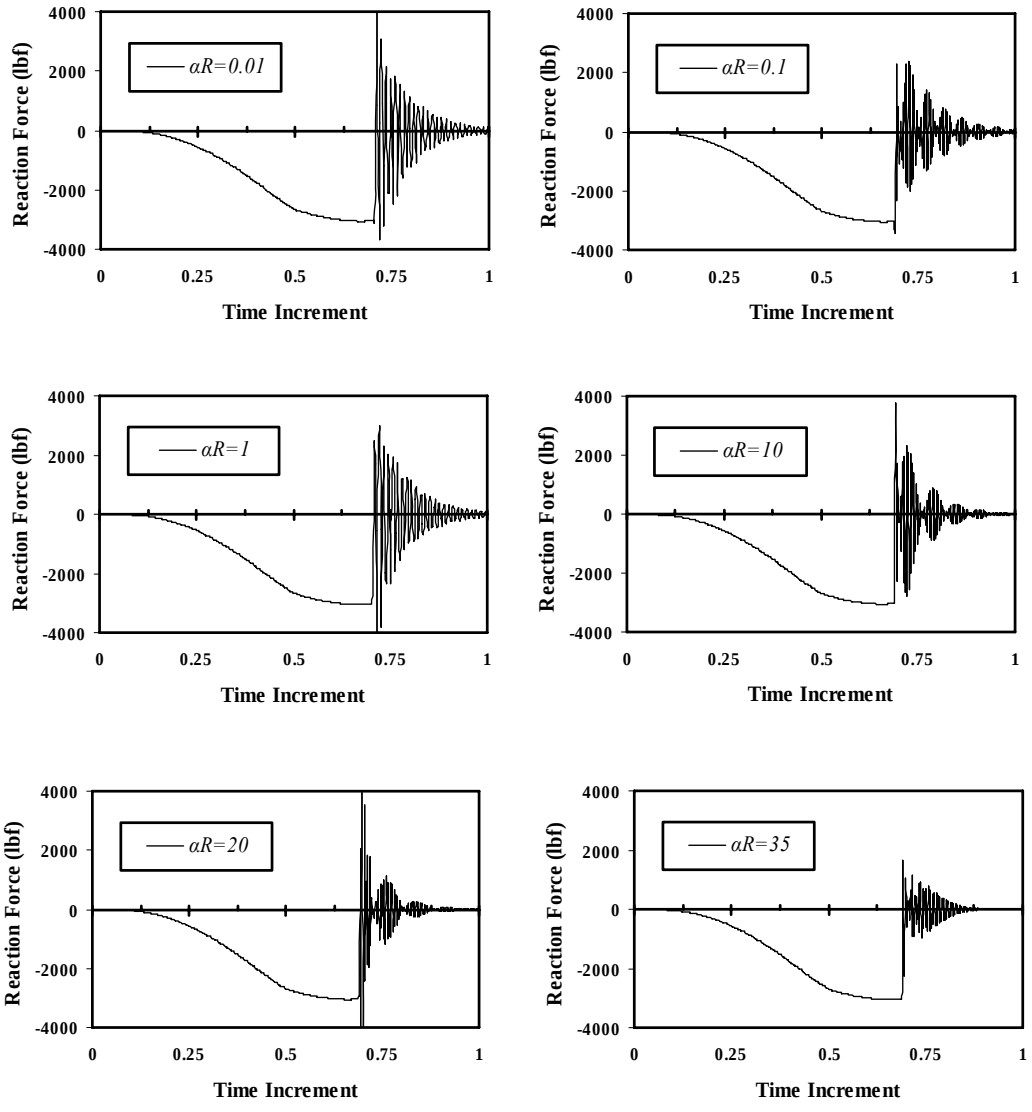

Figure 3.25. Dynamic responses versus various damping factor α_R (real densities used for adherend and adhesive).

Evidently, the larger the values of α_R, the faster converge is obtained, as expected. The numerical solutions from different α_R are almost the same. Therefore, α_R is given by 10 in this study, which is 10^4 or 10^5 larger than usual [55,56] in order to speed up the processing. Although, the critical damping is accepted by any given positive value in ABAQUS and consequently results in any positive α_R, it should be cautioned that over damping causes the dynamic response slightly less than in the real solution. This is confirmed from the comparison between static, over-damping, and under-damping solutions. Research [55] shows the effect of α_R on the critical step size tested for a wide range of material properties to verify Courant condition. When α_R is smaller than 2, the accuracy is maintained with excessive processing; whilst, the dynamic response is underestimated with the rise of critical step size when α_R is over 10. In addition, the over damping might cause body motion, if the section of larger damping occupies a significant volume percentage of the whole structure.

3.5.4 Drucker Prager Plasticity Model

The Drucker-Prager model is used to compare the finite element results from two different advanced plastic hardening models, namely the linear and the general exponent Drucker-Prager models which correspond to the Standard/static and the Explicit/dynamic, respectively. The main difference between these two analytic models was discussed in section 2.6.2 and the distinction between the Explicit/dynamic and the Implicit/dynamic models is the time integration for calculation of acceleration. The same hindrance encountered has been reported in the researches [45-47]. The application of the Implicit/dynamic analytic model leads to the difficulty of convergence even in the beginning of a small extension range. Accordingly, the dynamic Drucker-Prager plasticity model only relies on the Explicit/dynamic analytic model. The ABAQUS results with different Drucker-Prager plasticity models are

plotted in Figures 3.26 to 3.28. Evidently, the difference between the static and dynamic simulation is revealed from the result curves. Due to the conditionally time stable condition, more response data can be extracted from the Explicit/dynamic than the Standard/static analysis.

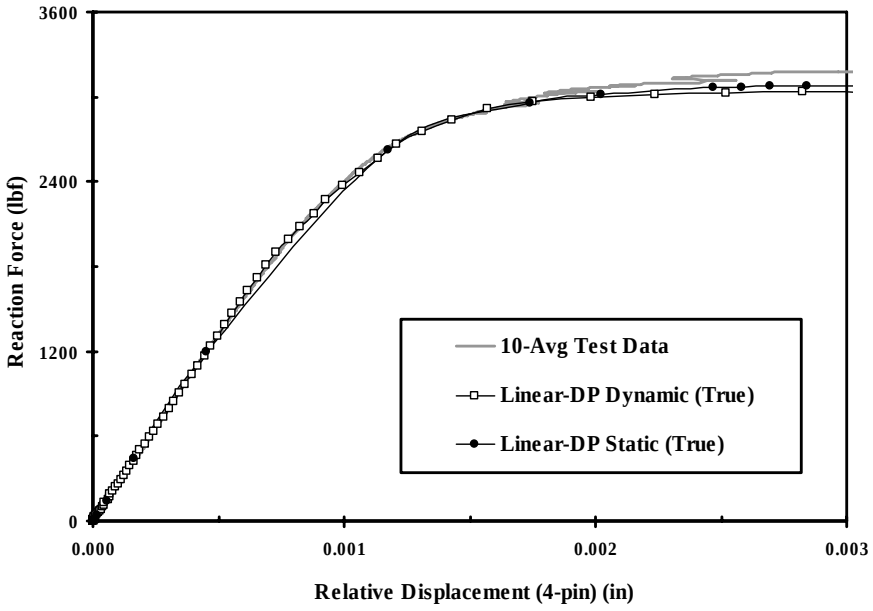

Figure 3.26. Linear Drucker-Prager model results versus 10-average test data (real density and true stress-strain).

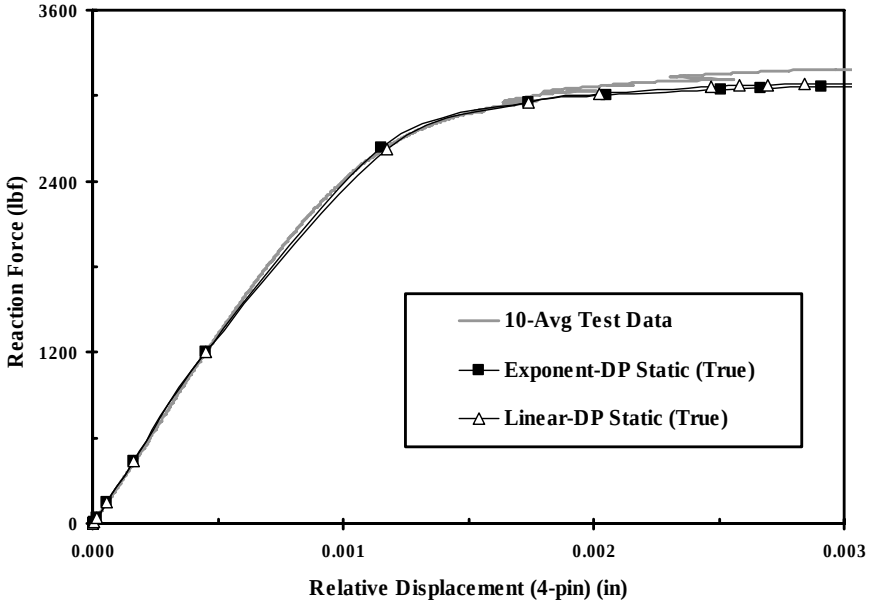

Figure 3.27. Results from different static Drucker-Prager models versus 10-average test data (real density and true stress-strain).

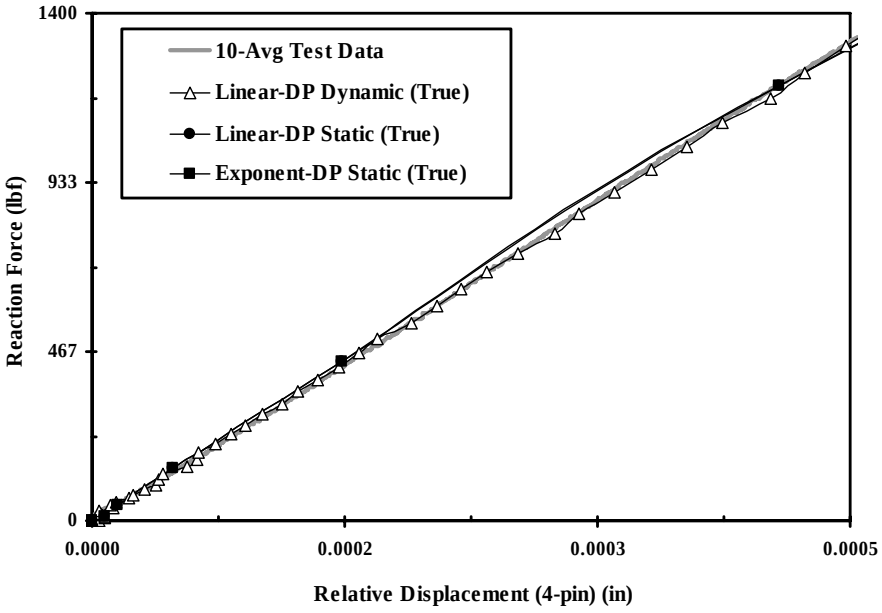

Figure 3.28. Different Drucker-Prager model results versus 10-average test data under linear region (real density and true stress-strains).

Compared to the classical metal plasticity, the Drucker-Prager model requires much more material parameters of plasticity, which were mentioned in section 2.4.4 and 2.4.5. These can be calculated reversely according to ABAQUS results (presented in section 3.4) through iteration. All calculations will be divided into two sets in parallel, namely explicit and standard result data, which are marked by (a) and (b), correspondingly. First, the friction angle (β) can be acquired from Table 3.10 and λ ,which stands for the measure of the sensitivity of yielding to hydrostatic stress, can be computed by equations (2.17) from the shear and tension tests,. Second, the plastic component of Poisson's ratio (v_p) can be calculated by taking advantage of the equation (2.23) in which dilation angle (ψ) is obtained from Table 3.10. Based on curve-fit level, either of those plastic parameters inputted can produce admissible results from ABAQUS. Notice that the friction angle in Standard/static models is very small and then ends up with the plastic Poisson's ratio close to 0.5. This implies that the inelastic deformation of the material is

incompressible. Third, λ can be employed to predict the ratio of the yield stress in shear to the yield stress in tension at the same equivalent plastic strain (σ_S/σ_T) via equation (2.18).

As the exponent Drucker-Prager model, λ is calculated by equation (2.29), hardening defined from shear and tension tests); the ratio (σ_S/σ_T) is already given by equation (2.18); '*a*' is given by equation (2.30). σ_T can be derived from the test data and equation (2.18). Compared with K, the ratio of the yield stress in triaxial tension to the yield stress in triaxial compression, defined in ABAQUS, is restricted $0.778 \leq K \leq 1.0$ to ensure the yield surface is convex. After all, the material properties regarding the Drucker-Prager plasticity model are tabulated in Table 3.16.

TABLE 3.16

ELASTIC AND DRUCKER-PRAGER PLASTIC PROPERTIES OF THE ADHESIVE

Explicit/Dynamic Linear Model				
Adhesive	*G*	*v*	*E*	σ_S/σ_T
FM 1515-3	64,683.3 psi	0.35	174,645 psi	0.5874
λ	v_p	β	ψ	K
1.0355	0.483	3	2	0.875
Standard/Static Linear Model				
Adhesive	*G*	*v*	*E*	σ_S/σ_T
FM 1515-3	64,683.3 psi	0.35	174,645 psi	0.5841
λ	v_p	β	ψ	K
1.0235	0.491	2	1	0.835
Standard/Static General Exponent Model				
Adhesive	*G*	*v*	*E*	σ_S/σ_T
FM 1515-3	64,683.3 psi	0.35	174,645 psi	0.5841
λ	v_p	b	a	ψ
1.0235	0.491	2	0.0025	1

During the iteration in ABAQUS, the curve-fit shows that '*b*' can be also replaced by '3' and the range of '*a*' varies from 0.001 to 0.03 under the general exponent Drucker-Prager plasticity model. The finite element results remain satisfactory in curve-fit level. If there is no ratio (σ_S/σ_T) available from equation (2.18) to perform the general exponent Drucker-Prager

plasticity, '*a*' can be guessed by using larger value multiplied by 10^{-2} and then reducing the value gradually. The '*b*' can be set at '2' or '3' to perform the iteration in finite element analysis.

For nonassociated plastic flow, the dilation angle ($\psi \approx 1\sim2$) obtained in the ASTM D5656 is remarkably smaller than other finite element results proposed by most researches ($\psi>20$). This is because the Drucker-Prager strain hardening data are defined in 'tension' in ABAQUS for most related researches. Nevertheless, the hardening should be given by 'shear' for ASTM D5656, which ends up with much a smaller dilation angle (ψ). Actually, not only the dilation angle (ψ) but also the friction angle (β) and the ratio of the yield stress in triaxial tension to the yield stress in triaxial compression (K) are smaller in the 'shear' case than those in the 'tension' case. Besides, in this study the loading speed/strain rate which affects the stress-strain relations is omitted for convenience. Furthermore, some issues such as whether the strain hardening data should be obtained from tests in tension or in shear, and the specimen prepared should be bulk (dumbbell-shaped), V-notched (Acran), or joint (butt or lap joint) are still in question. The test data resulting from either combined case are different, so that they produce various plastic parameters.

3.5.5 Comparison of 3-D and 2-D Analysis

As mentioned in section 2.4, the ASTM D5656 model is simplified as a 2-D plane strain problem. Therefore, currently the elastic constants and plastic parameters are obtained based on 2-D analysis. If the ASTM D5656 simulation is expended to 3-D analysis, the deviation between 2-D and 3-D results and stress/strain concentrations around critical bonded areas or edges can be examined. Those critical regions contain high stress and strain gradients, especially peel and shear stresses [42,52,58]. Here, the premise is made such that all the elastic, plastic constants and parameters for failure criterion resulted from 2-D analysis are

preserved and imported into 3-D material input files. The classical metal plasticity model, with nominal strain hardening data and incorporated with the dynamic shear failure model, is applied to the adhesive part. The results of reaction force-relative displacement from ABAQUS are converted using the 4-pinned method. The comparisons of numerical result data (Table 3.17) and reaction force-relative displacement curve from 3-D and 2-D are compiled in Figure 3.29.

TABLE 3.17

STRENGTH AND EXTENSION COMPARISONS FROM ABAQUS RESULTS BETWEEN ASTM D5656 AND 3-D SIMULATIONS

2-D Model S_f =0.25 (Nominal Stress-Strain Case) **Element-CPE4R**			
ρ= real density, α_R=20	FEM Data	Test Data	Error %
Ultimate load (lbf)	3,056.88	3,063.976	-0.23
Failure load (lbf)	3,032.67	3,039.647	-0.23
Relative displacement at Ultimate, in	0.002330	0.0023244	0.24
Relative displacement at Failure, in	0.002591	0.0027396	-5.42
3-D Model S_f =0.25 (Nominal Stress-Strain Case) **Element-C3D8R**			
ρ= real density, α_R=20	FEM Data	Test Data	Error %
Ultimate load (lbf)	2,983.360	3,063.976	-2.63
Failure load (lbf)	2,934.730	3,039.647	-3.45
Relative displacement at Ultimate, in	0.002436	0.0023244	4.80
Relative displacement at Failure, in	0.002956	0.0027396	7.89

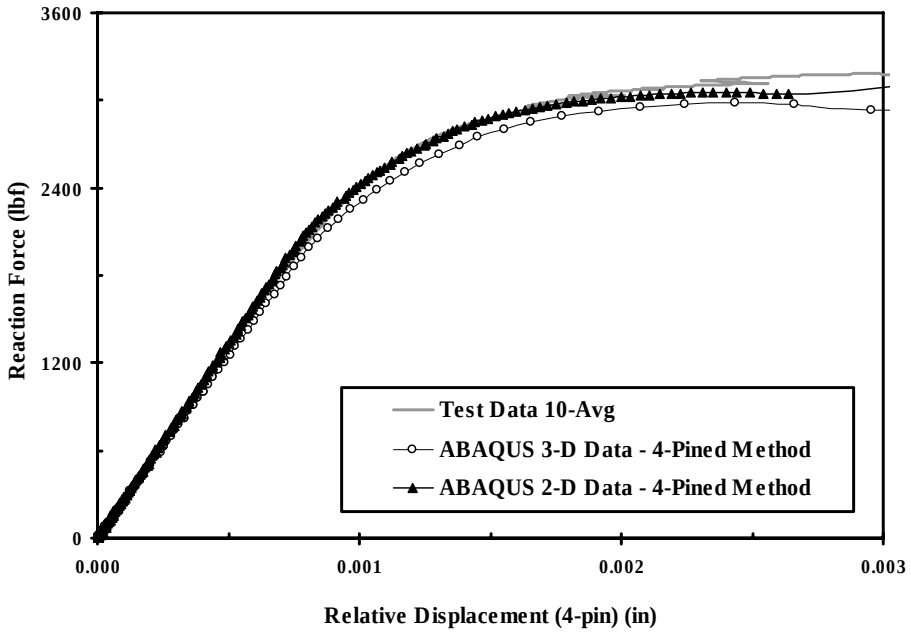

Figure 3.29. Comparison of dynamic responses between ASTM D5656 2-D and 3-D ABAQUS simulations (nominal stress-strain case).

It should be noted that, the premise made here is to compare the difference between 3-D and 2-D analyses under a roughly qualitative spectrum. More precise quantitative analysis using the 3-D model should be performed beginning from the elastic moduli and constants through the plastic stress-strain data and the failure parameters. The reaction force-relative displacement curve from 3-D simulation is clearly below that from 2-D simulation. This can be explained by equation (2.12a) of the Mises yield criterion, which is applied to the classical metal plasticity model. Under a 2-D plane strain state, there is only one term σ_{xy} contributing to effective stress (equation 3.6). Therefore, if the value of σ_e remains the same and is applied to a 3-D stress state, this critical stress value will be earlier to reach in 3-D analysis. In 3-D analysis, there are more stress components (namely σ_{xz} and σ_{yz} in equation 3.7) taken into account due to non-zero strains along the z-direction (3-direction in ABAQUS).

$$\sigma_e = \frac{1}{\sqrt{2}}\sqrt{6\left(\sigma_{xy}^2\right)} \tag{3.6}$$

$$\sigma_e = \frac{1}{\sqrt{2}}\sqrt{6\left(\sigma_{xy}^2 + \sigma_{yz}^2 + \sigma_{xz}^2\right)} \tag{3.7}$$

Accordingly, the effective stress is attributed to three shear stress components, which more quickly achieves the critical value and, in turn, a reduction in the reaction force.

Concerning stress concentrations, although there are more than one stress component appearing in equation (3.7), the reaction force-relative displacement curve from 3-D simulation is slightly below that from 2-D simulation. That means there is no existence of significant increase/jump in any shear stress component, i.e., there are no noteworthy stress concentrations occurring around bonded areas or overlap edges in ASTM D5656 models. Otherwise, the reaction force-relative displacement curve from 3-D simulation must be far below that from 2-D simulation and, meanwhile, the ultimate strength drops down remarkably. The 3-D simulation

is not used very often due to the requirement of excessive processing and memory unit. However, in some cases, the 2-D plane stress or plane strain state may not adequately simulate some distribution of parameters interested through the depth or width.

3.5.6 Element Type

Although the cohesive element COH2D4 model gave similar responses in the curve-fit level as the element CPE4R did based on the graphic results, the numerical results (Table 3.13) of relative displacement (either at ultimate or failure) from the element COH2D4 are different from those obtained by the element CPE4R. If both the relative displacement and load at failure must be matched for the COH2D4 case, the shear failure should be reduced to 0.12. Still, the COH2D4 model cannot produce distinct ultimate and failure loads like the CPE4R model.

The advantage of using COH2D4 is to reduce the mesh layer of the adhesive section (usually one layer) and the adhesive elements along with adjacent adherend elements may not necessary to have common nodes. This can reduce the amount of processing time for some huge models. The restrictions of using COH2D4 are (1) the COH2D4 has an orientation defining the thickness direction of the element and should be consistent throughout the cohesive layer; (2) the geometry of the adhesive section should be regular in order to apply swept or offset meshing techniques which are required for COH2D4; (3) the use of more than one layer through the thickness of the adhesive could produce unreliable results and is not recommended; (4) the analysis model cannot create any compression load/stress which can compress the adhesive fatally along the thickness direction and cause the analysis to be aborted in ABAQUS. For ASTM D5656 case, either COH2D4 or CPE4R is applicable due to the regular shape of its adhesive. But for composite scarf joints, it is not suggested, owing to the critical geometry shape and orientation, making it is difficult to perform the swept mesh technique. Based on

previous simulation, COH2D4 cannot produce the distinct ultimate and failure load/relative displacement like CPE4R in the characterization of the adhesive. Therefore, CPE4R is preferred to COH2D4 in the following composite scarf joint analysis.

3.5.7 Displacement Correction

As mentioned before, the relative displacement data converted by the 4-pinned method best match the physical phenomenon and it can be proved by the results from the finite element method [52]. From the classical metal plasticity simulation shown as Figure 3.30, the relative displacement data based on the 4-pinned method and the projective extension along the *x*-direction (X-Projection, similar to laser extensimeter) are paralleled in order to compare the dissimilarity. Evidently, the curve from 4-pinned method almost superimposes the test data curve except for the hardening portion.

Furthermore, the reaction force and relative displacement data converted and recorded from ABAQUS can be inputted to be the data source for ASTM D5656 Standard. Using the calculation described within ASTM D5656 Standard to generate both apparent stress-strain curve and true stress-strain, the degree of similarity between the physical test and the finite element simulation can be assessed (plotted as Figures 3.31 and 3.32). In accordance with the Figures 3.31 and 3.32, apparently all the results from finite element analyses deviate slightly from test data within the entire linear region, which implies the slope (apparent shear modulus) is larger than the test data. The slope of the entire linear region of the test data is roughly 70,000~75,000 psi (shown in Figure 3.15 G=75,000 psi) and the input value of finite element model is given by 64,683.3 (psi), which is determined from the estimation of test and previous linear finite element analysis.

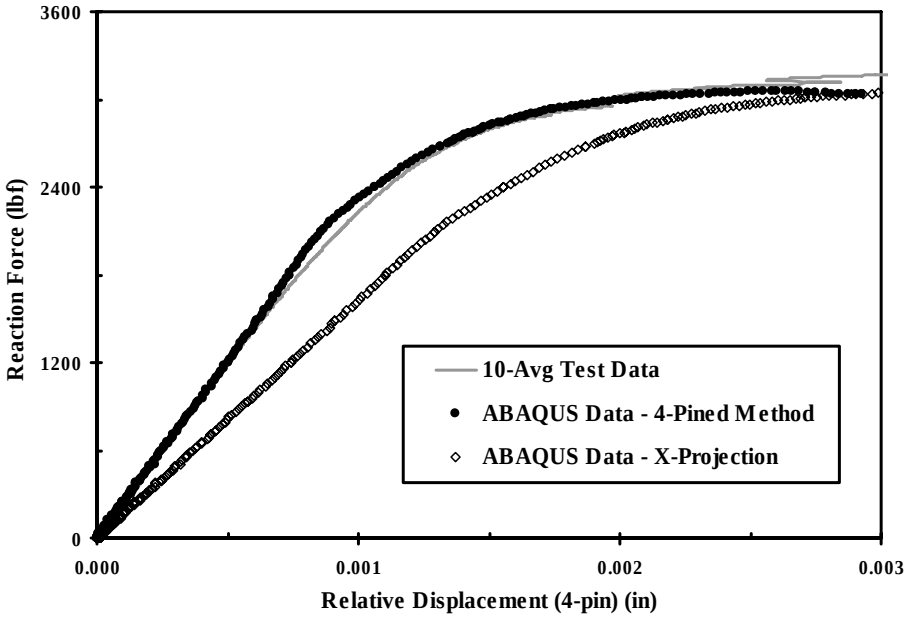

Figure 3.30. Comparison of different approaches for relative displacement (nominal stress-strain case).

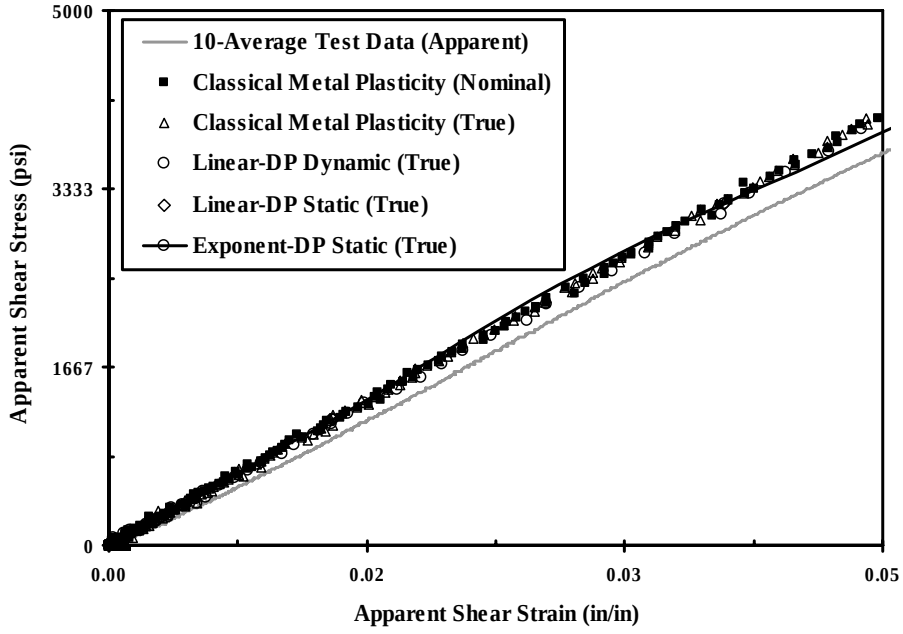

Figure 3.31. Results from various finite element analysis models versus 10-average test data (based on apparent stress-strain scale) under linear region.

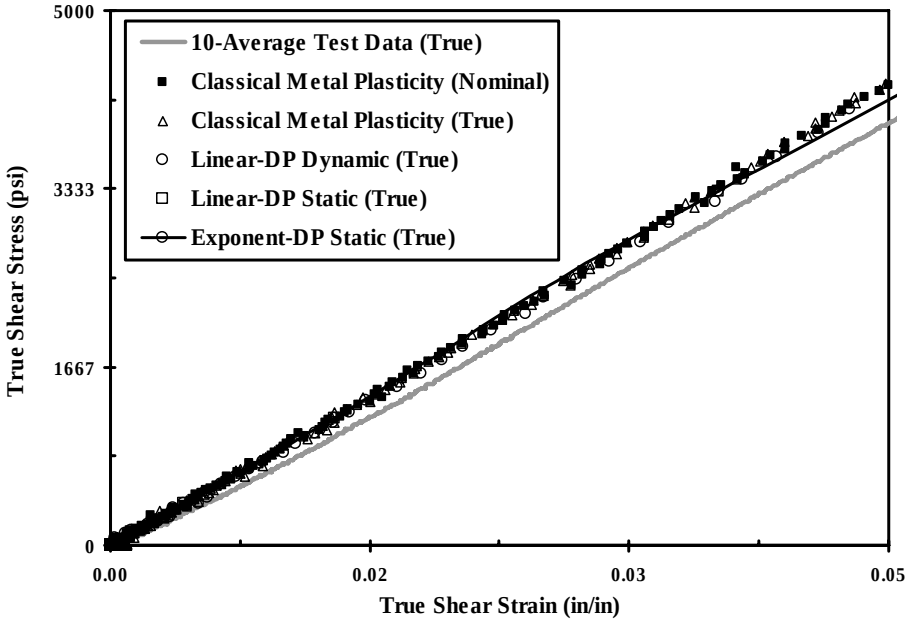

Figure 3.32. Results from various finite element analysis models versus 10-average test data (based on true stress-strain scale) under linear region.

The reasons why the apparent shear modulus 64,683.3 (psi) has been chosen are explained as follows:

(1) The value 64,683.3 (psi) is the best fit around the very beginning section of the completely elastic linear region (Figure 3.33). (2) Another explanation is supported by other research [42]. It shows when the bonded thickness of the adhesive (bondline) is greater than 0.02 in. (optimum value), the apparent elastic shear modulus obtained from finite element simulation along with 4-pinned method is lower than the true value. If the bondline is less than 0.01 in., the calculated shear modulus from the finite element model will be higher than the true value [42,52]. The thickness of ASTM D5656 adhesive is 0.008 in. which is less than 0.01 in. so that the apparent shear modulus is possibly higher than the true value. (3) In addition, when the bonded thickness of the adhesive is thinner than 0.01 in. the slope (apparent shear modulus) of stress-strain curve from ASTM D5656 test is actually higher than the true value [42,52].

This is because the effect of non-uniformity of the adherend deformation is no longer negligible when the adhesive is very thin. (4) Moreover, most studies state that adhesives made of polymer epoxy have a particular characteristic where the stress-train or load-displacement test data curve exhibits a slight curvature in the beginning elastic section under constant loading speed/deformation rate. As illustrated in Figure 3.33, the curve of the 10-average test data deviates with a certain curvature in the elastic region where the behavior is usually assumed elastic [47]. This kind of adhesive made of polymer is called rubber toughened material and belonging to viscoelastic materials. The properties of such viscoelastic material are time-dependent and a function of temperature as well.

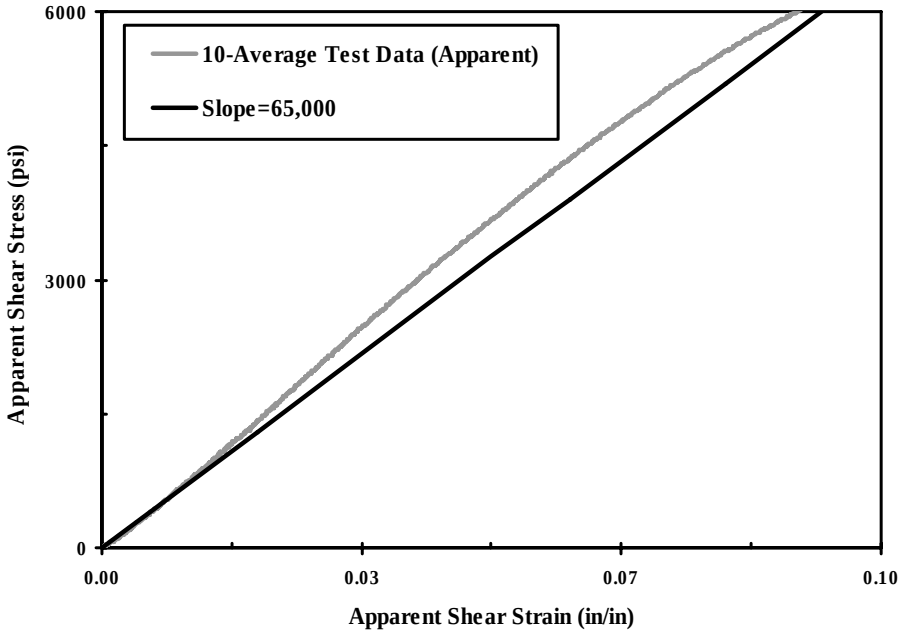

Figure 3.33. Straight line with slope 65,000 versus 10-average test data (based on apparent stress-strain scale) under liner elastic region.

(5) The elastic moduli will decrease with time under creep (constant stress) or stress relaxation (constant strain). In dynamic analysis, the elastic moduli increase with frequency along with damping property [47]. (6) Another factor of the adhesive namely cavitation (void) is also

included to be a parameter, especially contributing to a yield function. However, the cavitation, defect, and condition of cure process also accounts for the slight digression. In-depth research to explain this characteristic is still wanting.

3.6 Conclusions of Finite Element Analysis on ASTM D5656

Considering the dynamic finite element models, namely the classical metal plasticity model and the linear Drucker-Prager plasticity model, the latter model fits the 10-average test data quite well. Of all models, based on curve-fit without consideration of rate-dependence, the explicit linear Drucker-Prager combined with the dynamic shear failure model is the best dynamic plastic model for ASTM D5656 adhesive study, especially around the hardening portion of the curve (proved as Figure 3.34).

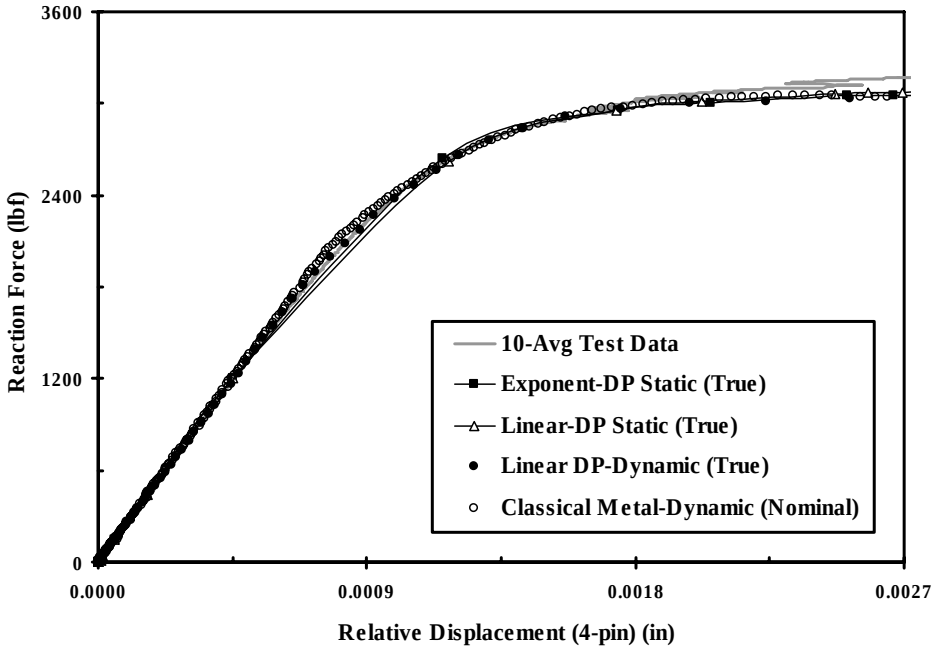

Figure 3.34. Comparison of dynamic plastic models versus 10-average test data.

Figure 3.34 also demonstrates all the models can fairly match the test data including the elastic and the plastic regions. Therefore, all the analogical curve-fit results declare that both the elastic and the plastic properties of the adhesive inputted are correct. They also satisfy all

kinds of the 10-average test data curves associated with different stress-strain scales. Based on the numerical data from ABAQUS, Tables 3.13 and 3.14 prove that the strength and relative displacement at failure, predicted by dynamic shear failure criterion, agree with the test data quite closely. Therefore, the conclusion can be made that the shear failure criterion is realistic and correct for a lap joint bonded with epoxy adhesive.

By focusing on the post-yielding behavior, the explicit classical metal plasticity model with the dynamic shear failure, based on the nominal stress-strain hardening data, can describe the ultimate and failure loads distinctly. For more complicated geometry of specimens, the classical metal plasticity model is easier to converge than is the linear Drucker-Prager plasticity model, in the sense that, the classical metal plasticity model with the dynamic shear failure must be applied to apply to the analysis of composite scarf joints. In addition, comparing the calculation of the relative displacement of ASTM D5656 models, the 4-pinned method is a truthful and highly recommended method of calibration.

For the advanced analysis of ASTM D5656 test, the loading speed (cross-head speed), strain-rate dependent hardening data, and more precise frequency/damping data need to be studied further. In this study, all above are simplified or assumed, which has the potential unanticipated flaws. Any of those events could generate significant effects on the results from finite element simulations. For instance, a lack of rate-dependence factor, the linear and exponent Drucker-Prager model would produce different strain hardening data shown in Tables 3.10 and 3.11. Under the strict frame of material property theory, this alternative approach is not reasonable. All the parameters required within a Drucker-Prager model can only be modified under the same hardening data combined with different rate-dependent factors, namely strain rate/loading speed. Even within the linear elastic region, the elastic properties of

adhesive are proved to be rate-independent such that the rate-dependent (strain rate) behavior should be added to assure the accuracy of the moduli, stress, and strain calculations [47]. Moreover, the sources from which the strain hardening tabular data are derived should be at least based on two different test methods (usually tension and shear tests). Only relying on the shear test data is tentative, due to the deviation and variation of the specimen tested. Different shear test standards and geometry of specimens designed could result in scattered stress-strain data. The quality or manipulation control of the adhesive and the specimen should be well prepared such that scattered test data as Figures 2.2 and 2.3 can be avoided while increasing reliability. Most of the time, the impediment to implementing analysis is due to the dearth of complete or representative data. Moreover, the strain-stress concentration and distribution within the bonded overlap are not discussed profoundly in this study. Such an in-depth study could explain in more detail the failure model and failure path. For comprehensive analysis, both the 3-D finite element model and more complete, reliable tests data are required at the same time.

CHAPTER 4

SCARF-PATCH-REPAIRED COMPOSITE LAMINATES

The simplified flush scarf-patch-repaired composite laminates (designated as OPT53 composite scarf joint models throughout this study, in which 'OPT53' stands for the code of specimens) were machined in a shape of rectangular panel due to the simplification of symmetry of loading and geometry. The original scarf configuration, in fact, has been transformed into taper-taper (single scarf) joint as mentioned in section 1.3. The repair patches, laid up in different stacking sequences (according to the parent plates), were tailored as a taper at one end and co-cure-bonded with a film adhesive (Metlbond FM 1515-3) onto the tapered parent plate (Figures 1.3 and 1.4) to form a taper-taper joint (a simplified single scarf joint [9]). In order to keep consistent through the text, the 'scarf joint' still used instead of taper-taper joint in this study.

Currently, analytical non-linear and elasticity solutions on scarf-patch-repaired composite laminates are difficult to obtain so that the finite element method is alternatively performed to analyze the stress distributions along the repair patch, the adhesive layer, and the parent plate. As a result, the project first attempts to obtain the ultimate load associated with a variety of stacking sequences, scarf angles, and the size of the composite specimens by physical testing. Second, the finite element analysis is performed to inspect and verify the strength of the specimens. Figure 4.1 shows the procedure and mutual relations between the test and the finite element analysis from ASTM D5656 Standard test to the repaired composite scarf joint project (OPT53).

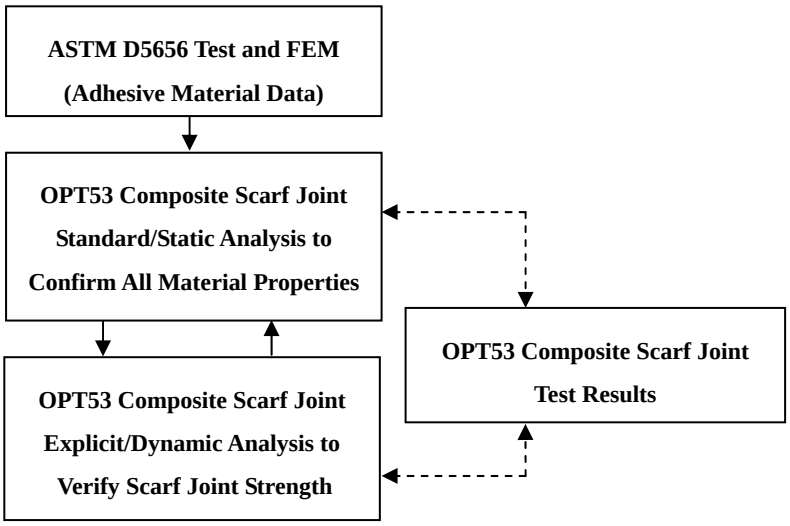

Figure 4.1. Procedure and mutual relations of finite element analysis from ASTMD5656 to OPT53 composite scarf joint.

Based on results proposed by study [51], scarf joints resists tensile load almost 2 times larger than single lap joints with similar dimensions. Owing to this particular geometric feature, both the adherends and the adhesive within scarf joints have less peel and shear stress nearby the tapered ends (within the overlap) than those from single lap joints under similar dimensions and in-plane loading [22]. Therefore, the adhesive in scarf joints is abele to endure higher shear stress than that in single lap joints. The scarf length (as a function of scarf angle) is designed in several dimensions in order to achieve an optimum. The parent and repaired adherends of the specimens were laid up with Torayca 800 carbon-epoxy unidirectional composite tapes (T-800 S-3900-2B or T-800S/3900-2) and were bonded with the epoxy film adhesive (FM 1515-3) were co-cured in an autoclave. The cure cycle for composite adherends was first to apply a temperature ramp from ambient to 270±10°F at a rate of 3.0±1°F per minute and then to maintain the cure temperature at 270±10°F for 120~150 minutes. In final, the temperature was cooled down to 170°F or lower at a rate of 4.5±0.5°F per minute before removing the vacuum. After cooling, the specimens were tested at room temperature under in-plane quasi-static

uni-axial tension only and were loaded monotonically until failure. Two dimensional strain contours (upper surface strains along and transverse to the loading direction) right at failure of the structure tested were recorded using the ARAMIS system.

All the properties of the adhesive including elasticity, plasticity, and failure criterion follow the previous ASTM D5656 test, inspected and validated by finite element analyses in chapter 3. The material properties of the adherends (laminated composites) are calculated using CLPT. From CLPT 2-D plane stress state, the reduced stiffness/compliance matrices are expended to 3-D complete constitutive matrices to determine all the elastic moduli of T800/3900-2 composites. The material properties of T-800S/3900-2 composites are in terms of different elasticity models defined in ABAQUS. In scarf joints, all loads are transferred through the adhesively bonded interfaces. After losing the support of patch, the damaged plate (a plate with a tapered open hole) still carries load for a while. Therefore, 2-D analysis would underestimate the strength of the repaired laminates and 3-D stress analysis should be utilized. Both 2-D and 3-D numerical models are performed respectively and compared with each other to accomplish the comprehensive analysis. Once all the material properties of T800/3900-2 are confirmed using Standard/static analysis, the extended dynamic analysis with a failure criterion is executed to predict the scarf joint strength under various geometric factors and stacking sequences. All the finite element results are compared and validated by the upper surface strain data recorded by the ARAMIS systems throughout the testing.

4.1 Fundamentals of Scarf-Patch-Repaired Composite Laminates

4.1.1 Pre-Processing of OPT53 Composite Scarf Joint

The scarf-patch-repaired composite laminate (Figure 4.2a) is generally a 3-D problem, which is over simplified by a taper-taper (simplified scarf) joint model. First, only one-half of

the panel is modeled due to symmetric loading and geometry. Second, a rectangular piece of the circular repaired patch, including the parent laminate, can be abstracted from the half part for ease of manufacture and testing. As a result, the transformed composite taper-taper or single scarf joint (as shown in Figures 1.4 and 4.2) is studied to approximate a various analyses of the scarf-patch-repaired composite laminates.

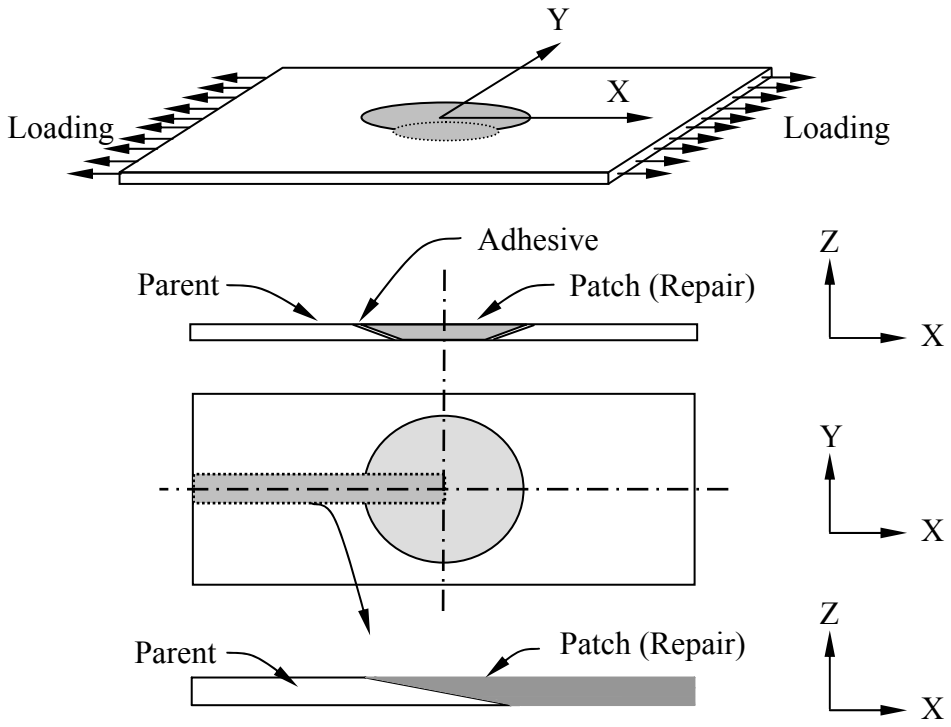

Simplified Scarf Joint (taper-taper) Specimen (Analyzed Part)

Figure 4.2(a). Geometry and terminology of the flush scarf-type bonded repair plate [11].

A typical scarf joint bonded specimen is designed to have two high-stiffness and high-strength adherends bonded by a thin adhesive layer along a scarf angle θ (taper angle) as shown in Figure 4.2(b). In a real repair specimen as mentioned in section 1.3, it is divided into a parent adherend (original pre-cured laminate) and a repair (patch) adherend, which has been co-cure-bonded by a film adhesive with the same stacking sequence as parent's as shown in Figure 1.4. Under some situations, the cure temperature, the moisture content, and the joint

shape (not ideally a scarf shape but actually approximated by a stepped joint shape) of the repair part are different from those of the parent part. However, both the parent and repair adherends are theoretically identical in the finite element model, including geometry and material properties in this study.

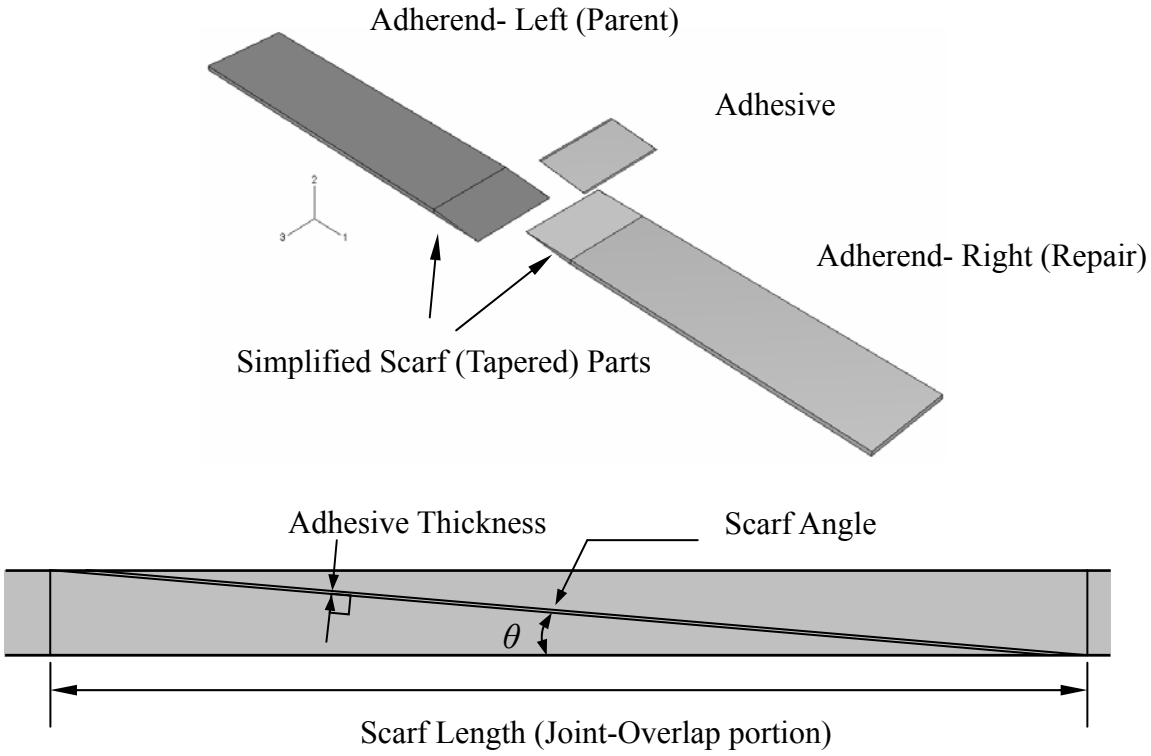

Figure 4.2(b). Geometry and Terminology of scarf-patch-repaired laminate plate.

The specific dimensions for each specimen are integrated in Table 4.1. The scarf length is a function of the scarf angle and the angle is measured in the 'degree' in this study. For example, the geometry of the overlap portion for OPT53-1 and OPT53-2 is drawn in Figure 4.3. In order to obtain better finite element mesh, to reduce the singularity in analysis, to increase the accuracy of solution, and to simulate a real repaired adherend, a stepped joint is introduced in the finite element method as an alternative to simulate the scarf joint model (illustrated in Figure 4.4).

TABLE 4.1

DIMENSIONS OF OPT53 COMPOSITE SCARF JOINT SPECIMENS

Specimen Code	**Length**	**Width**	**Specimen Thickness**	**Scarf Length**	**Scarf Angle**	**Adhesive Thickness**
OPT53-1	24.17 in	3 in	0.144 in	1.9 in	4.334 º	0.005 in
OPT53-2	24.17 in	3 in	0.144 in	1.9 in	4.334 º	0.005 in
OPT53-3	24.48 in	3 in	0.236 in	3.6 in	3.763 º	0.005 in
OPT53-4	23.98 in	3 in	0.236 in	4.1 in	3.305 º	0.005 in
OPT53-5	20.67 in	3 in	0.360 in	5.4 in	3.763 º	0.005 in
OPT53-6	19.68 in	3 in	0.360 in	6.4 in	3.814 º	0.005 in

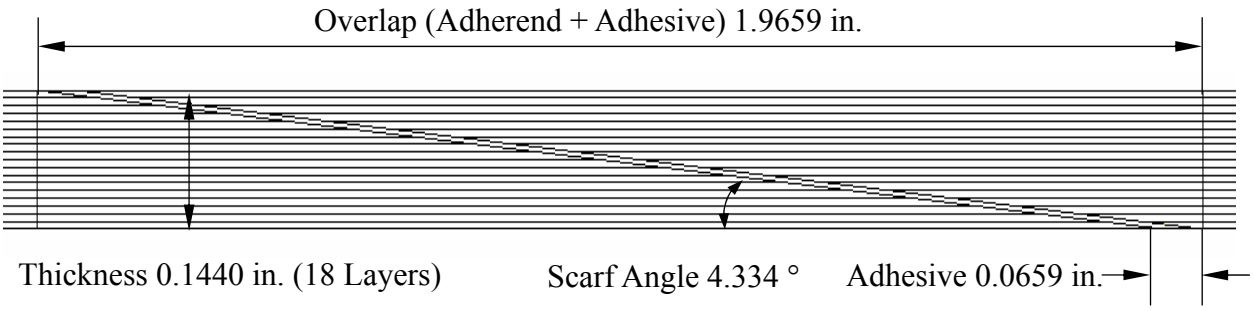

Figure 4.3. OPT53-1and OPT53-2 composite scarf joint model.

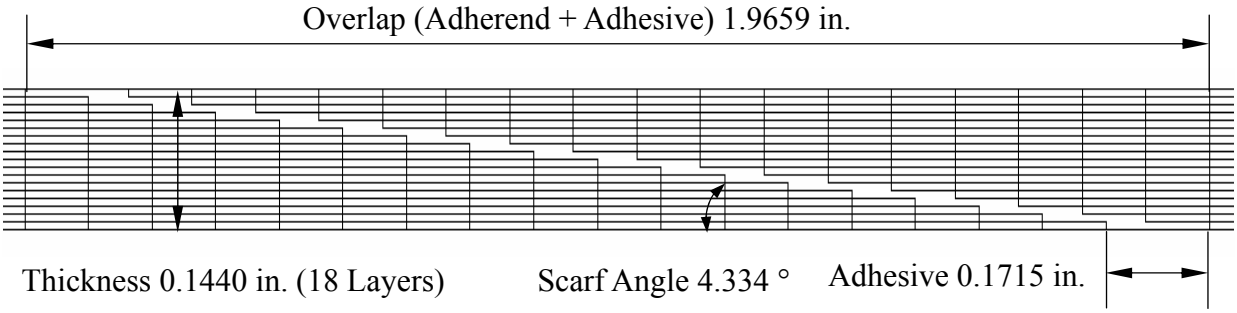

Figure 4.4. OPT53-1and OPT53-2 composite stepped joint model.

4.1.2 Material Properties of Lamina and Adhesive

The unidirectional carbon-epoxy fiber-reinforced composite consists of the Torayca 800 (T-800S/3900-2) prepregs. The specific gravity of T-800S/3900-2 fiber is 1.8 and the fiber volume fraction within the T-800S/3900-2B unidirectional lamina is 60~75%. The specific

gravity of T-800S/3900-2 composites is given by 1.65 and is converted to the volume density of 1.5446×10^{-4} lbf s^2/in^4. The volume density of the adhesive, according to its thickness 0.005 in., is converted to a value of 1.7427 lbf s^2/in^4. To reduce the processing time, the artificial density is carefully used (Table 4.2). The elastic and plastic material properties of the FM 1515-3 adhesive follow the confirmed results from the ASTM D5656 analysis in Chapter 3.

TABLE 4.2

DENSITIES FOR ADHESIVE AND ADHEREND IN OPT53 COMPOSITE SCARF JOINTS

Unit	Adhesive-FM 1515-3	Adherend-Torayca 800S
lbf s^2/in^4	1.7427×10^{-4}	1.5546×10^{-4}
Artificial Density	3.5725	3.2019

The care should be taken for explicit dynamic analysis regarding the mass and damping of system. The governing dynamic equilibrium equation with damping [44] is expressed by

$$M_l\ \ddot{u} = P - I\text{, and } I = Ku + C_{damp}\ \dot{u} \tag{4.1}$$

where M_l means the lumped element mass (diagonal element mass),

$\ddot{u}$ stands for the nodal acceleration at the beginning of time increment,

$\dot{u}$ and u represent the velocity and displacement integrated through time,

P and I mean the external force and internal element force correspondingly,

K and C_{damp} account for the stiffness and damping matrix for an element.

K is a function of the characteristic length of an element (the size of an element). For example, in one-dimension models, K is a function of the length of an element. Since the structure has been trimmed (the length of the adherends outside of the overlap is reduced) and refined (the element size is changed), K should not remain the same. In addition, the Rayleigh damping factor α_R is given by 20 to speed up the processing, and the damping matrix C_{damp} increases consequently. Over all, the internal force matrix (I) changes in magnitude. In order to remain

the same reaction force/external force (P) from the finite element analysis, a correction factor (C_f) for the lumped mass/density needs to be added. The governing dynamic equilibrium equation (4.1) becomes

$$P = (M_l C_f)\ddot{u} + \hat{I}\text{, where } \hat{I} \neq I \tag{4.2}$$

For each OPT53 composite scarf joint specimen, the ratio of the full-scale volume to the reduced volume is listed in Table 4.3. C_f is difficult to calculate precisely for the structure because the global stiffness matrix should be assembled in advance for the whole structure. Therefore, based on the investigation of the results from ABAQUS for all models, C_f is empirically estimated by 2.02×10^5, which at least satisfies all the OPT53 models. The elastic engineering constants for T-800S/3900-2 prepregs are evaluated from test results directly (Table 4.4) rather from effective moduli expressed by the volume fraction, Young's modulus, and Poisson's ratio of the fiber and matrix, individually.

TABLE 4.3

THE VOLUME RATIO OF THE FULL-SCALE TO REDUCED SPECIMEN FOR EACH OPT53 SPECIMEN

	OPT53-1	OPT53-2	OPT53-3	OPT53-4	OPT53-5	OPT53-6
Volume Ratio	5.536	5.536	4.028	3.640	2.624	2.214

TABLE 4.4

TORAYCA 800S/3900-2B PREPREG PROPERTIES

	Longitudinal Tensile Modulus	**Transverse Tensile Modulus**	**In-Plane Shear Modulus**	**Major Poisson's Ratio**
T-800S	$E_x = 21.384\times10^6$ psi	$E_y = 1.185\times10^6$ psi	$G_{xy} = 3.51\times10^5$ psi	$v_{xy} = 0.317$

4.1.3 Stacking Sequences and Characteristics of Composite Laminates

The stacking sequence/lay-up sequence for each composite model is listed as follows.

- OPT53-1 Composite Scarf Joint

  Stacking Sequence: $[(45/90/-45/0)_2/45]s$

- OPT53-2 Composite Scarf Joint

  Stacking Sequence: [45/-45/0/90/0/90/0/-45/45]s

- OPT53-3 Composite Scarf Joint

  Stacking Sequence: $[(45/90/-45/0)_4]s$

- OPT53-4 Composite Scarf Joint

  Stacking Sequence: [45/-45/0/90/0/-45/45/0/90/0/45/-45/0/90/-45/45]s

- OPT53-5 Composite Scarf Joint

  Stacking Sequence: $[(45/90/-45/0)_6]s$

- OPT53-6 Composite Scarf Joint

  Stacking Sequence: $[45/90/-45/45/0/0/90/0/0/(45/90/-45/0)_4]s$

The volume percentage of each orientation ply-group within each model is also tabulated in Table 4.5. As shown, all the composite models are laid up symmetrically about the mid-plane of composite laminates in order to uncouple in-plane strains, out-of-plane curvatures, and twists, i.e., matrix [*B*] equal to zero. From CLPT, the extensional stiffness matrix [*A*], bending-extension coupling stiffness matrix [*B*], and bending stiffness matrix [*D*] are calculated under a plane stress state [1] using the 'Maple' program software and verified using the 'CLASS' composite software.

Based on the constant ply thickness and the amount of *n* lay-up ply, those stiffness matrices are calculated using

$$A_{ij} = \sum_{k=1}^{n} (\overline{Q}_{ij})_k (z_k - z_{k-1}) \quad B_{ij} = \frac{1}{2} \sum_{k=1}^{n} (\overline{Q}_{ij})_k (z_k^2 - z_{k-1}^2) \quad D_{ij} = \frac{1}{3} \sum_{k=1}^{n} (\overline{Q}_{ij})_k (z_k^3 - z_{k-1}^3) \tag{4.3}$$

where $\overline{Q}_{ij}$ is the stiffness of each ply orientation with respect to the global coordinates, and z denotes the out-of-plane coordinate.

TABLE 4.5

PERCENTAGE OF EACH ORIENTATION PLY-GROUP WITHIN OPT53 MODELS

Ply Group	0-degree	90-degree	45-degree	-45-degree	Total
OPT53-1					
Number of Ply	4	4	6	4	18
(%) of Ply	0.22 %	0.22 %	0.33 %	0.22 %	100 %
OPT53-2					
Number of Ply	6	4	4	4	18
(%) of Ply	0.33 %	0.22 %	0.22 %	0.22 %	100 %
OPT53-3					
Number of Ply	8	8	8	8	32
(%) of Ply	0.25 %	0.25 %	0.25 %	0.25 %	100 %
OPT53-4					
Number of Ply	10	6	8	8	32
(%) of Ply	0.31 %	0.19 %	0.25 %	0.25 %	100 %
OPT53-5					
Number of Ply	12	12	12	12	48
(%) of Ply	0.25 %	0.25 %	0.25 %	0.25 %	100 %
OPT53-6					
Number of Ply	16	12	12	10	50
(%) of Ply	0.32 %	0.24 %	0.20 %	0.24 %	100 %

An adherend with different stacking sequences would result in different stiffness matrices. The reduced 2-D stiffness matrices and the characteristics of the adherend with respect to each OPT53 composite scarf joint model are remarked below.

- **OPT53-1 Composite Scarf Joint**

Stacking Sequence: $[(45/90/-45/0)_2/45]$s, ply thickness t_p=0.008 in.

Composite Property: 1. unbalanced ($A_{16}, A_{26} \neq 0$) but symmetric ($[B]=0$)

2. not quasi-isotropic (even $A_{11}=A_{22}$, $2A_{66} \approx A_{11}-A_{12}$)

$$[A] = \begin{bmatrix} 1.22335\,10^{6} & 4.65113\,10^{5} & 8.12488\,10^{4} \\ 4.65113\,10^{5} & 1.22336\,10^{6} & 8.12488\,10^{4} \\ 8.12488\,10^{4} & 8.12488\,10^{4} & 4.61264\,10^{5} \end{bmatrix} \text{(lbf/in)}$$

$$[B] = [0] \text{(lbf)}$$

$$[D] = \begin{bmatrix} 1.70451\ 10^{3} & 8.38765\ 10^{2} & 2.30529\ 10^{2} \\ 8.38765\ 10^{2} & 2.45330\ 10^{3} & 2.30529\ 10^{2} \\ 2.30529\ 10^{2} & 2.30529\ 10^{2} & 8.32111\ 10^{2} \end{bmatrix} \text{(lbf-in)}$$

- **OPT53-2 Composite Scarf Joint**

Stacking Sequence: [45/-45/0/90/0/90/0/-45/45]s, ply thickness t_p=0.008 in.

Composite Property: balanced (A_{16}, A_{26} = 0) and symmetric ([B]=0)

$$[A] = \begin{bmatrix} 1.46800\ 10^{6} & 3.82969\ 10^{5} & 0 \\ 3.82969\ 10^{5} & 1.14300\ 10^{6} & 0 \\ 0 & 0 & 3.79120\ 10^{5} \end{bmatrix} \text{(lbf/in)}$$

$$[B] = [0] \text{(lbf)}$$

$$[D] = \begin{bmatrix} 2.40709\ 10^{3} & 7.84440\ 10^{2} & 7.27982\ 10^{1} \\ 7.84440\ 10^{2} & 1.8627\ 10^{3} & 7.27982\ 10^{1} \\ 7.27982\ 10^{1} & 7.27982\ 10^{1} & 7.77786\ 10^{2} \end{bmatrix} \text{(lbf-in)}$$

- **OPT53-3 Composite Scarf Joint**

Stacking Sequence: [(45/90/-45/0)$_4$]s, ply thickness t_p=0.0074 in.

Composite Property: 1. balanced (A_{16}, A_{26} = 0) and symmetric ([B]=0)

2. quasi-isotropic (A_{11}=A_{22}, $2A_{66}$ = A_{11}-A_{12})

$$[A] = \begin{bmatrix} 2.07927\ 10^{6} & 6.97312\ 10^{5} & 0 \\ 6.97312\ 10^{5} & 2.07927\ 10^{6} & 0 \\ 0 & 0 & 6.90982\ 10^{5} \end{bmatrix} \text{(lbf/in)}$$

$$[B] = [0] \text{(lbf)}$$

$$[D] = \begin{bmatrix} 8.46215\ 10^{3} & 3.52473\ 10^{2} & 5.59710\ 10^{2} \\ 3.52473\ 10^{2} & 1.04376\ 10^{4} & 5.59710\ 10^{2} \\ 5.59710\ 10^{2} & 5.59710\ 10^{2} & 3.49514\ 10^{3} \end{bmatrix} \text{(lbf-in)}$$

- **OPT53-4 Composite Scarf Joint**

Stacking Sequence: [45/-45/0/90/0/-45/45/0/90/0/45/-45/0/90/-45/45]s, ply thickness t_p=0.0074 in.

Composite Property: balanced (A_{16}, A_{26} = 0) and symmetric ([B]=0)

$$[A] = \begin{bmatrix} 2.37990\ 10^{6} & 6.97312\ 10^{5} & 0 \\ 6.97312\ 10^{5} & 1.77866\ 10^{6} & 0 \\ 0 & 0 & 6.90982\ 10^{5} \end{bmatrix} \text{(lbf/in)}$$

$$[B] = [0] \text{(lbf)}$$

$$[D] = \begin{bmatrix} 1.14574\ 10^{4} & 3.34997\ 10^{3} & 7.40800\ 10^{1} \\ 3.334997\ 10^{3} & 7.79187\ 10^{3} & 7.40800\ 10^{1} \\ 7.40800\ 10^{1} & 7.40800\ 10^{1} & 3.32039\ 10^{3} \end{bmatrix} \text{(lbf-in)}$$

- **OPT53-5 Composite Scarf Joint**

Stacking Sequence: $[(45/90/-45/0)_6]$s, ply thickness t_p=0.0075 in.

Composite Property: 1. balanced (A_{16}, A_{26} = 0) and symmetric ([B]=0)

2. quasi-isotropic (A_{11}=A_{22}, $2A_{66} \approx A_{11}$-A_{12})

$$[A] = \begin{bmatrix} 3.16108\ 10^{6} & 1.06010\ 10^{6} & 0 \\ 1.06010\ 10^{6} & 3.16108\ 10^{6} & 0 \\ 0 & 0 & 1.05048\ 10^{6} \end{bmatrix} \text{(lbf/in)}$$

$$[B] = [0] \text{(lbf)}$$

$$[D] = \begin{bmatrix} 3.11506\ 10^{4} & 1.20729\ 10^{4} & 1.28537\ 10^{3} \\ 1.20729\ 10^{4} & 3.58808\ 10^{4} & 1.28537\ 10^{3} \\ 1.28537\ 10^{3} & 1.28537\ 10^{3} & 1.19690\ 10^{4} \end{bmatrix} \text{(lbf-in)}$$

- **OPT53-6 Composite Scarf Joint**

Stacking Sequence: [45/90/-45/45/0/0/90/0/0/(45/90/-45/0)$_4$]s, ply thickness t_p=0.0072in.

Composite Property: unbalanced (A_{16}, $A_{26} \neq 0$) but symmetric ([B]=0)

$$[A] = \begin{bmatrix} 3.56444\ 10^6 & 9.49210\ 10^5 & 7.31232\ 10^4 \\ 9.49210\ 10^5 & 2.97948\ 10^6 & 7.31232\ 10^4 \\ 7.31232\ 10^4 & 7.31232\ 10^4 & 9.39586\ 10^5 \end{bmatrix} \text{(lbf/in)}$$

$$[B] = [0] \text{(lbf)}$$

$$[D] = \begin{bmatrix} 3.8065\,0\ 10^4 & 1.04360\ 10^4 & 2.62670\ 10^3 \\ 1.04360\ 10^4 & 3.25310\ 10^4 & 2.62670\ 10^3 \\ 2.62670\ 10^3 & 2.62670\ 10^3 & 1.02240\ 10^4 \end{bmatrix} \text{(lbf-in)}$$

4.2 Elastic Material Property Model in ABAQUS

Unlike the ASTM D5656 case, the elastic properties of the OPT53 composite laminates are much more sophisticated and need to be detailed. In ABAQUS, the linear elasticity model is valid for small elastic strains (normally less than 5%) and there are three primary options for linear elastic materials such as isotropic, orthotropic, and fully anisotropic model embedded in the 'Property Module' of ABAQUS.

Selection of the elastic model depends on the number of plane of material property symmetry for elastic properties. A material can be classified as

-Isotropic-an infinite number of symmetry planes throughout every point.

-Orthotropic-has two orthogonal planes passing through every point.

-Anisotropic-has no plane of material property symmetry.

The number of the independent constants/components of elasticity tensor (stiffness or compliance) depends on such planes of material property symmetry.

4.2.1 Isotropic Elasticity

Isotropic elasticity is the simplest linear elastic behavior, and the stress-strain relations are completely expressed by two independent elastic constants, namely Young's modulus (E) and Poisson's ratio (v). The shear modulus (G) can be obtained by equation (2.1). The stability criterion or the Drucker stability [1,44] (discussed in section 4.3.2), which the linear elastic materials must satisfy, requires that the elasticity tensor be positive definite. Therefore, E and G must be greater than 0, which results in $-1 \leq v \leq 0.5$ (where $v = 0.5$ accounts for nearly incompressible behavior). For composite laminates, the moduli E and G should be called effective or equivalent moduli measured by one equivalent (in a manner) homogeneous and isotropic laminate, which has similar stress and strain responses to the original composite laminate consisting of several different ply orientations. The restrictions of using the 2-D isotropic model for a composite laminate under the state of plane stress require that the stacking sequence should be

1. balanced (extensional stiffness $A_{16}=A_{26}=0$ but bending stiffness D_{16} and D_{26} may not equal to zero)
2. may or may not symmetric (bending-extension stiffness [B] may not =0)
3. containing n ply groups spaced at $180°/n$ degrees ($n \geq 3$) and the equal number of ply in each group
4. $A_{11}=A_{22}$, and $2A_{66}=A_{11}-A_{12}$

Therefore, the property results in $E_{11}=E_{22}$, including $v_{12}=v_{21}$ (proved by equation (4.15)). A composite laminate containing such stacking sequence is called quasi-isotropic. Note that the quasi isotropic model still remains certain inherently difference from the isotropic model, especially tending toward the application of 3-D models.

4.2.2 Orthotropic Elasticity in Terms of Engineering Constants

Linear orthotropic elasticity is most easily and clearly defined by the amount of 9 independent engineering constants: three stiffness moduli (E_{11}, E_{22}, and E_{33}), shear moduli (G_{12}, G_{23}, and G_{13}), and Poisson's ratios (v_{12}, v_{23}, and v_{13}) associated with the principal material directions (i.e., 0 or 90-degree lamina). The other Poisson's ratios (v_{21}, v_{32}, and v_{31}) can be derived by the reciprocal rule, equation (4.15).

For 2-D plane stress state, the reduced stiffness/compliance matrices require only 4 independent engineering constants, excluding E_{33}, G_{23}, G_{13}, v_{23}, and v_{13} terms. The restrictions of using the orthotropic elasticity by specifying the engineering constants are basically similar to those of the isotropic elasticity, which the composite laminate is laid up in a balanced ($A_{16}=A_{26}=0$, and $D_{16}=D_{26}=0$ for principal material axes aligned with the global axes) and symmetric sequence ($[B]=0$). The reasons of the stacking sequence subject to balance and symmetry are explained as follows.

1. A_{16} and A_{26} are derived from the coupling terms of the stiffness, namely Q_{16} and Q_{26}, bridging the shear-extension in stress-strain relations. Upon the definition of orthotropic materials, Q_{16} and Q_{26} are zero so that the stacking sequence of an orthotropic composite laminate should have zeros for A_{16} and A_{26} terms according to equation (4.1).
2. The $[B]$ matrix couples the extension and bending. If the stacking sequence is not symmetric to eliminate the $[B]$ matrix, the curvatures (κ_{ij}) and moment (M_{ij}) resultants may get involved not only in producing out-of-plane twisting or bending, which is not realistic for orthotropic materials, but also in creating more coupling equations to be solved simultaneously.

4.2.3 Orthotropic Elasticity in Terms of Elastic Stiffness Matrix

Linear orthotropic elasticity also can be pristinely defined by 9 independent elastic stiffness/compliance parameters rather than the engineering constants. Via the constitutive equation (4.12), the stiffness matrix [Q] or the compliance matrix [S] is derived from test data of E_x, E_y, G_{xy}, and v_{xy} in the fiber direction or at zero degree. Therefore the [T]matrix, a global-local coordinate transform matrix, is used to determine [Q] or [S] in different material orientations by substituting different values of angle (θ) for the trigonometric equations within [T]. Similarly, the restriction of symmetric and balanced stacking sequence is required because the 9 engineering constants are derived from these 9 constants of [Q] or [S].

4.2.4 Orthotropic Elasticity in Plane Stress

Under 2-D plane stress condition (σ_{33} =0), only E_{11}, E_{22}, v_{12}, G_{12}, G_{23}, and G_{13} are required to defined orthotropic materials. Because the plane stress model is based on the in-pane analysis (the 1-2 plane as shown in Figure 4.5b) and ignores the out-of-plane stresses (assumed zero), the constants E_{33}, v_{23}, and v_{13} can be omitted. However, the strain components in the 3-direction still exist, which results in need of G_{13} and G_{23}. In ABAQUS, this property option is given in 'Lamina' under 'Property-Elastic', which is used for plane stress elements, but 2-D shell elements are not included.

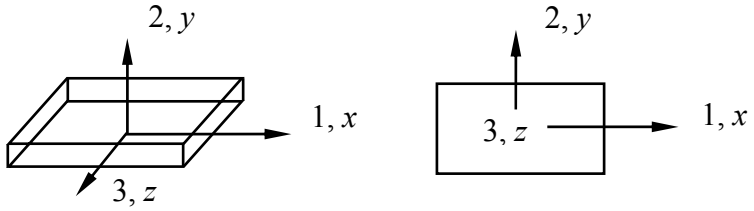

a. 3-D Model b. 2-D Model

Figure 4.5. Definition of the coordinate system in ABAQUS.

4.2.5 Transversely Isotropic Elasticity

Transversely isotropy is a special subclass of orthotropy (anisotropic material symmetry [59]), which is characterized by a plane of isotropy at every point in materials. In other words, at every point of a material, there is one plane in which the mechanical properties are equal in all directions. Usually but not necessary the 1-2 plane (Figure 4.5) is defined as a plane of isotropy [1,59,60] at every point and the fiber direction is along the *z*-direction (the 3-direction). Especially if composite failure is observed from a crack, running between the cylindrical fiber and the matrix [60], the finite element model should be built as Figure 4.5b. The cylindrical fiber is along the 3-direction (*z*-direction). Therefore, if the 1-2 plane is an isotropic plane, the moduli and Poisson's ratios of the isotropic plane, namely $E_{11}=E_{22}$, $G_{13}=G_{23}$, $v_{13}= v_{23}$, and $v_{31}= v_{32}$ are the same. In fact, the isotropic plane and the fiber direction are determined by how to create a model in the finite element software. Provided that the 1-direction is the fiber direction, which is usually aligned with the loading direction, in turn, the 2-3 plane is the isotropic plane [59]. For such a modeling space as 2-D plane strain modeling, the related coordinates should be swapped (2- and 3-direction) in advance before the associated elastic moduli and Poisson's ratios imported into the input file of finite element analysis. At last, the required constants within the stiffness/compliance matrices can be reduced from 9 to 5 independent constants. Basically this model is simplified from the orthotropic behavior so that the restrictions $A_{16}=A_{26}=0$ and $[B] =0$ still hold.

4.2.6 Anisotropic Elasticity

Fully anisotropic elasticity requires 21 independent elastic stiffness constants (*triclinic* elasticity/symmetry [59]) to describe material behaviors. When characteristics of the strain energy are considered, $S_{ij}=S_{ji}$ (or $Q_{ij}=Q_{ji}$) and the original 36 elastic constants can be shown to

reduce into 21 independent ones for elastic materials (discussed in section 4.3.2). Usually, there are some additional assumptions, such as plane stress state (σ_{33}=0) or one more symmetric plane is added into the anisotropic elasticity. Then the 21 elastic constants can be reduced to 13 (symmetry about the 1-2 plane or z=0) and the elasticity is referred to as monoclinic elasticity (reduced anisotropy) [1,59]. Its stiffness/compliance matrices still keep shear-extension coupling terms, namely S_{16}, S_{26}, S_{36} (Q_{16}, Q_{26}, Q_{36}), and one more shear-shear coupling term, S_{45} (Q_{45}). When the principal material axes of a unidirectional fiber-reinforced lamina are aligned to the global axes (at 0 and 90-degree of the fiber direction with respect to the global direction), the material belongs to the orthotropic elasticity. Otherwise, the shear-extension coupling and the shear-shear coupling terms may not be zero. In such cases, the elastic property of the lamina should be expressed by the anisotropy in conjunction with the orthotropy, in the sense that, the elastic constants could be reduced to 5 constants. In fact, the amount of independent elastic constants depends on various conditions or analytical models assumed.

4.3 Material Property Calculations of OPT53 Composite Laminates

For each elasticity model discussed in section 4.2, it requires related elastic constants and may not be the same or compatible for each model. Typically, unidirectional fiber-reinforced laminae have a particular material property—transversely isotropy that differs from the general orthotropy and complete anisotropy. Usually CLPT follows the plane stress state and develops sequent theories for various applications. The 2-D modeling of OPT53 composite scarf joints is under the plane strain state in order to analyze the special feature-scarf joint. The elastic constants cannot be merely replaced by those calculated using CLPT or the CLASS software. The foremost difference is in the constitutive equations, which will be discussed later. In this study, three material models, namely the anisotropy (transversely isotropy), the engineering

constant (orthotropy) and the equivalent isotropy are used to describe the material properties of composite laminates associated with different stacking sequences.

4.3.1 Material Property Assumption

The out-of-plane elastic engineering constants of composites are usually not reported in the vender's mechanical material data sheet. Therefore, they are assumed based on certain material property symmetry models for Torayca 800 composites. Under the considerations of physical phenomena and the natures of unidirectional fiber-reinforced laminae, the material property is symmetric about the 3-axis (the 1-2 plane is a material symmetric plane). Such a monoclinic material requires 13 constants to describe its behavior. Besides, another material symmetric plane, the 1-3 plane about the 2-axis, is taken and the shear-extension and shear-shear coupling terms are truncated so that only 9 independent constants remain. Eventually, the 2-3 plane is treated as a plane of isotropy at every point and the 1-axis is the axis of symmetry. The material properties are independent of orientation on the 2-3 plane so that the 9 independent constants can be reduced to 5 independent ones. This kind of material is marked as transversely isotropic especially for unidirectional fiber-reinforced laminae [59]. The complicated measure of 9 independent constants (for orthotropic materials) can be avoided. Furthermore, using these 5 constants can calculate the engineering constants without out-of-plane material data. The procedures are described associated with CLPT and the definition of ABAQUS in following sections.

4.3.2 Anisotropic Material Model

For orthotropic materials, it is usually assumed that the principal material axes (*1,2,3*) are aligned with the natural body axes/global axes (*x,y,z*) (Figure 4.6).

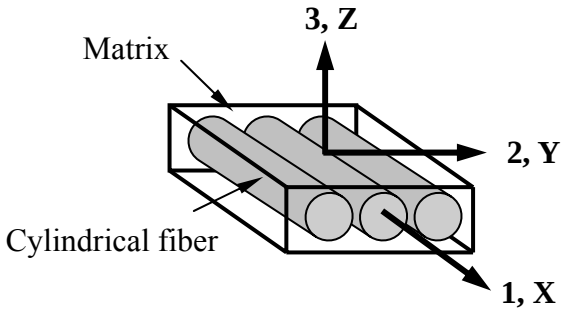

Figure 4.6. Specially orthotropic material (principal material axes of fiber-reinforced lamina aligned with global axes).

There are two symmetric orthogonal plane sets for the elastic properties so that the stiffness/compliance matrices can be described by 9 constants, which may not be absolutely independent. The material is called specially orthotropic [1] and can be explained using equation (4.4)

$$[\bar{S}_{ij}]=[T][S_{ij}][T]^{T} \tag{4.4}$$

where $[S_{ij}]$ is defined as compliance matrix, expressed by equation (4.5) and the transformation matrix [T].

$$\begin{bmatrix} \varepsilon_{11} \\ \varepsilon_{22} \\ \varepsilon_{33} \\ \gamma_{23} \\ \gamma_{31} \\ \gamma_{12} \end{bmatrix} = \begin{bmatrix} S_{11} & S_{12} & S_{13} & S_{14} & S_{15} & S_{16} \\ S_{12} & S_{22} & S_{23} & S_{24} & S_{25} & S_{26} \\ S_{13} & S_{23} & S_{33} & S_{34} & S_{35} & S_{36} \\ S_{14} & S_{24} & S_{34} & S_{44} & S_{45} & S_{46} \\ S_{15} & S_{25} & S_{35} & S_{45} & S_{55} & S_{56} \\ S_{16} & S_{26} & S_{36} & S_{46} & S_{56} & S_{66} \end{bmatrix} \begin{bmatrix} \sigma_{11} \\ \sigma_{22} \\ \sigma_{33} \\ \tau_{23} \\ \tau_{31} \\ \tau_{12} \end{bmatrix} \tag{4.5}$$

Within the compliance matrix $[S_{ij}]$ of orthotropic materials, the shear-extension coupling terms, namely S_{14}, S_{15}, S_{16}, S_{24}, S_{25}, S_{26}, S_{34}, S_{35}, S_{36}, and shear-shear coupling terms, namely S_{45}, S_{46}, S_{56}, are all equal to zero. Only S_{11}, S_{12}, S_{22}, S_{13}, S_{23}, S_{33}, S_{44}, S_{55}, and S_{66} in total 9 constants are left. Provided that the principal material axes are not aligned with the global axes or the stressed axes of materials are not aligned with the global axes (Figure 4.7), the foregoing shear-extension

terms such as S_{16}, S_{26}, S_{36} and shear-shear coupling term S_{45} are not all zeros [1,28,29,59]. This kind of material is called generally orthotropic, especially for off-axis laminae whose principal material coordinates do not coincide with the global coordinates. In other word, the global coordinate system is oriented at some angle (θ) to the principal material coordinate system (Figure 4.7). For example, a ±45-degree unidirectional fiber-reinforced lamina behaves such characteristics that its principal material axes are rotated by ±45-degree from the global coordinate system. The generally orthotropic should be applied for a ±45-degree lamina (or other off-axis lamina).

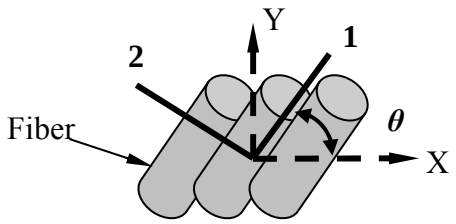

Figure 4.7. Generally orthotropic material (principal material axes of fiber-reinforced lamina not aligned with global axes).

For 2-D deformable shell solid structures (solid element), in the 'Property Module' of ABAQUS/CAE under linear elastic material options, the orthotropic elasticity can be defined by specifying (1) the elastic stiffness and (2) the engineering constants, or (3) defining the orthotropic elasticity in the plane stress: type: lamina. Note that the first two are applicable for 9 constant orthotropic materials, while the third is used for the state of plane stress in ABAQUS/CAE. Since the feature of scarf should be constructed in the finite element model, the lateral surface of a specimen will be modeled on the *x*-*y* plane in ABAQUS (Figure 4.8). The state of plane strain must be chosen rather than that of plane stress. Furthermore, an auxiliary option with 2-D shell elements-composite is embedded in ABAQUS/CAE. This option is better for same parallel plates (surfaces) under the state of plane stress analysis.

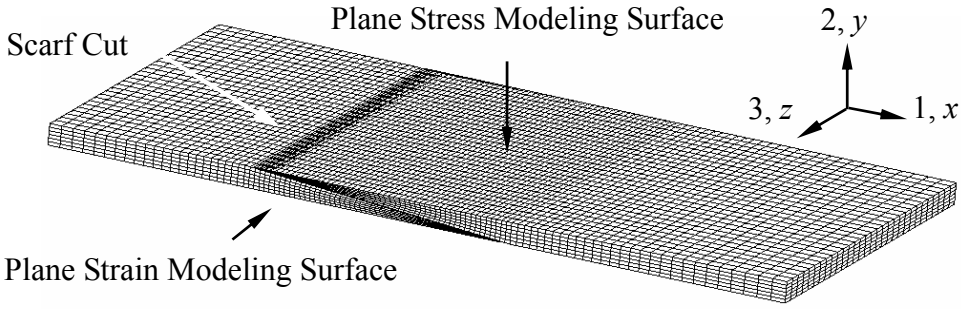

Figure 4.8. Definition of plane stress and plane strain modeling surface in finite element model.

Options (1) and (2) in ABAQUS are admissible for 0 and 90-degree laminae. For non-principal materials, i.e., ±45-degree laminae, the shear-extension coupling terms exist. As discussed above, the engineering constant (specially orthotropic) method is not appropriate for ±45-degree laminae. Accordingly, it is better to keep the original stiffness or compliance form, including positive and negative values and possibly including S_{16}, S_{26}, S_{36}, and S_{45}, rather than using the 9 positive engineering constants. In ABAQUS/CAE, the anisotropic material property is introduced to solve this problem. For fully anisotropic materials, the relations of stress-strain are defined as stiffness matrix shown in equation (4.6), which is inverted by 21 independent constants within the symmetric compliance matrix (S_{ij}=S_{ji}, equation (4.5)). In equation (4.6), the elastic stiffness is written in the tensor form (D_{ijkl}) defined in ABAQUS. Because the principal material axes still exist within the unidirectional fiber-reinforced lamina, even though the fiber rotated by ±45-degree, the shear-shear coupling terms and some shear-extension terms can be deleted [1]. Furthermore, the transversely isotropic property (isotropy about the 2-3 plane in OPT53 cases as shown in Figure 4.8) model can be added. Eventually, the final simplified anisotropic matrix consists of only 13 constants for ±45-degree laminae, but actually only 9 of the constants are independent.

$$\begin{bmatrix}\sigma_{11}\\ \sigma_{22}\\ \sigma_{33}\\ \tau_{12}\\ \tau_{13}\\ \tau_{23}\end{bmatrix}=\begin{bmatrix}D_{1111} & D_{1122} & D_{1133} & D_{1112} & D_{1113} & D_{1123}\\ D_{2211} & D_{2222} & D_{2233} & D_{2212} & D_{2213} & D_{2223}\\ D_{3311} & D_{3322} & D_{3333} & D_{3312} & D_{3313} & D_{3323}\\ D_{1211} & D_{1222} & D_{1233} & D_{1212} & D_{1213} & D_{1223}\\ D_{1311} & D_{1322} & D_{1333} & D_{1312} & D_{1313} & D_{1323}\\ D_{2311} & D_{2322} & D_{2333} & D_{2312} & D_{2313} & D_{2323}\end{bmatrix}\begin{bmatrix}\varepsilon_{11}\\ \varepsilon_{22}\\ \varepsilon_{33}\\ \gamma_{12}\\ \gamma_{13}\\ \gamma_{23}\end{bmatrix} \tag{4.6}$$

As how Q_{ij} tensor defined in CLPT, D_{ijkl} tensor is denoted in ABAQUS. They indicate the same meanings of the elastic stiffness. In this study, the Q_{ij} (or S_{ij}) is used for the notation within the calculations of various formulas from the plate theory. For the tensor $\bar{Q}_{ij}$, by definition, it can be also derived from the inverse of $[\bar{S}_{ij}]$,

$$[Q_{ij}]=[S_{ij}]^{-1} \quad \text{and} \quad [\bar{Q}_{ij}]=[\bar{S}_{ij}]^{-1} \tag{4.7}$$

where $[\bar{S}_{ij}]$ denotes the compliance rotated by θ degree from the global axes and $[S_{ij}]$ indicates the compliance of fiber direction/ zero degree. The Reuter's Matrix and the transformation matrix [T] can be used to obtain the local compliance matrix [1] based on the local coordinate/principal material axis system (1,2,3). The symbols defined here, the 1-direction represents the fiber direction, the 2-direction means the in-plane transverse direction, and the 3-direction denotes the out-of-plane direction of laminae. The entire transform equations of compliance [1] are defined as

$$\begin{aligned}
\bar{S}_{11} &= S_{11}\cos^4\theta+(2S_{12}+S_{66})\sin^2\theta\cos^2\theta+S_{22}\sin^4\theta\\
\bar{S}_{12} &= S_{12}\left(\sin^4\theta+\cos^4\theta\right)+(S_{11}+S_{22}-S_{66})\sin^2\theta\cos^2\theta\\
\bar{S}_{22} &= S_{11}\cos^4\theta+(2S_{12}+S_{66})\sin^2\theta\cos^2\theta+S_{22}\cos^4\theta\\
\bar{S}_{16} &= \left(2S_{11}-2S_{12}-S_{66}\right)\sin\theta\cos^3\theta-(2S_{22}-2S_{12}-S_{66})\sin^3\theta\cos\theta\\
\bar{S}_{26} &= \left(2S_{11}-2S_{12}-S_{66}\right)\sin^3\theta\cos\theta-(2S_{22}-2S_{12}-S_{66})\sin\theta\cos^3\theta\\
\bar{S}_{66} &= 2\left(2S_{11}+2S_{22}-4S_{12}-S_{66}\right)\sin^2\theta\cos^2\theta+S_{66}\left(\sin^4\theta+\cos^4\theta\right)
\end{aligned} \tag{4.8}$$

In the same manner, the tensor $\bar{Q}_{ij}$ also can be derived by inversing equation (4.4). When $[Q_{ij}]$ is rotated by an arbitrary angle, the special trigonometric property can also be utilized for transformation matrix [T], i.e.,

$$[T_{(-\theta)}]=[T_{(\theta)}]^{-1} \text{ and } [T_{(-\theta)}]^{T}=[T_{(\theta)}]^{-T} \tag{4.9}$$

When the axis is rotated by an angle (θ), equation (4.4) with (4.7) can be rearranged using equation (4.9) as

$$[\bar{S}_{ij}]_{\theta}=[T_{(\theta)}][S_{ij}][T_{(\theta)}]^{T} \rightarrow [\bar{Q}_{ij}]_{\theta}=[T_{(\theta)}]^{-1}[Q_{ij}][T_{(\theta)}]^{-T}$$
$$[\bar{Q}_{ij}]_{\theta}=[T_{(-\theta)}][Q_{ij}][T_{(-\theta)}]^{T} \tag{4.10}$$

As a result, all the components of $[\bar{Q}_{ij}]$ are converted individually from equations (4.11).

$$\begin{aligned}
\bar{Q}_{11} &= Q_{11}\cos^4\theta + (2Q_{12}+2Q_{66})\sin^2\theta\cos^2\theta + Q_{22}\sin^4\theta \\
\bar{Q}_{12} &= Q_{12}\left(\sin^4\theta+\cos^4\theta\right) + (Q_{11}+Q_{22}-4Q_{66})\sin^2\theta\cos^2\theta \\
\bar{Q}_{22} &= Q_{11}\sin^4\theta + 2(Q_{12}+2Q_{66})\sin^2\theta\cos^2\theta + Q_{22}\cos^4\theta \\
\bar{Q}_{16} &= (Q_{11}-Q_{12}-2Q_{66})\sin\theta\cos^3\theta + (Q_{12}-Q_{22}+2Q_{66})\sin^3\theta\cos\theta \\
\bar{Q}_{26} &= (Q_{11}-Q_{12}-2Q_{66})\sin^3\theta\cos\theta + (Q_{12}-Q_{22}+2Q_{66})\sin\theta\cos^3\theta \\
\bar{Q}_{66} &= (Q_{11}+Q_{22}-2Q_{12}-2Q_{66})\sin^2\theta\cos^2\theta + Q_{66}\left(\sin^4\theta+\cos^4\theta\right)
\end{aligned} \tag{4.11}$$

Same as $[S_{ij}]$ at zero degree, the complete 3-D stiffness matrix $[Q_{ij}]$ can be defined in terms of the 9 independent engineering constants (E_{11}, E_{22}, E_{33}, G_{12}, G_{23}, G_{31}, ν_{12}, ν_{31}, and ν_{32}). Therefore, the 3-D constitutive equations [1,59], following the Hooke's law, are expressed as

$$\begin{bmatrix}\sigma_{11}\\ \sigma_{22}\\ \sigma_{33}\\ \tau_{23}\\ \tau_{31}\\ \tau_{12}\end{bmatrix}=\begin{bmatrix}\frac{1-\nu_{23}\nu_{32}}{E_{22}E_{33}\Delta} & \frac{\nu_{21}+\nu_{31}\nu_{23}}{E_{22}E_{33}\Delta} & \frac{\nu_{31}+\nu_{21}\nu_{32}}{E_{22}E_{33}\Delta} & 0 & 0 & 0\\ \frac{\nu_{12}+\nu_{13}\nu_{32}}{E_{33}E_{11}\Delta} & \frac{1-\nu_{31}\nu_{13}}{E_{33}E_{11}\Delta} & \frac{\nu_{32}+\nu_{31}\nu_{12}}{E_{33}E_{11}\Delta} & 0 & 0 & 0\\ \frac{\nu_{13}+\nu_{12}\nu_{23}}{E_{11}E_{22}\Delta} & \frac{\nu_{23}+\nu_{13}\nu_{21}}{E_{11}E_{22}\Delta} & \frac{1-\nu_{12}\nu_{21}}{E_{11}E_{22}\Delta} & 0 & 0 & 0\\ 0 & 0 & 0 & G_{23} & 0 & 0\\ 0 & 0 & 0 & 0 & G_{31} & 0\\ 0 & 0 & 0 & 0 & 0 & G_{12}\end{bmatrix}\begin{bmatrix}\varepsilon_{11}\\ \varepsilon_{22}\\ \varepsilon_{33}\\ \gamma_{23}\\ \gamma_{31}\\ \gamma_{12}\end{bmatrix} \tag{4.12}$$

$$\Delta=\frac{1-\nu_{12}\nu_{21}-\nu_{23}\nu_{32}-\nu_{31}\nu_{13}-2\nu_{12}\nu_{23}\nu_{31}}{E_{11}E_{22}E_{33}} \tag{4.13}$$

Due to the symmetry of the stiffness matrix, it requires that

$$\begin{aligned}\frac{\nu_{21}+\nu_{31}\nu_{23}}{E_{22}E_{33}\Delta}&=\frac{\nu_{12}+\nu_{13}\nu_{32}}{E_{33}E_{11}\Delta}\\ \frac{\nu_{31}+\nu_{21}\nu_{32}}{E_{22}E_{33}\Delta}&=\frac{\nu_{13}+\nu_{12}\nu_{23}}{E_{11}E_{22}\Delta}\\ \frac{\nu_{32}+\nu_{31}\nu_{12}}{E_{33}E_{11}\Delta}&=\frac{\nu_{23}+\nu_{13}\nu_{21}}{E_{11}E_{22}\Delta}\end{aligned} \tag{4.14}$$

in the sense that the reciprocal rule, equation (4.15), is generated as

$$\nu_{ji}=\frac{\nu_{ij}E_j}{E_i}\qquad(i\neq j) \tag{4.15}$$

Based on the state of 2-D plane strain, the tensor Q_{ij} can be simplified and rewritten as

$$\begin{aligned}Q_{11}&=D_{1111}=\frac{E_{11}(1-\nu_{12})}{1-\nu_{12}-2\nu_{12}\nu_{21}}\\ Q_{22}&=D_{2222}=\frac{E_{22}(1-\nu_{12}\nu_{21})}{(1+\nu_{12})(1-\nu_{12}-2\nu_{12}\nu_{21})}\\ Q_{12}&=D_{1122}=\frac{\nu_{12}E_{22}}{1-\nu_{12}-2\nu_{12}\nu_{21}}=\frac{\nu_{21}E_{11}}{1-\nu_{12}-\nu_{12}\nu_{21}}\\ D_{1212}&=G_{12}=Q_{66}\end{aligned} \tag{4.16}$$

While under 2-D plane stress state, the constitutive equations become as

$$
\begin{aligned}
Q_{11} &= D_{1111} = \frac{E_{11}}{1-\nu_{12}\nu_{21}} \\
Q_{22} &= D_{2222} = \frac{E_{22}}{1-2\nu_{12}\nu_{21}} \\
Q_{12} &= D_{1122} = \frac{\nu_{12}E_{22}}{1-\nu_{12}\nu_{21}} = \frac{\nu_{21}E_{11}}{1-\nu_{12}\nu_{21}} \\
D_{1212} &= G_{12} = Q_{66}
\end{aligned}
\tag{4.17}
$$

Same as the compliance matrix, according to the orthotropic theory, D_{1113}, D_{1123}, D_{2213}, D_{2223}, D_{3312}, D_{3313}, D_{3323}, D_{1213}, D_{1223}, and D_{1323} all remain zero (compared with the complete stiffness matrix in equation (4.12)). Analysis under either the plane stress or the plane strain state is a 2-D problem and certain out-of-plane components are ignored. The difference in the constitutive equations between the state of plane strain and plane stress is spoken from the equations (4.16) and (4.17)). From CLPT, the plane stress state is applied and the properties converted cannot be directly imported to OPT53 plane strain models. Note that, even though the OPT53 model is constructed in 2-D space and analyzed by the plane strain state in ABAQUS, the element type is still defined by continuum/solid plane strain elements. The material properties applied to ABAQUS in the 'Property Module' should keep the complete 3-D form, i.e., using the tensor Q_{ij} in equation (4.12) rather than in equations (4.16) and (4.17).

From the definition of the stiffness/compliance for anisotropic materials and the physical phenomena of unidirectional fiber-reinforced laminae, it can be proved [1,52,59] that

$$
Q_{ij} = \begin{bmatrix}
Q_{11} & Q_{12} & Q_{12} & 0 & 0 & 0 \\
Q_{12} & Q_{22} & Q_{23} & 0 & 0 & 0 \\
Q_{12} & Q_{23} & Q_{22} & 0 & 0 & 0 \\
0 & 0 & 0 & \frac{1}{2}(Q_{22}-Q_{23}) & 0 & 0 \\
0 & 0 & 0 & 0 & Q_{66} & 0 \\
0 & 0 & 0 & 0 & 0 & Q_{66}
\end{bmatrix}
\tag{4.18}
$$

Therefore, the amount of independent elastic constants required is reduced to 5, because Q_{44} and Q_{55} terms can be rewritten by equation (4.19) from equation (4.12).

$$\begin{aligned} Q_{44} &= G_{31} = D_{1313} = \tfrac{1}{2}(Q_{22} - Q_{23}) \\ Q_{55} &= D_{2323} = G_{23} = Q_{66} = D_{1212} = Q_{66} = G_{12} \end{aligned} \tag{4.19}$$

After all required equations are completely defined, two more conditions as E_{22} =E_{33}=1.185 Msi. and v_{12} = v_{13} = v_{23}= 0.317 or v_{23}= 0.444 are added to the material properties of T-800S/3900-2 prepregs (listed in Table 4.4). The former assumption is generally valid for unidirectional fiber-reinforced laminae, while the latter v_{23} is an admissible value just for ease of calculation. In fact, from the reported data of similar carbon fiber-reinforced materials [52,57,61], v_{23} is around 1.25~1.55 times v_{12} and the G_{23} is roughly around 0.5~0.7 times G_{12}, if v_{12} = v_{13}, E_{22}=E_{33}, and G_{12}=G_{13} are valid. Therefore, based on the premise v_{23}= 0.317, the stiffness matrices of different orientations (90 and ±45-degree) are obtained using equations (4.12) to (4.15) and the 3-D coordinate transformation matrix [T]. To consist with ABAQUS definition, as equation (4.6), the constants within the matrices associated with the 2- and the 3-direction should be swapped in advance and the final results are summarized in the matrix form as follows.

0-degree Lamina D_{ijkl} (psi)

$$[Q]_0 = \begin{bmatrix} 2.17385\,10^7 & 5.59108\,10^5 & 5.59108\,10^5 & 0 & 0 & 0 \\ 5.59108\,10^5 & 1.33176\,10^6 & 4.31991\,10^5 & 0 & 0 & 0 \\ 5.59108\,10^5 & 4.31991\,10^5 & 1.33176\,10^6 & 0 & 0 & 0 \\ 0 & 0 & 0 & 3.51000\,10^5 & 0 & 0 \\ 0 & 0 & 0 & 0 & 3.51000\,10^5 & 0 \\ 0 & 0 & 0 & 0 & 0 & 4.49884\,10^5 \end{bmatrix}$$

90-degree Lamina D_{ijkl} (psi)

$$[Q]_{90}=\begin{bmatrix} 1.33176\,10^{6} & 4.31991\,10^{5} & 5.59108\,10^{5} & 0 & 0 & 0 \\ 4.31991\,10^{5} & 1.33176\,10^{7} & 5.59108\,10^{5} & 0 & 0 & 0 \\ 5.59108\,10^{5} & 5.59108\,10^{5} & 2.17385\,10^{6} & 0 & 0 & 0 \\ 0 & 0 & 0 & 4.49884\,10^{5} & 0 & 0 \\ 0 & 0 & 0 & 0 & 3.51000\,10^{5} & 0 \\ 0 & 0 & 0 & 0 & 0 & 3.51000\,10^{5} \end{bmatrix}$$

-45-degree Lamina D_{ijkl} (psi)

$$[Q]_{-45}=\begin{bmatrix} 6.39812\,10^{6} & 5.69612\,10^{6} & 4.95550\,10^{5} & 0 & -5.10168\,10^{6} & 0 \\ 5.69612\,10^{6} & 6.39812\,10^{6} & 4.95550\,10^{5} & 0 & -63558 & 0 \\ 4.95550\,10^{5} & 4.95550\,10^{5} & 1.33176\,10^{6} & 0 & -5.10168\,10^{6} & 0 \\ 0 & 0 & 0 & 4.00442\,10^{5} & 0 & 49442 \\ -5.10164\,10^{6} & -63558 & -5.10164\,10^{6} & 0 & 5.48796\,10^{6} & 0 \\ 0 & 0 & 0 & 49442 & 0 & 4.00442\,10^{5} \end{bmatrix}$$

45-degree Lamina D_{ijkl} (psi)

$$[Q]_{45}=\begin{bmatrix} 6.39812\ 10^{6} & 5.69612\ 10^{6} & 4.95550\ 10^{5} & 0 & 5.10168\ 10^{6} & 0 \\ 5.69612\ 10^{6} & 6.39812\ 10^{6} & 4.95550\ 10^{5} & 0 & 63558 & 0 \\ 4.95550\ 10^{5} & 4.95550\ 10^{5} & 1.33176\ 10^{6} & 0 & 5.10168\ 10^{6} & 0 \\ 0 & 0 & 0 & 4.00442\ 10^{5} & 0 & -49442 \\ 5.10164\ 10^{6} & 63558 & 5.10164\ 10^{6} & 0 & 5.48796\ 10^{6} & 0 \\ 0 & 0 & 0 & -49442 & 0 & 4.00442\ 10^{5} \end{bmatrix}$$

- **Stability restriction on Engineering Constants**

Elastic materials are required to satisfy the restrictions of material (the Drucker stability), which leads to certain conditions on the values of the elastic constants. The work done by the stress is defined by the product of the stress and corresponding strain. In order to avoid the generation of energy, which results in an unstable system, the summation of the work done by all stresses should be positive. This condition constitutes a thermodynamic constraint on the engineering constants. The restriction for orthotropic materials, proposed by Lempriere, says

the matrices (both the stiffness and compliance matrices) relating stress to strain must be positive-definite [1], that is, the matrices contain positive principal values or invariants. For orthotropic materials, the stability [1,45] derived from the compliance matrix is given by inequality (4.20) or expressed in terms of the engineering constants (4.21).

$$S_{11},\ S_{22},\ S_{33},\ S_{44},\ S_{55},\ S_{66} > 0 \tag{4.20}$$

$$E_{11},\ E_{22},\ E_{33},\ G_{23},\ G_{31},\ G_{12} > 0 \tag{4.21}$$

Likewise, from equations (4.12) and (4.13) they can be written as

$$\left(1-\nu_{23}\nu_{32}\right)>0 \qquad \left(1-\nu_{31}\nu_{13}\right)>0 \qquad \left(1-\nu_{12}\nu_{21}\right)>0 \tag{4.22}$$

$$\bar{\Delta}=1-\nu_{12}\nu_{21}-\nu_{23}\nu_{32}-\nu_{31}\nu_{13}-2\nu_{21}\nu_{32}\nu_{13}>0 \tag{4.23}$$

Due to the matrix being positive-definite, the determinant of the matrix must be positive and, from the reciprocal relations (4.15), the requirements can be rewritten as

$$\left|\nu_{21}\right|<\sqrt{\frac{E_{22}}{E_{11}}} \qquad \left|\nu_{32}\right|<\sqrt{\frac{E_{33}}{E_{22}}} \qquad \left|\nu_{13}\right|<\sqrt{\frac{E_{11}}{E_{33}}} \tag{4.24}$$

$$\left|\nu_{12}\right|<\sqrt{\frac{E_{11}}{E_{22}}} \qquad \left|\nu_{23}\right|<\sqrt{\frac{E_{22}}{E_{33}}} \qquad \left|\nu_{31}\right|<\sqrt{\frac{E_{33}}{E_{11}}} \tag{4.25}$$

When the left-hand side of the inequality attains zero, the material behaves incompressible. These stability restrictions can be applied to the engineering constants for orthotropic materials in order to verify the experimental or assumed data whether they physically consist with the skeleton of the mechanical elasticity theorem.

For fully anisotropic materials, the restrictions of stability that the elasticity $[D_{ijkl}]$ matrix is positive definite requires all of the eigenvalues of $[D_{ijkl}]$ are positive [45]. From the foregoing $[D_{ijkl}]$ matrix of different orientation laminae, their eigenvalues are computed as shown in the following matrices, respectively.

$$\lambda_0 = \begin{bmatrix} 2.17698\,10^7 \\ 1.73250\,10^6 \\ 8.99769\,10^5 \\ 3.51000\,10^5 \\ 3.51000\,10^5 \\ 4.49884\,10^5 \end{bmatrix} \quad \lambda_{90} = \begin{bmatrix} 2.17698\,10^7 \\ 8.99769\,10^5 \\ 1.73250\,10^6 \\ 4.49884\,10^5 \\ 3.51000\,10^5 \\ 3.51000\,10^5 \end{bmatrix}$$

$$\lambda_{-45} = \begin{bmatrix} 1.67514\,10^7 \\ 1.47658\,10^6 \\ 7.02000\,10^5 \\ 6.85990\,10^5 \\ 4.49884\,10^5 \\ 3.51000\,10^5 \end{bmatrix} \quad \lambda_{45} = \begin{bmatrix} 1.67514\,10^7 \\ 1.47658\,10^6 \\ 7.02000\,10^5 \\ 6.85990\,10^5 \\ 4.49884\,10^5 \\ 3.51000\,10^5 \end{bmatrix}$$

The above results show that all [D_{ijkl}] matrices based on the assumptions satisfy the restrictions of stability and are permissible.

4.3.3 Orthotropic Material Model

If the orthotropic elasticity is expressed in terms of the 9 engineering constants, namely E_{11}, E_{22}, E_{33}, G_{12}, G_{23}, G_{13}, v_{12}, v_{13}, and v_{23}, it should be restricted to the specially orthotropy, i.e., no existence of shear-extension coupling terms. Otherwise, it should be incorporated with other engineering constants, namely coefficients of mutual influence/shear-extension coupling coefficients and Chentsov coefficient/ shear-shear coupling coefficient, which are relative to Poisson's ratio/extension-extension coupling coefficients [1]. The coefficients, used to describe the in-plane shear-extension terms such as S_{16} and S_{26}, are proposed by Lekhnitskii. The Chentsov coefficients are related to S_{45}, S_{46}, and S_{56} and do not affect in-plane behaviors [1]. None of these cofficients arises in any orthotropic material (no shear-extension coupling terms) unless its principal material axes are not aligned with the global coordinates.

0-degree and 90-degree laminae are orthotropic, but ±45-degree laminae are generally orthotropic which have shear-extension coupling terms. To determine the orthotropic

characteristics of ±45-degree plies within the OPT53 models, the elastic properties must be obtained from the balanced and symmetric composite laminate consisting of ±45-degree plies only [1,62,63], i.e., the stacking sequence is [45/-45/-45/45]. The shear-extension coupling terms can be eliminated. From equations (4.18) and (4.12) to (4.15) or using the compliance stiffness matrix (equation (4.26)), the engineering constants can be evaluated.

$$S_{ij} = \begin{bmatrix} S_{11} & S_{12} & S_{12} & 0 & 0 & 0 \\ S_{12} & S_{22} & S_{23} & 0 & 0 & 0 \\ S_{12} & S_{23} & S_{22} & 0 & 0 & 0 \\ 0 & 0 & 0 & S_{44} & 0 & 0 \\ 0 & 0 & 0 & 0 & S_{66} & 0 \\ 0 & 0 & 0 & 0 & 0 & S_{66} \end{bmatrix} \tag{4.26}$$

From the result of section 4.3.2, the in-plane elastic constants corelate to the out-of-plane constants. Furthermore, Q_{13}, Q_{33}, Q_{44} and Q_{55} are not completely indepdent, in the sense that, the engineering constants G_{13}, G_{23}, and v_{13} are not necessary tested for. Inverting the matrix (equation (4.18)) and substituting for the constitutive equations of $[Q_{ij}]$ results in

$$S_{ij} = \begin{bmatrix} \frac{Q_{22}+Q_{23}}{R} & \frac{-Q_{12}}{R} & \frac{-Q_{12}}{R} & 0 & 0 & 0 \\ \frac{-Q_{12}}{R} & \frac{Q_{22}Q_{11}-Q_{12}^2}{H} & \frac{-Q_{23}Q_{11}+Q_{12}^2}{H} & 0 & 0 & 0 \\ \frac{-Q_{12}}{R} & \frac{-Q_{23}Q_{11}+Q_{12}^2}{H} & \frac{Q_{22}Q_{11}-Q_{12}^2}{H} & 0 & 0 & 0 \\ 0 & 0 & 0 & \frac{2}{Q_{22}-Q_{23}} & 0 & 0 \\ 0 & 0 & 0 & 0 & \frac{1}{Q_{66}} & 0 \\ 0 & 0 & 0 & 0 & 0 & \frac{1}{Q_{66}} \end{bmatrix} \tag{4.27}$$

where
$$R = Q_{11}(Q_{22}+Q_{23}) - 2Q_{12}^2$$
$$H = Q_{11}(Q_{22}^2 - Q_{23}^2) - 2Q_{12}^2(Q_{22}-Q_{23})$$

Recall the 3-D compliance matrix; it can be expressed in terms of the 9 engineering constants as shown in equation (4.28). Based on the same definition of $[S_{ij}]$, equation (4.28) is equated to equation (4.27) and the 9 engineering constants for each orientation ply can be solved. All the engineering constants for 0, 90, and ±45-degree laminae are shown in Table 4.6. The bottom column of Table 4.6 remarks the coordinate system in ABAQUS, which the 2- and 3-direction should be swapped from the regular plane theory coordinate system.

$$S_{ij} = \begin{bmatrix} \frac{1}{E_{11}} & \frac{-\nu_{21}}{E_{22}} & \frac{-\nu_{31}}{E_{33}} & 0 & 0 & 0 \\ \frac{-\nu_{12}}{E_{11}} & \frac{1}{E_{22}} & \frac{-\nu_{32}}{E_{33}} & 0 & 0 & 0 \\ \frac{-\nu_{13}}{E_{11}} & \frac{-\nu_{23}}{E_{22}} & \frac{1}{E_{33}} & 0 & 0 & 0 \\ 0 & 0 & 0 & \frac{1}{G_{23}} & 0 & 0 \\ 0 & 0 & 0 & 0 & \frac{1}{G_{31}} & 0 \\ 0 & 0 & 0 & 0 & 0 & \frac{1}{G_{12}} \end{bmatrix} \tag{4.28}$$

TABLE 4.6

ENGINEERING CONSTANTS FOR DIFFERENT ORIENTATIONS

T800S Composite	*Exx*	*Eyy*	*Ezz*	*vxy*	*vxz*	*vyz*	*Gxy*	*Gxz*	*Gyz*
	$2.138\ 10^7$	$1.185\ 10^6$	$1.185\ 10^6$	0.3170	0.3170	0.3170	$3.510\ 10^5$	$3.510\ 10^5$	$4.498\ 10^5$
Lamina	E_{11}	E_{22}	E_{33}	ν_{12}	ν_{13}	ν_{32}	G_{12}	G_{13}	G_{23}
0-degree	$2.138\ 10^7$	$1.185\ 10^6$	$1.185\ 10^6$	0.3170	0.3170	0.3170	$3.510\ 10^5$	$3.510\ 10^5$	$4.498\ 10^5$
90-degree	$1.185\ 10^6$	$2.138\ 10^7$	$1.185\ 10^6$	0.0175	0.3170	0.0175	$3.510\ 10^5$	$4.498\ 10^5$	$3.510\ 10^5$
45-degree	$1.324\ 10^6$	$1.324\ 10^6$	$1.291\ 10^6$	0.8870	0.0454	0.0409	$5.487\ 10^6$	$4.004\ 10^5$	$4.004\ 10^5$
-45-degree	$1.324\ 10^6$	$1.324\ 10^6$	$1.291\ 10^6$	0.8870	0.0454	0.0409	$5.487\ 10^6$	$4.004\ 10^5$	$4.004\ 10^5$
ABAQUS	$\boldsymbol{E_{11}}$	$\boldsymbol{E_{33}}$	$\boldsymbol{E_{22}}$	$\boldsymbol{\nu_{13}}$	$\boldsymbol{\nu_{12}}$	$\boldsymbol{\nu_{23}}$	$\boldsymbol{G_{13}}$	$\boldsymbol{G_{12}}$	$\boldsymbol{G_{23}}$

(The unit for moduli is in psi and unit-less for Poisson's ratio)

- **Stability restriction on Engineering Constants**

For engineering constant model, the examination of stability restrictions in equations

(4.21) to (4.25) is integrated in Table 4.7 (defined in the ABAQUS coordinates). All the plausible data satisfy the restrictions, yet the confirmation via ABAQUS is still needed to ensure they are physical and reliable.

TABLE 4.7

INSPECTION OF STABILITY RESTRICTIONS FOR EACH ORIENTATION LAMINA

T800S 0-degree Ply	v_{12}	0.3170	$<(E_{11}/E_{22})^{0.5}=$	4.247
	v_{13}	0.3170	$<(E_{11}/E_{33})^{0.5}=$	4.247
	v_{23}	0.3170	$<(E_{22}/E_{33})^{0.5}=$	1.000
	$\overline{\Delta} = 0.88489 > 0$			
T800S ±45-degree Ply from [45/-45]s	v_{12}	0.0454	$<(E_{11}/E_{22})^{0.5}=$	1.012
	v_{13}	0.8870	$<(E_{11}/E_{33})^{0.5}=$	1.000
	v_{23}	0.0409	$<(E_{22}/E_{33})^{0.5}=$	0.987
	$\overline{\Delta} = 0.20674 > 0$			
T800S 90-degree Ply	v_{12}	0.3170	$<(E_{11}/E_{22})^{0.5}=$	1.000
	v_{13}	0.0175	$<(E_{11}/E_{33})^{0.5}=$	0.235
	v_{23}	0.0175	$<(E_{22}/E_{33})^{0.5}=$	0.235
	$\overline{\Delta} = 0.88489 > 0$			

4.3.4 Equivalent Isotropic Material Model

From section 4.1.3, the specified stacking sequences and the [*A*] matrices speak that only OPT53-3 and OPT53-5 composite scarf joint models satisfy the quasi-isotropic restriction. When using the engineering constants, the distinction among the plane stress, plane strain, and 3-D constitutive equations is clarified by Tables 4.8 to 4.10. Evidently, the results from the plane strain state are close to those from the 3-D complete constitutive equations. If $E_{yy}=E_{zz}$ and $v_{xy}= v_{yz}= v_{xz}$ are assumed for theT-800S prepregs, the properties from the plane strain state condition would be the same as the complete 3-D results. The values of E_{xx}, G_{xy}, and v_{xy} in Table 4.10 will be imported to *E*, *G*, and *v* in the isotropic material module in ABAQUS to simulate OPT53 composite scarf joint models using the equivalent/quasi isotropic model.

TABLE 4.8

EQUIVALENT ELASTIC PROPERTIES (psi) CONVERTED FROM PLANE STRESS STATE

Model	E_{xx}	E_{yy}	G_{xy}	ν_{xy}
OPT53-1	$7.267\ 10^6$	$7.267\ 10^6$	$3.203\ 10^6$	0.3801
OPT53-2	$9.303\ 10^6$	$7.243\ 10^6$	$2.632\ 10^6$	0.3350
OPT53-3	$7.793\ 10^6$	$7.793\ 10^6$	$2.918\ 10^6$	0.3353
OPT53-4	$8.895\ 10^6$	$6.648\ 10^6$	$2.918\ 10^6$	0.3920
OPT53-5	$7.793\ 10^6$	$7.793\ 10^6$	$2.918\ 10^6$	0.3353
OPT53-6	$9.061\ 10^6$	$7.574\ 10^6$	$2.609\ 10^6$	0.3185

TABLE 4.9

EQUIVALENT ELASTIC PROPERTIES (psi) CONVERTED FROM PLANE SRAIN STATE

Model	E_{xx}	E_{yy}	G_{xy}	ν_{xy}
OPT53-1	$7.339\ 10^6$	$7.339\ 10^6$	$3.204\ 10^6$	0.3931
OPT53-2	$9.390\ 10^6$	$7.340\ 10^6$	$2.634\ 10^6$	0.3501
OPT53-3	$7.875\ 10^6$	$7.875\ 10^6$	$2.919\ 10^6$	0.3488
OPT53-4	$8.970\ 10^6$	$6.736\ 10^6$	$2.919\ 10^6$	0.4066
OPT53-5	$7.875\ 10^6$	$7.875\ 10^6$	$2.919\ 10^6$	0.3488
OPT53-6	$9.151\ 10^6$	$7.670\ 10^6$	$2.611\ 10^6$	0.3333

TABLE 4.10

EQUIVALENT ELASTIC PROPERTIES (psi) CONVERTED FROM 3-D COMPLETE CONSTITUTIVE EQUATIONS

Model	E_{xx}	E_{yy}	G_{xy}	ν_{xy}
OPT53-1	7.33910^6	$7.339\ 10^6$	$3.204\ 10^6$	0.3931
OPT53-2	$9.390\ 10^6$	$7.340\ 10^6$	$2.634\ 10^6$	0.3501
OPT53-3	$7.875\ 10^6$	$7.875\ 10^6$	$2.919\ 10^6$	0.3488
OPT53-4	$8.970\ 10^6$	$6.736\ 10^6$	$2.919\ 10^6$	0.4066
OPT53-5	$7.875\ 10^6$	$7.875\ 10^6$	$2.919\ 10^6$	0.3488
OPT53-6	$9.151\ 10^6$	$7.670\ 10^6$	$2.611\ 10^6$	0.3333

CHAPTER 5

FINITE ELEMENT ANALYSIS ON SCARF-PATCHE-REPAIRED COMPOSITE LAMINATES

Following the processes similar to ASTM D5656 analysis in ABAQUS, both 3-D stress and 2-D plane strain finite element models are created for scarf-patch-repaired composite laminates (OPT53 composite scarf joint). The 3-D stress models (Figures 5.1and 5.2) use laminated composite material and equivalent isotropic material ply-merged constructions, respectively. The 2-D plane strain models use only laminated composite material constructions. The purposes of using the 3-D equivalent isotropic ply-merged models (Figure 5.2) are (1) faster to verify the elastic material properties with test results and (2) roughly to examine the 'edge effect' of specimens. The purposes of using the 2-D dynamic models are to more quickly (1) determine the strength of scarf joints using a dynamic failure model and (2) to apply a failure criterion to certain parts such as matrix (resin) and ply layers within the adherend. Without doubt, the 3-D laminated composite model accommodates all advantages except for long processing time, fair aspect ratio, and convergent difficulty. The comparisons between 3-D and 2-D simulation results will be presented in this chapter. The main disparity between laminated models and isotropic ply-merged models is the layer-by-layer pattern of the adherends. Adherends within laminated composite models are assembled layer by layer according to the specified stacking sequence exactly and each layer represents one ply. On the other hand, the isotropic ply-merged models under one equivalent material property are built up with appropriate mesh layers, not necessarily equal to the specified number of ply, and each layer does not represent certain ply group.

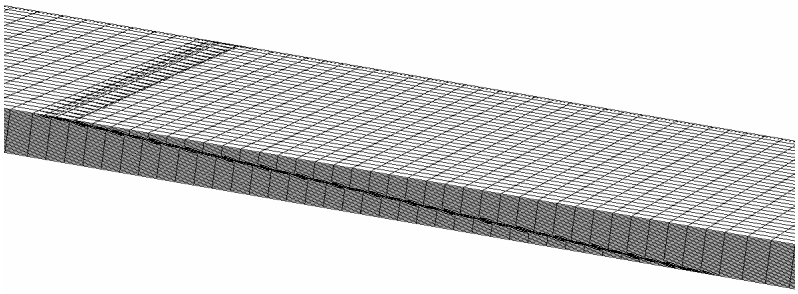

Figure 5.1. OPT53 composite scarf joint 3-D finite element model.

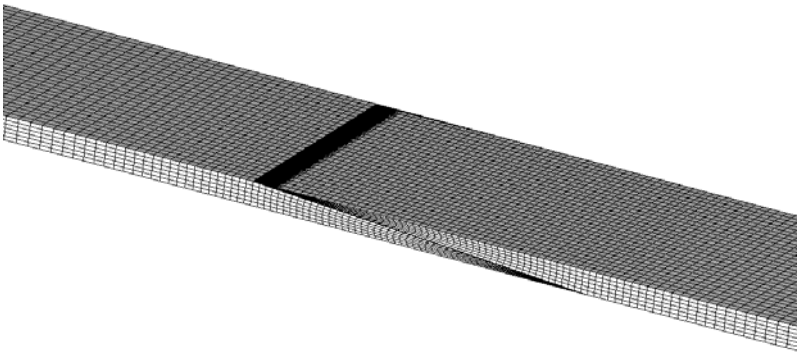

Figure 5.2. OPT53 scarf joint 3-D isotropic ply-merged finite element model.

Barriers in Finite Element

Compared with finite element models of ASTM D5656, OPT53 composite scarf joint models are much larger in the number of nodes and elements so that some negligible or tolerable errors in ASTM D5656 models could be enlarged or magnified in OPT53 scarf joint models. The dominant problems are processing time and the mesh in the adhesive section.

- **Processing Time**

  In dynamic analysis, according to the equations (3.1) and (3.2), the smaller element size results in longer calculation time. The number of elements and the density of materials used also influences the processing time. Due to the pre-requisite of using composite laminate adherends and adopting an acceptable aspect ratio, the number of the layers and elements cannot be reduced easily. Furthermore, in explicit analysis, the element type is

restricted to linear 4-node per element, in the sense that second or higher order element types cannot be applied. Alternatively, larger element size and larger mass density can be adopted to reduce processing time in dynamic analysis, but the accuracy of the analysis may be reduced as well. As a result, a high performance computer system with clusters of CPUs and a large pre-memory unit is required.

- **Mesh in Critical Area**

The scarf joint contains sections with tiny angles at both ends of the adherends and adhesive, especially for layer-by-layer composite adherend models. Lots of triangles with minute angles arise in these sections. Numerical evaluation of integrals over actual element involves the coordinate transformation from an actual element to a master element using one-to-one/unique mapping. This numerical approach requires the determinant of Jacobian matrix, J^e, greater than zero everywhere within the element (Ω^e) [53].

$$J^e \equiv \text{det. } [J^e] > 0 \tag{5.1}$$

The geometrical meaning of the Jacobian (2-D plate problem) matrix denotes the ratio of an area element in the real element to a corresponding area element in the master element. It can be expressed as

$$d\text{A} \equiv dx\, dy = J^e\, d\xi\, d\eta \tag{5.2}$$

where (ξ,η) signifies the natural coordinates in Gauss-Legendre quadrature. It is not allowed that if J^e is zero or very close to zero, a nonzero area element in the real element is mapped into a zero area element in the master element. Usually, this mapping is used for a distorted element transformed to a rectangular master element. Once the deformed shape of a real element exceeds the limits of acceptable distortion, the finite element

analysis will encounter errors and the job will be aborted.

Reducing the amount of triangular elements and total elements or enlarging the mesh size and density (artificial density) as much as possible are the accesses to achieve converged analysis. In the beginning, the 3-D composite models (Figure 5.1) are reduced to 2-D (plane strain) composite models in ABAQUS/Explicit. The mesh for 2-D dynamic models has been modified several times until it can converge. Figures 5.3 to 5.5 show the fine, medium, and coarse mesh of 2-D dynamic models used in ABAQUS, respectively. As extensive computation is taken to process dynamic analysis when using the mesh shown in Figure 5.4, the scarf joint is alternatively approximated by a stepped joint (Figure 5.5). The feature of stepped joints avoids extremely distorted triangular elements and provides finer and more uniform mesh within the adhesive section, which results in the higher accuracy of analysis. Based on the test results and finite element simulations of full-scale equivalent isotropic static models, the remote adherends (away from the overlap) maintain analogous stresses and surface strains along the loading direction. The adherends are then trimmed in length and referred to as 'reduced' finite element models for higher computational efficiency. In the reduced models, the adherend outside the overlap region is trimmed to 1.2 inches at each side of the overlap. The dimensions of reduced OPT53 composite joint models are tabulated in Table 5.1.

TABLE 5.1

DIMENSIONS OF REDUCED MODELS OF OPT53 COMPOSITE SCARF JOINTS

	Length	Width	Thickness	**Scarf Length**	**Scarf Angle**	**Adhesive Thickness**
OPT53-1	4.3659 in.	3 in.	0.144 in.	1.9 in.	4.334 º	0.005 in.
OPT53-2	4.3659 in.	3 in.	0.144 in.	1.9 in.	4.344 º	0.005 in.
OPT53-3	6.0760 in.	3 in.	0.236 in.	3.6 in.	3.763 º	0.005 in.
OPT53-4	6.5865 in.	3 in.	0.236 in.	4.1 in.	3.305 º	0.005 in.
OPT53-5	7.8750 in.	3 in.	0.360 in.	5.4 in.	3.763 º	0.005 in.
OPT53-6	8.8888 in.	3 in.	0.360 in.	6.4 in.	3.814 º	0.005 in.

The 2-D composite models maintain one element per ply in stepped joint models and two elements per ply, by default, in scarf joint models to reflect the composite properties. For convenience, the 2-D composite scarf joint model in Figure 5.4 is labeled as OP53-SCF and the 2-D composite stepped joint model in Figure 5.5 is marked as OPT53-STP.

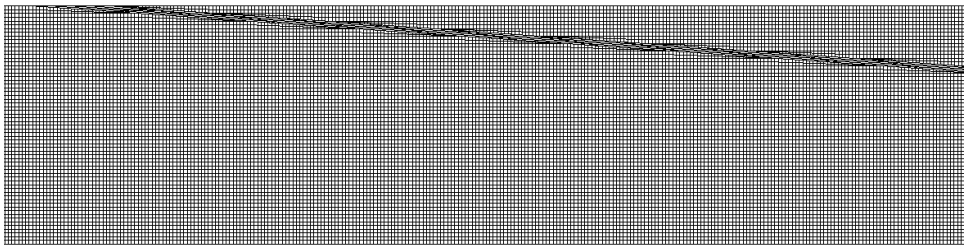

Figure 5.3. Fine mesh of OPT53-SCF 2-D static model (scarf joint) (non-uniform shape mesh in the adhesive).

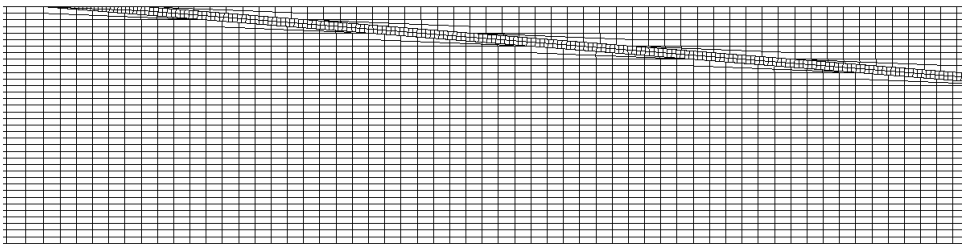

Figure 5.4. Medium mesh of OPT53-SCF 2-D dynamic model (scarf joint) (refined and uniform shape mesh in the adhesive).

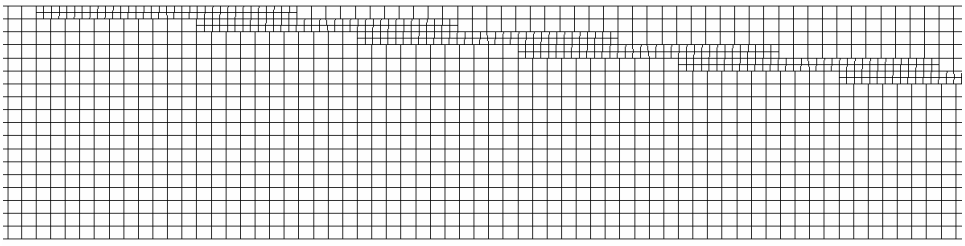

Figure 5.5. Coarse mesh of OPT53-STP 2-D dynamic model (stepped joint) (uniform shape mesh both in the adherends and the adhesive).

It should be noted that, the 'Material Orientation' must be defined within the created part under 'Property Module' in ABAQUS except for isotropic materials. Because in section 4.3,

all material properties with different material orientations are pre-calculated in terms of stiffness or engineering constants associated with the global coordinates. The 'Material Orientation' here is set identical to the global coordinates in ABAQUS. In 2-D model when only using shell, composite material, and plane stress state, then the material orientation can be defined in the 'Property Module' by a given angle. Otherwise, either changing to 3-D model or the pre-calculation of material properties with respect to different orientations becomes inevitable. The CPE4R plane strain element is used for both the adherend and the adhesive parts for 2-D models, whilst the C3D8R element that represents the 8-node linear brick, reduced integration, hourglass control, and explicit element is used in 3-D models. To further reduce the number of total elements, some 3-D models are cut into either half or quarter sections of the specimens due to the symmetry of loading and geometry. The information of mesh about each OPT53 reduced specimen is summarized in Tables 5.2 and 5.3. The geometry of 3-D dynamic finite element reduced models will be discussed in section 5.1.

TABLE 5.2

INFORMATION ON MESH IN 2-D REDUCED OPT53 FINITE ELEMENT ANALYSIS MODELS

Specimen Code	Reduced Adherend		Adhesive	
	Element	Node	Element	Node
OPT53-1STP	5,526	6,058	1,224	1,652
OPT53-1SCF	10,404	10,902	1,388	2,084
OPT53-2STP	5,526	6,058	1,224	1,652
OPT53-2SCF	10,404	10,902	1,388	2,084
OPT53-3STP	13,768	14,593	2,688	3,570
OPT53-3SCF	27,510	28,317	2,796	4,196
OPT53-4STP	13,472	14,300	2,688	3,570
OPT53-4SCF	23,552	24,266	2,796	4,196
OPT53-5STP	27,360	28,498	3,360	4,479
OPT53-5SCF	48,096	49,072	4,662	6,995
OPT53-6STP	24,600	25,589	3,400	4,515
OPT53-6SCF	55,836	56,956	4,982	7,475

(SCF: Scarf Joint Model; STP: Stepped Joint Model)

TABLE 5.3

INFORMATION ON MESH IN 3-D REDUCED (QUARTER SIZE) OPT53 DYNAMIC STEPPED JOINT MODELS

Specimen Code	Element		Node	
	Adherend	Adhesive	Adherend	Adhesive
OPT53-1-COM-QUA	28,230	7,050	33,168	9,856
OPT53-2-COM-QUA	28,230	7,050	33,168	9,856
OPT53-3-COM-QUA	79,395	22,755	89,856	29,792
OPT53-4-COM-QUA	76,355	22,800	86,592	30,256
OPT53-5-COM-QUA	137,325	32,760	153,120	43,152
OPT53-6-COM-QUA	154,020	39,000	171,424	51,040

5.1 Finite Element Analysis Results of OPT53 Composite Scarf Joints

5.1.1 Standard/Static Analysis

The purpose of using a static model is faster to confirm the linear elastic material properties of the adherends without defining any dynamic parameter and failure criterion. The load applied (pressure load) for each specimen is given by the average ultimate stress from the test results. The surface longitudinal strain (ε_{11}) along the loading direction from the nodes on the top surface within the overlap portion are extracted from the finite element results and compared with test data recorded by the ARAMIS system.

a. Equivalent Isotropic 3-D Model

The 3-D full-scale equivalent isotropic ply-merged models (Figure 5.2) are analyzed and the surface longitudinal strains (ε_{11}) on the top surface are outputted from the nodes which are spaced from the edge by a distance 'h' that is the individual thickness of each specimen, in order to diminish the interference of 'edge effect'. The equivalent elastic material properties such as E, G, and v of the composite adherends follow Table 4.10. The results from static analysis are marked as '-3D-ISO', which represent 3-D models with equivalent isotropic properties. The finite element data and test data curves are plotted in Figures 5.6 to 5.11.

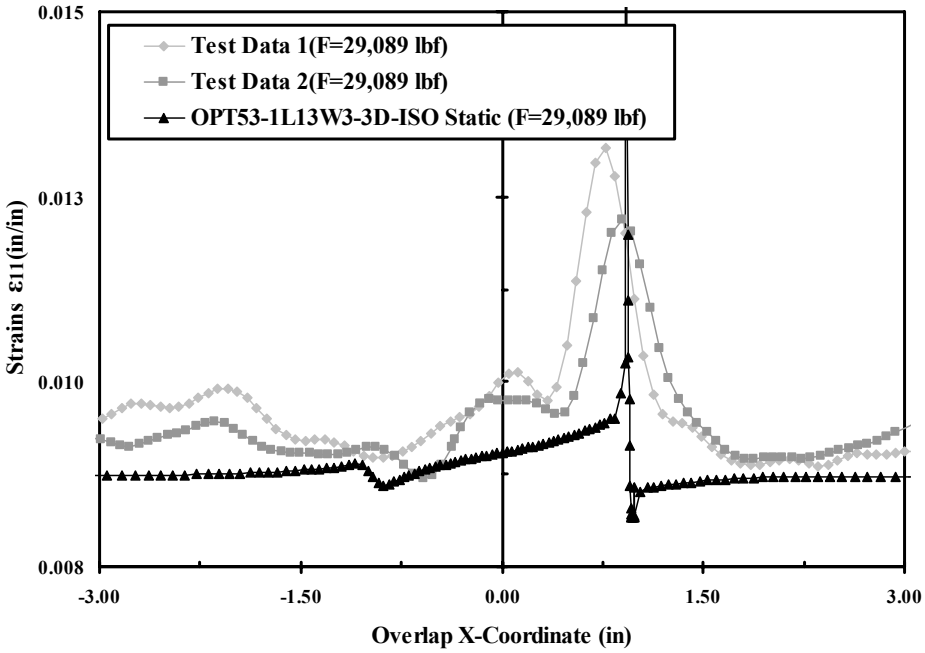

Figure 5.6. Longitudinal surface strain comparison of test data and OPT53-1 SCF 3-D static full-scale model.

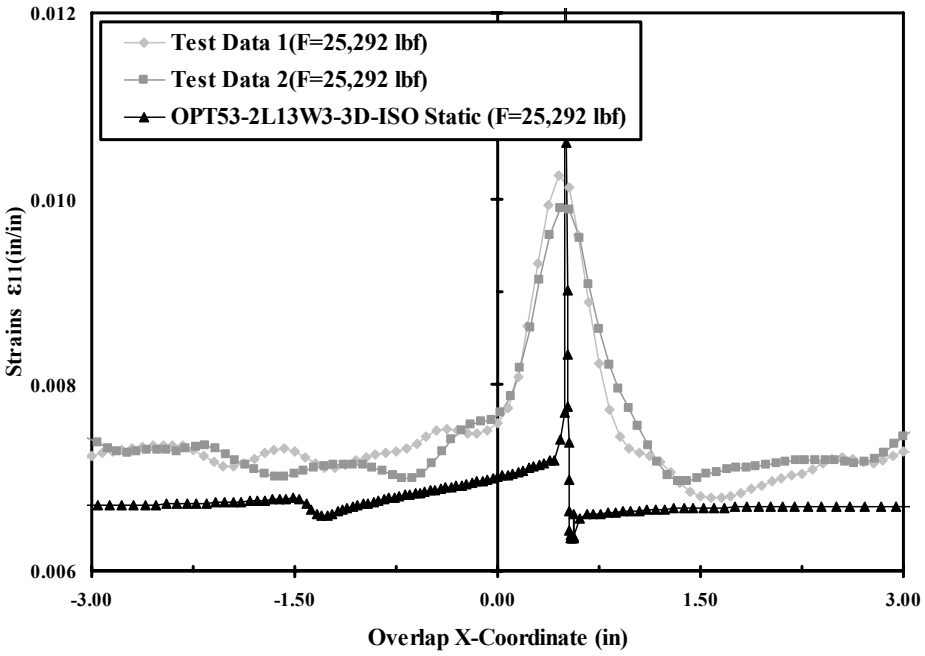

Figure 5.7. Longitudinal surface strain comparison of test data and OPT53-2 SCF 3-D static full-scale model.

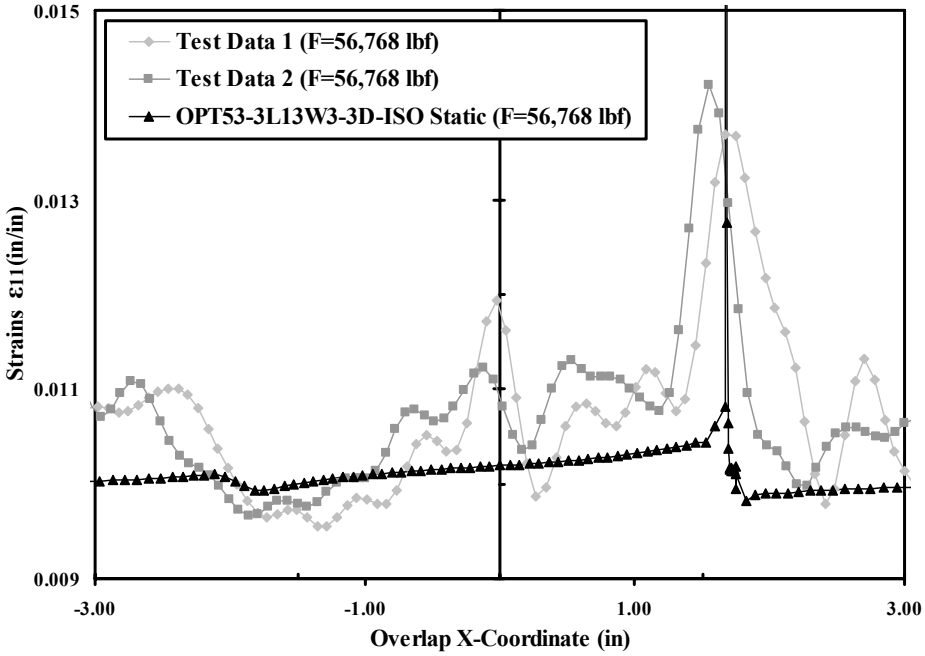

Figure 5.8. Longitudinal surface strain comparison of test data and OPT53-3 SCF 3-D static full-scale model.

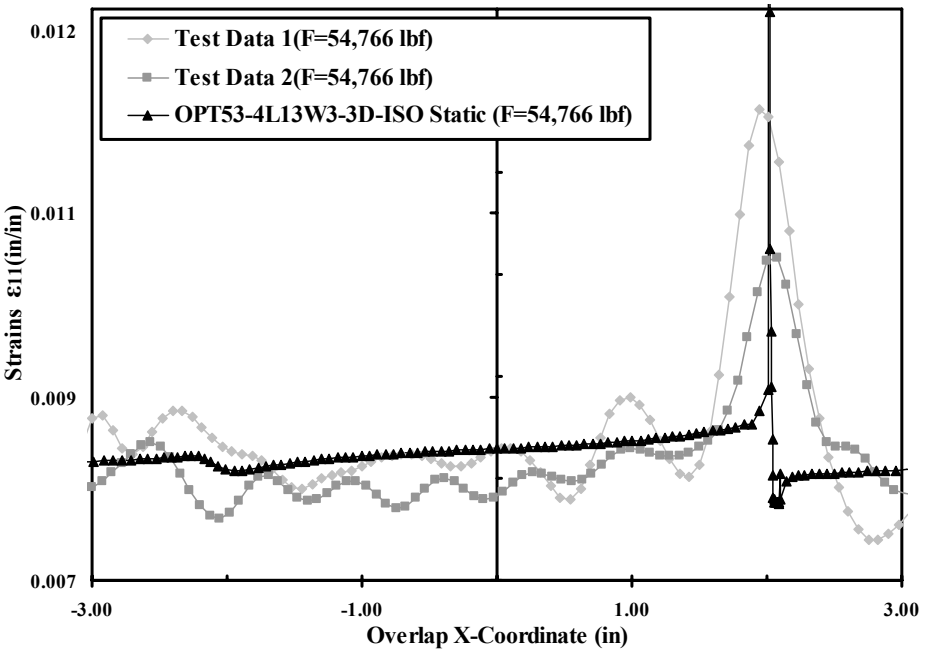

Figure 5.9. Longitudinal surface strain comparison of test data and OPT53-4 SCF 3-D static full-scale model.

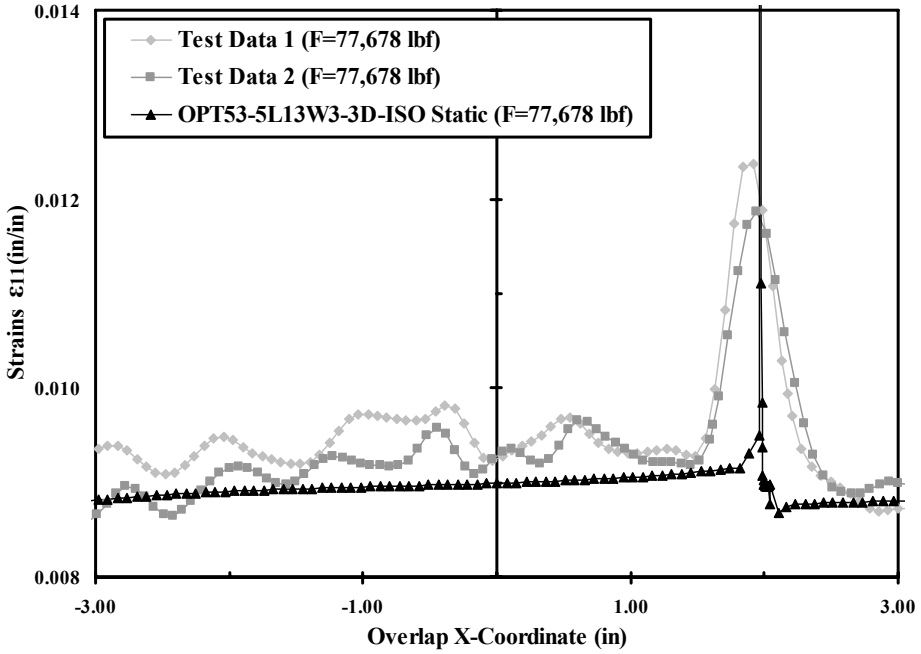

Figure 5.10. Longitudinal surface strain comparison of test data and OPT53-5 SCF 3-D static full-scale model.

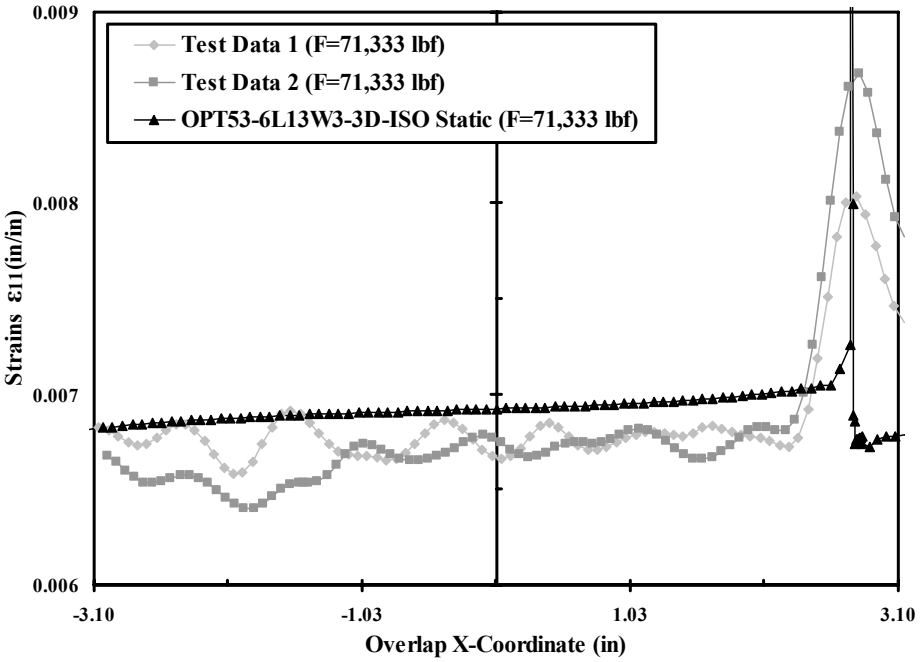

Figure 5.11. Longitudinal surface strain comparison of test data and OPT53-6 SCF 3-D static full-scale model.

b. Composite Laminate 3-D Reduced Model

Similar to the size reduction method based on the symmetry of the geometry and loading of the specimens, which were utilized in various researches [4,5,11,20,21,25,26,64], OPT53-1 and OPT53-2 3-D composite laminate models (Figure 5.1), are further reduced to one half the size (Figure 5.12) of the original reduced models (dimensions specified in Table 5.1). Based on the antisymmetry of the geometry about the geometric center of the specimen and symmetric loading conditions for large-sized models of OPT53-3 to OPT53-6 specimens, they are further reduced into quarter size models (as Figure 5.13) to reduce the immense number of elements and nodes so that the job can be implemented successfully.

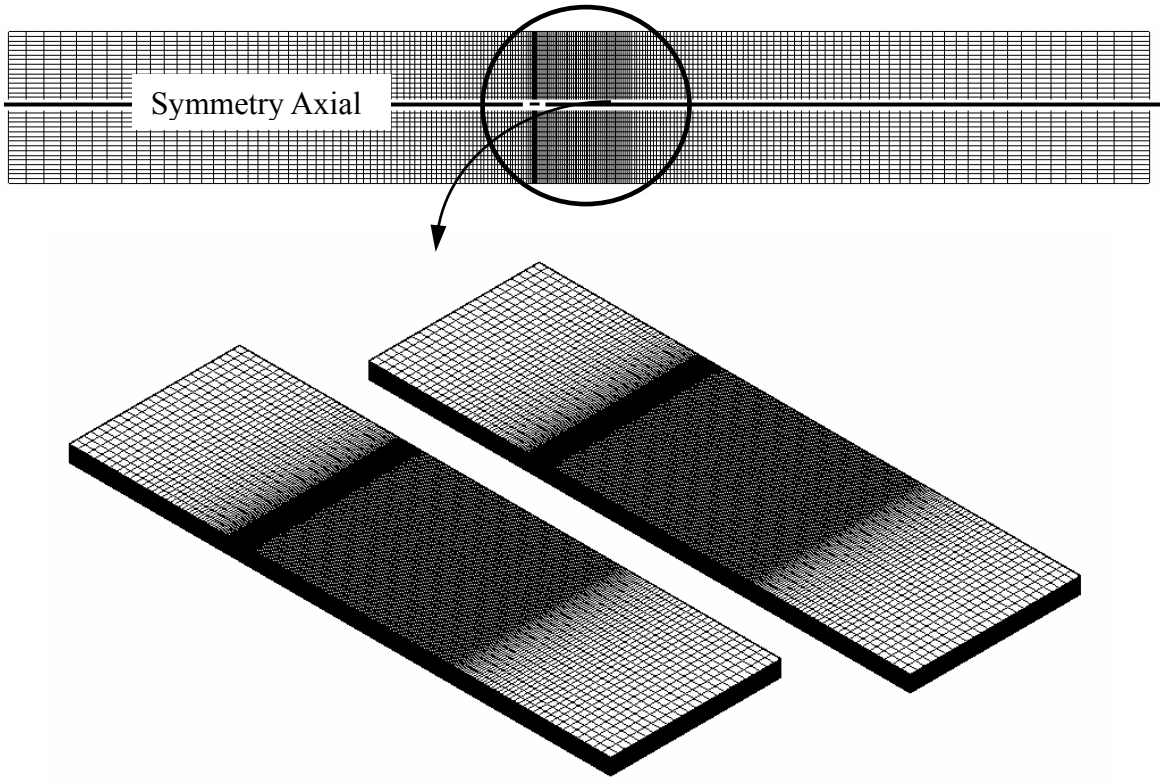

Figure 5.12. One half size OPT53 SCF reduced model.

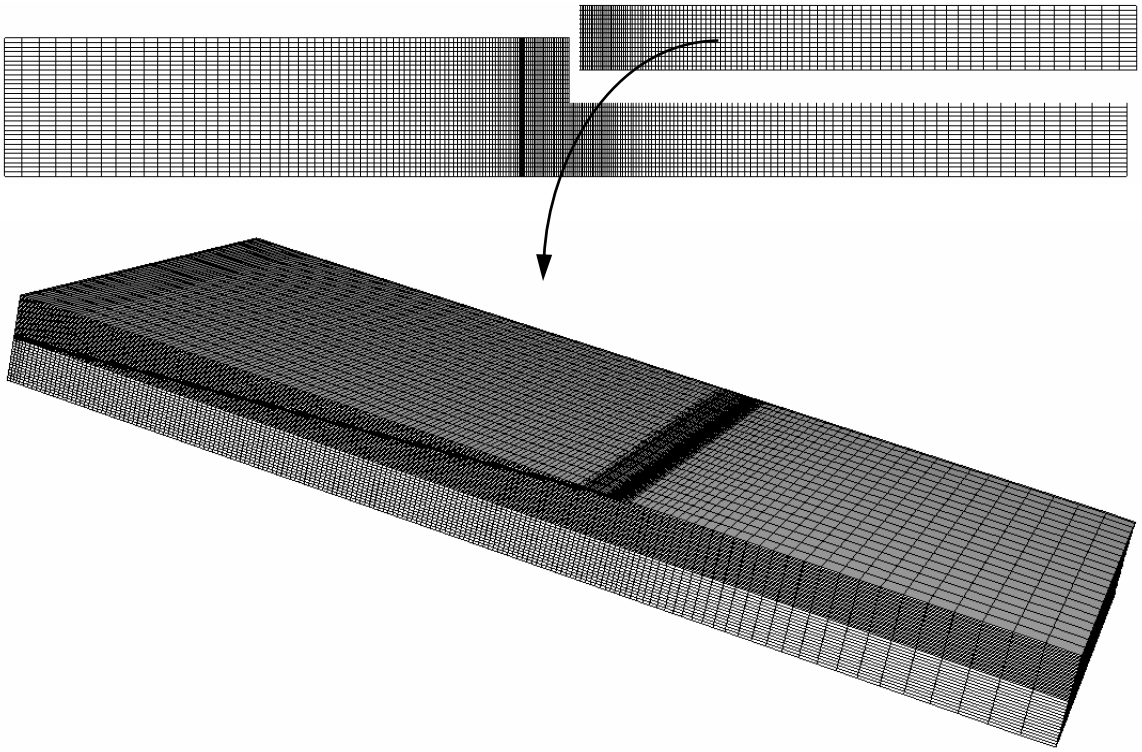

Figure 5.13. Quarter size OPT53 SCF reduced model.

The anisotropically elastic material properties of the composites follow the anisotropic matrices (section 4.3.2 $[D_{ijkl}]$ for each degree lamina). The results converted from tests and static finite element analyses are plotted together for each OPT53 composite scarf joint model in Figures 5.14 to 5.19. The static finite element results, scripted as '3D-COM-SYM' in Figures 5.14 and 5.15 for specimens OPT53-1 and OPT53-2, represent 3-D symmetrically half size composite model with anisotropic material properties. For specimens OPT53-3 to OPT53-6, the curves symbolized as '3D-COM-QUA' (in Figures 5.16 to 5.19) stand for quarter size composite models with anisotropic material properties.

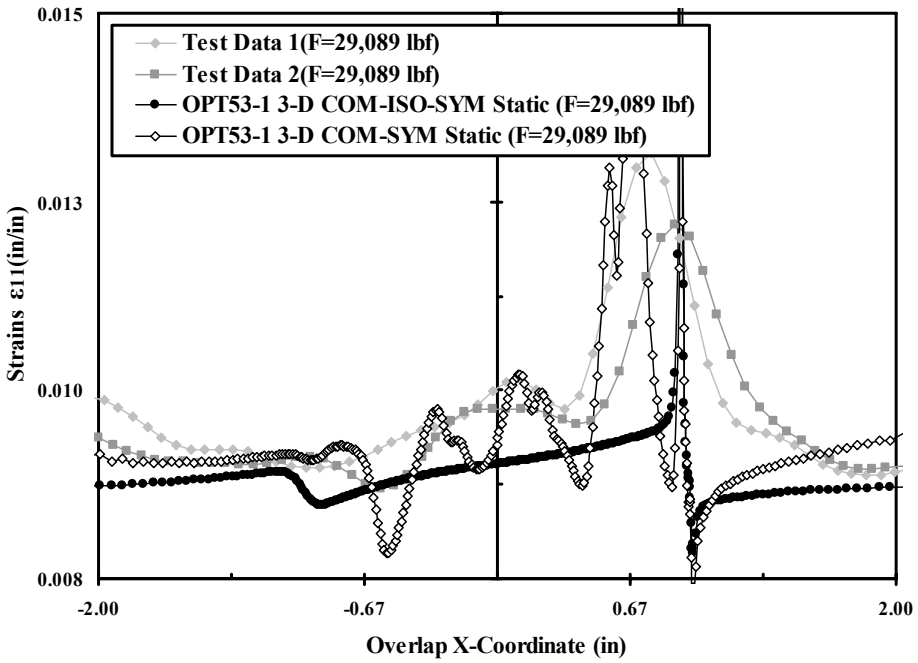

Figure 5.14a. Longitudinal surface strain comparison of test data and half size OPT53-1 3-D static-reduced model (anisotropic and isotropic properties).

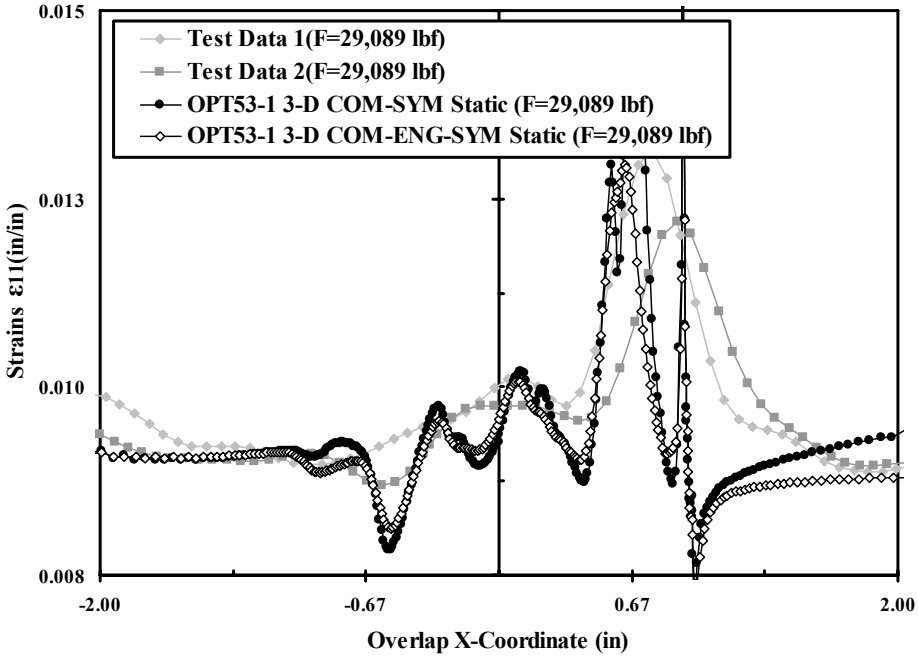

Figure 5.14b. Longitudinal surface strain comparison of test data and half size OPT53-1 3-D static-reduced model (anisotropic and engineering constant properties).

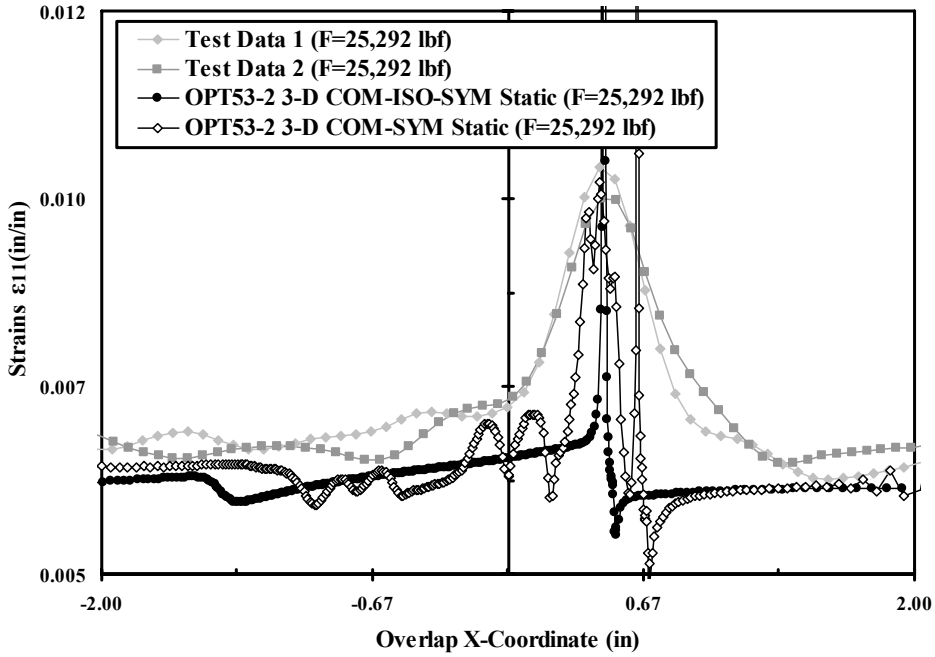

Figure 5.15a. Longitudinal surface strain comparison of test data and half size OPT53-2 3-D static-reduced model (anisotropic and isotropic properties).

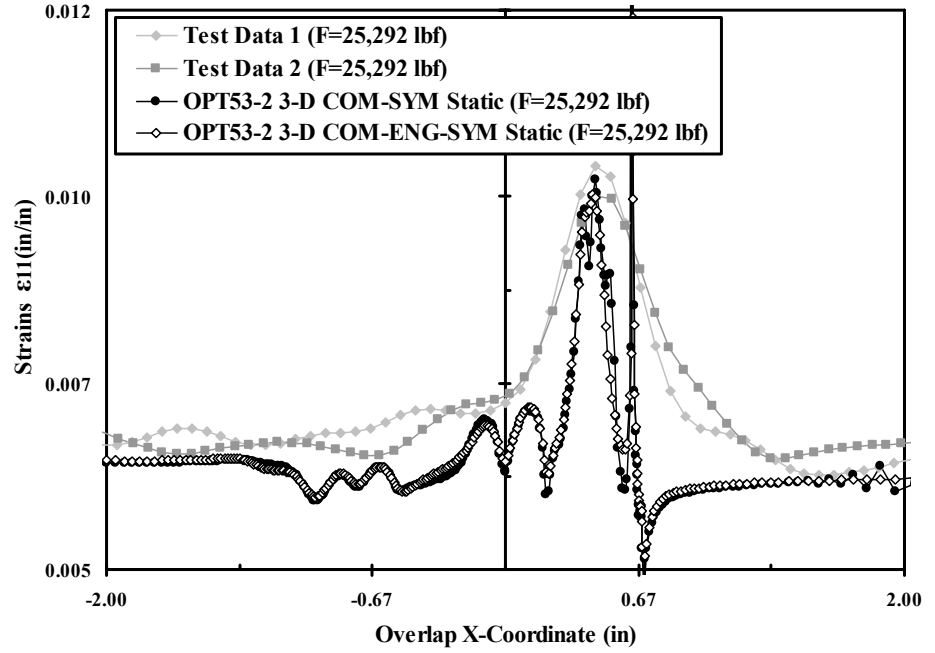

Figure 5.15b. Longitudinal surface strain comparison of test data and half size OPT53-2 3-D static-reduced model (anisotropic and engineering constant properties).

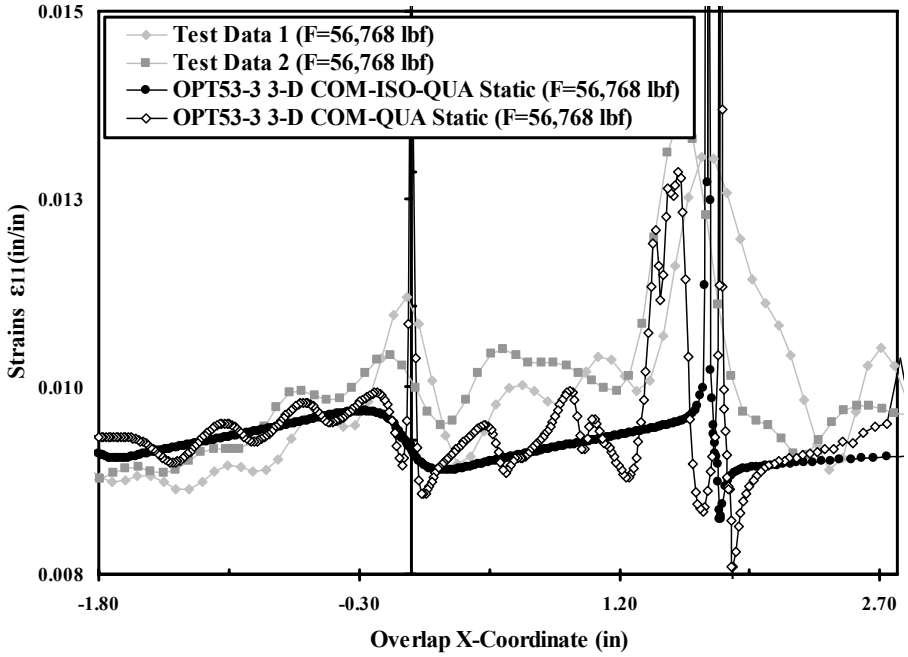

Figure 5.16a. Longitudinal surface strain comparison of test data and quarter size OPT53-3 3-D static-reduced model (anisotropic and isotropic properties).

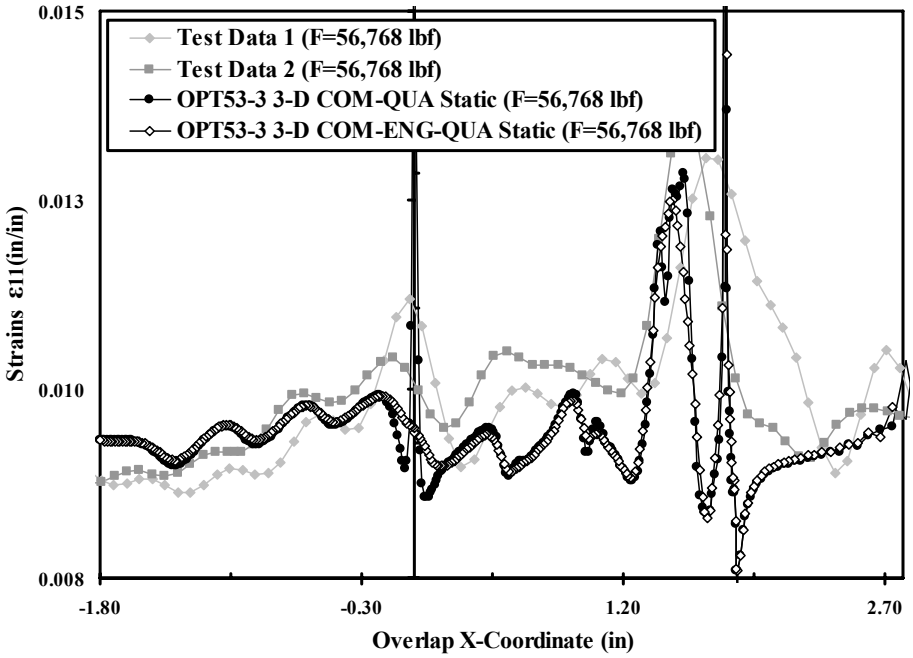

Figure 5.16b. Longitudinal surface strain comparison of test data and quarter size OPT53-3 3-D static-reduced model (anisotropic and engineering constant properties).

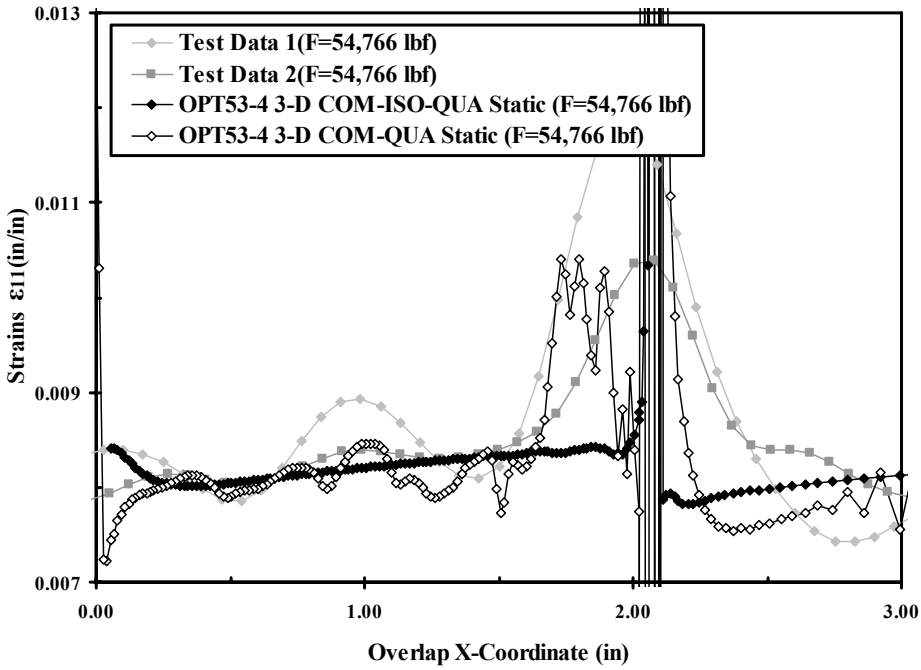

Figure 5.17a. Longitudinal surface strain comparison of test data and quarter size OPT53-4 3-D static-reduced model (anisotropic and isotropic properties).

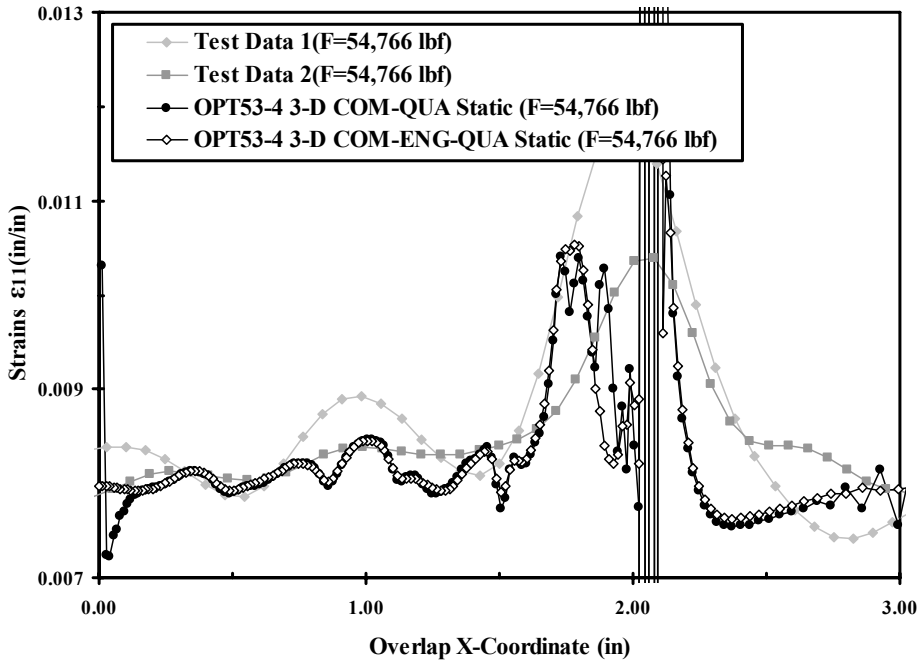

Figure 5.17b. Longitudinal surface strain comparison of test data and quarter size OPT53-4 3-D static-reduced model (anisotropic and engineering constant properties).

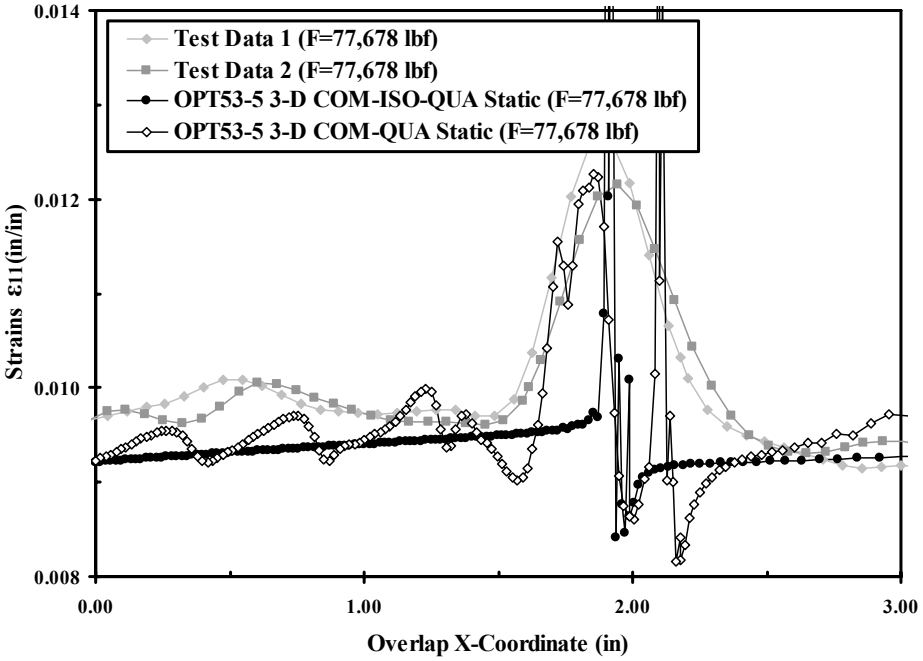

Figure 5.18a. Longitudinal surface strain comparison of test data and quarter size OPT53-5 3-D static-reduced model (anisotropic and isotropic properties).

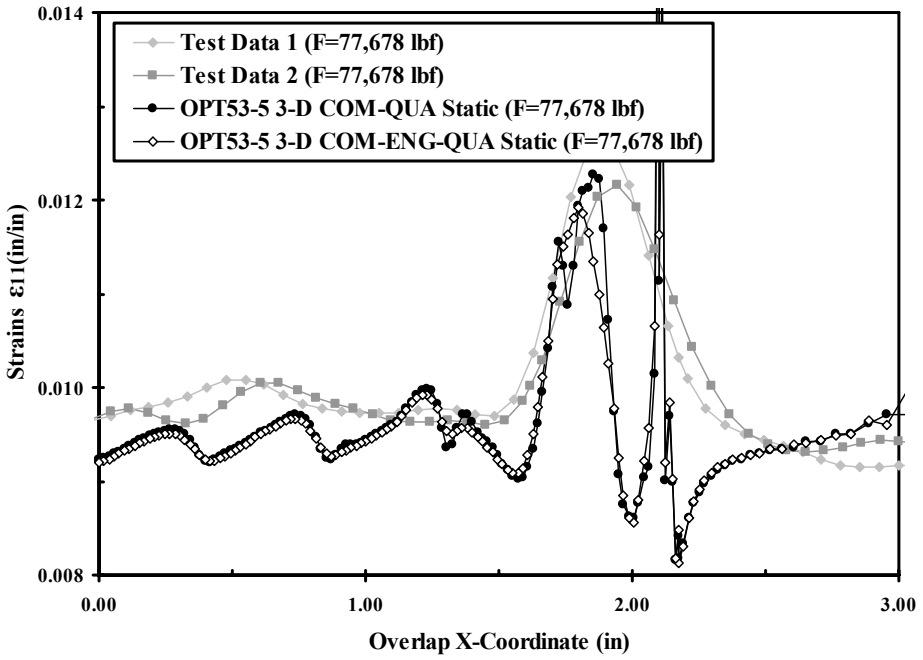

Figure 5.18b. Longitudinal surface strain comparison of test data and quarter size OPT53-5 3-D static-reduced model (anisotropic and engineering constant properties).

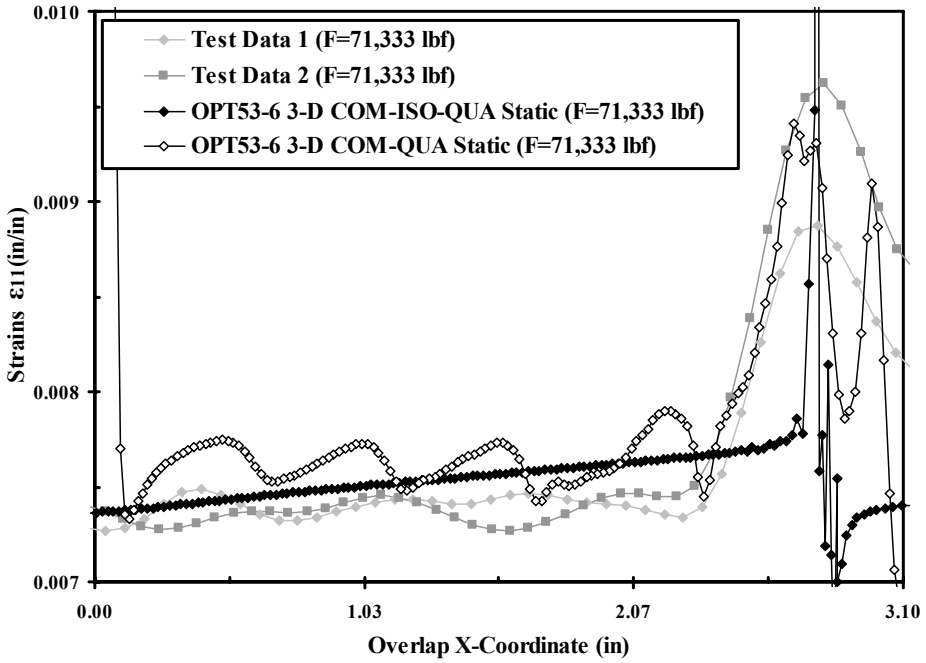

Figure 5.19a. Longitudinal surface strain comparison of test data and quarter size OPT53-6 3-D static-reduced model (anisotropic and isotropic properties).

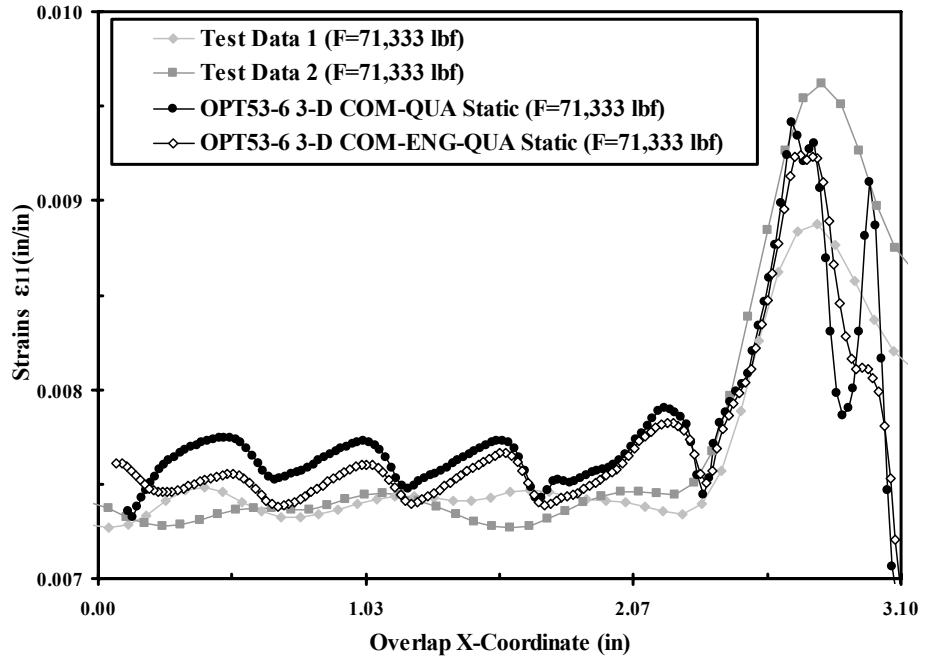

Figure 5.19b. Longitudinal surface strain comparison of test data and quarter size OPT53-6 3-D static-reduced model (anisotropic and engineering constant properties).

c. Composite Laminate 2-D Reduced Model

For 2-D plane strain models, the surface longitudinal strains (ε_{11}) are extracted from the nodes on the top surface. In the results shown in Figures 5.20 to 5.25, 'SCF-ANISO' and 'STP-ANISO' denote a scarf joint and a stepped joint with the adherends of anisotropic material properties, respectively. '-ENG' accounts for the orthotropic material model using the engineering constants for their adherends.

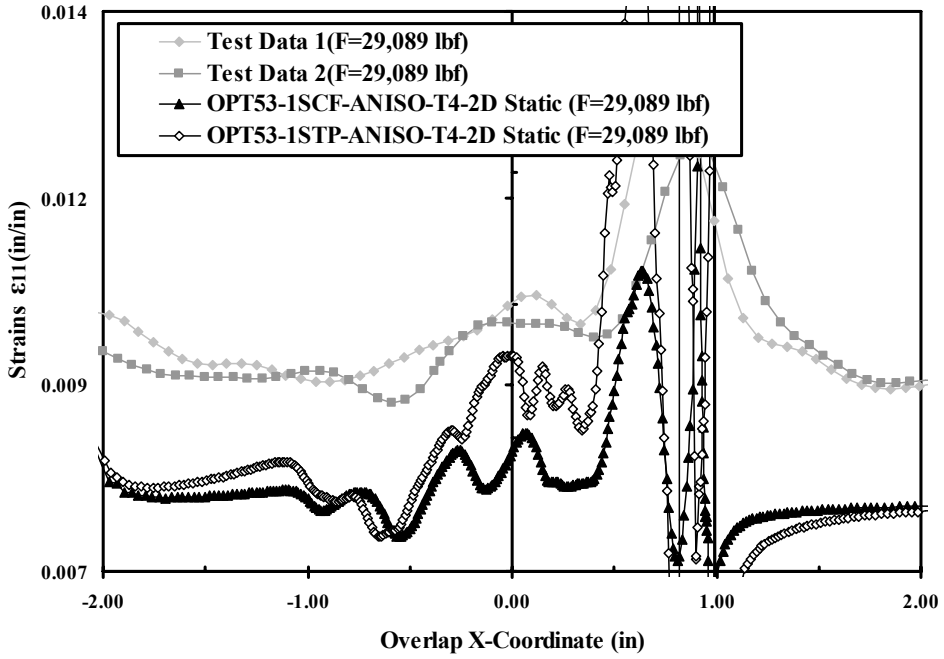

Figure 5.20a. Longitudinal surface strain comparison of test data and OPT53-1 2-D static-reduced model (anisotropic material properties).

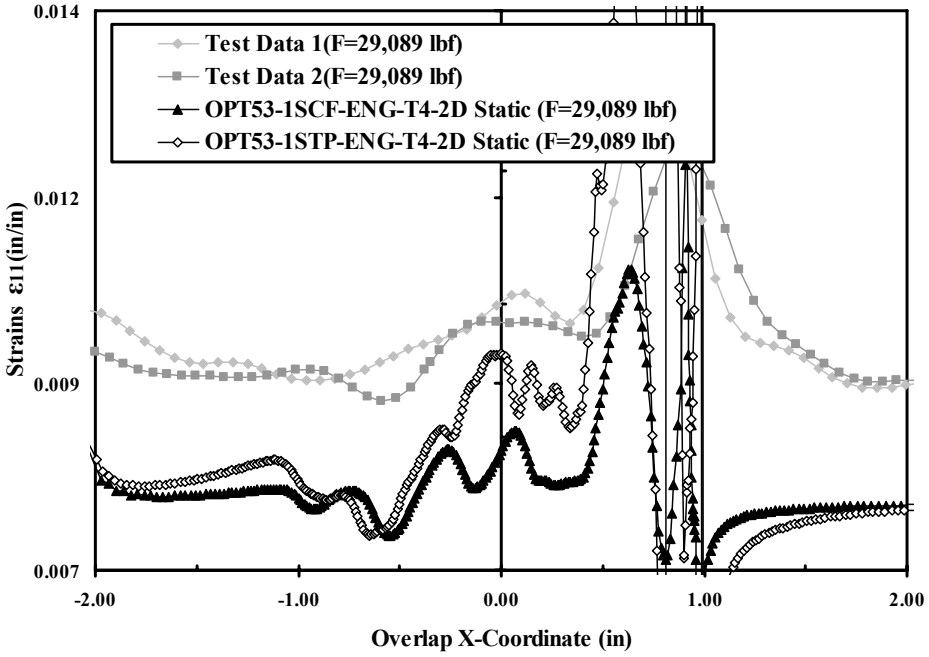

Figure 5.20b. Longitudinal surface strain comparison of test data and OPT53-1 2-D static reduced-model (engineering constant material properties).

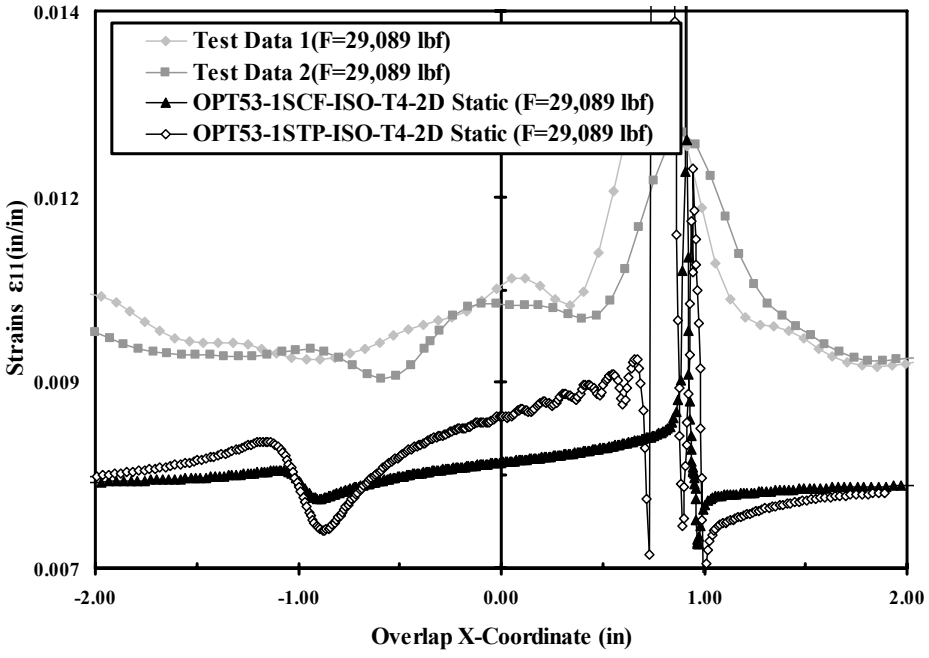

Figure 5.20c. Longitudinal surface strain comparison of test data and OPT53-1 2-D static reduced-model (isotropic material properties).

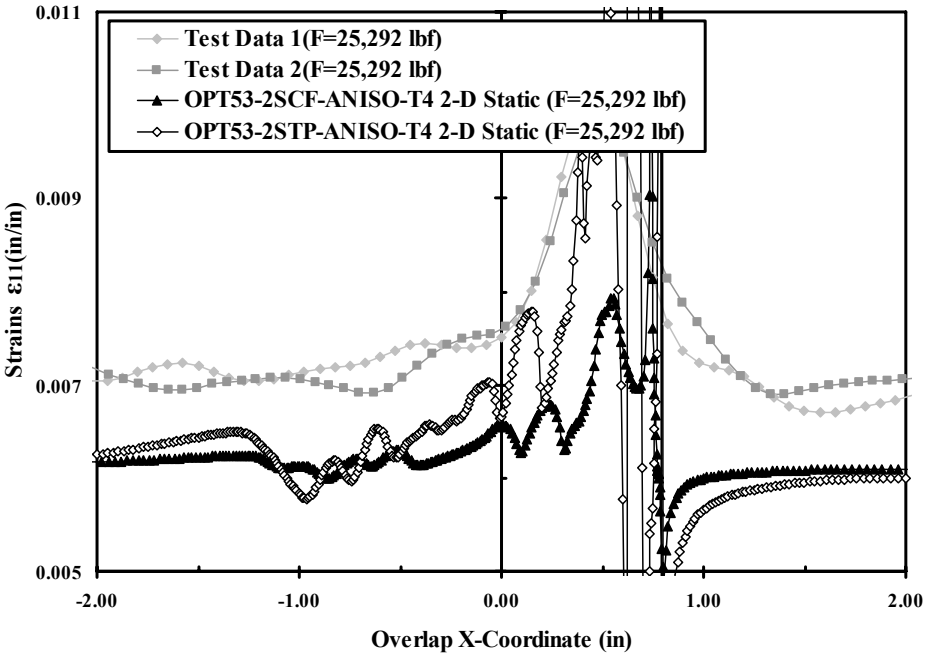

Figure 5.21a. Longitudinal surface strain comparison of test data and OPT53-2 2-D static reduced-model (anisotropic material properties).

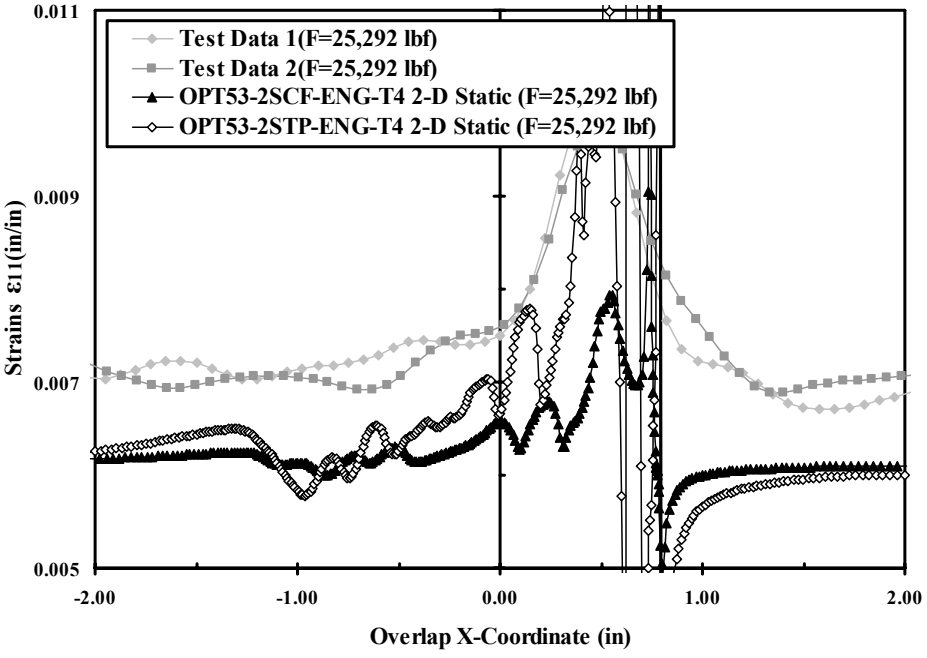

Figure 5.21b. Longitudinal surface strain comparison of test data and OPT53-2 2-D static reduced-model (engineering constant material properties).

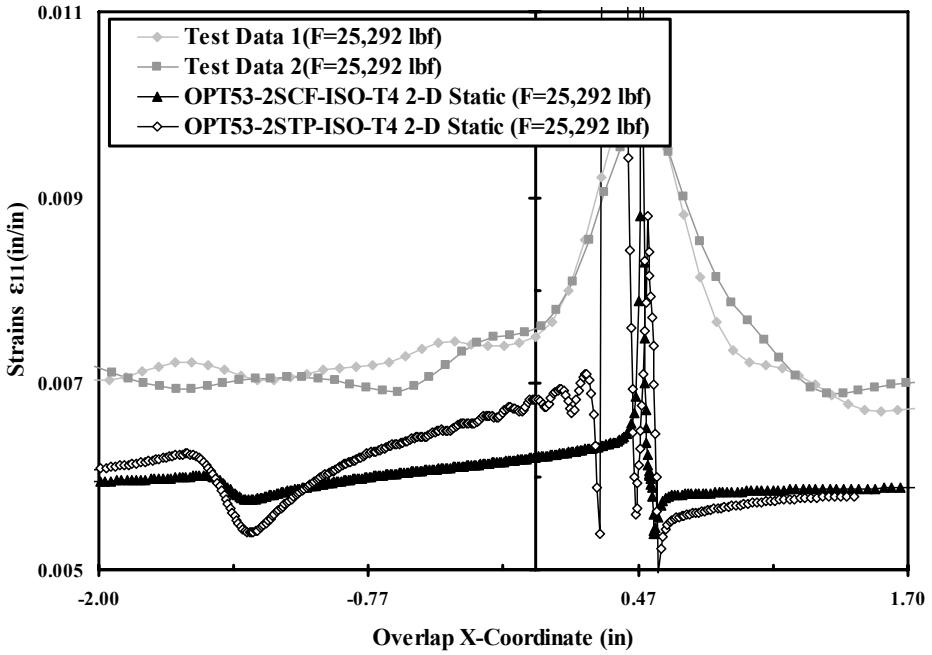

Figure 5.21c. Longitudinal surface strain comparison of test data and OPT53-2 2-D static-reduced model (isotropic material properties).

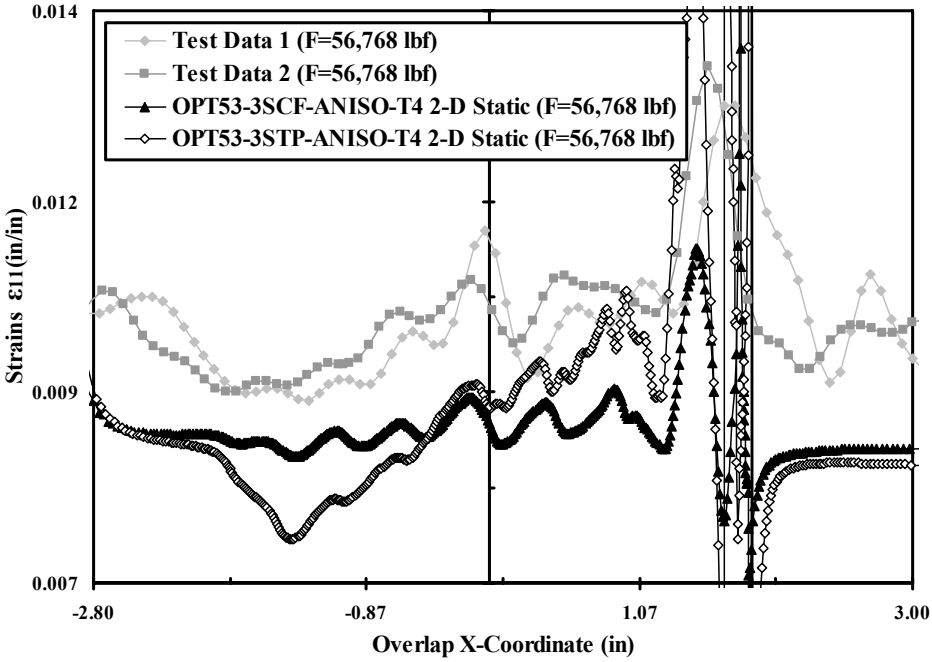

Figure 5.22a. Longitudinal surface strain comparison of test data and OPT53-3 2-D static-reduced model (anisotropic material properties).

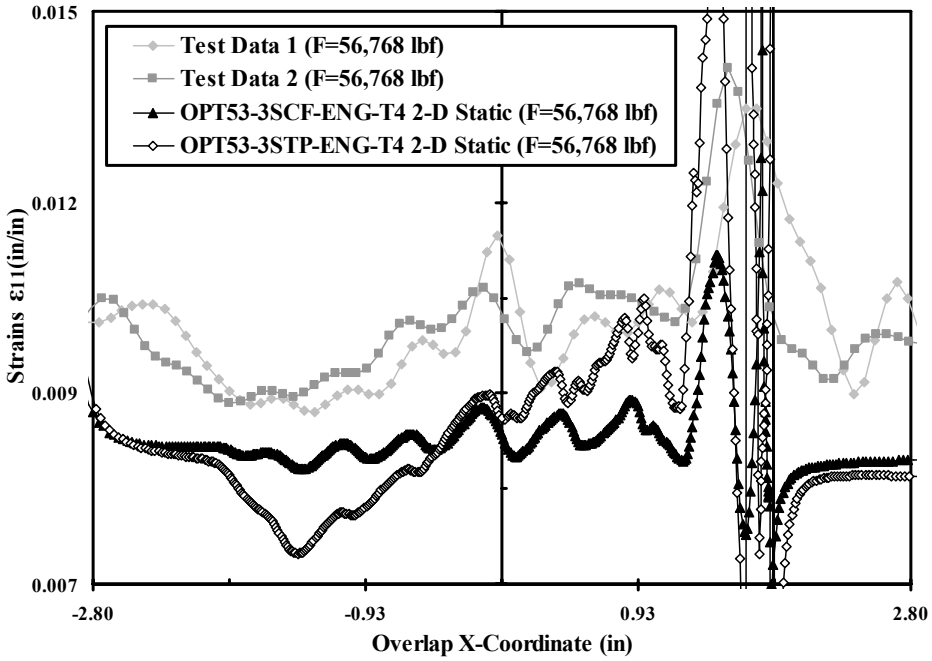

Figure 5.22b. Longitudinal surface strain comparison of test data and OPT53-3 2-D static-reduced model (engineering constant material properties).

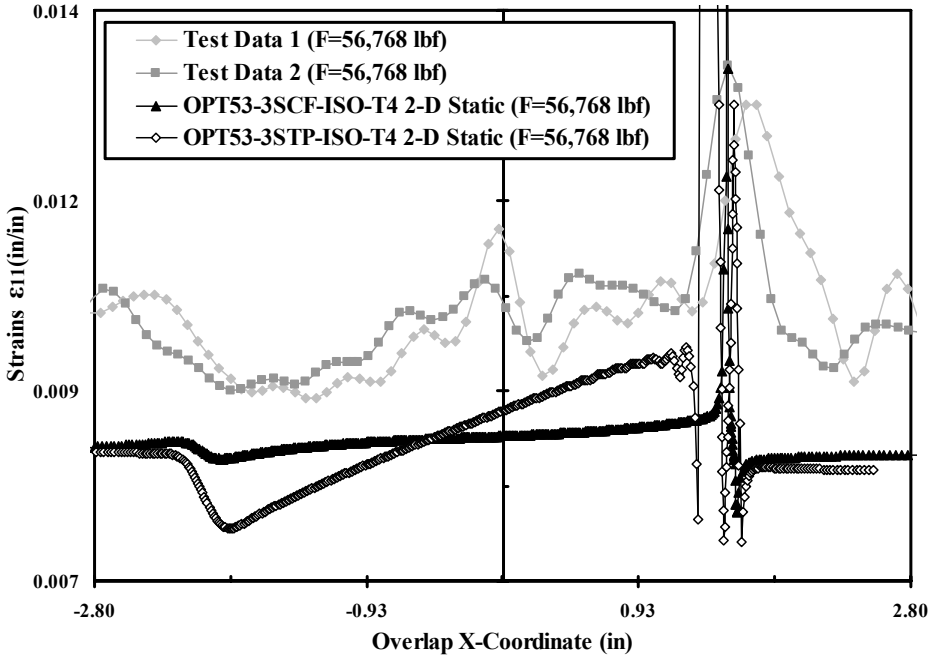

Figure 5.22c. Longitudinal surface strain comparison of test data and OPT53-3 2-D static-reduced model (isotropic material properties).

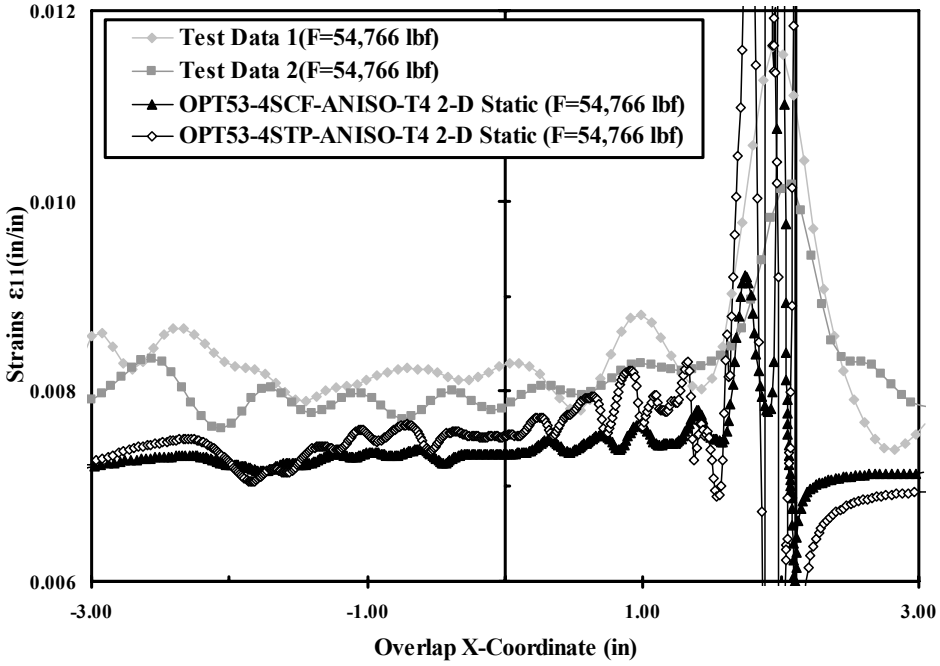

Figure 5.23a. Longitudinal surface strain comparison of test data and OPT53-4 2-D static-reduced model (anisotropic material properties).

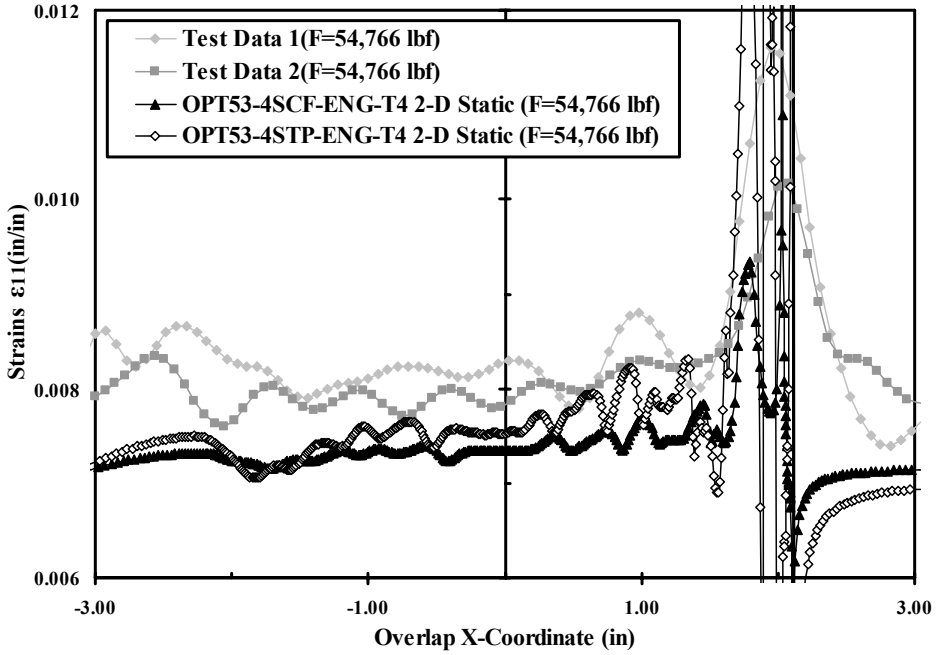

Figure 5.23b. Longitudinal surface strain comparison of test data and OPT53-4 2-D static-reduced model (engineering constant material properties).

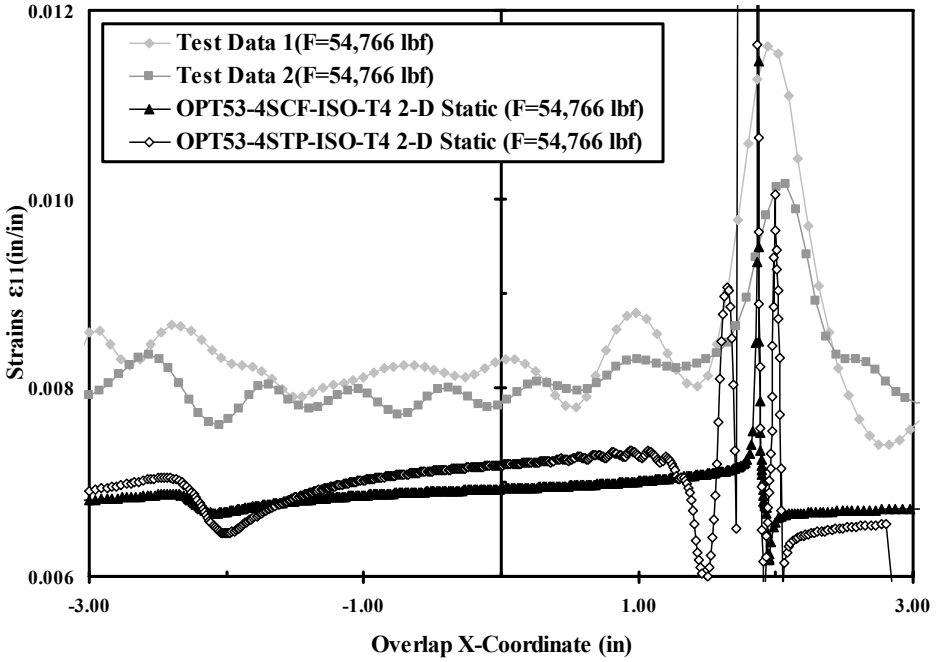

Figure 5.23c. Longitudinal surface strain comparison of test data and OPT53-4 2-D static-reduced model (isotropic material properties).

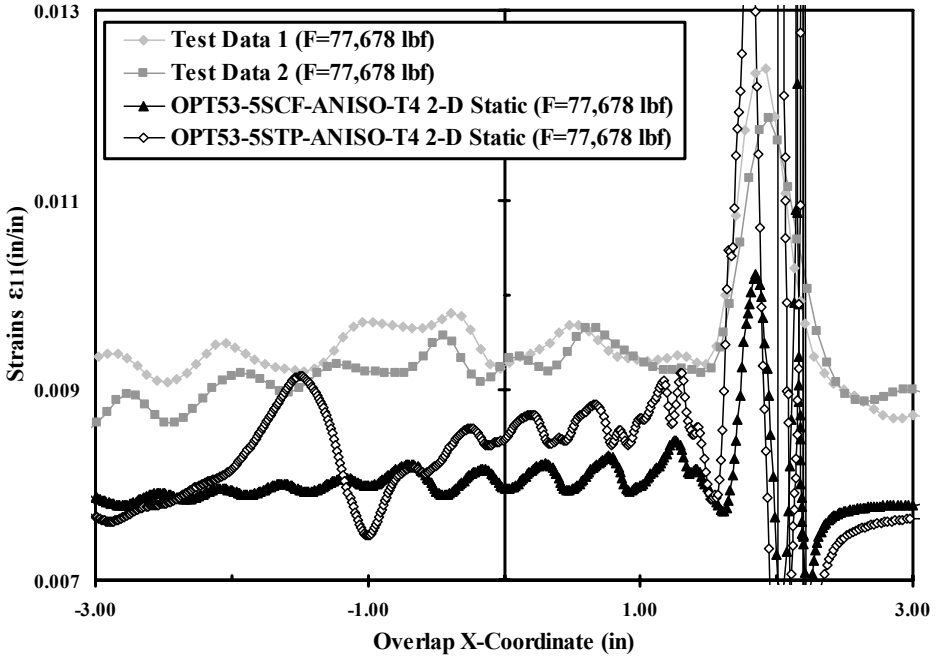

Figure 5.24a. Longitudinal surface strain comparison of test data and OPT53-5 2-D static-reduced model (anisotropic material properties).

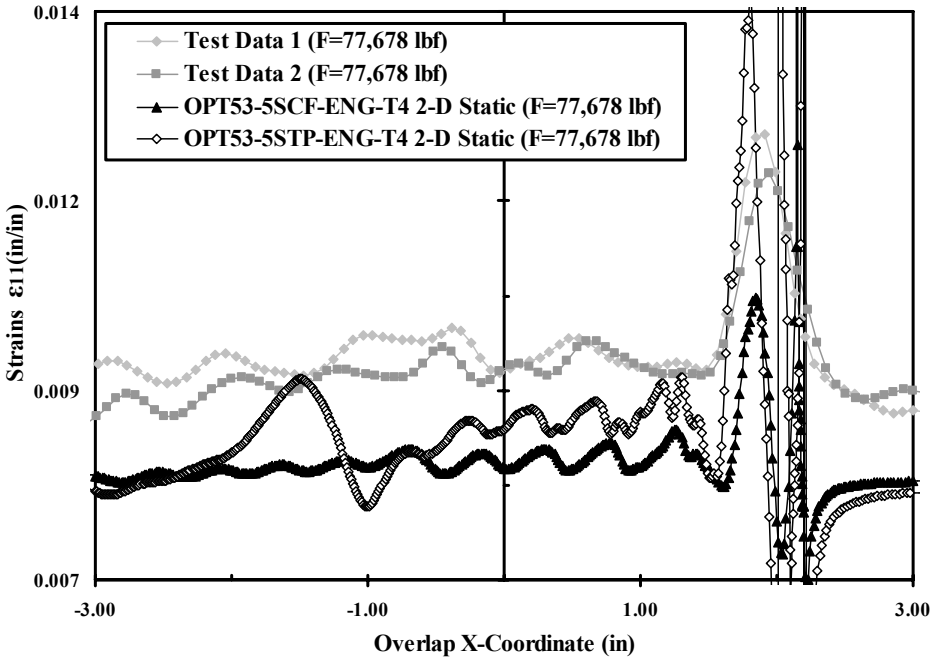

Figure 5.24b. Longitudinal surface strain comparison of test data and OPT53-5 2-D static-reduced model (engineering constant material properties).

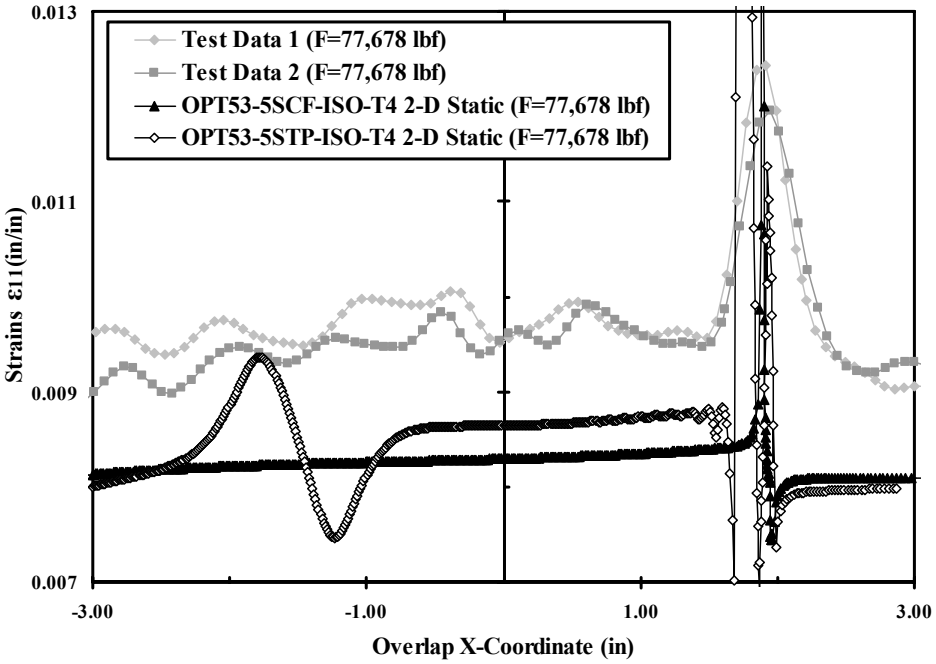

Figure 5.24c. Longitudinal surface strain comparison of test data and OPT53-5 2-D static-reduced model (isotropic material properties).

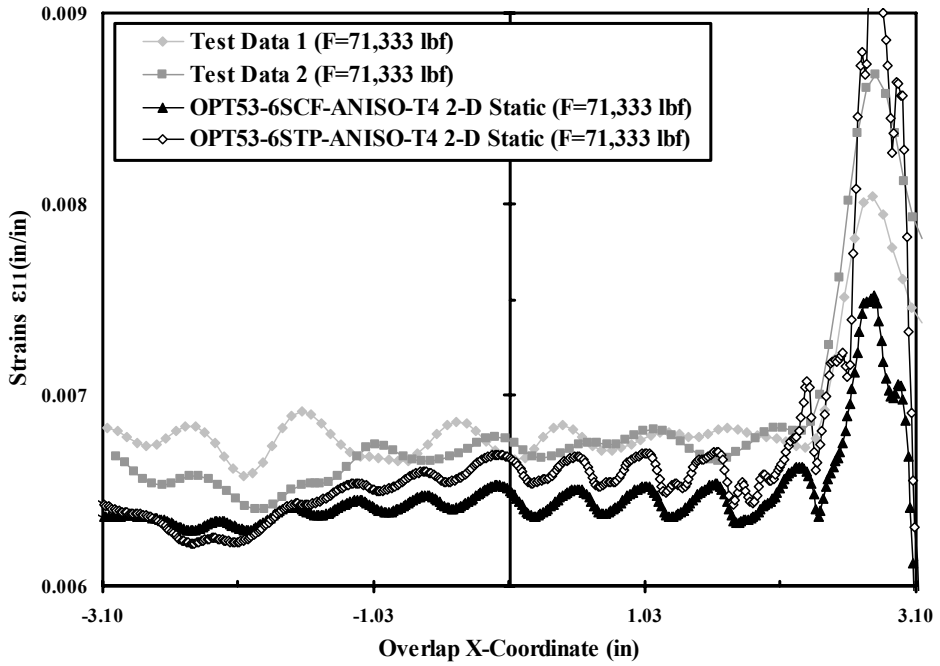

Figure 5.25a. Longitudinal surface strain comparison of test data and OPT53-6 2-D static-reduced model (anisotropic material properties).

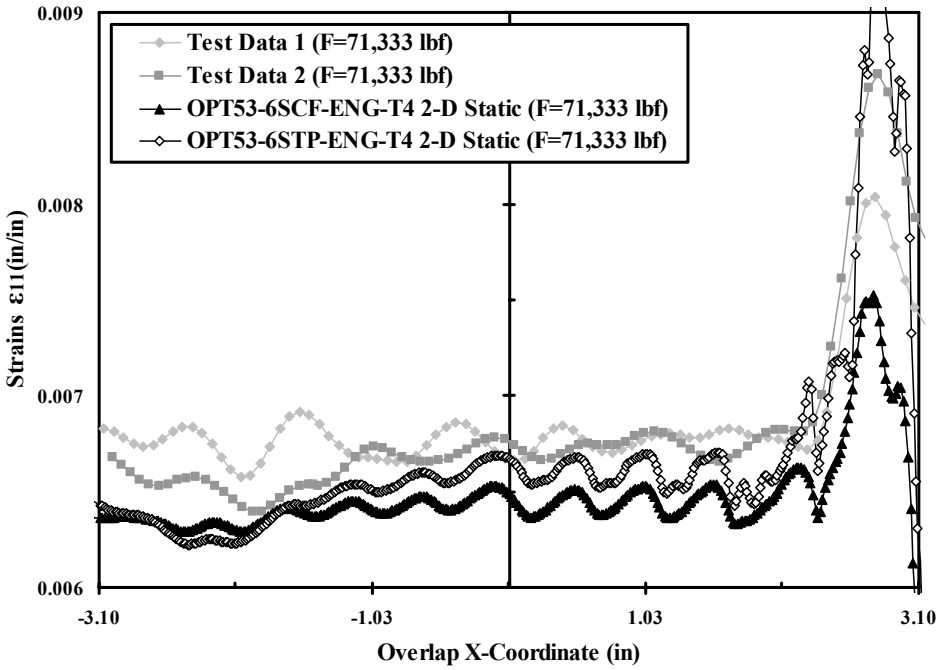

Figure 5.25b. Longitudinal surface strain comparison of test data and OPT53-6 2-D static-reduced model (engineering constant material properties).

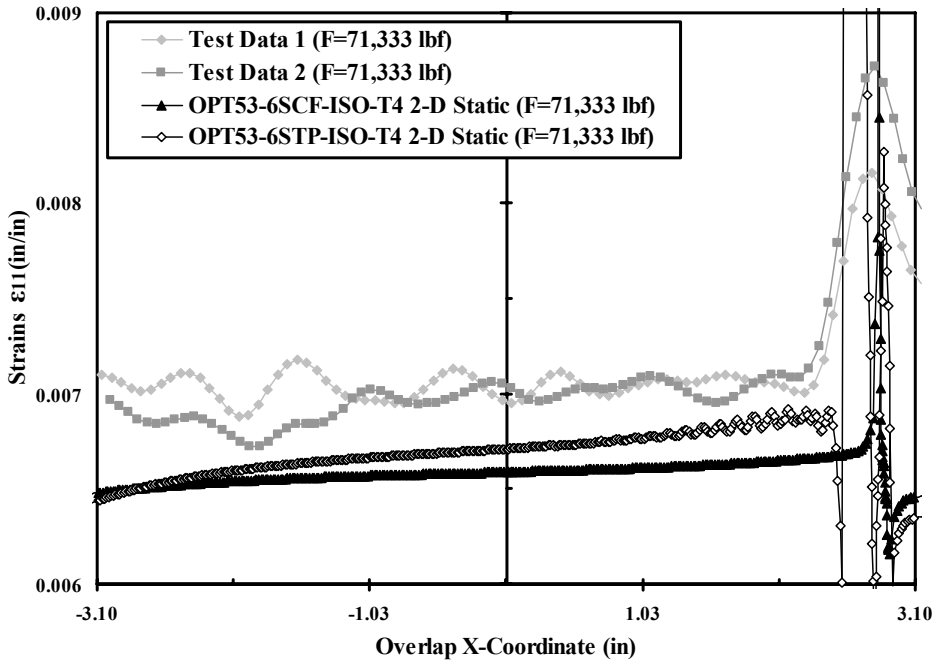

Figure 5.25c. Longitudinal surface strain comparison of test data and OPT53-6 2-D static-reduced model (isotropic material properties).

5.1.2 Comparison and Observation of Standard/Static Finite Element Analysis Results

The finite element analysis of scarf joints using Standard/static analytical model are accomplished by the 3-D models and the 2-D plane strain models based on different assumptions. After comparing all results, several conclusions can be drawn:

a. As expected, the 3-D models are superior to the 2-D plane strain models in all respects. The reduced models, 3-D half and 3-D quarter size models, produce as satisfactory results as do full-scale models. It confirms that the simplification of geometry is a valid method.

b. The 3-D models with pre-calculated anisotropic material properties produce results which correlate well with the test results. Compared with the work [22] using cross ply composite laminates in 3-D simulations, OPT53 3-D composite scarf joint results within the overlap from ABAQUS display much higher fidelity. It confirms that the

transversely isotropy (anisotropic elasticity model) assumed is correct and realistic. Compared with other elasticity models, the anisotropic (transversely isotropy) models provide the most satisfactory curve-fitting results, while the orthotropy—engineering constant models produce slightly less accurate but smoother strain curves than anisotropy. This can be explained by that the shear-shear coupling terms of ± 45 degree plies are deleted using the stacking sequence [45/-45]s, which generates less mismatch of elastic constants between of ± 45 degree plies and adjacent plies and results in smoother strain distributions.

c. As discussed in section 4.1.3, only the stacking sequences of OPT53-3 and OPT53-5 models satisfy the restrictions of quasi-isotropic elasticity model. From the 3-D finite element simulations (as shown in Figures 5.15, 5.16, and 5.18), OPT53-1, OPT53-2, and OPT53-4 models are still applicable for the quasi-isotropic elasticity model, especially OPT53-1 which is very close to quasi-isotropic stacking sequence..

d. For 3-D quasi-isotropic elasticity models, irrespective of the construction or modeling manner (ply-merged models or layer-by-layer composite laminate models for adherends), the same results are generated under the same material properties. It also implies that the irregularly fluctuating strain distributions obtained from other elasticity models (except for quasi-isotropic models) are not caused by the layer-by-layer modeling, but by the mismatch of elastic constants of various ply orientations.

e. The highly fluctuating strain distributions are mainly due to the anisotropic characteristics of the adherends, whose elastic constants vary in different orientations resulting in different load-carry capacity of each ply orientation within the adherends [18]. It is also attributable to the displacement continuity restrictions, which must be satisfied

between ply orientations in the laminates. Mismatch of moduli and Poisson's ratios in adjacent plies with different orientations should be adjusted to satisfy continuity and equilibrium restrictions. Without existence of any fracture and crack, the displacement filed must be continuous in the sense that the deformation becomes piece-wise smooth. It can be confirmed by the smooth strain distributions yielded from the composite models using quasi-isotropic materials without non-homogeneity nature, i.e., no mismatch of moduli and Poisson's ratios.

f. Compared with experimental results, the numerical results tend to display extreme strain values near the taper tip. Singularity occurs in this area with steep geometry change, which results in high stress gradient. It can be shown by the plastic strain or effective plastic strains distributions from ABAQUS contours. This tapered part, especially at scarf tip, is difficult to modify and still contains singularity problems even though the stepped feature has been applied. Furthermore, too many transition elements such as triangular elements (2-D) or hexagonal (3-D) fully integrated brick elements exist in this area and those elements are so rigid that they cause 'shear locking' which produces erroneous solutions. Under these considerations, the extreme values near the taper tip should be neglected.

g. Even though the load is applied in-plane only (along the *x*-direction) and the stacking sequence is designed symmetrically, the loading pattern twists to eccentric loading owing to the geometry feature—antisymmetric taper-taper. The deformed specimen shows that there exists bending effects, which are significantly magnified nearby the overlap, and the bending effects are minimized around the constrained (fixed) and the loading end of specimens.

h. For 3-D orthotropic elasticity models using the engineering constants, the finite element results agree with the results from anisotropic (transversely isotropy) models completely. It speaks that the engineering constants pre-calculated for all ply orientations are realistic. The most important issue is that the engineering constants of a ±45 degree lamina derived from the stacking sequence [+45/-45]s or [-45/+45]s should be used. In other words, the elasticity of laminates can only be described in terms of the engineering constants when utilizing a balanced and symmetric stacking sequence.

i. For 3-D anisotropic models, the stiffness constants derived, based on the assumption v_{12}= v_{13}= v_{23}=0.317, provide almost the same results as those from assumption v_{23}=0.444. It suggests that, without test data of v_{23}, the premise v_{12}= v_{13}= v_{23} is valid. However, for unidirectional fiber-reinforced composites, the assumption G_{12}= G_{13}= G_{23} is inappropriate due to its physical phenomenon.

j. Regarding the simplification or size reduction of the 3-D model, in addition to the reduced model used in this study, some other options, such as lumping of layers [62,63] and change of the 3-D solid element to 2-D shell element can be used. The method of the lumping of layers as discussed in other researches [62,63] can be treated as a special case under consideration of the material properties v_{12}= v_{13}= v_{23} and G_{12}= G_{13}= G_{23}. Furthermore, if the adjacent layers are the same fiber orientation (could have ± angle as [+θ/-θ]s angle ply), or the lumped layers can generate a balanced and symmetric stacking sequence equivalent to orthotropic materials, and the lumped layers should be far from the critical regions interested (which contain high gradients of stress/strain states or geometry change); then, the use of lumping could be applicable. However, the amount of the layer which can be lumped depends on the results of the simulation.

k. For OPT53 2-D plane strain models, where the static finite element simulations have more than a 15% deviation from the test results, except for OPT53-6. The implication is that the interlaminar or out-of-plane stress/strain state is significant and must not be neglected. Generally, 2-D plane stress or plane strain models provide lower or upper bound of the solutions compared with 3-D models. In this study, the 2-D static plane strain model provides the lower bound of the strain distributions within the overlap. Furthermore, the 2-D stepped joint models give much agreeable results than 2-D scarf joint models, which means that the error contributed by element shape and type in composite scarf joint is significant (explained in remark f).

5.2 Explicit/Dynamic Analysis

Based on the observation of failed specimens, the blue color film adhesive was intact on both bonded interfaces within the tapered portion of each torn apart specimen. It suggests that the failure of the composite joint is basically adhesive failure mode—cohesive fracture in shear [27,52] as shown in Figure 5.26.

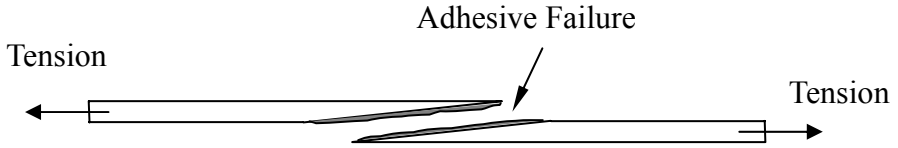

Figure 5.26. Adhesive failure mode of cohesive fracture-shear[27].

The failure mechanism-dynamic shear failure is defined only in the adhesive for each specimen. The failure criterion and plastic properties required for the Metlbond F1515-3 adhesive film follow the results from the analysis of ASTM D5656 using the classical metal plasticity model. All bonded interfaces (matrix/resin to fiber, ply to ply, and adherend to adhesive) are assumed to be perfectly bonded and no voids or cracks exist within OPT53

composite scarf joint models. Once the adhesive fails, the ultimate load and the surface longitudinal strains (ε_{11}) recorded right at failure are read from historical output files at the same time. Table 5.4 shows the numerical data from 2-D dynamic anisotropic reduced models under Explicit/dynamic analysis are compared with test data. The comparisons focus on the overlap portion along the loading direction only. The appropriate artificial density and damping factor are applied and all processes repeated are similar to ASTM D5656 simulation.

TABLE 5.4

ULTIMATE LOAD COMPARISONS BETWEEN TEST DATA
AND 2-D ANISOTROPIC DYNAMIC FINITE ELEMENT ANALYSIS DATA

Adhesive Failure (Adhesive Shear Failure = 0.25)			
OPT53 2D Models	**Test Data**	**ABAQUS Data**	**Deviation %**
OPT53-1STP-ANISO	29,089.3 lbf	35,813.5 lbf	23.1
OPT53-1SCF-ANISO		36,845.9 lbf	26.7
OPT53-2STP-ANISO	25,292.0 lbf	35,760.5 lbf	41.4
OPT53-2SCF-ANISO		42,773.3 lbf	69.1
OPT53-3STP-ANISO	56,768.3 lbf	68,322.8 lbf	20.4
OPT53-3SCF-ANISO		62,276.7 lbf	9.7
OPT53-4STP-ANISO	54,765.6 lbf	65,975.2 lbf	20.5
OPT53-4SCF-ANISO		80,956.1 lbf	47.8
OPT53-5STP-ANISO	77,678.3 lbf	82,294.9 lbf	5.9
OPT53-5SCF-ANISO		82,423.3 lbf	8.5
OPT53-6STP-ANISO	71,333.3 lbf	109,229.0 lbf	53.1
OPT53-6SCF-ANISO		92,867.2 lbf	30.2

Evidently, all the ultimate loads are substantially over-estimated. The surface strains are not necessary to plot and compare with test data. The specimens of composite scarf joints need to be examined microscopically to inspect 90-degree or 45-degree plies whether they failed at the same time or earlier than the complete failure of the adhesive. In fact, the fracture or failure happens so instantaneous that it is difficult to determine whether the failure initiated from the composite or the adhesive. In addition, the finite element analysis should be investigated and any other possible failure mode should be taken into account to explain this over-estimation.

5.2.1 90-Degree Ply Failure

Due to the incorrect dynamic simulations, all the failed OPT53 specimens need to be scrutinized microscopically. From the lateral free surfaces of the real specimens and the interfaces of the adherend and the adhesive as sketched in Figure 5.28), the failure or delamination of mostly 90-dgree plies is observed.

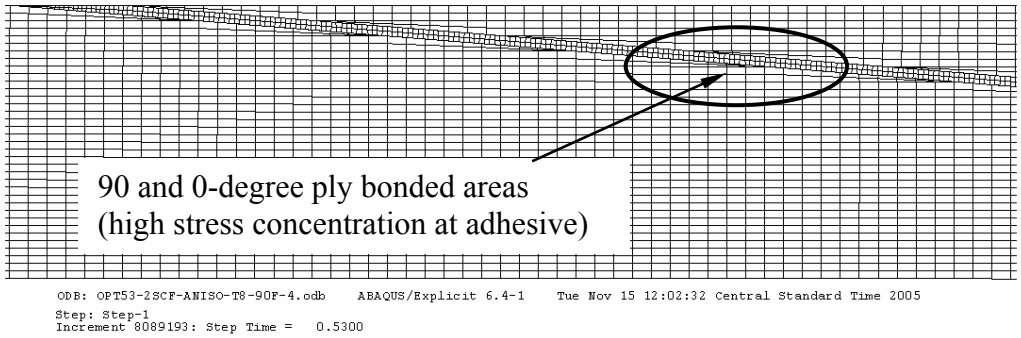

Figure 5.27. Stress concentrations within adhesive
(OPT53-2 2D anisotropic dynamic model).

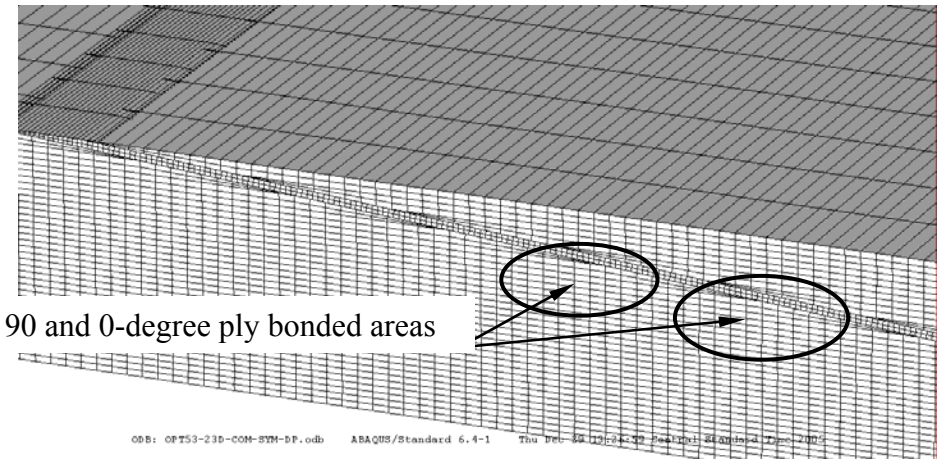

Figure 5.28. 90 and 0-dgree ply bonded areas within free edge parts of the overlap
(OPT53-2 3D anisotropic static model).

As a result, since the failure of the entire adhesive cannot reduce the over-estimation of reaction force, another failure mechanism-the lamina failure or the delamination of 90-degree ply should be considered. A close-up contour on the adhesive in ABAQUS provides that there exist

localized stress concentrations nearby the portions adjacent to 90 and 0-degree plies (Figure 5.27) or ±45 and 0-degree plies. This high stress gradient is caused by the mismatch of elastic constants and Poisson's ratios from 90 and 0-degree plies bonded together. The adhesive around these portions may reach the failure criterion first, and then the failure propagates to other portions of the adhesive, and finally breaks through it (Figure 5.26). Concerning all different orientations of lamina, the 90-degree ply is the weakest one and is assumed to be an additional failure mechanism.

In ABAQUS, the restriction of the dynamic shear failure is limited to isotropic materials only, because the failure criterion is based on the classical metal plasticity (von Mises criterion) and is only applicable for isotropic materials. It implies that failure strengths in any direction are the same. Even though the dynamic shear failure can be combined with Hill's failure criterion, where the strengths vary in different directions, the elastic properties of the material under this criterion are still subject to isotropy. This is completely against the characteristics of the orthotropic material, a 90-degree lamina. Alternatively, the concept of an interface resin-rich epoxy interlayer modeling (matrix layer) is introduced from other researches [28,30] to overcome this bottleneck. This artifact interlayer modeling more realistically expresses the interfaces of laminates and demonstrates that the continuously varying material properties through the plies do not generate singular interlaminar stresses at free edges [28]. The drawback to this interlayer modeling is that it only generates concentrated finite interlaminar stresses.

The intensity of singularity relies on the material properties of adjacent dissimilar materials. If each ply is considered as a dissimilar anisotropic elastic material, the free edge elasticity analysis gives singular interlaminar stresses. As a result, elasticity modeling with

singular free edge stresses is not appropriate in the prediction of the interlaminar tresses. Furthermore, in reality, the thin epoxy-matrix (resin) interlayer exists between adjacent plies (Figure 5.29).

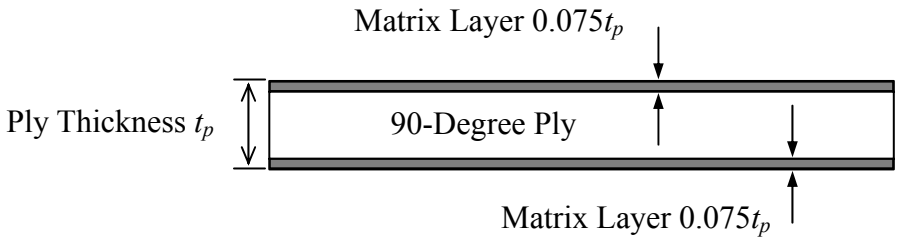

Figure 5.29. Matrix layer modeling within 90-degree ply.

Neither matrix nor fiber can completely occupy the volume of a lamina. The matrix holds the fibers together and extra matrix surrounds the bundle of fibers. As a result, between the adjacent plies a very thin layer of matrix can be added into finite element models. The purpose of adding an isotropic matrix layer is under the premise that the 90-dehree ply failure (delamination) is caused by matrix failure. The failure of matrix decomposes the cohesion of fibers in the sense that the 90-degree ply delaminates consequently. Such a composite failure mechanism of the matrix and fiber failure is classified as intra-laminar failure, and the delamination of the 90-degree ply is referred to as inter-laminar failure [49]. Both of the failures belong to internal damage modes [65], namely matrix cracking, matrix-crack-induced micro-cracks, matrix-crack-induced delamination, and fiber breakage.

Typically, for a carbon-epoxy lamina, the fiber has higher strength than the matrix in the longitudinal fiber direction, whilst the transversely and shear properties of the lamina are matrix-dominated [1]. The matrix is more vulnerable to shear stress than the fiber and usually fails first within a laminate. From reference [12], both uniform lap repair and scarf repair models use interlayer failure (adhesive layer) in shear to predict joint failure using computational

code, RAS. Therefore, the intra-layer (matrix layer) exists between plies and is suitable for shear failure model because the stress transfer across the matrix is dominated mostly by shear. In references [27,49], in-plane shear strength and in-plane shear terms were utilized in the matrix failure criterion (Hashin-Rotem criterion) for matrix cracking in tension and compression tests. Dávila et al. [66] also developed a new set of failure criteria for fiber reinforced laminates by modifying the Hashin's criteria for unidirectional composite laminates and Puck's action plane concept. A modified term, effective in-plane shear strength, for matrix shear and compression has been presented by Sun et al. [67] and Puck et al. [68]. Puck also determined that the matrix failure dominated by in-plane shear occurs in a plane that is normal to the ply and parallel to the fibers. Accordingly, from the Hashin criteria under plane stress and modified criteria [60] for the matrix failure under tension or compression, the shear strength, shear stress, and effective in-plane shear strength are determined to be a critical factor in the mechanism of fibrous composite failure.

The isotropic matrix layer follows the isotropic material properties of epoxy [30] and the isotropy failure model (dynamic shear failure) is valid. The 90-degree ply keeps orthotropic nature and is bonded by the top and bottom layers of isotropic matrix (Figure 5.29). Note that the dynamic shear failure is now applied to surrounding isotropic matrix layers instead of 90-degree anisotropic plies directly. The matrix layer is the site of failure investigation. There is no failure criterion defined in 90-degree laminates in ABAQUS. Using 3-D finite element method, the stress profile of six stress components in the isotropic matrix region are calculated and subsequently are imported into the dynamic shear failure criterion for failure predication.

5.2.2 Adhesive Combined with 90-Degree Ply Failure

Modeling Change of a 90-Degree Ply

The failure criterion of 90-degree plies is founded on the matrix failure premise. There is no existence of plastic or post-yielding behavior of brittle materials like carbon fiber reinforced composites whose yield criterion can be treated as their failure criterion. Once the brittle materials yield, the failure occurs as well. In contrast, polymer matrix (resin) such as epoxy behaves with a high degree of plasticity after yielding. The failure mechanism has been changed to the matrix failure (isotropic material failure) within 90-degree plies. In ABAUQS, this mechanism can be implemented by the classical metal plasticity model. The effective stress limit (effective yield stress) of the epoxy matrix layer is given by test data 5,548 psi, which is equivalent to the tensile strength associated with the von Mises criterion. Note that this value is determined by the tensile strength test of a T-800S/3900-2B 90-degree prepreg using ASTM D3039 Standard at room temperature instead of the mechanical property of the pure epoxy matrix. Because the interactions between the fiber and matrix should be considered, in the sense that, the effective stress limit of 5,548 psi given for matrix layers is to approximate the overall failure stress for 90-degree plies. Once the stress state of the matrix layers reaches this limit, the matrix layers fail and the bonded 90-degree ply delaminates at the same time. This can be interpreted as that both 90-degree ply and its matrix layers failing at the stress limit of 5,548 psi. The isotropic hardening model of the epoxy matrix is assumed to be perfectly plastic. The dynamic shear failure parameter (S_f) is given by 0.24, which is taken from epoxy adhesive data and is modified by iteration based on the results from ABAQUS. Two matrix layers (top and bottom layers) modeled within a 90-degree ply are assumed to be 15% of the original ply thickness for each specimen (0.15 t_p). The thickness of the top and bottom matrix layers is the same as 0.075 t_p but is different from one specimen to another (Table 5.5).

TABLE 5.5

THICKNESS OF THE MATRIX LAYER WITHIN A 90-DEGREE PLY

Model	Matrix Layer Thickness	Model	Matrix Layer Thickness
OPT53- 1	0.00060 in	OPT53- 4	0.00055 in
OPT53- 2	0.00060 in	OPT53- 5	0.00056 in
OPT53- 3	0.00055 in	OPT53- 6	0.00054 in

In 3-D Dynamic analysis, the governing equations of motion become more sophisticated due to the appearance of additional 'shear terms' and additional degrees of freedom, especially for composite materials (components of extension stiffness and bending-extension stiffness are different from one to another). Therefore, there are more 'modes' to be solved in eigenvalue equation sets, which require excessive processing and memory unit. Furthermore, the damping factor or frequency (ω) obtained in the 3-D model differs from those in the 2-D model, especially for non-isotropic materials. In addition, more stress concentrations will occur in those areas (especially through the width of the specimens) subjected to steep gradient of geometry change or high stress gradient [1, 69].

For composite laminates, the interlaminar stress and edge effects should be taken into account as well [1,49,65] and will be presented in section 5.3. The results of dynamic simulations for both the 2-D and 3-D models, including the surface strain distributions along the loading direction (longitudinal surface strains) for each composite joint model outputted from ABAQUS, are compared with their experimental data, respectively. Figures 5.30 to 5.35 display the 2-D plane strain numerical results. Figures 5.36 to 5.41 illustrate the 3-D numerical results. The ultimate loads from ABAQUS and test results are tabulated and compared, correspondingly (Table 5.6 for 2-D plane strain anisotropic models and Table 5.7 for 3-D anisotropic models). Note that the 2-D numerical data are obtained from scarf joint models, whilst the 3-D numerical data are from stepped joint models, due to the convergent difficulties of

3-D scarf joint models in ABAQUS. The alphanumerical code '-90MATRIX' marked for finite element results represents the result from the matrix failure within 90-degree plies dynamic model. Note that all the data are from finite element simulations using the matrix layer failure within 90-degree plies.

TABLE 5.6

ULTIMATE LOAD COMPARISON BETWEEN TEST DATA
AND 2-D ANISOTROPIC DYNAMIC FINITE ELEMENT ANALYSIS DATA

90-Degree Ply Failure (Effective Stress Limit = **5,548** psi) Adhesive Shear Failure PEEQ = **0.25** / Matrix Shear Failure PEEQ = **0.24**			
OPT53 2D Models	Test Data	ABAQUS Data	Deviation %
OPT53-1SCF-ANISO	29,089.3 lbf	31,807.7 lbf	9.3
OPT53-2SCF-ANISO	25,292.0 lbf	22,241.3 lbf	-12.1
OPT53-3SCF-ANISO	56,768.3 lbf	54,758.1 lbf	-3.5
OPT53-4SCF-ANISO	54,765.6 lbf	54,105.6 lbf	-1.2
OPT53-5SCF-ANISO	77,678.3 lbf	79,426.0 lbf	2.2
OPT53-6SCF-ANISO	71,333.3 lbf	79,216.4 lbf	11.1

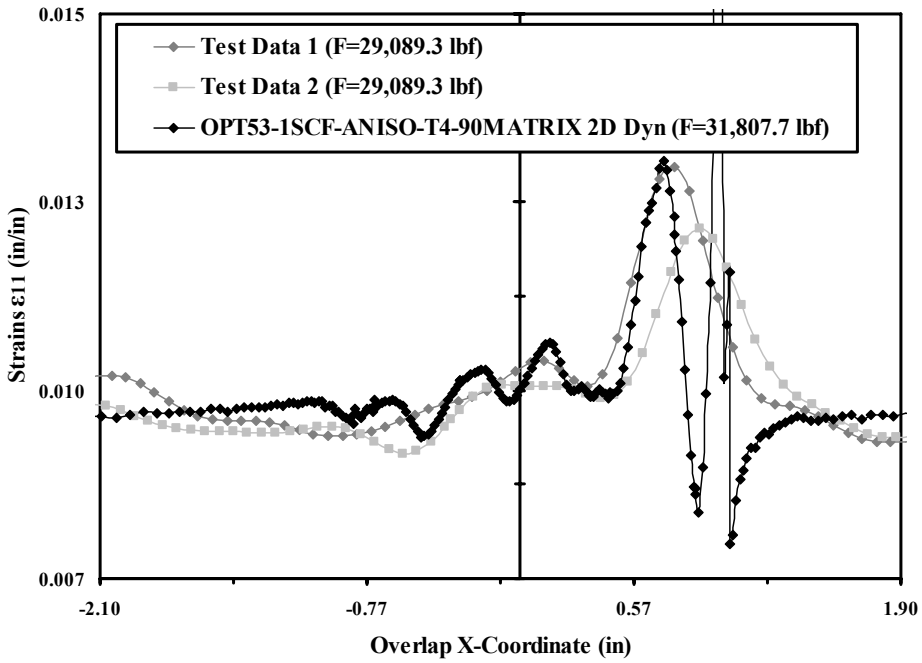

Figure 5.30. Longitudinal surface strain comparison of test data and OPT53-1 2-D anisotropic dynamic-reduced model.

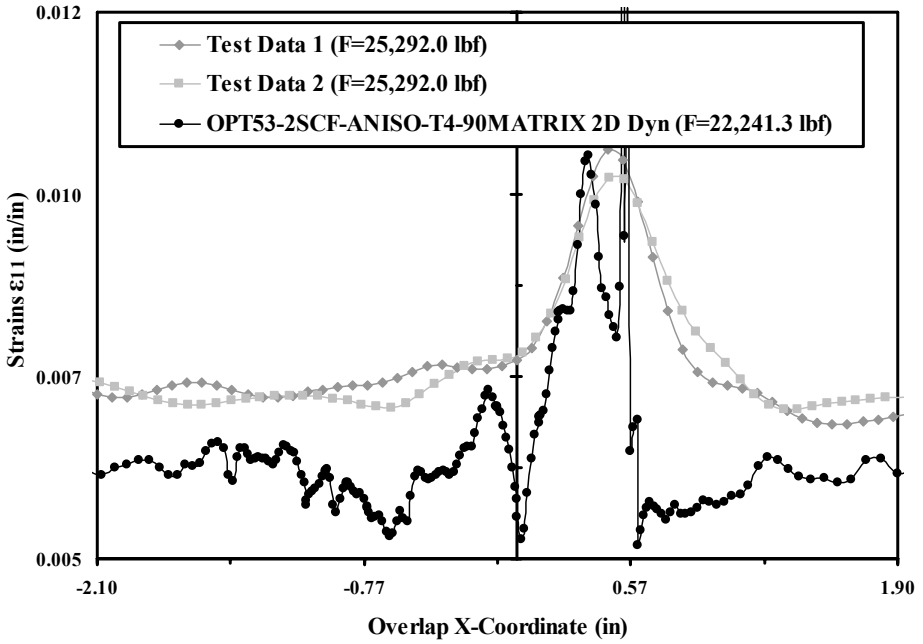

Figure 5.31. Longitudinal surface strain comparison of test data and OPT53-2 2-D anisotropic dynamic-reduced model.

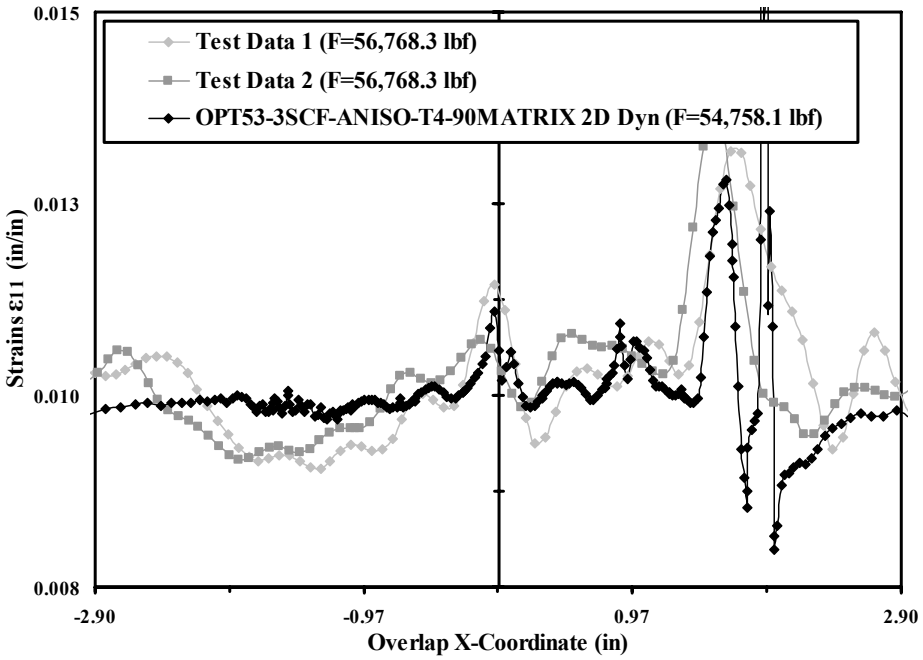

Figure 5.32. Longitudinal surface strain comparison of test data and OPT53-3 2-D anisotropic dynamic-reduced model.

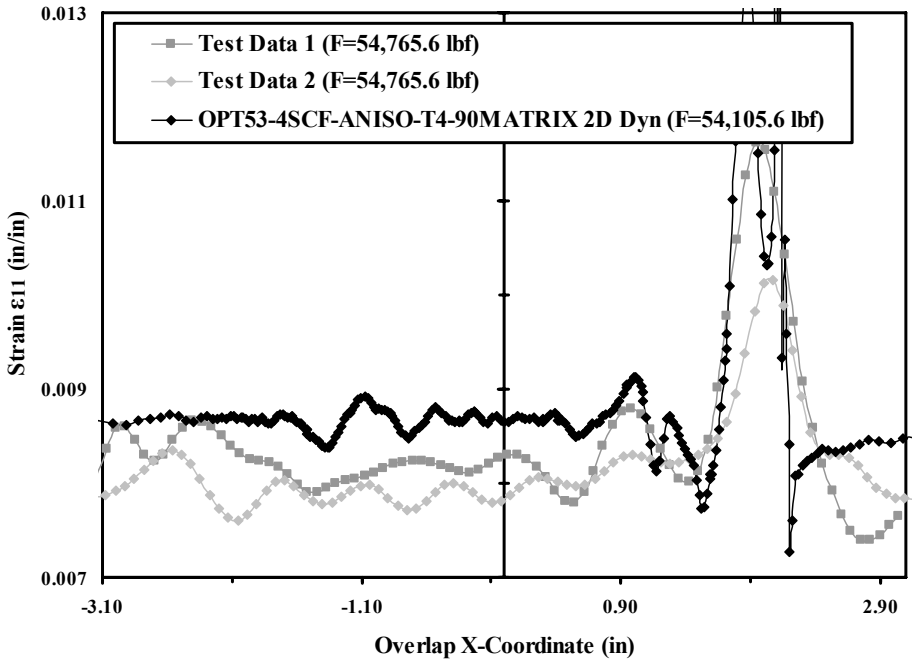

Figure 5.33. Longitudinal surface strain comparison of test data and OPT53-4 2-D anisotropic dynamic-reduced model.

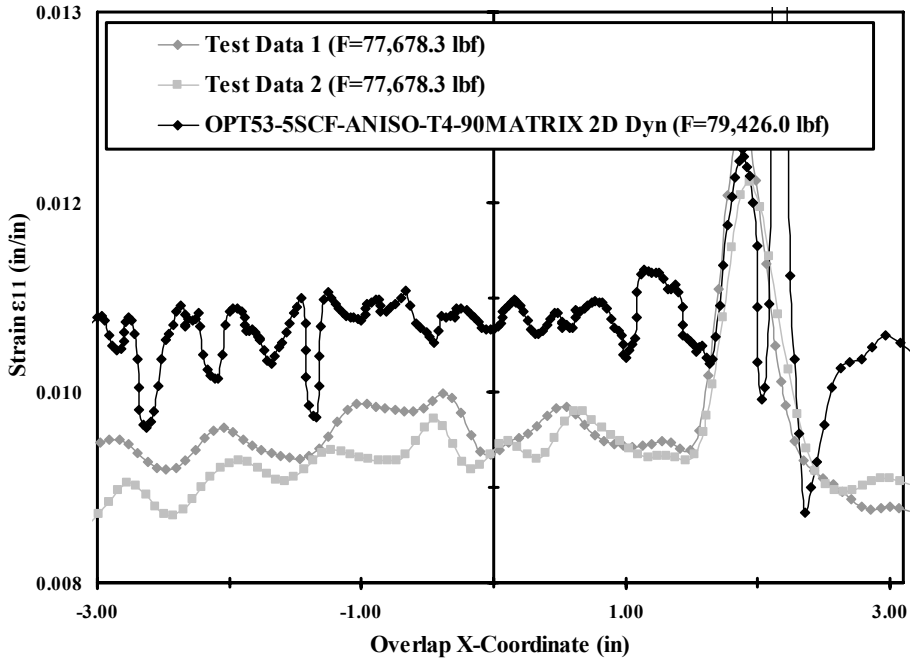

Figure 5.34. Longitudinal surface strain comparison of test data and OPT53-5 2-D anisotropic dynamic-reduced model.

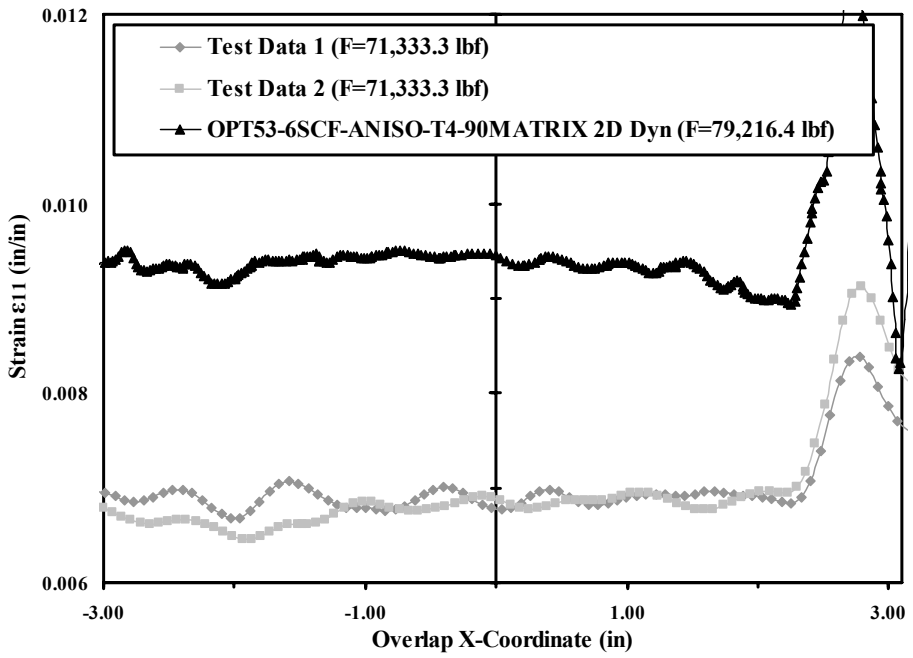

Figure 5.35. Longitudinal surface strain comparison of test data and OPT53-6 2-D anisotropic dynamic-reduced model.

TABLE 5.7

ULTIMATE LOAD COMPARISONS BETWEEN TEST DATA
AND 3-D ANISOTROPIC DYNAMIC FINITE ELEMENT ANALYSIS DATA

90-Degree Ply Failure (Effective Stress Limit = **5,548** psi) Adhesive Shear Failure PEEQ = **0.25** / Matrix Shear Failure PEEQ = **0.24**			
OPT53 3D Models	Test Data	ABAQUS Data	Deviation %
OPT53-1 COM-QUA	29,089.3 lbf	14,035.5 lbf	-51.8
OPT53-2 COM-QUA	25,292.0 lbf	18,166.0 lbf	-28.2
OPT53-3 COM-QUA	56,768.3 lbf	27,660.4 lbf	-51.3
OPT53-4 COM-QUA	54,765.6 lbf	38,727.2 lbf	-29.3
OPT53-5 COM-QUA	77,678.3 lbf	45,984.8 lbf	-40.8
OPT53-6 COM-QUA	71,333.3 lbf	36441.4 lbf	-48.9
90-Degree Ply Failure (Effective Stress Limit = **16,000** psi) Adhesive Shear Failure PEEQ = **0.28** / Matrix Shear Failure PEEQ = **0.28**			
OPT53-1 COM-QUA	29,089.3 lbf	30,582.6 lbf	5.1
OPT53-2 COM-QUA	25,292.0 lbf	28,551.0 lbf	12.9
OPT53-3 COM-QUA	56,768.3 lbf	63,658.2 lbf	12.1
OPT53-4 COM-QUA	54,765.6 lbf	48,648.2 lbf	-11.2
OPT53-5 COM-QUA	77,678.3 lbf	86,959.0 lbf	11.9
OPT53-6 COM-QUA	71,333.3 lbf	69,174.2 lbf	-3.0

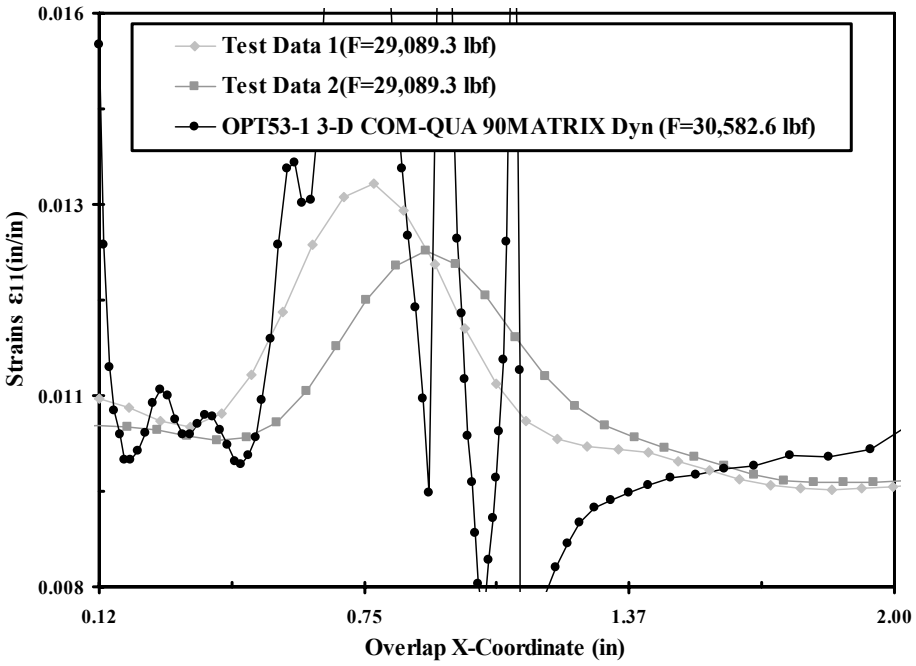

Figure 5.36. Longitudinal surface strain comparison of test data and OPT53-1 3-D anisotropic dynamic-reduced model.

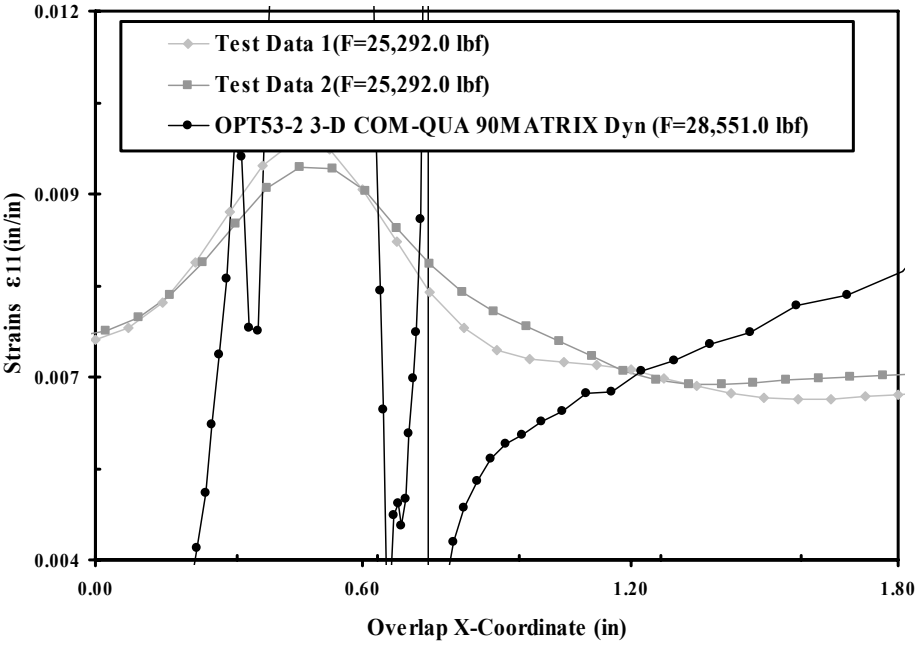

Figure 5.37. Longitudinal surface strain comparison of test data and OPT53-2 3-D anisotropic dynamic-reduced model.

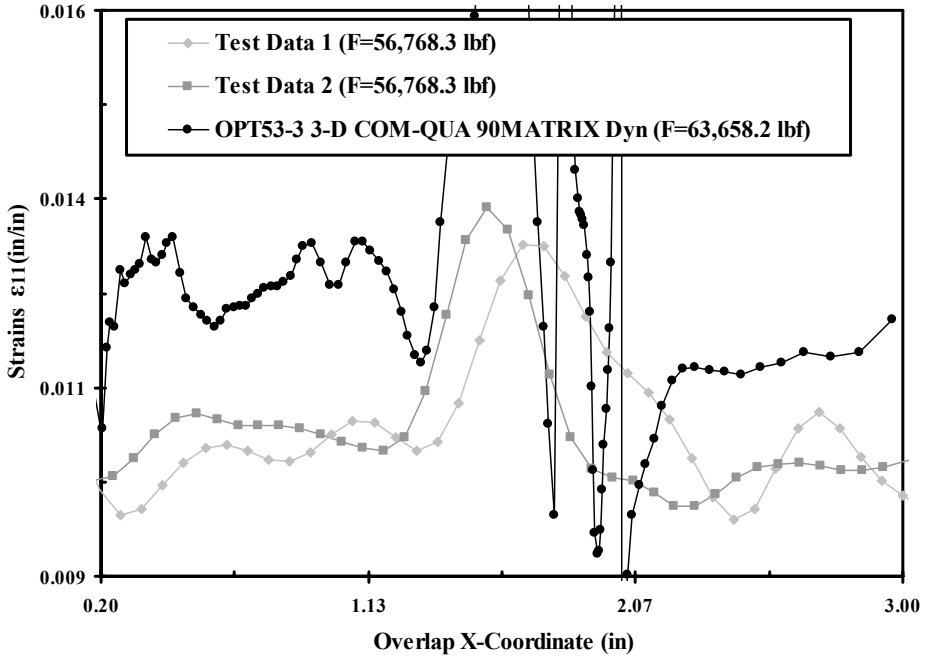

Figure 5.38. Longitudinal surface strain comparison of test data and OPT53-3 3-D anisotropic dynamic-reduced model.

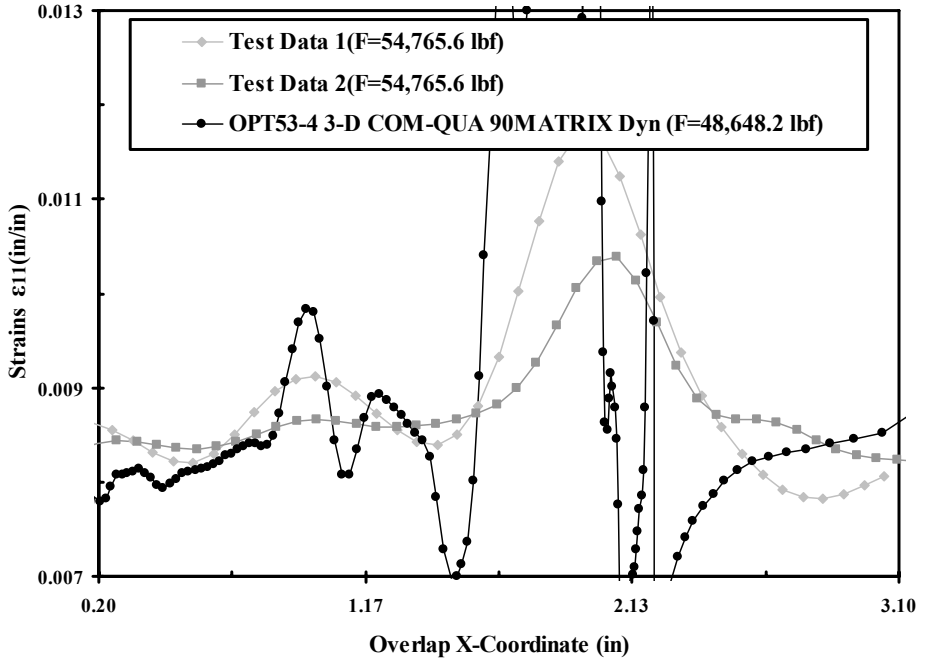

Figure 5.39. Longitudinal surface strain comparison of test data and OPT53-4 3-D anisotropic dynamic-reduced model.

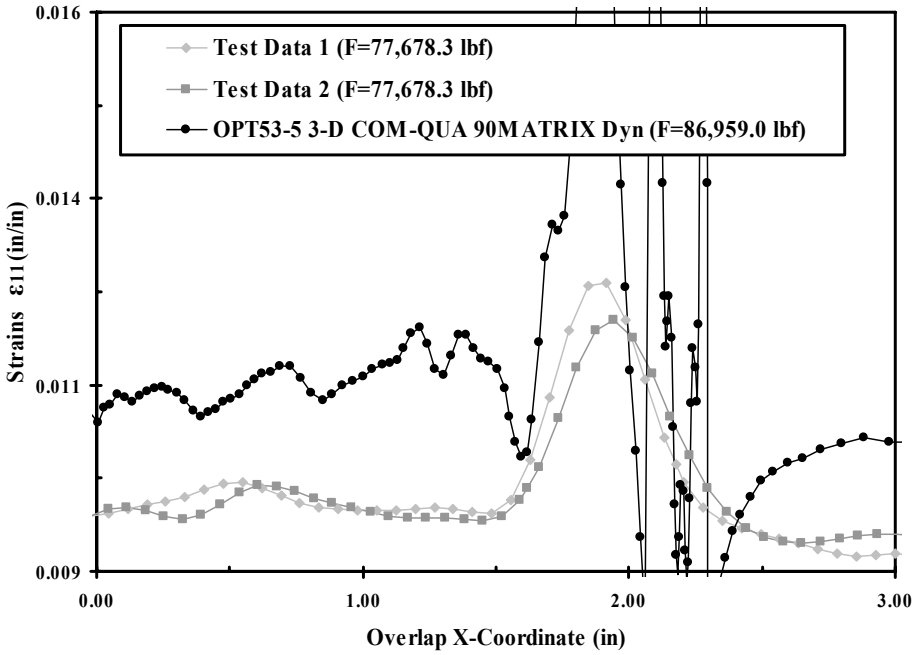

Figure 5.40. Longitudinal surface strain comparison of test data and OPT53-5 3-D anisotropic dynamic-reduced model.

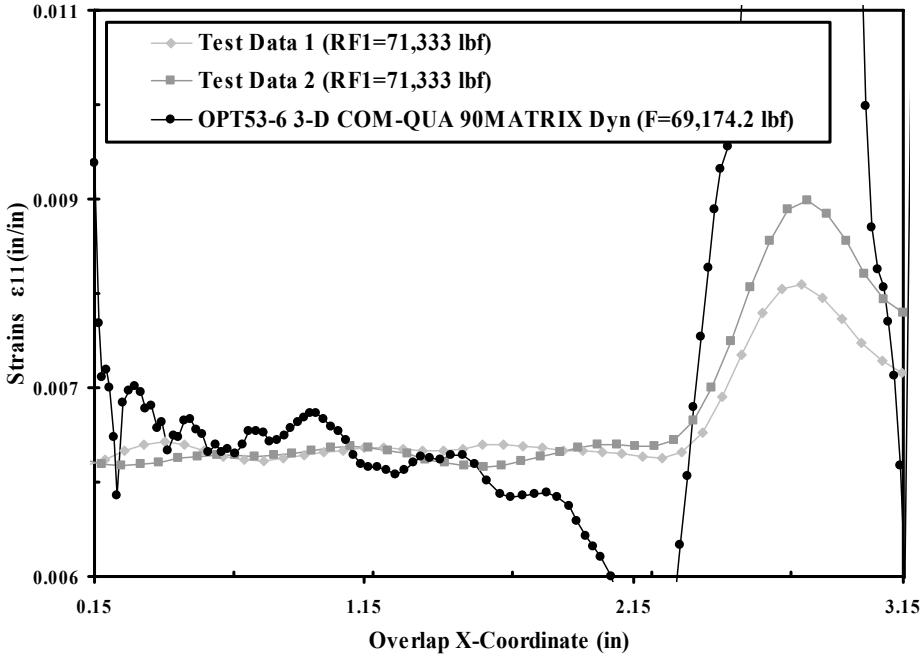

Figure 5.41. Longitudinal surface strain comparison of test data and OPT53-6 3-D anisotropic dynamic-reduced model.

5.2.3 Comparison and Observation of Explicit/Dynamic Finite Element Analysis Results

a. In contrast to static models, the 2-D dynamic composite scarf joint models gave more satisfactory strain distributions than did stepped joint models due to their more precise geometric feature. Moreover, the reduced integrated liner elements were used in dynamic analysis so that some inherent error source such as 'shear locking' is avoided. However, during the simulation, the 2-D composite scarf joint models were much more unstable and difficult to converge than the stepped joint models, and also took more processing time, particularly in OPT53-3 and OPT53-4 composite scarf joint models. Due to the irregular element shapes and material non-linearity in scarf joint models, the ratio of deformation speed to wave speed is easier to exceed 1.0 in ABAQUS, which caused job to abort. Accordingly, either the time-consuming iteration of applied force should be performed or the 'section control' or the high value of artificial density can be utilized to accomplish the analysis.

b. For 3-D composite scarf joint models, the tapered part of the adhesive causes geometry convergence problems. The elements within this part are difficult to adjust and easily exceed distortion limit in ABAQUS, even though the element refinement (adaptive meshing) is applied. Accordingly, the 3-D composite scarf joint configuration is altered to a stepped joint shape, whose elements are more uniform (Figure 5.5) in both the adhesive and adherend. From the stepped joint models, the range of value in the vicinity of the peak in the surface longitudinal strain distributions is wider than the test data or that obtained from the scarf joint models. This is owing to the fact that the adhesive layer within the stepped joint is modeled larger in length when it reaches the upper surface of the specimen. The surface layer of the adherend nearby the overlap is

trimmed to delete its angular taper tip, and the neighboring adhesive is merged to fill in this trimmed end.

c. Regarding the ultimate load of the OPT53-1, OPT53-3, and OPT53-5 model whose stacking sequences are classified as quasi-isotropic or close to quasi-isotropic (OPT53-1), their ultimate loads under tension are higher than those of the OPT53-2, OPT53-4, and OPT53-6 models, respectively. Although the percentage of 0-degree ply within the stacking sequence is lower (Table 4.5), the quasi-isotropic models still exhibit higher tensile strength. Those simulations are consistent with test data, which can be shown by comparisons between OPT53-1 and OPT53-2 models. Their geometry and dimension are identical; however, the OPT53-1 model whose stacking sequence is closer to quasi-isotropic, has a higher tensile strength.

d. Comparing the 3-D with the 2-D dynamic ABAQUS results, the failure parameters (PEEQ and effective stress limit) defined in the 2-D dynamic models significantly underestimated the ultimate loads as expected when they were applied to the 3-D analytical models (Table 5.7). The adhesive failure criterion parameter—PEEQ is changed from 0.25 to 0.28 and the effective stress limits of the adhesive and the matrix layers are higher in 3-D dynamic analysis than those used in 2-D analysis (Table 5.6 versus Table 5.7). The reason for this change can also be explained by the equations (2.7), (3.6) and (3.7). In order to maintain the same ultimate load or effective stress under the existence of the out-of-plane terms in the 3-D dynamic model, the failure PEEQ based on equation (2.8) must be increased. This increase is significant in OPT53 composite scarf joint models owing to remarkable strain concentrations, caused by the composite's characteristics such as anisotropy, the edge effect, and the stacking sequences

followed by interlaminar stress and strain components. It also can be proved by the fact that the adhesive failure PEEQ of OPT53 2-D composite scarf joint models is consistent with that in ASTM D5656 2-D models. This implies the importance of using consistent 2-D or 3-D models for material characterization and subsequent failure analysis.

e. Concerning the progressive failure results, the loading trends outputted from ABAQUS show that the 2-D non-quasi-isotropic specimens (OPT53-1, OPT53-2, OPT53-4, and OPT53-6) have an evidently progressive (stepped) decrease (Figure 5.42). The quasi-isotropic specimens, OPT53-3 and OPT53-5 do not behave in the same manners (Figure 5.43). Because OPT53-1 is close to quasi-isotropic, its loading trend does not exhibit this significantly progressive (stepped) decrease. Those loading trends clearly provide the progressive failure history of laminated composites. It indicates that the failure of the non-quasi-isotropic specimens (the 90-degree plies are grouped in the manner of [45/90/-45/0]) propagates from one 90-degree ply to another 90-degree ply until the structure collapses. For quasi-isotropic specimens (the 90-degree plies are grouped in the manner of [0/90/0]), the failure of the adhesive and 90-degree plies occurs almost at the same time. The different results between quasi-isotropic and non-isotropic models could be caused by the stacking sequences. The mismatch of the elastic constants in the manner of [0/90/0] is severer than those in [45/90/-45/0] and then the stress gradient of the 90-degree plies within [0/90/0] is higher. Therefore, the failure of 90-degree plies in the manner of [0/90/0] affects the tensile strength more significantly. These stress distributions through the thickness (ply-to-ply) of the specimen can be verified by the outputs of stress components from ABAQUS contours. In fact, from ABAQUS steps/frames PEEQ contours, the failure initiates first from the adhesive layer

and then to certain 90-degree plies.

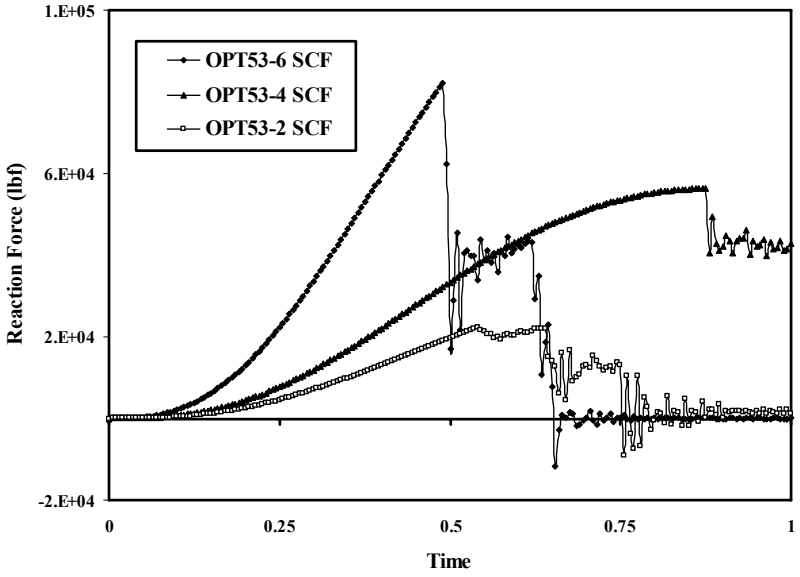

Figure 5.42. Dynamic trends of OPT53 non-quasi-isotropic composite scarf joint models.

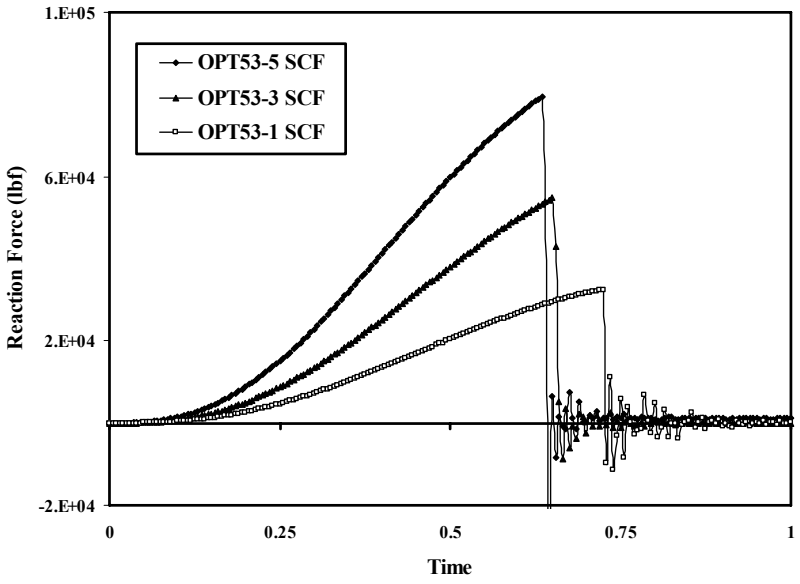

Figure 5.43 Dynamic trends of OPT53 quasi-isotropic composite scarf joint models

f. The edge effect in 3-D dynamic models reveals that it can be considered as one of the failure models of composite laminates. The edge effect is remarkable nearby the joint area especially within 90-degree plies. From the stress contours abstracted from

ABAQUS (Figures 5.44 to 5.46), it can be seen that the edge effect and stress concentration do, indeed, exist on different dimensional analyses for OPT53-1 specimen. The remarkable stress concentrations are localized nearby the free edge within the overlap shown in 3-D simulation. Those elements which reach the failure criterion and fail first (Figure 5.46) are initiated from the edge portions within the overlap. Those high stress concentrations, which trigger the failure of the elements, are not only owing to geometric changes, but are also owing to the inherent characteristics of composite laminates. Therefore, the failure model mentioned in section 5.3 is valid and realistic.

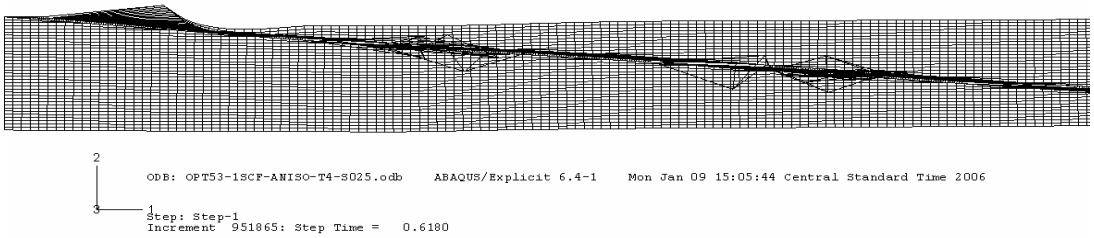

Figure 5.44. OPT53-1SCF 2-D dynamic model—adhesive failure only.

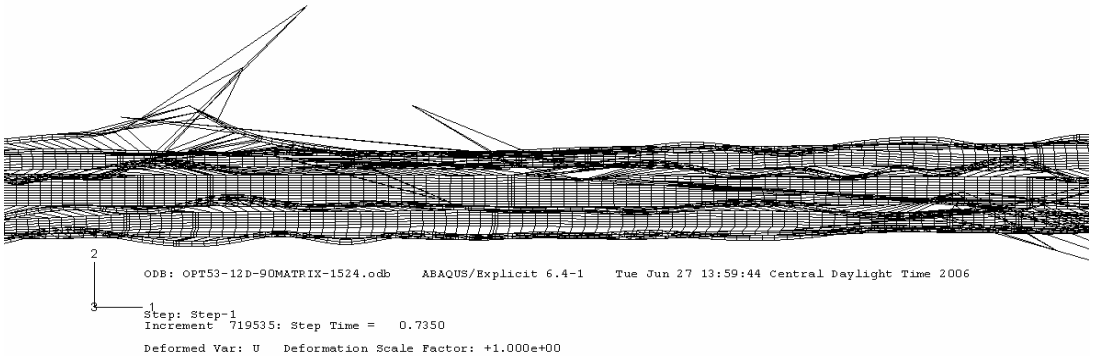

Figure 5.45. OPT53-1SCF 2-D dynamic model—adhesive and 90-degree ply failure.

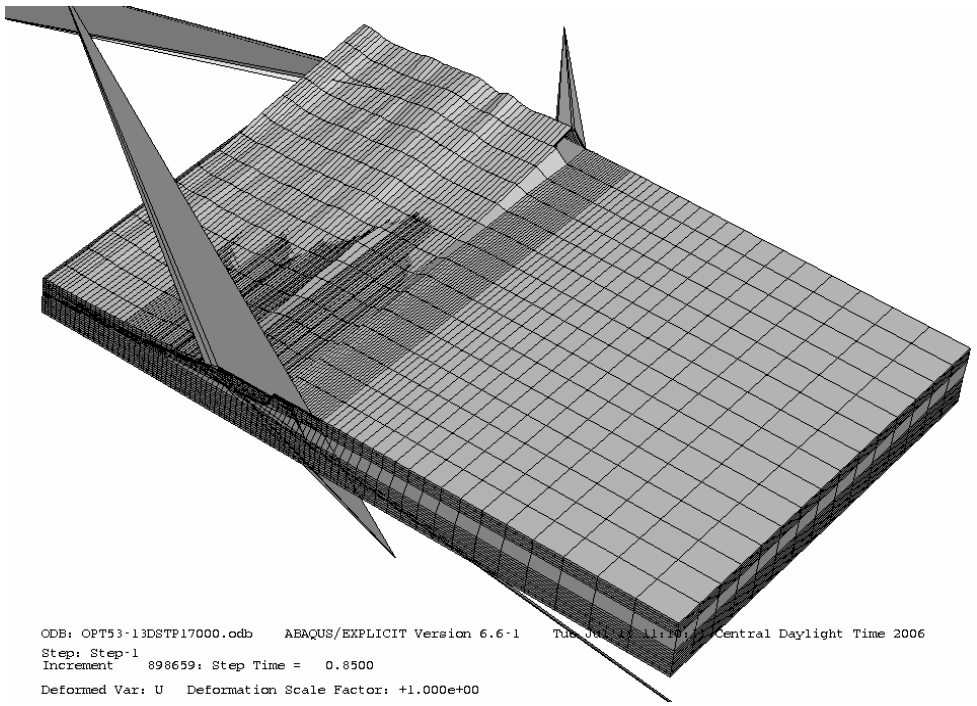

Figure 5.46. OPT53-1COM-QUA 3-D dynamic model—adhesive and 90-degree ply failure (edge effects accounted).

5.3 Interlaminar Stress and Edge Effect

In CLPT, the interlaminar stresses such as σ_{zz}, τ_{xz}, and τ_{yz} (σ_{22}, τ_{12}, and τ_{32} in ABAQUS) along the out-of-plane direction are not taken into account [1]. These interlaminar stresses are caused by mismatches in elastic properties between different orientation plies [1,30] and exist on surfaces between neighboring layers and also can subsist within the plies themselves. However, the largest value usually occurs at the layer interface and is zero at the top and bottom stress-free surfaces of the specimen. The reason why the interlaminar stress components should be considered is that those highest interlaminar stresses are considered to be an important factor for failure mechanisms—delamination. Dissimilar (heterogeneous) material properties between different orientation plies usually generate serious stress concentration/singularity near the free edges (or stress free boundaries) of composite laminates [28,29]. The free-edge stresses are distinctive characteristics of composite laminates, which initiate the failure of laminates called

free-edge delamination. Actually, the edge effect also exists in isotropic models (quasi-isotropic laminate models). This edge effect is caused by the high transverse shear and peel stress gradient around free edges/ends. They are shown in various studies [22,42,52,58,69] and the ABAQUS contours of OPT53 3-D isotropic ply-merged models, especially the stress distributions of the adhesive nearby the free ends. This kind of edge effect is due to geometric factors and is not discussed here.

Generally, the free-edge can be either the side face of a laminate, penetrating holes, or notches inside a laminate and the interlaminar stresses around these areas can be high enough to de-bond the laminate (crack or gap occurred/initiated) [26,61-63,69,70]. The initiation of the debonding or the delamination of a laminate nearby a free-edge area will propagate; therefore, the laminate's failure is caused by the growth of the delamination breaking through the bonding interface along its width. From reference [26], a 3-D finite element $[\pm 45_2/0_4]$s tapered composite beam has been analyzed. The stress-free edge decreases the interlaminar normal stress σ_{zz} while increasing the interlaminar shear stress σ_{xz} at the free edge. These effects may influence the prediction of free-edge delamination, especially the effects on σ_{yz}. Under in-plane loading, changing the stacking sequences (but remaining the same number of plies) results in changes of tensile strength. Such changes of strength, due to different stacking sequences, could be explained by the effect of interlaminar stresses [18]. Different adjacent plies produce different interlaminar stresses and result in the changes of strength.

Edge Effect and Transverse Surface Strains

In order to explore the edge effect, a test is designed to record the distribution of surface longitudinal strains ε_{xx}, across the width (y-direction) of the specimen (Figure 5.47) at structure failure. This experimental confirmation, referred to as the Moiré technique, has been performed

by *Pipes* and *Daniel* [1]. Additional detailed experimental investigations on a hole in laminated composites are shown by David H. Mollenhauer [71].

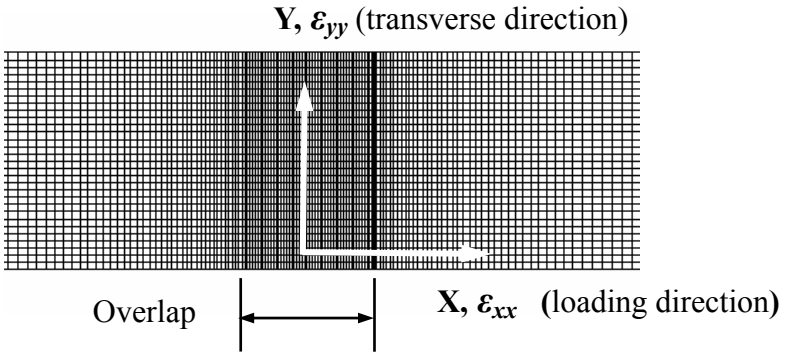

Figure 5.47. Transverse strains measured on upper surface within overlap through the Y-direction of OPT53 3-D composite model.

Therefore, within the overlap and across the width of the specimen including the boundary (free-edge), the stress variation that causes changes of strain can be interpreted. Using this indirect method, the extent of the laminate failure caused by the edge effect can be evaluated. In this study, the transverse strain distributions within the overlap, obtained from ABAQUS 3-D anisotropic models (3 inches wide) using 3-D solid/brick elements under the failure loads (given by test data), are compared with experimental results. The distributions of transverse surface strain outputted from both the 3-D static model, without the matrix interlayer modeling, and the 3-D dynamic model, with the matrix interlayer modeling, are plotted together to compare with experimental data (Figures 5.48 to 5.53).

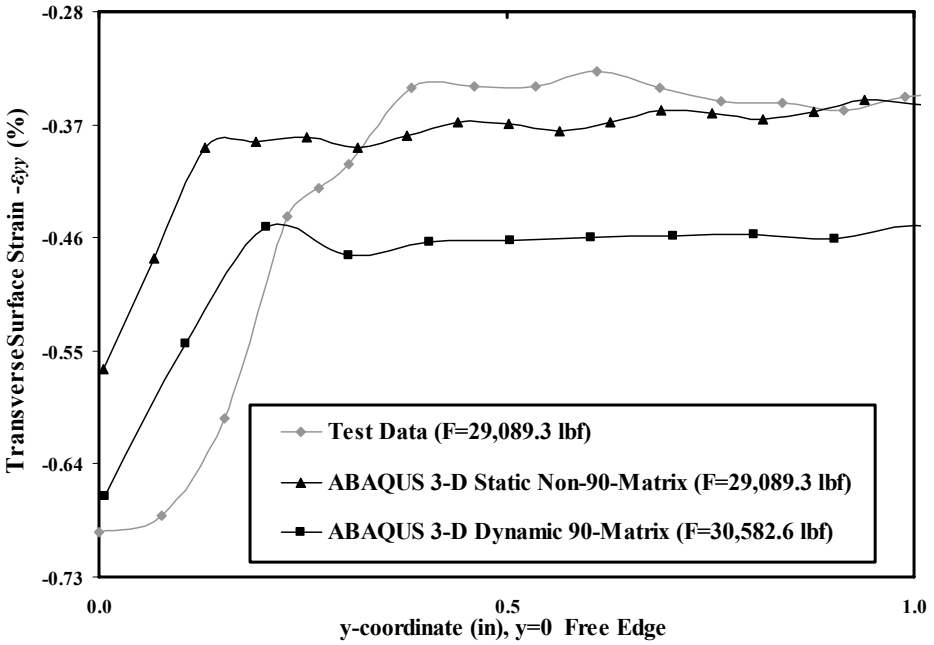

Figure 5.48. OPT53-1 3-D transverse surface strain ε_{yy} through the Y-direction within overlap (anisotropic static model).

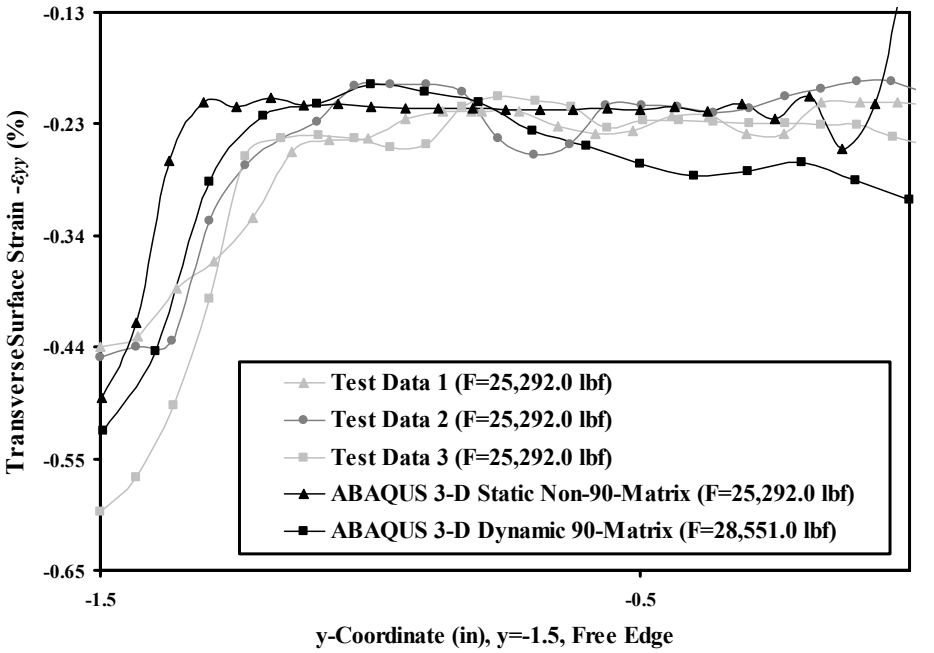

Figure 5.49. OPT53-2 3-D transverse surface strain ε_{yy} through the Y-direction within overlap (anisotropic static model).

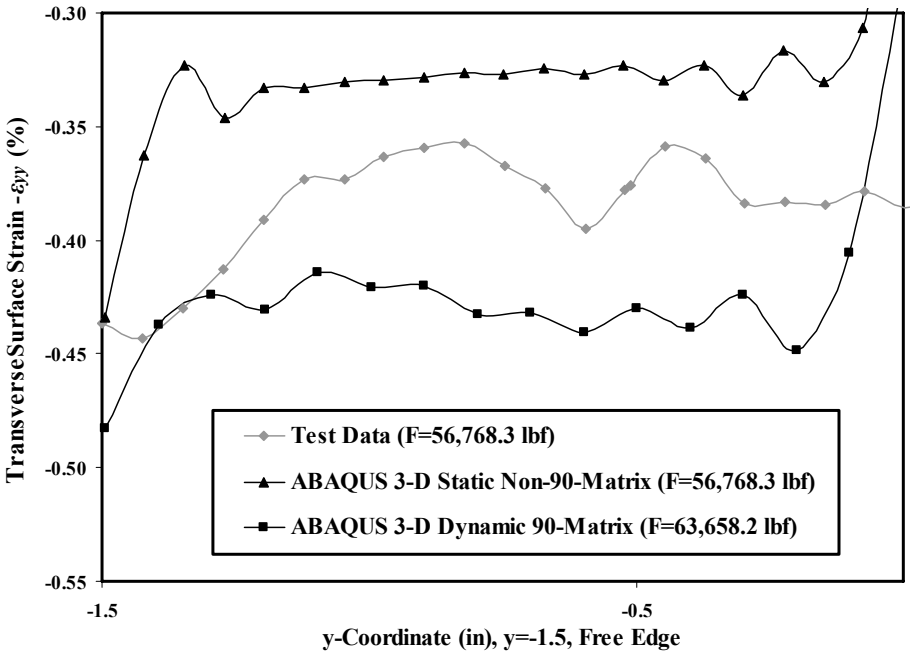

Figure 5.50. OPT53-3 3-D transverse surface strain ε_{yy} through the Y-direction within overlap (anisotropic static model).

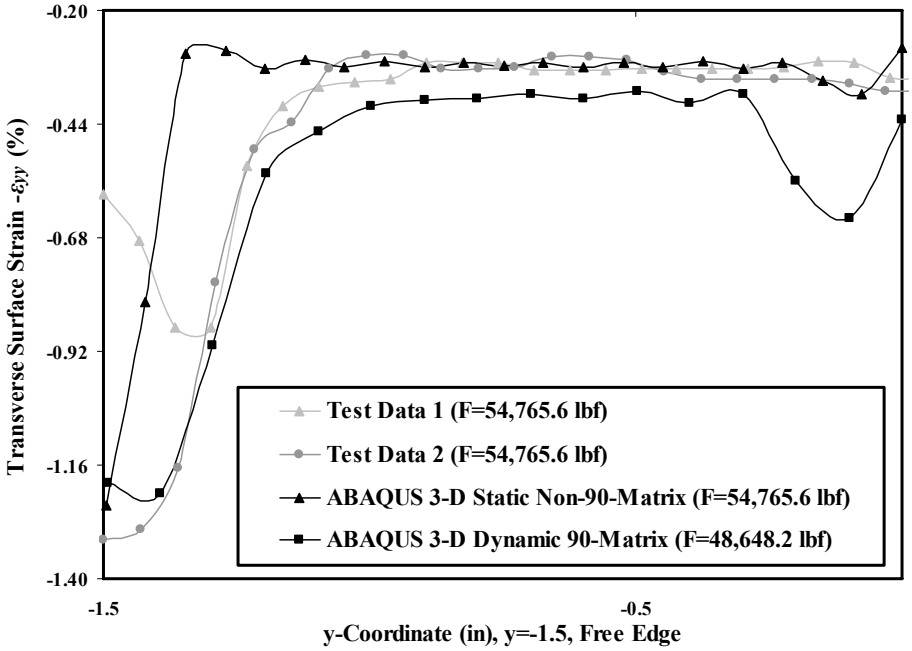

Figure 5.51. OPT53-4 3-D transverse surface strain ε_{yy} through the Y-direction within overlap (anisotropic static model).

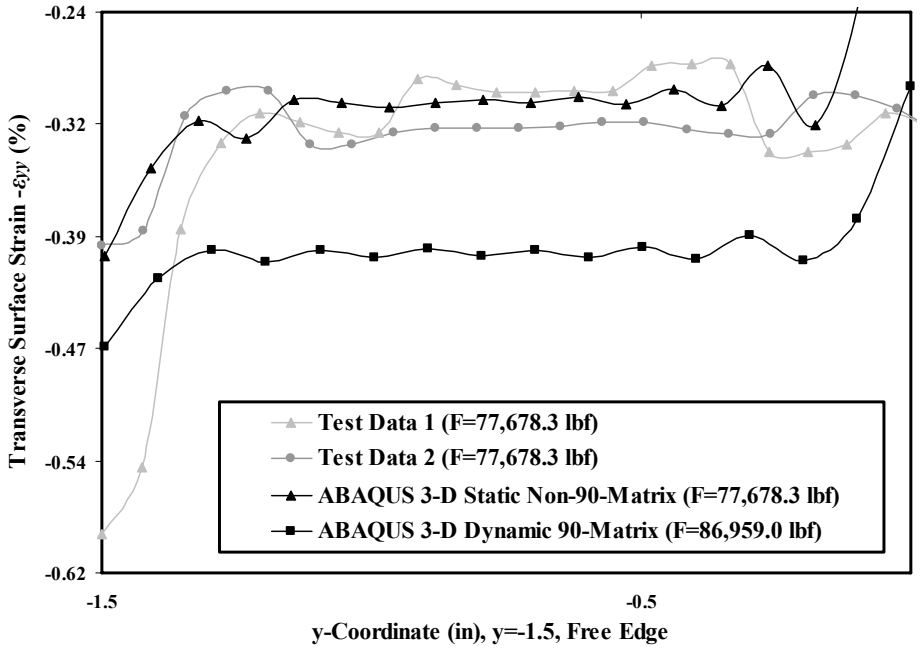

Figure 5.52. OPT53-5 3-D transverse surface strain ε_{yy} through the Y-direction within overlap (anisotropic static model).

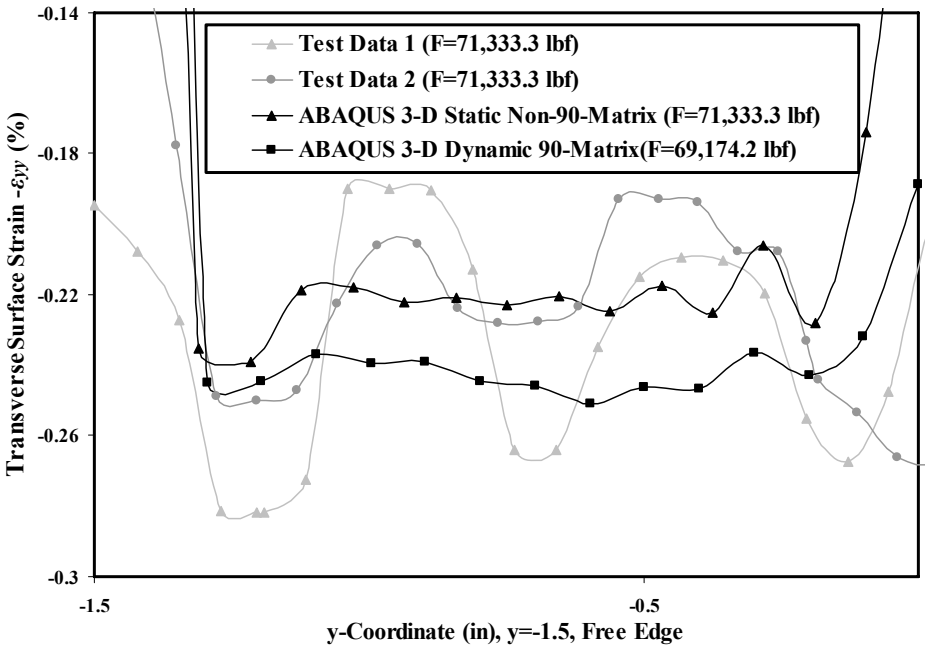

Figure 5.53. OPT53-6 3-D transverse surface strain ε_{yy} through the Y-direction within overlap (anisotropic static model).

From ABAQUS deformed contour of OPT53-1 3-D dynamic failure model (Figure 5.54), the 1-direction defines loading direction. The lateral face behind the model is the axisymmetric face, and the lateral face in the left-hand side is the stress-free face. For OPT53-1 laminated composite, these portions within the overlap that are close to the free edge as well as the stress-free face both delaminated furiously. In Figure 5.54b, the shaded layer, which denotes a 90-degree ply with matrix layers, delaminated dramatically. This 3-D contour demonstrates that the edge effect is also an important factor, causing the delamination of the 90-degree ply with matrix layers. In addition, the 3-D contour (Figure 5.54) confirms the existence of edge effect by approximating the interlaminar stress test results shown in Figure 5.48. The 3-D dynamic model offsets the inadequacy of 2-D plane strain dynamic analysis, which cannot account for this edge effect.

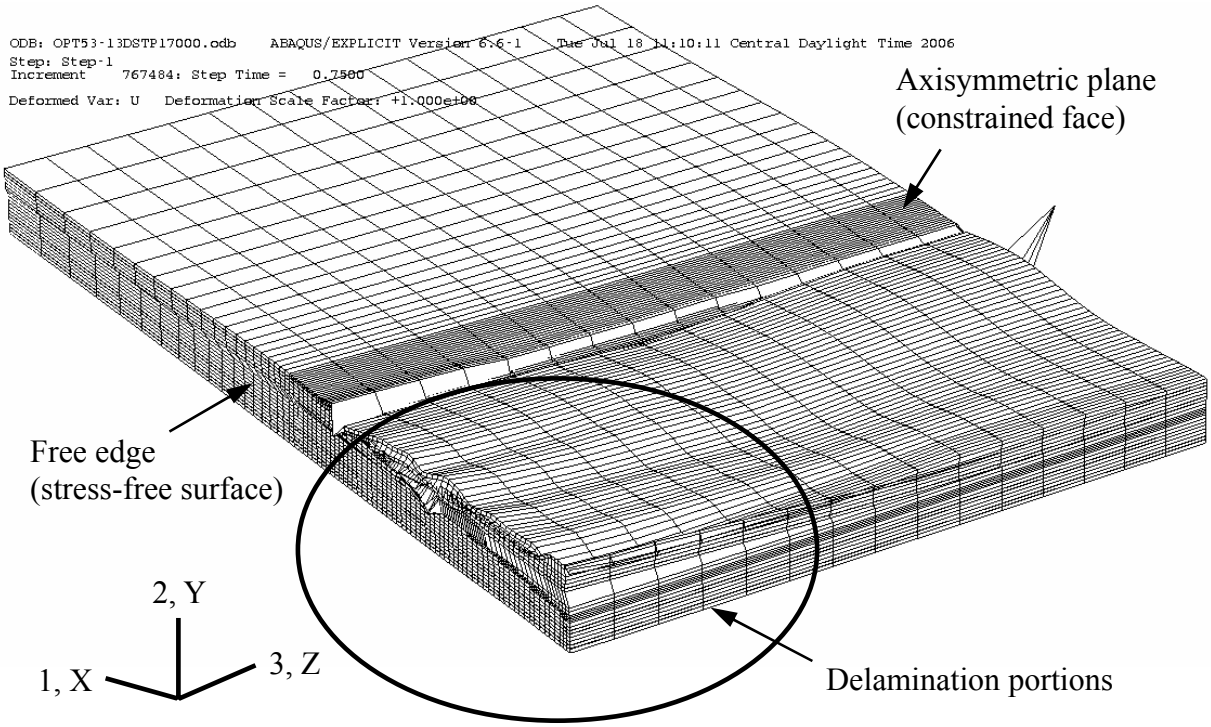

Figure 5.54a. OPT53-1 3-D delamination of 90-degree ply with matrix layers within overlap from dynamic model contour (edge effect causes delamination).

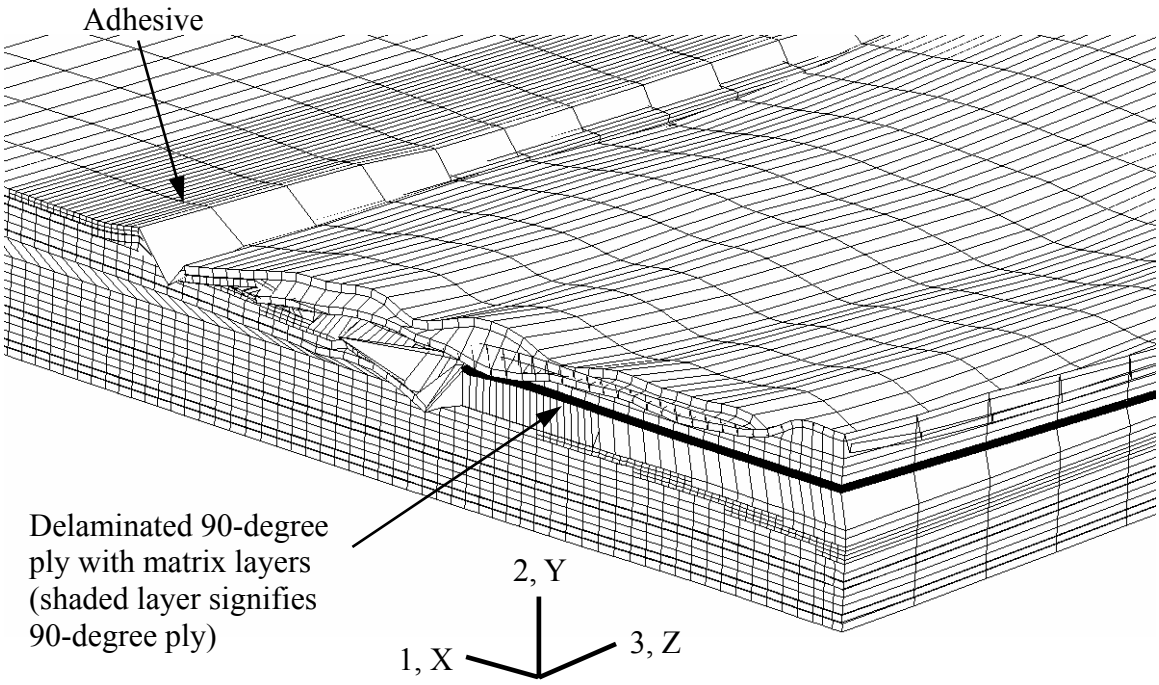

Figure 5.54b. Enlarged OPT53-1 3-D delamination of 90-degree ply with matrix layers within overlap from dynamic model contour.

5.4 Conclusions and Remarks Regarding Finite Element Analysis on Scarf-Patch-Repaired Composite Laminates

Through all the finite element analyses, some conclusions can be drawn.

a. Considering the material property only, static finite element analysis is the best choice requiring neither density nor damping factors. Usually after the high temperature curing process and cooling procedure, the density and conditions of specimens sometimes degrade or change unexpectedly. Because information concerning the damping property of the materials is frequently not available from the venders, it is usually necessarily to perform the frequency extraction of the material and the structure studies in advance so that the dynamic analysis can be executed.

b. If the structure analysis is focused on the 3-D model, the initial characterization of the materials should be obtained consistently from 3-D analysis in order to obtain higher

accuracy. Although 3-D and 2-D analysis may not deviate too much for isotropic materials, there is the potential that error will occur in analysis of composites (non-isotropic), especially for large stress/strain and post-yielding behavior analysis. Moreover, the frequency/damping extraction, involving the eigenvalue problem, will result in different values in 3-D and in 2-D analysis for non-isotropic materials.

c. The material properties of Torayca 800 (G_{12}=0.351 Msi), obtained from the tests in this study, may not reflect the true material behaviors. The test data obtained are significantly lower than any data mentioned in related researches [11,20,24,27,33,34,49,57,64] or the technical data sheets in the Torayca website (Table 5.8), especially in reference [49], which uses the same material T800/3900-2. This is possibly the reason why the 2-D dynamic composite scarf joint models, such as OPT53-3 and OPT53-4, have encountered difficulty of convergence. The reasonable value of G_{12} should be around 0.5~0.7 Msi or as high as 0.9 Msi [49] when compared with the E_{11}, E_{22}, and v_{12} of similar material composites. Moreover, based on the earlier finite element iterations, the G_{12} of 0.6 Msi can complete all OPT53 dynamic 2-D analyses without any convergence problems.

TABLE 5.8

TORAYCA COMPOSITE PROPERTIES (1)

Composite Properties - Cured Semi-Toughened Epoxy			
	Longitudinal (0°) Tensile Modulus (Msi) ASTM D-3039		In-plane Shear Modulus (Msi)
T300	19.5 (350 °F cure epoxy)	20.0 (250 °F cure epoxy)	0.64 (350 °F cure epoxy)
T300J	19.5 (350 °F cure epoxy)	-	0.64 (350 °F cure epoxy)
T400H	20.5 (350 °F cure epoxy)	21.5 (250 °F cure epoxy)	0.64 (350 °F cure epoxy)
T700S	19.5 (350 °F cure epoxy)	20.0 (250 °F cure epoxy)	0.64 (350 °F cure epoxy)
T800H	23.5 (350 °F cure epoxy)	25.0 (250 °F cure epoxy)	0.64 (350 °F cure epoxy)
T800S	22.5 (350 °F cure epoxy)	22.5 (250 °F cure epoxy)	-

(Data abstracted from Torayca website)

d. In edge effect analysis (as shown in Figures 5.48 to 5.53), the 3-D simulation results across the width of the models correlate fairly well with the test results except for quasi-isotropic models (OPT53-1, OPT53-3 and OPT53-5 model). Furthermore, based on experience, the ABAUQS results from the material property data set with G_{12} =0.6 Msi are relatively closer to the test results than are those from the currently used material property data set with G_{12}=0.351 Msi. From conclusion (c) and (d), the test results of Torayca 800 lamina and the test results from the edge effect analysis should be inspected and discussed in order to determine those factors causing such noticeable deviation.

e. Concerning the tensile strength of 90-ply lamina tested at room temperature, the test results is 5,548 psi, which is much lower than that from the technical data sheet reported by Torayca (Table 5.9) for other similar materials. In addition, the material properties and strength data of T800/3900-2 tabulated in reference [49] show the tensile strength in the transverse direction to be 8,720 psi.

TABLE 5.9

TORAYCA COMPOSITE PROPERTIES (2)

Composite Properties - Cure Epoxy (ASTM D-3039)		
	Transverse (90°) Tensile Strength (ksi)	
T300	11.5 (350 °F cure epoxy)	11.0 (250 °F cure epoxy)
T400H	11.5 (350 °F cure epoxy)	9.5 (250 °F cure epoxy)
T700S	10.0 (350 °F cure epoxy)	10.0 (250 °F cure epoxy)
T800H	11.5 (350 °F cure epoxy)	9.0 (250 °F cure epoxy)
T1000G	-	8.5 (250 °F cure epoxy)

(Data abstracted from Torayca website)

Based on the 3-D numerical results from ABAQUS, the effective stress limit of a 90-degree ply is 16,000 psi (based on the von Mises criterion) which is close to the in-plane shear strength of 13,760 psi listed in reference [49]. The results could be interpreted by that the intra-laminar failure (matrix failure mode in this study) is

dominated primarily by shear rather than tensile. Accordingly, the tensile strength in the transverse direction (90-degree ply) is not appropriate to use, even though the 2-D dynamic models (using tensile strength 5,548 psi) produce desirable results. Since the finite element method is based on the dynamic shear failure, the use of in-plane shear strength is more appropriate for performing numerical simulation.

f. The finite element results of composite scarf joint are compared with test results only in this study because the analytical/theoretical data are not applied. In the case of interlaminar stress analysis, the current analytical/theoretical model for composite laminate plates is based on a simple plate, ignoring geometric factors (cut or bonded with a joint). Therefore, the interlaminar stress components, such as σ_{zz}, through the thickness of a laminate plate are difficult to test/measure. Without analytical results and test data, it is more expedient to compare the results from 2-D and 3-D simulations or the results from different finite element packages.

g. It is not recommended to apply the Drucker-Prager plasticity model to the adhesive within OPT53 composite scarf joints due to the extreme convergent difficulties. The possible reason is explained by the geometric shape of the scarf with tiny angles, which results in unacceptable elements, such as vertex angle elements [53]. Large numbers of vertex angle elements (linear triangular element) exist in the tapered area and cause singularity and lead to convergent problems. The Drucker-Prager plasticity model is a more robust model with more complicated functions than the von Mises plasticity model; therefore, it is more suitable for finite element models with uniform element shape and mesh.

h. From Figures 5.48 to 5.53, the results from 3-D 90-matrix dynamic failure models produce lower responses in transverse surface strain than those from 3-D non-90-matrix failure static models, especially for quasi-isotropic models. Furthermore, the surface longitudinal strains from the 3-D 90-matrix dynamic failure models (Figures 5.36 to 5.41) and 2-D 90-matrix dynamic failure models (Figures 5.34 and 5.35) are more difficult to match with the test data. These are owing to the stacking sequences, involvement of interlaminar stress/strain components, and the matrix layer modeling. The effects of the stacking sequence are discussed in remark (e) in section 5.2.3. The stress variations of σ_{yy} through the thickness of the specimen obtained from ABAQUS (also can be proved by the reduced stiffness matrices predicted in section 4.1.3) provide that the σ_{yy} stress values are higher in quasi-isotropic models (OPT53-1,-3, and -5). Furthermore, the poison of the 90-degree plies in quasi-isotropic models is right under the surface layer (45-degree surface layer). Once the 90-degree plies within quasi-isotropic models fail (delaminate), the surface strain distributions (especially for transverse strains) of the 45-degree surface ply are affected and result in lower responses.

i. Regarding the matrix layer modeling, reference [28] stated that the matrix modeling can reduce the singularity problem and peak values of interlaminar stress, but no effect on interlaminar strain along the y-direction were mentioned. Moreover, the thickness of the interface matrix layer was assumed to be (t_p/12.5) in reference [28] and was given as 0.1 t_p in reference [30] respectively. These values were chosen irrespective of any values confirmed by other theories or criteria. The thickness of the matrix layer could be treated as an experimentally fitting parameter. In this study, the isotropic matrix layers are only given within 90-degree plies rather than given for every ply within the

composite laminates [28,30]. The degree of the influence of modeling matrix layers into an inter-ply needs more studies on the various thicknesses of matrix layers in finite element simulation. The relations among the thickness of the matrix layer, the ultimate load, and the distributions of transverse surface strain across the width needs further study.

j. Guided by the integration of the adhesive failure and the 90-degree ply failure, together with the matrix interlayer modeling method, and edge effect estimation procedure, the failure mechanism of OPT53 specimens becomes more complete and realistic. It can be postulated that the strength of composite scarf joints should be predicted via a combination of these three failure models, namely adhesive failure, 90-degree ply failure, and edge effects. In conclusion, (i) the characteristics of the adhesive, (ii) high stress/strain gradient and concentrations within the adhesive caused by partial failure of the 90-degree plies and (iii) the edge effect contributed by the stacking sequence of orthotropic composites, together construct a good guideline for strength analysis.

REFERENCES

LIST OF REFERENCES

[1] Robert M. Jones, "Mechanics of Composite Materials," 2/E, Taylor & Francis, Inc. PA, 1999.

[2] Naveen Rastogi, Som R. Soni and Jason J. Denney, "Analysis of Bonded Composite Patch Repaired Metallic Structures - An Overview," AIAA-1998-1883, Collection of Technical Papers. Pt. 2 (A98-25092 06-39).

[3] M. Das, A. Barut, E. Madenci, D. Ambur, "Nonlinear Analysis of a Bonded Patch Repair of a Skin with a Cutout," AIAA-2003-1999, Materials Conference, Norfolk, Virginia, Apr. 7-10, 2003.

[4] K. E. Metzinger and T. R. Guess, "Increasing the Strength of Adhesively Bonded Joints by Tapering the Adherends," AIAA-2000-60, Collection of Technical Papers (A00-16885 03-44).

[5] K. E. Metzinger and T. R. Guess, "How Geometric Details can Affect the Strength of Adhesive Lap Joints," AIAA-1997-954, Aerospace Sciences Meeting and Exhibit, 35th, Reno, NV, Jan. 6-9, 1997.

[6] G. A. Clark and K. I. Clayton, "Structural Techniques for Joining Filamentary Composites,"AIAA-1968-1038, American Inst. Of Aeronautics and Astronautics, Annual Meeting and Technical Display, 5th Philadelphia, PA., Oct. 21-24, 1968.

[7] E. Beck, "Advanced Composite Structure Repair Guide," *Journal of Aircraft*, 0021-8669 Vol.18, No.9 (766-769), 1981.

[8] S. H. Myhre and J. D. Labor, "Repair of Advanced Composite Structures," *Journal of Aircraft*, 0021-8669 Vol.18, No.7 (546-552), 1981.

[9] S. H. Myhre and C. E. Beck, "Repair Concepts for Advanced Composite Structures," *Journal of Aircraft*, 0021-8669 Vol.16, No.10 (720-728), 1979.

[10] F. Darwish, K. Shivakumar, S. Hamoush, and D. Hsu, "Performance of Patch Repaired Composite Panels – Static and Fatigue," AIAA-2006-2271, 14th AIAA/ASME/AHS Adaptive Structures Conference 7th, Newport, Rhode Island, May 1-4, 2006.

[11] C. Soutis, F. Z. Hu, "Failure Analysis of Scarf-Patch-Repaired Carbon Fiber/Epoxy Laminates under Compression," AIAA-0001-1452 Vol.38, No.4 (737-740), 2000.

[12] Won-Shik Chu and Sung-Hoon Ahn, "Internet-Based Composite Repair," *Journal of Composite Materials*, 39: 827 - 845. May 2005.

[13] Naveen Rastogi, B. P. Deepak, and Som R. Soni, “Stress Analysis Codes for Bonded Joints in Composite Structures,”AIAA-1997-1341, Collection of Technical Papers, Pt. 4 (A97-24112 05-39).

[14] Naveen Rastogi, Ming Xie, and Som R. Soni , “Strength Prediction Codes for Bolted Joints in Composite Structures,” AIAA-1997-1223, Collection of Technical Papers, Pt. 2 (A97-24112 05-39).

[15] S. S. Wang and J. F. Yau, “Interfacial Cracks in Adhesively Bonded Scarf Joints,” AIAA -0001-1452 Vol.19, No.10 (1350-1356), 1981.

[16] D. Kutscha, “Mechanics of Adhesive-Bonded Lap-type Joints: Survey and Review,” AFML-TDR-64-298, December 1964, Air Force Materials Laboratory, Wright-Patterson AFB. OH-45433.

[17] D. Kutscha and K. E. Hofer Jr., “Feasibility of Joining Advanced Composite Flight Vehicles: Survey and Review,” AFML-TR-68-391, January 1969, Air Force Materials Laboratory, Wright-Patterson AFB. OH-45433.

[18] Caryl L. Johnson, “Effect of Ply Stacking Sequence on Stress in a Scarf Joint,” AIAA-0001-1452 Vol.27, No.1 (79-86), 1989.

[19] Caihua Cao, “Damage and Failure Analysis of Co-Cured Fiber-Reinforced Composite Joints with Unidirectional Lay-Up,” http://etd.gatech.edu/theses/available/etd-12012003-122120/unrestricted/Cao_Caihua_20 0312_phd.pdf

[20] C. Soutis and F. Z. Hu “A 3-D failure analysis of scarf patch repaired CFRP plates,” AIAA-1998-1943, Collection of Technical Papers. Pt. 3 (A98-25178 06-39).

[21] Antonio S. Llanos, Sung W. Lee, and Anthony J. Vizzini, “Delamination Prevention in Tapered Composite Structures under Uniaxial Tensile Loads,” AIAA-1990-1063, Collection Technical Papers. Part 2 (A90-29283 11-39).

[22] T. Pervez, A. Karrech, R.A. Siddiqui and S. A. Al-Araimi, “Simulation of Taper-Taper Joint for Laminated Composite Plate Using Finite Element Method,” Proceeding of MDP-8, Cairo University Conference on Mechanical Design and Production, Cairo, Eyipt, January 4-6, 2004.

[23] K. Roy, S. L. Donaldson, and G. A. Schoeppner, “Bonded joints of unidirectional and cross-ply laminates - An experimental study,”AIAA-1997-1121, Collection of Technical Papers, Pt. 3 (A97-24112 05-39).

[24] Alexander E. Bogdanovich and Sergei P. Yushanov, “3-D Progressive Failure Analysis of Bonded Composite Joints,”AIAA-1998-1888, Collection of Technical Papers. Pt. 2 (A98-25092 06-39).

[25] S. P. Engelstad, O. T. Berry, R. C. Averill, and D. J. Eby, "Implementation and Application of Zig-Zag Finite Elements for Composite Bonded Tee-Joint Modeling," AIAA-2001-1487, AIAA/ASME/ASCE/AHS/ASC Structures, Structural Dynamics, and Materials Conference and Exhibit, 42nd, Seattle, WA, Apr. 16-19, 2001.

[26] Anthony J. Vizzini and Sung W. Lee, "Damage Analysis of Composite Tapered Beams,"http://www.core.umd.edu/Papers/Articles/LeeJAHS95.pdf

[27] P. Yarrington, J. Zhang, C. Collier, and B. Bednarcyk, "Failure Analysis of Adhesively Bonded Composite Joints," AIAA-2005-2376, 46th AIAA/ASME/ASCE/AHS/ASC Structures, Structural Dynamics and Materials Conference , Austin, Texas, Apr. 18-21, 2005.

[28] Maenghyo Cho and Heung S. Kim, "Free-Edge Stress Analysis of Composite Laminates With Interface Modeling," AIAA-1999-1224, Collection of Technical Papers. Vol. 1 (A99-24601 05-39).

[29] Maenghyo Cho and Heung S. Kim, "Iterative Free Edge Stress Analysis of Composite Laminates under Extension, Bending, Twisting and Thermal Loadings,"AIAA-1998-1880, Collection of Technical Papers. Pt. 2 (A98-25092 06-39).

[30] Matthew T. Fenske and Anthony J. Vizzini, "The Inclusion of In-Plane Stresses in Delamination Criteria,"AIAA-1998-1743, Collection of Technical Papers. Pt. 1 (A98-25001 06-39).

[31] Naveen Rastogi, Som R. Soni, and Arvind Nagar, "A Combined Analytical and Experimental Study of Design Parameters in Composite Bonded Joints," AIAA-1998-1882, Collection of Technical Papers. Pt. 2 (A98-25092 06-39).

[32] Naveen Rastogi, "Three-Dimensional Analysis of Composite Structures using Variable-Order Solid Elements," AIAA-1999-1226, Collection of Technical Papers. Vol. 1 (A99-24601 05-39).

[33] David W. Sleight, Norman F. Knight Jr., and John T. Wang, "Evaluation of a progressive failure analysis methodology for laminated composite structures," AIAA-1997-1187, Collection of Technical Papers, Pt. 3 (A97-24112 05-39).

[34] John Klug, Scott Maley, C. T. Sun, "Characterization of Fatigue Behavior of Bonded Composite Repairs," *Journal of Aircraft*, 0021-8669 Vol.36, No.6 (1016-1022), 1999.

[35] R. S. Long, "Static Strength of Adhesively Bonded ARALL-1 Joints," *Journal of Composite Materials*, 1991, Vol. 25, pp.391-415.

[36] J. W. Renton and J. R. Vinson, "On the Behavior of Bonded Joints in Composite Material Structures," *Engineering Fracture Mechanics*, 1975, Vol. 7. pp. 41-60.

[37] R. D. Adams, "Strength Predictions for Lap Joints, Especially with Composite Adherends. A Review," *Journal of Adhesion*, 1989. Vol. 30. pp. 219-242.

[38] A. K. Roy, S. L. Donaldson, and G. A. Schoeppner, "Bonded Joints of Unidirectional and Cross-Ply Laminates: An Experimental Study," *A Collection of Technical Papers*, 38th AIAA/ASME/ASCE/AHS/ASC Structures, Structural Dynamics, and Materials Conference, April 7-10,1997, Kissimmee, FL, Part 3, AIAA-97-1121, pp. 1994-2003.

[39] T. K. O'Brien, "Characterization of Delamination Onset and Growth in Composite Materials," ASTM STP 775, K. L Reifsnider. Ed., American Society for Testing and Materials, 1982, pp. 140-167.

[40] T. K. O'Brien, "Interlaminar Fracture of Composites," NASA Technical Report, NSAS-TR-85768, June, 1984.

[41] L. Flaggs and J. R. Vinson, "Shear Properties of Promising Adhesives for Bonded Joints in Composite Material Structures," *Journal of Aircraft*, 0021-8669 Vol.16, No.1 (51-54), 1979.

[42] Chihdar Yang, Hai Hung, John S. Tomblin, and Donald W. Oplinger, "Evaluation and Adjustment for ASTM D5656 Standard Test Method for Thick-Adherend Metal Lap-Shear Joints for Determination of the Stress-Strain Behavior of Adhesives in Shear by Tension Loading."

[43] Designation: D5656-95, "Standard Test Method for Thick-Adherend Metal Lap-Shear Joints for Determination of the Stress-Strain Behavior of Adherend in Shear by Tension Loading," American Society for Testing and Materials, 1916 Race St. Philadeiphia, PA 19103, USA.

[44] "ABAQUS Analysis User's Manual," Hibbitt, Karlsson & Sorensen, Inc., 2002.

[45] G. D. Dean and L. E. Crocker, "Temperature Dependence of the Properties of and Epoxy Adhesive," NPL Report CMMT (A) 43, August 2001.

[46] G. D. Dean, G. J. Lord, and B. C. Duncan, "Comparison of Measured and Predicted Performance of Adhesive Joints under Impact," NPL Report CMMT (A) 198, October 1999.

[47] G. D Dean and L. E. Crocker, "The Use of Finite Element Method for Design with Adhesive," NPL Report ISSN 1368 6550, August 2001.

[48] R. J. Amos, BAE System, Royal Ordnance, "On a Viscoplastic Characterisation of Solid Propellant and the Prediction of Grain Failure on Pressurisation Cold," AIAA Report 2001-3719, July 2001.

[49] P. Bogert, A. Satyanarayana, and P. Chunchu, “Comparison of Damage Path Predictions for Composite Laminates by Explicit and Standard Finite Element Analysis Tools,” AIAA-2006-1750, 14th AIAA/ASME/AHS Adaptive Structures Conference 7th, Newport, Rhode Island, May 1-4, 2006.

[50] Norman F. Knight Jr., Charles C. Rankin, and Frank A. Brogan , “Controlling progressive failure analyses using artificial viscous damping,” AIAA-2001-1181, AIAA/ASME/ASCE/AHS/ASC Structures, Structural Dynamics, and Materials Conference and Exhibit, 42nd, Seattle, WA, Apr. 16-19, 2001

[51] W. R. Broughton, L. E. Crocker, and J. M. Urquhart, “Strength of Adhesive Joints: A Parameter Study,” NPL Report MATC (A) 27, July 2001.

[52] Chihdar Yang, John S. Tomblin, and Zhidong Guan, “Analytical Modeling of ASTM Lap Shear Adhesive Specimens,” FAA Technical Report DOT/FAA/AR-02/130, February 2003.

[53] J. N. Reddy, “An Introduction to the Finite Element Method,”2/E, McGraw-Hill, Inc. NJ, 1993.

[54] Indrajit Chowdhury and Shambhu P. Dasgupta, “Computation of Rayleigh Damping Coefficients for Large Systems,” http://www.ejge.com/2003/Ppr0318/Ppr0318.pdf

[55] Shaun P. Marlatt and Shahram Payandeh, “Modeling the Effect of Rayleigh Damping on the Stability of Real-time Finite Element Models.”

[56] Osama N. Ashour and Ali H. Nayfeh, “Nonlinear Control of Plate Vibrations,” 42nd AIAA Structures, Structural Dynamics, and Materials Conference and Exhibit, A01-25042, AIAA-2001-1233, April 2001.

[57] John A. Lips, Joseph D. Mello, Peter M. Wegner, and Jeffry S. Welsh, “Finite Element Methods for the Frequency Response Prediction of Bonded Composite Structures,” AIAA Report 2003-6323, September 2003.

[58] Chihdar Yang and Su-Seng Pang, “Stress-Strain Analysis of Single-Lap Composite Joints under Tension,” *Journal of Engineering Materials and Technology,* Vol. 118, pp. 247-255, April 1996.

[59] Stephen W. Tsai, “Theory of Composites Design,” THINK Composites, 1992, ISBN 0-9618090-3-5.

[60] F. París, E. Correa and V. Mantč, “Micromechanical Bases for the Prediction of Failure of the Matrix in Fibrous Composites,” AIAA-2003-1850, 44th AIAA/ASME/ASCE/AHS/ASC Structures, Structural Dynamics, and Materials Conference, Norfolk, Virginia, Apr. 7-10,2003.

[61] Ronald Krueger, Isabelle L. Paris, T. Kevin O'Berin, and Pierre J. Minguet, "Comparison of 2D Finite Element Modeling Assumptions with Results from 3D Analysis for Composite Skin-Stiffener Debonding," NASA Langley Research Center, The Boeing Company.

[62] D. J. Chen and Wen S. Chan, "Use of Composite Effective Moduli for Lumping Layers in Finite Element Analysis," AIAA Meeting Papers on Disc, A96-27017, AIAA Paper 96-1568-CP, pp. 2199-2209, 1996.

[63] Wen S. Chan and S. Vedhagiri, "Analysis of Composite Bonded/Bolted Joints Used in Repairing," *Journal of Composite Materials*, Vol. 35, No.12, 2001.

[64] G. Shi, C. Poon, and Y. Xiong, "Finite Element Design and Analysis of a Bolted Patch Repair for Composites," AIAA-2001-1489, AIAA/ASME/ASCE/AHS/ASC Structures, Structural Dynamics, and Materials Conference and Exhibit, 42nd, Seattle, WA, Apr. 16-19, 2001.

[65] Patrick Johnson and Fu-Kuo Chang, "Accumulated damage and failure of finite-width composite laminates," AIAA-1996-1356,
AIAA/ASME/ASCE/AHS/ASC Structures, Structural Dynamics, and Materials Conference and Exhibit, 37th, Salt Lake City, UT, Apr. 15-17, 1996, Technical Papers. Pt. 1 (A96-2680106-39).

[66] C. Dávila, N. Jaunky and S. Goswami, "Failure Criteria for FRP Laminates in Plane Stress," AIAA-2003-1991, 44th AIAA/ASME/ASCE/AHS/ASC Structures, Structural Dynamics, and Materials Conference, Norfolk, Virginia, Apr. 7-10, 2003.

[67] C. T. Sun, B. J. Quinn, and D. W. Oplinger, "Comparative Evaluation of Failure Analysis Methods for Composite Laminates," DOT/FAA/AR-95/109, 1996.

[68] A. Puck and H. Schurmann, "Failure Analysis pf FRP Laminates by Means of Physically Based Phenomenological Models," Composites Science and Technology, Vol. 62, No. 12-13, 2002, pp.1633-1662.

[69] Chihdar Yang and Su-Seng Pang, "A Laminated Plate Model of an Adhesive-Bonded Taper-Taper Joint under Tension," *Journal of Engineering Materials and Technology,* Vol. 119, pp. 408-414, October 1997.

[70] Jian Zhang, Brett A. Bednarcyk, Craig Collier, Phil Yarrington, Yogesh Bansal, and Marek-Jerzy Pindera, "3D Stress Analysis of Adhesively Bonded Composite Joints," AIAA Report 2005-2021, 2005.

[71] David H. Mollenhauer, "Interlaminar Deformation at a Hole in Laminated Composites: A Detailed Experimental Investigation Using Moiré Interferometry,"
http://scholar.lib.vt.edu/theses/available/etd-72197-23122/unrestricted/ETD.PDF

APPENDIX

APPENDIX A

RELATIVE DISPLACEMENT CALCULATION OF 4-PINED (KGR-1) MODIFED METHOD

The concept of 4-pinned revised method [44] is illustrated as Figure A-1 below. The specimen is deformed and the four points remarked as nodal numbers represent the 4 holes to which the KGR-1 is mounted. Points A and B are the mid points of nodes 4462 and 3482 and nodes 2559 and 2879, respectively. Figure A-2 depicts, V_1 and V_2 denoting the position vectors from point A to B and node 2559 to 2879, respectively. The angle θ is measured between vector V_1 and V_2 after deformation of the specimen. The relative displacement, measured from mid point A to B, using this revised method represents the average relative displacement of the four nodes (pinholes). The relative displacement is along the direction from node 2559 to 2879, which is the direction vector of V_1. The relative displacement calculated is not equal to the relative displacement along the global x-direction.

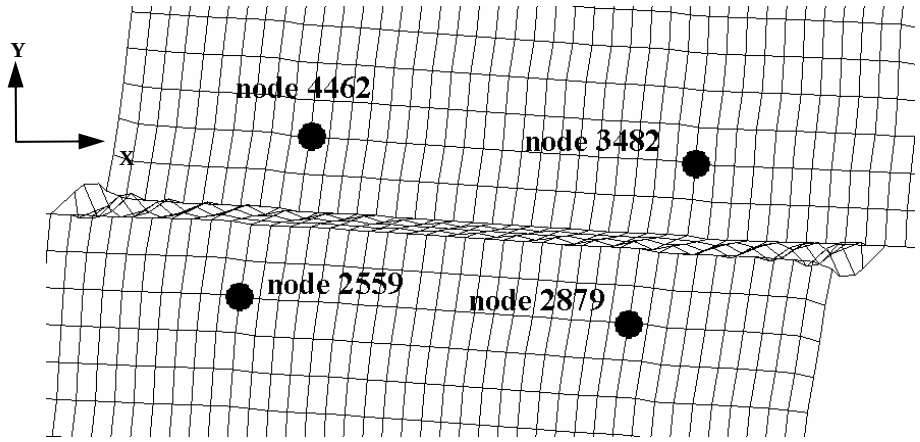

Figure A-1. 4-Pined (KGR-1) conceptual contour after specimen deformed (abstracted from finite element results).

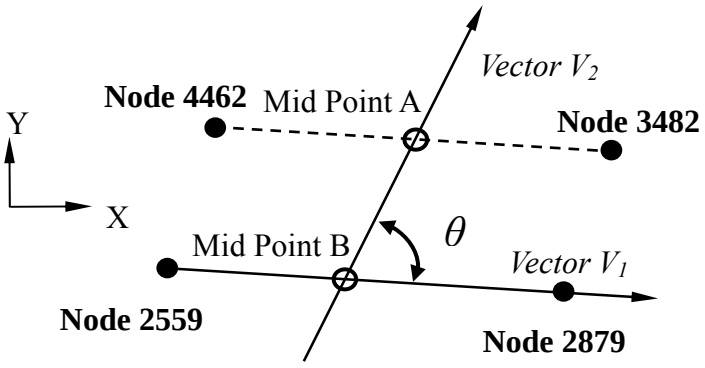

Figure A-2. Symbolic scheme for KGR-1 after deformation of specimen.

The location of the nodes, in terms of mathematical expression (refer to Figure A-2), can be described by

Node 2559 (x_1,y_1) Node 2879 (x_2,y_2)

Node 3482 (x_3,y_3) Node 4462 (x_4,y_4)

The coordinate data of the four pins (nodes) can be either recorded by a test machine or from finite element software for each time increment.

Mid point A $(\frac{1}{2}(x_3+x_4),\frac{1}{2}(y_3+y_4))$ Mid point B $(\frac{1}{2}(x_1+x_2),\frac{1}{2}(y_1+y_2))$

Position vector V_1 $[(x_2\text{-}x_1),(y_2\text{-}y_1)]$ Position vector V_2 $[(x_3\text{-}x_4),(y_3\text{-}y_4)]$

According to the dot product rule, the angle can be obtained by

$$\cos(\theta)=\frac{V_1\cdot V_2}{|V_1||V_2|},\qquad \theta=\cos^{-1}(\frac{V_1\cdot V_2}{|V_1||V_2|}) \tag{A-2}$$

The length of the point A to B is signified as

$$L_{AB}=|V_2|=\sqrt{(x_3-x_4)^2+(y_3-y_4)^2} \tag{A-3}$$

Therefore, the relative displacement of point A to B along the direction V_1 is equal to

$$L_R=L_{AB}\cos(\theta)=|V_2|\frac{V_1\cdot V_2}{|V_1||V_2|}=\frac{V_1\cdot V_2}{|V_1|} \tag{A-4}$$

The first-order shear deformation plate theory (*Hencky-Mindlin assumptions*) has applied to describe the displacement field of lap joints. The rotation angle of the cross section of the overlap (contributed from adherends, owing to their large thickness relative to thin adhesive) can be derived from equation (A-4). From other researches [44,50], the adhesive stress states can be expressed in terms of the moduli of the adhesive with associated strain states of the adherends. Because the displacements measured are from the adherend parts rather than directly from the adhesive itself. The displacement field along loading direction (x-direction) and the rotated angle can be defined as

$$u(x) = u_o + z\varphi(x) \qquad \varphi(x) = \frac{dx}{dw} = 90 - \theta \tag{A-5}$$

in which u_o indicates mid-plane displacement and θ is replaced by equation (A-2). The angle θ quantifies the rotation of the adherends due to shear and implies the extent of deformation of the adhesive.